

# Mining Science and Technology

Горные науки  
и технологии

Vol. **10** № **1**  
Том **10** № **1**  
**2025**



<https://mst.misis.ru/>

<https://t.me/MinSciTech>



**Activities of the Mining Science and Technology (Russia) (Gornye nauki i tekhnologii)** international journal are aimed at developing international scientific and professional cooperation in the field of mining.

**The journal target** audience comprises researchers, specialists in the field of mining, representatives of academic and professional communities.

**The journal publishes** original papers describing research findings, experience in the implementation of projects in mining industry, review publications.

The journal seeks to develop interdisciplinary areas that contribute to progress in mining, for example, technological and environmental safety, project organization and management in mining industry, development of territories, legal aspects of natural resource use, and other areas studied by researchers and practitioners. The journal always welcomes new developments. Papers are accepted in English or Russian.

## EDITOR-IN-CHIEF

**Vadim L. Petrov**, Prof., Dr.Sci.(Eng.), University of Science and Technology MISIS, Moscow, Russian Federation

## DEPUTIES EDITOR-IN-CHIEF

**Oleg I. Kazanin**, Prof., Dr.Sci.(Eng.), Empress Catherine II Saint Petersburg Mining University, St. Petersburg, Russian Federation

**Svetlana A. Epshtein**, Dr.Sci.(Eng.), University of Science and Technology MISIS, Moscow, Russian Federation

## EDITORIAL BOARD

**Zach Agioutantis**, Prof., Ph.D., University of Kentucky, Lexington, Kentucky, USA

**Maksim A. Bogdasarou**, Prof., Dr.Sci.(Geol. and Min.), Brest State A. S. Pushkin University, Brest, Belarus

**Grigory Yu. Boyarko**, Prof. Dr. Sci. (Econ.), Cand. Sci. (Geol. and Miner.), National Research Tomsk Polytechnic University, Tomsk, Russian Federation

**Xuan Nam Bui**, Prof., Dr.Sci., Hanoi University of Mining and Geology, Duc Thang – Bac Tu Liem, Hanoi, Vietnam

**Carsten Drebenstedt**, Prof., Ph.D., Freiberg University of Mining and Technology, Freiberg, Germany

**Faramarz Doulati Ardejani**, Prof., Ph.D., Colledge of Engineering, University of Tehran, Tehran, Iran

**Mikhail S. Ershov**, Prof., Dr.Sci.(Eng.), National University of Oil and Gas "Gubkin University", Moscow, Russian Federation

**Alexandr N. Evdokimov**, Dr.Sci. (Geol. and Min.), Empress Catherine II Saint Petersburg Mining University, St. Petersburg, Russian Federation

**Alper A. Feyzullaev**, Prof., Dr.Sci.(Geol. and Min.), Institute of Geology and Geophysics of the National Academy of Sciences of Azerbaijan, Baku, Azerbaijan

**Ochir Gerel**, Prof., Dr.Sci.(Geol. and Min.), Geoscience Center, the Mongolian University of Science and Technology, Ulaanbaatar, Mongolia

**Zoran Gligorić**, Prof., Dr.Sci. (Mining-Underground Mining), University of Belgrade, Belgrade, Republic of Serbia

**Monika Hardygora**, Prof., Ph.D., Wroclaw University of Technology, Wroclaw, Poland

**Nikolae Ilias**, Prof., Dr.Sci.(Eng.), University of Petrosani, Petrosani, Romania

**Vladislav Kecojevic**, Prof., Ph.D., Benjamin M. Statler College of Engineering and Mineral Resources, West Virginia University, Morgantown, West Virginia, USA

**Aleksey A. Khoreshok**, Prof., Dr.Sci.(Eng.), Gorbachev Kuzbass State Technical University, Kemerovo, Russian Federation

**Vladimir I. Klishin**, Prof., Dr.Sci.(Eng.), Institute of Coal, Siberian Branch, Russian Academy of Sciences, Kemerovo, Russian Federation

**Vladimir N. Koshelev**, Prof., Dr.Sci.(Chem.), National University of Oil and Gas "Gubkin University" (Gubkin University), Moscow, Russian Federation

**Jyant Kumar**, Prof., Ph.D-Geotech.Eng., Indian Institute of Science, Bengaluru, India

**Vladimir A. Makarov**, Prof., Dr.Sci.(Geol. and Min.), Siberian Federal University, Krasnoyarsk, Russian Federation

**Sergey I. Malafeev**, Prof., Dr.Sci.(Eng.), Vladimir State University named after Alexander and Nikolay Stoletovs, Vladimir, Russia

**Oleg S. Misnikov**, Prof., Dr.Sci.(Eng.), Tver State Technical University, Tver, Russian Federation

**Valery V. Morozov**, Prof., Dr.Sci.(Eng.), University of Science and Technology MISIS, Moscow, Russian Federation

**Igor M. Petrov**, Dr.Sci.(Eng.), Infomine Research Group LLC, Moscow, Russian Federation

**Bakhadirzhan R. Raimzhanov**, Prof., Dr.Sci.(Eng.), University of Science and Technology MISIS (branch), Almalyk, Uzbekistan

**Bayan R. Rakishev**, Prof., Dr.Sci.(Eng.), Kazakh National Research Technical University named after K.I. Satpayev, Alma-Ata, Kazakhstan

**Oscar Jaime Restrepo Baena**, Prof., Ph.D., National University of Colombia, Medellín, Colombia

**Alexander N. Shashenko**, Prof., Dr.Sci.(Eng.), National Mining University, Dnipro, Ukraine

**Vadim P. Tarasov**, Prof., Dr.Sci.(Eng.), University of Science and Technology MISIS, Moscow, Russian Federation

**Denis P. Tibilov**, Prof., Dr.Sci.(Econ.), Moscow State Institute of International Affairs (University) under the Ministry of Foreign Affairs of Russia, Moscow, Russian Federation

**Niyaz G. Valiev**, Prof., Dr.Sci.(Eng.), The Ural State Mining University, Ekaterinburg, Russian Federation

**Natalia Zhuravleva**, Prof., Dr.Sci.(Eng.), West Siberian Testing Center JSC (WSTCenter JSC), Novokuznetsk, Russian Federation

**Vera V. Yurak**, Assoc. Prof., Dr. Sci. (Econ.), Ural State Mining University, Yekaterinburg; Institute of Economics, Ural Branch of the Russian Academy of Sciences, Yekaterinburg, Russian Federation

## EDITORIAL COUNCIL

**Yuri G. Agafonov**, Assoc. Prof., Cand.Sci.(Eng.), University of Science and Technology MISIS, Moscow, Russian Federation

**Michael R. Filonov**, Prof., Dr.Sci.(Eng.), University of Science and Technology MISIS, Moscow, Russian Federation

**Leonid A. Plaschansky**, Prof., Cand.Sci.(Eng.), University of Science and Technology MISIS, Moscow, Russian Federation

**Yuri I. Razorenov**, Prof., Dr.Sci.(Eng.), Empress Catherine II Saint Petersburg Mining University, Saint Petersburg, Russian Federation

## EXECUTIVE SECRETARY

**Daria P. Galushka**, University of Science and Technology MISIS, Moscow, Russian Federation

## QUARTERLY

**FOUNDED** in 2016

## REGISTRATION

The journal science and applied research journal is registered by the Federal Service for Communication, IT and Mass Communication Control on August 10, 2015.  
Registration Certificate E-No. ФС77-62652

## INDEXATION

Scopus, CAS, EBSCO, DOAJ, РИНЦ, ВИНТИ РАН, Dimensions, BASE, J-Gate, Jisc Library Hub Discover.

## FOUNDER AND PUBLISHER



**MISIS** UNIVERSITY  
MISIS University of Science and Technology

## CONTACT

4 Leninsky Prospect, Moscow 119049, Russian Federation  
Phone: +7 (495) 955-00-77  
e-mail: [send@misis.ru](mailto:send@misis.ru)



This work is licensed under a  
[Creative Commons Attribution 4.0 License](https://creativecommons.org/licenses/by/4.0/).



Деятельность научно-практического журнала «Горные науки и технологии» (Mining Science and Technology (Russia)) направлена на развитие международного научного и профессионального сотрудничества в области горного дела.

Целевая аудитория журнала – исследователи, специалисты в области горного дела, представители академического и профессионального сообществ.

В журнале публикуются оригинальные статьи, описывающие результаты исследований, опыт реализации проектов в горнопромышленном комплексе, обзорные публикации.

Журнал стремится развивать такие междисциплинарные направления, как технологическая и экологическая безопасность, организация и управление проектами в горной промышленности, развитие территорий, правовые аспекты использования природных ресурсов и другие, которые способствуют прогрессу в горном деле и реализуются исследователями и практиками.

## ГЛАВНЫЙ РЕДАКТОР

**Петров Вадим Леонидович**, проф., д.т.н., Университет науки и технологий МИСИС, г. Москва, Российская Федерация

## ЗАМЕСТИТЕЛИ ГЛАВНОГО РЕДАКТОРА

**Казанин Олег Иванович**, проф., д.т.н., Санкт-Петербургский горный университет императрицы Екатерины II, г. Санкт-Петербург, Российская Федерация

**Эпштейн Светлана Абрамовна**, д.т.н., Университет науки и технологий МИСИС, г. Москва, Российская Федерация

## РЕДАКЦИОННАЯ КОЛЛЕГИЯ

**Агиутантис Зак**, проф., д-р наук, Университет Кентукки, г. Лексингтон, Кентукки, США

**Богдасаров Максим Альбертович**, проф., д.г.-м.н., Брестский государственный университет им. А.С. Пушкина, г. Брест, Беларусь

**Боярко Григорий Юрьевич** – проф., д.э.н., к.г.-м.н., Национальный исследовательский Томский политехнический университет, г. Томск, Российская Федерация

**Буи Суан Нам**, проф., д-р наук, Ханойский университет горного дела и технологии, г. Ханой, Вьетнам

**Валиев Нияз Гадым оглы**, проф., д.т.н., Уральский государственный горный университет, г. Екатеринбург, Российская Федерация

**Герел Очир**, проф., д.г.-м.н., Центр геолого-геофизических исследований, Монгольский университет науки и технологии, г. Улан-Батор, Монголия

**Глигорич Зоран**, проф., д-р наук, Белградский университет, г. Белград, Республика Сербия

**Дребенштедт Карстен**, проф., д-р наук, Технический университет Фрайбергская горная академия, г. Фрайберг, Германия

**Дулати Ардежани Фарамарз**, проф., д-р наук, Инженерный колледж, Тегеранский университет, г. Тегеран, Иран

**Евдокимов Александр Николаевич**, проф., д.г.-м.н., Санкт-Петербургский горный университет императрицы Екатерины II, г. Санкт-Петербург, Российская Федерация

**Ершов Михаил Сергеевич**, проф., д.т.н., Российский государственный университет нефти и газа (национальный исследовательский университет) им. И.М. Губкина, г. Москва, Российская Федерация

**Журавлева Наталья Викторовна**, проф., д.т.н., АО «Западно-Сибирский испытательный центр» (АО «ЗСИЦентр»), г. Новокузнецк, Российская Федерация

**Илиаш Николае**, проф., д.т.н., Университет Петрошани, г. Петрошани, Румыния

**Кеоджевич Владислав**, проф., д-р наук, Институт инженерного дела и минеральных ресурсов им. Бенджамина М. Статлера Университета Западной Вирджинии, г. Моргантаун, Западная Вирджиния, США

**Клишин Владимир Иванович**, проф., д.т.н., Институт угля Сибирского отделения Российской академии наук, г. Кемерово, Российская Федерация

**Кошелев Владимир Николаевич**, проф., д.х.н., Российский государственный университет нефти и газа им. И.М. Губкина, г. Москва, Российская Федерация

**Кумар Джьянт**, проф., д-р наук (геотехнический инжиниринг), Индийский институт науки (Indian Institute of Science), г. Бангалор, Индия

**Макаров Владимир Александрович**, проф., д.г.-м.н., Сибирский федеральный университет, г. Красноярск, Российская Федерация

**Малафеев Сергей Иванович**, проф., д.т.н., Владимирский государственный университет имени А.Г. и Н.Г. Столетовых, г. Владимир, Российская Федерация

**Мисников Олег Степанович**, проф., д.т.н., Тверской государственный технический университет, г. Тверь, Российская Федерация

**Морозов Валерий Валентинович**, проф., д.т.н., Университет науки и технологий МИСИС, г. Москва, Российская Федерация

**Петров Игорь Михайлович**, д.т.н., ООО «Исследовательская группа «Информайн»», г. Москва, Российская Федерация

**Раимжанов Бахадиржан Раимжанович**, проф., д.т.н., филиал Университета науки и технологий МИСИС, г. Алматы, Узбекистан

**Ракишев Баян Ракишевич**, проф., д.т.н., Казахский национальный исследовательский технический университет им. К.И. Сатпаева, г. Алма-Ата, Казахстан

**Рестрепо Баэна Оскар Хайме**, проф., д-р наук, Национальный университет Колумбии, г. Медельин, Колумбия

**Тарасов Вадим Петрович**, проф., д.т.н., НИТУ «МИСиС», г. Москва, Российская Федерация

**Тиболов Денис Петрович**, проф., д.э.н., Московский государственный институт международных отношений (Университет) Министерства иностранных дел России, г. Москва, Российская Федерация

**Фейзуллаев Акпер Акпер оглы**, проф., д.г.-м.н., Институт геологии и геофизики (ИГГ) Национальной Академии Наук Азербайджана, г. Баку, Азербайджан

**Хорешок Алексей Алексеевич**, проф., д.т.н., Кузбасский государственный технический университет им. М.С. Горбачева, г. Кемерово, Российская Федерация

**Шашенко Александр Николаевич**, проф., д.т.н., Национальный горный университет, г. Днепр, Украина

**Хардигора Моника**, проф., д-р наук, Вроцлавский технологический университет, г. Вроцлав, Польша

**Юрак Вера Васильевна**, доц., д.э.н., Уральский государственный горный университет, г. Екатеринбург; старший научный сотрудник, Институт экономики Уральского отделения Российской академии наук (ИЭ УрО РАН), г. Екатеринбург, Российская Федерация

## РЕДАКЦИОННЫЙ СОВЕТ

**Агафонов Юрий Григорьевич**, доц., к.т.н., Университет науки и технологий МИСИС, г. Москва, Российская Федерация

**Плащанский Леонид Александрович**, проф., к.т.н., Университет науки и технологий МИСИС, г. Москва, Российская Федерация

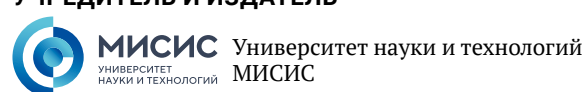
**Разоренов Юрий Иванович**, проф., д.т.н., Санкт-Петербургский горный университет императрицы Екатерины II, г. Санкт-Петербург, Российская Федерация

**Филонов Михаил Рудольфович**, проф., д.т.н., Университет науки и технологий МИСИС, г. Москва, Российская Федерация

## ОТВЕТСТВЕННЫЙ СЕКРЕТАРЬ

**Галушка Дарья Петровна**, Университет науки и технологий МИСИС, г. Москва, Российская Федерация

## УЧРЕДИТЕЛЬ И ИЗДАТЕЛЬ



## АДРЕС УЧРЕДИТЕЛЯ И ИЗДАТЕЛЯ

119049, г. Москва, Ленинский проспект, д. 4

## КОНТАКТЫ РЕДАКЦИИ

Адрес: 119049, г. Москва, Ленинский проспект, д. 4

Телефон: +7 (495) 955-00-77

e-mail: [send@misis.ru](mailto:send@misis.ru)



Контент доступен под лицензией  
Creative Commons Attribution 4.0 License.

## ПЕРИОДИЧНОСТЬ 4 раза в год

ОСНОВАН в 2016 году

## РЕГИСТРАЦИЯ

Зарегистрирован Федеральной службой по надзору в сфере связи, информационных технологий и массовых коммуникаций 10 августа 2015 года.

Свидетельство о регистрации Эл № ФЦ77-62652.

## ИНДЕКСИРОВАНИЕ

Scopus, CAS, EBSCO, DOAJ, РИНЦ, ВИНТИ РАН, Dimensions, BASE, J-Gate, Jisc Library Hub Discover.



Журнал открытого доступа.



## CONTENTS

### MINING ROCK PROPERTIES. ROCK MECHANICS AND GEOPHYSICS

Fracture toughness of rock-concrete interfaces and its prediction based on acoustic properties ..... 5

*A. S. Voznesenskii, E. I. Ushakov, Ya. O. Kutkin*

Experimental research of stress-strain properties of sandy soil when strengthened  
with polyurethane compounds ..... 15

*T. V. Shilova, S. V. Serdyukov, A. N. Drobchik*

### TECHNOLOGICAL SAFETY

Influence of the sorption properties of potash salts on the gas environment  
in dead-end mine workings ..... 25

*A. N. Starikov, S. V. Maltsev, A. E. Sukhanov*

Evaluation of variation of salt dust hygroscopic aerosol particle size  
as a function of relative air humidity ..... 34

*K. A. Chernyi, G. Z. Faynburg*

### ENVIRONMENTAL PROTECTION

Preparation of adsorbents for the extraction of heavy metals from mining wastewater ..... 45

*E. I. Mirzaeva, N. F. Isaeva, E. Ya. Yalgashev, D. P. Turdiyeva, R. M. Boymonov*

### MINING MACHINERY, TRANSPORT, AND MECHANICAL ENGINEERING

Material composition of magnetic fractions of copper-smelting slag flotation tailings ..... 56

*A. L. Kotelnikova, E. S. Zolotova*

### BENEFICIATION AND PROCESSING OF NATURAL AND TECHNOGENIC RAW MATERIALS

Impact of the technical condition of main pumps on fuel consumption  
in a hydraulic excavator ..... 67

*M. G. Rakhutin, V. H. Tran, A. E. Krivenko, Q. Kh. Giang*

### POWER ENGINEERING, AUTOMATION, AND ENERGY PERFORMANCE

Mechatronic system for running-in and testing of mechanical transmissions  
in mining shovels ..... 75

*S. I. Malafeev, A. A. Malafeeva, V. I. Konyashin, A. A. Novgorodov*

Assessment of energy efficiency improvement strategies for ventilation  
and hoisting systems during the reconstruction of the Molibden mine ..... 84

*R. V. Klyuev*



## СОДЕРЖАНИЕ

### СВОЙСТВА ГОРНЫХ ПОРОД. ГЕОМЕХАНИКА И ГЕОФИЗИКА

Трещиностойкость границ между горными породами и бетоном и ее прогнозирование по акустическим свойствам ..... 5

*А. С. Вознесенский, Е. И. Ушаков, Я. О. Куткин*

Экспериментальные исследования деформационно-прочностных свойств песчаного грунта при его укреплении полиуретановыми составами ..... 15

*Т. В. Шилова, С. В. Сердюков, А. Н. Дробчик*

### ТЕХНОЛОГИЧЕСКАЯ БЕЗОПАСНОСТЬ

Влияние сорбционных свойств калийных солей на газовую обстановку в тупиковых горных выработках ..... 25

*А. Н. Стариков, С. В. Мальцев, А. Е. Суханов*

Оценка изменения размера гигроскопического аэрозоля соляной пыли в зависимости от относительной влажности воздуха ..... 34

*К. А. Черный, Г. З. Файнбург*

### ОХРАНА ОКРУЖАЮЩЕЙ СРЕДЫ

Получение адсорбентов для извлечения тяжелых металлов из сточных вод горнорудной промышленности ..... 45

*Е. И. Мирзаева, Н. Ф. Исаева, Э. Я. Ялгашев, Д. П. Турдиева, Р. М. Боймонов*

### ОБОГАЩЕНИЕ, ПЕРЕРАБОТКА МИНЕРАЛЬНОГО И ТЕХНОГЕННОГО СЫРЬЯ

Вещественный состав магнитных фракций хвостов флотации медеплавильных шлаков ..... 56

*А. Л. Котельникова, Е. С. Золотова*

### ГОРНЫЕ МАШИНЫ, ТРАНСПОРТ И МАШИНОСТРОЕНИЕ

Влияние технического состояния главных насосов гидравлического экскаватора на расход топлива ..... 67

*М. Г. Рахутин, В. Х. Чан, А. Е. Кривенко, К. К. Занг*

### ЭНЕРГЕТИКА, АВТОМАТИЗАЦИЯ И ЭНЕРГОЭФФЕКТИВНОСТЬ

Мехатронная система для обкатки и испытаний механических передач карьерных экскаваторов ..... 75

*С. И. Малафеев, А. А. Малафеева, В. И. Коняшин, А. А. Новгородов*

Обоснование решений по повышению энергоэффективности вентиляторных установок и подъемных машин в условиях реконструкции рудника «Молибден» ..... 84

*Р. В. Ключев*



## MINING ROCK PROPERTIES. ROCK MECHANICS AND GEOPHYSICS


Research paper

<https://doi.org/10.17073/2500-0632-2024-10-316>

UDC 622.023.23

**Fracture toughness of rock-concrete interfaces and its prediction based on acoustic properties**A. S. Voznesenskii   , E. I. Ushakov  , Ya. O. Kutkin  

University of Science and Technology MISIS, Moscow, Russian Federation

 [asvoznensenskii@misis.ru](mailto:asvoznensenskii@misis.ru)**Abstract**

The relevance of the subject is determined by the need to solve the problem of ensuring the safety and prevent failure of facilities containing an interface between rock and concrete. These include mine shafts, hydroelectric dams in mountainous areas, reinforced concrete tunnel supports and others that are subjected to both static loads from overlying rocks and soils and dynamic loads from explosions and earthquakes. We performed laboratory tests according to the International Society for Rock Mechanics (ISRM) methodology on specimens with interfaces between gypsum stone and sand-cement mortar. The fracture toughness coefficient  $K_{IC}$  of the interfaces in the specimens was investigated. The cylindrical specimens were 40 mm in diameter and 150 mm long with a V-shaped notch in the middle part. The specimens bending strain measured using a three-point pattern allowed the  $K_{IC}$  to be determined based on the maximum force at 5–6 cycles. The average  $K_{IC}$  value for interface between rock and concrete proved much lower than that for rock and even for specimens made entirely of concrete. For the specimens without concrete, the average value was  $1.327 \text{ MPa}\sqrt{\text{m}}$ , and for fully concrete specimens,  $0.858 \text{ MPa}\sqrt{\text{m}}$ . The average value  $K_{IC}$  for the specimens with concrete was  $0.323 \text{ MPa}\sqrt{\text{m}}$ , which was 4 times lower than that for the specimens without concrete and 2.5 times lower than that for the concrete specimens. The formation of a calibrated fracture during testing results in a relative increase in the internal mechanical loss factor  $Q^{-1}$ , determined by the resonance method, by up to 30%. This allows estimating  $K_{IC}$  fracture toughness coefficients of rock-concrete interfaces using  $Q^{-1}$ . The obtained results can be used in actual practice in the design, operation, and organization of nondestructive testing and monitoring of industrial mining facilities that include these interfaces.

**Keywords**

rocks, concrete, gypsum, flintstone, interface, properties, fracture toughness, acoustics, study, testing, acoustic measurements, elastic waves, velocity, losses, prediction, strain

**Financing**

The research was carried out at the expense of grant No. 24-27-00103 of the Russian Science Foundation, <https://rscf.ru/project/24-27-00103>

**Acknowledgments**








The authors would like to thank O. V. Savitsky, Chief Engineer of the Knauf Gips Novomoskovsk mine, for his assistance in rock sampling, and V. B. Ivanov, P. I. Dubinin for the assistance in the fabrication of the testing installation and preparation of specimens for testing.

**For citation**

Voznesenskii A. S., Ushakov E. I., Kutkin Ya. O. Fracture toughness of rock-concrete interfaces and its prediction based on acoustic properties. *Mining Science and Technology (Russia)*. 2025;10(1):5–14. <https://doi.org/10.17073/2500-0632-2024-10-316>

## СВОЙСТВА ГОРНЫХ ПОРОД. ГЕОМЕХАНИКА И ГЕОФИЗИКА

Научная статья

**Трещиностойкость границ между горными породами и бетоном и ее прогнозирование по акустическим свойствам**А. С. Вознесенский   , Е. И. Ушаков  , Я. О. Куткин  

Университет науки и технологий МИСИС, г. Москва, Российская Федерация

 [asvoznensenskii@misis.ru](mailto:asvoznensenskii@misis.ru)**Аннотация**

Актуальность темы определяется необходимостью решения задачи обеспечения сохранности и отсутствия разрушения объектов, содержащих границы раздела между горной породой и бетоном. К ним относятся шахтные стволы, плотины гидроэлектростанций в горных районах, железобетонная крепь



тоннелей и другие, испытывающие воздействия как статических нагрузок от вышележащих пород и грунтов, так и динамические воздействия от взрывов и землетрясений. Лабораторные эксперименты проводились по методике Международного общества по механике горных пород (ISRM) на образцах с границами между гипсовым камнем и песчано-цементным раствором. Исследовался коэффициент трещиностойкости  $K_{IC}$  границ раздела в образцах. Цилиндрические образцы имели диаметр 40 мм и длину 150 мм с V-образным вырезом в средней части. Деформирование образцов при изгибе по трехточечной схеме позволило определить  $K_{IC}$  исходя из максимального усилия при 5–6 циклах. Среднее значение  $K_{IC}$  между породой и бетоном оказалось намного ниже, чем для горной породы и даже для образцов полностью из бетона. Для образцов без бетона среднее значение составило  $1,327 \text{ МПа}\sqrt{\text{м}}$ , а для полностью бетонных образцов  $0,858 \text{ МПа}\sqrt{\text{м}}$ . Среднее значение  $K_{IC}$  для образцов с бетоном составило  $0,323 \text{ МПа}\sqrt{\text{м}}$ , что в 4 раза меньше, чем для образцов без бетона, и в 2,5 раза меньше, чем для бетонных образцов. Образование калиброванной трещины при испытании приводит к относительному увеличению коэффициента внутренних механических потерь  $Q^{-1}$ , определяемого резонансным методом, до 30 %. Это позволяет оценить коэффициенты трещиностойкости  $K_{IC}$  границ раздела горная порода – бетон с использованием  $Q^{-1}$ . Полученные результаты могут быть использованы на практике при проектировании, эксплуатации, а также организации неразрушающего контроля и мониторинга промышленных объектов горного производства, включающих данные границы раздела.

#### Ключевые слова

горные породы, бетон, гипс, кремний, граница, свойства, трещиностойкость, акустика, исследование, эксперимент, акустические измерения, упругие волны, скорость, потери, прогнозирование, деформация

#### Финансирование

Исследование выполнено за счет гранта Российского научного фонда № 24-27-00103, <https://rscf.ru/project/24-27-00103/>.

#### Благодарности

Авторы выражают благодарность главному инженеру шахты «Кнауф Гипс Новомосковск» О.В. Савицкому за помощь в отборе образцов горных пород, В.Б. Иванову, П.И. Дубинину за помощь в изготовлении экспериментальной установки и подготовке образцов к испытаниям.

#### Для цитирования

Voznesenskii A.S., Ushakov E.I., Kutkin Ya.O. Fracture toughness of rock-concrete interfaces and its prediction based on acoustic properties. *Mining Science and Technology (Russia)*. 2025;10(1):5–14. <https://doi.org/10.17073/2500-0632-2024-10-316>

### Introduction

In current mining activities, the study subject is often the interface between rock and concrete taking place in many surface and underground structures such as mine shafts, hydroelectric dams in mountainous areas, reinforced concrete tunnel support and other similar facilities. One of the tasks in the construction and operation of such structures is to ensure their safety and prevent failure under the effect of both static loads from overlying rocks and soils and dynamic impacts. The sources of dynamic impacts are seismic waves from explosions [1] and earthquakes [2, 3]. The subject under consideration is an integral part of the solution of the above problem and requires experimental studies (testing) of the strength properties of the interface between rock and concrete.

The theoretical justification of the studies described below is based on the fundamental works of A. Griffiths [4]. Within this theory stress intensity factor  $K$  is considered [5]. Under tension, the stress intensity factor of the first strain mode  $K_I = \sigma\sqrt{\pi l}$ , where  $\sigma$  is the effective stress,  $l$  is fracture length. The ability of a material to maintain its integrity is evaluated by the corresponding fracture toughness coefficient

(FT)  $K_{IC}$  determined based on experimental data. It characterizes the maximum length of a fracture at which no fracture germination occurs. The condition of absence of fracture growth and subsequent failure is described by the expression  $K_I \leq K_{IC}$ .

Knowing the effective stresses  $\sigma$ , as well as FT in combination with the parameters of fractured rock masses and concrete supports will allow ensuring their safety in the design, construction, and operation of mining facilities under the conditions of static and dynamic loads.

FT is applicable to both separate materials such as metals, concrete, composites, and the interfaces between them. Many researchers have studied FT for metals and alloys [6, 7], including heterogeneous ones [8]. For composite materials, FT was investigated in [9, 10]. FT is also used in the evaluation of strength properties of concrete [11], including for special types of concrete such as fibre concrete [12]. FT was used for novel materials used for manufacturing articles at printers [13]. Far fewer publications are devoted to rock FT studies [14], especially concrete-rock interfaces [15].

Typically, experimental research techniques use three- or four-point bending loading schemes

for specimens and rectangular beams [16, 17], half-disks [18], disk specimens [19], and cubes with a notch [20]. For rocks, the FT determination methodology recommended by the International Society of Rock Mechanics (ISRM) is used [21]. FT of interfaces between different rocks or minerals is also of interest in assessing the stability of rock masses. In [22, 23], the methodology and results of determining the fracture toughness coefficient with respect to the interfaces between different rock types was described, and the FT ranges for some their combinations were determined.

The purpose as well as the novelty of this paper consists in evaluating FT of the first strain mode  $K_{IC}$  of the interfaces between different rock types and concrete. In addition, the acoustic properties of rock specimens were determined, and their relationship with  $K_{IC}$  was evaluated. These properties included longitudinal and transverse elastic wave velocities, as well as internal mechanical loss factor  $Q^{-1}$  [24, 25] to evaluate the feasibility of predicting KIC based on the data of acoustic measurements.

The tasks addressed included:

- justification of the testing technique for determining FT of rock-concrete interfaces;
- determination of elastic wave propagation velocities by ultrasonic pulse scanning before and after a test to assess the effect of a forming fracture on the velocities;
- determination of loss factor  $Q^{-1}$  and its changes during the formation of a reference fracture by the resonance method;
- ISRM bending testing of specimens to determine the  $K_{IC}$  of rock-concrete interfaces;

– processing and comparative analysis of the obtained results with determining the ranges of FT values for the interfaces between rocks of different types, as well as between rocks and concrete;

– practical conclusions on the obtained FT values of the interfaces between rocks of different types and concrete to be taken into account in the design and operation of structural elements of mining systems at mining enterprises.

## 1. Research Materials and Techniques

For testing, cylinder specimens 40 mm in diameter and 150 mm long were produced, consisting of two equal parts: rocks from the Novomoskovsk gypsum deposit (Novomoskovsk, Tula region, Russia) [22, 23] and sand-cement mortar. A series of 19 such specimens was prepared and aged for four months until the mortar was fully cured (Fig. 1, *a*). In addition, four specimens were made entirely of sand-cement mortar (Fig. 1, *b*). V-shaped notches were cut in the specimens for the ISRM testing described below.

The test specimens were labeled according to the original 150 mm long gypsum specimens, half of which were used to make concrete coated specimens C. They were labeled as:

- GGC gypsum stone;
- gypsum stone and GKC flintstone interfaces;
- KKC flintstone;
- gypsum-flintstone interface with veins of carbonaceous GUKC clays.

For example, GKC3-1 meant a specimen with an interface between concrete and half of the number 1 specimen made of gypsum and flintstone GK-3.

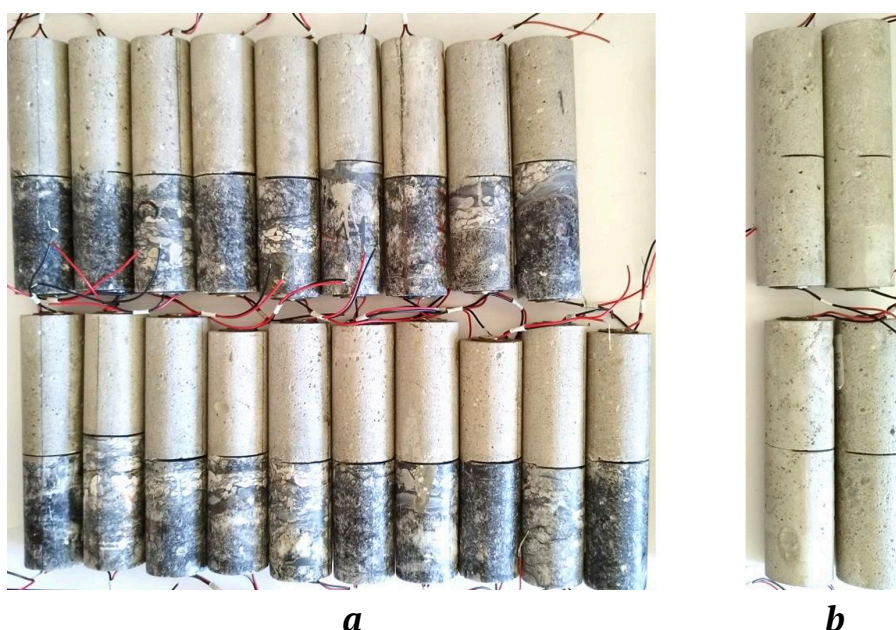


Fig. 1. Specimens with gypsum stone – cement stone interfaces (*a*) and cement stone specimens with notches (*b*)

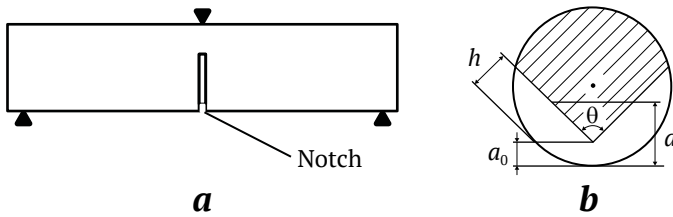


Fig. 2. Schematic of a three-point test on a notched specimen (a) and cross-section of a notched specimen (b)

Tests on 150 mm long cylindrical specimens with notches were carried out according to the three-point scheme shown in Fig. 2, a. The notch was V-shaped, Fig. 2, b, and the angle  $\theta$  was  $90^\circ$ .

In the calculations, formula (1) from [21] was used to determine the fracture toughness coefficient:

$$K_{IC} = \frac{A_{\min} P_{\max}}{D^{1.5}}, \quad (1)$$

$$A_{\min} = \left[ \frac{1.835 + 7.15a_0}{D} + 9.85 \left( \frac{a_0}{D} \right)^2 \right] \cdot \frac{S}{D},$$

where  $K_{IC}$  is fracture toughness coefficient,  $\text{MPa}\sqrt{\text{m}}$ ;  $P_{\max}$  is maximum bending force, kN;  $D$  is diameter of a chevron bending of specimen, cm;  $a_0$  is distance between the chevron indents and specimen surface, cm;  $S$  is distance between the support points, cm.

During the tests, an installation based on the ASIS complex (NPO Geotech LLC, Penza, Russia) was used. The specimens were tested using a three-point bending pattern. In addition to the system that set the cyclic motion of the frame, a second system was used to record the deflection force and magnitude. Two linear displacement transducers (LVDTs) with a measurement range of 10 mm recorded deflection directly on a specimen. These transducers were connected to the 18-bit ADC of the QMBox measuring system (R-Technology, Moscow, Russia).

The installation for determining internal mechanical losses included a JDS 2900 series signal generator with a DPA 1698 power amplifier, a GDS-71022 oscillograph with an external preamplifier, and a specimen holder. Piezoelectric transducers 1.2 mm thick were glued to the ends of a specimen to measure the acoustic losses using the resonance method.

Longitudinal  $P$ - and transverse  $S$ -wave velocities were measured using an ultrasonic instrument (Eco-geos Prom LLC, Tver, Russia). The velocities were determined based on the time taken by elastic pulses to travel through the specimens.

Cycle tests involved maximum frame displacements of 0.10, 0.15, 0.20, 0.25, 0.30, 0.35, 0.40 mm. The minimum displacement was 0.05 mm. The displacement speed was 0.2 mm/min.

Acoustic tests along the long axis of the specimens included the measurement of propagation velocities of longitudinal  $V_p$  and transverse  $V_s$  elastic waves in a rock using standard techniques. Internal mechanical losses were estimated based on the loss factor (or inverse  $Q$ -factor)  $Q^{-1}$ . These estimates were carried out in addition to the mechanical tests two times, before and after a specimen was tested.

Experimental  $Q^{-1}$  measurements were performed through frequency scanning of the resonance characteristics of a specimen. The signal from the SFG-2110 harmonic oscillator was applied to an exciting piezoelectric plate 20.0 mm in diameter and 1.5 mm thick, which was mounted at one end of a specimen. From a second similar piezoelectric plate at the opposite end of the specimen, the signal was fed to a preamplifier with a bandwidth of 20–500 kHz and then to GDS-71022 digital oscillograph. The  $Q^{-1}$  factor was calculated using the following formula:

$$Q^{-1} = \frac{\Delta f}{f_0}, \quad (2)$$

where  $\Delta f$  is frequency bandwidth at  $1/\sqrt{2}$  of the maximum of the resonance curve;  $f_0$  is resonance frequency.

## 2. Testing results

### 2.1. $K_{IC}$ coefficient measurement results for rock-concrete specimens

Figs. 3–6 show, for example, the curves of the time dependencies of a specimen load  $P$  and deflection  $y$ , as well as the load  $P$  dependence of deflection  $y$ . The complete set of plots for all 19 specimens with rock-concrete contacts and four concrete specimens are available in the data.mendeley.com repository [26].

### 2.2. Concrete specimens testing results

Fig. 6 shows similar test results for concrete specimens as an example.

### 2.3. Acoustic properties of specimens with rock-concrete interface

Tables 1 and 2 summarize the results of measuring  $K_{IC}$  using formula (1) and the acoustic properties of rock-concrete specimens and concrete specimens before and after testing. The following designations are used in the tables:

$P_{\max}$  is maximum load during cyclic loading of a specimen;

$K_{IC}$  is fracturing toughness coefficient of the first mode of strain;

$V_p$  is velocity of longitudinal wave propagation;

$V_s$  is velocity of transverse wave propagation;

$f_0$  is specimen resonance frequency;

$Q^{-1}$  is internal mechanical loss factor.

In Table 1, dashes indicate specimens broken up during testing.

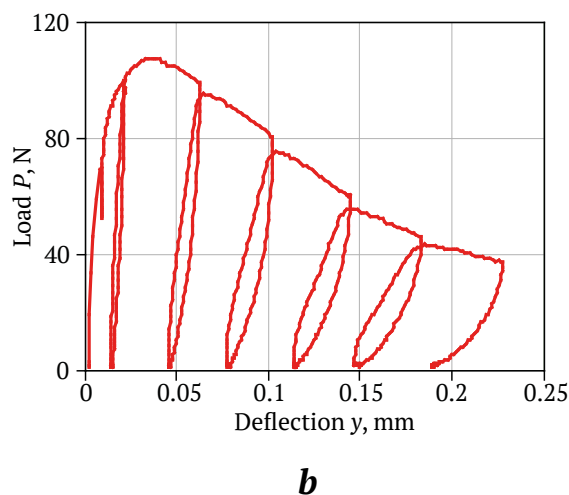
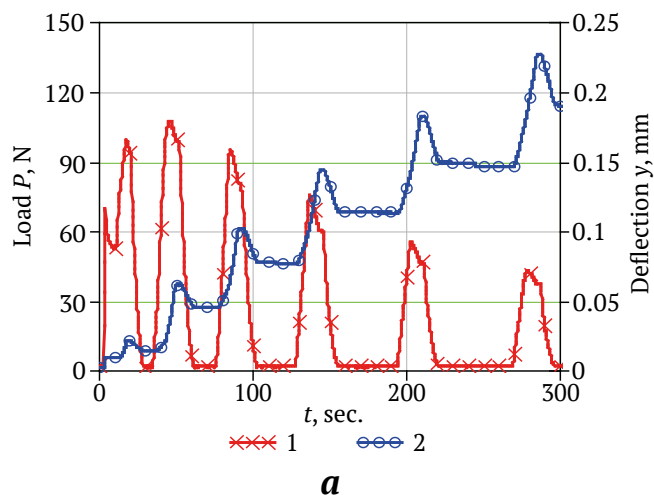


**Fig. 3.** Curves of time dependencies of load and deflection (*a*) and load dependence of deflection (*b*) under cyclic loading of specimen and GKC3-2

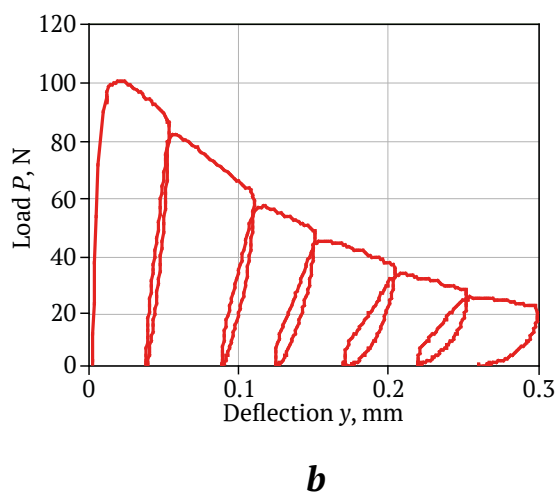
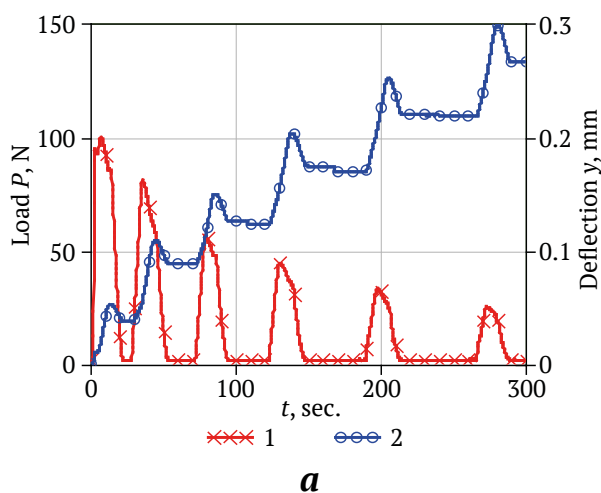


**Fig. 4.** Curves of time dependencies of load and deflection (*a*) and load dependence of deflection (*b*) under cyclic loading of specimen GKC3-2

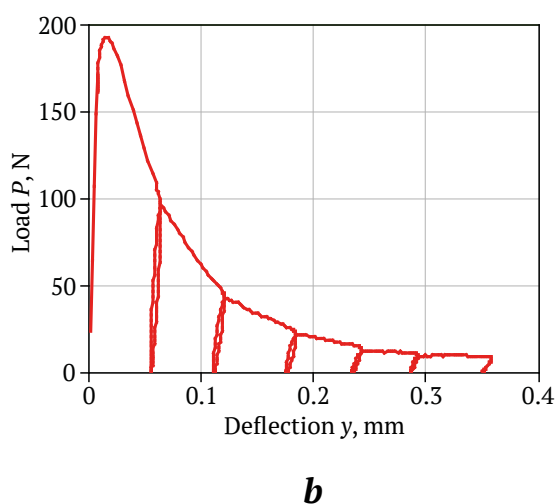
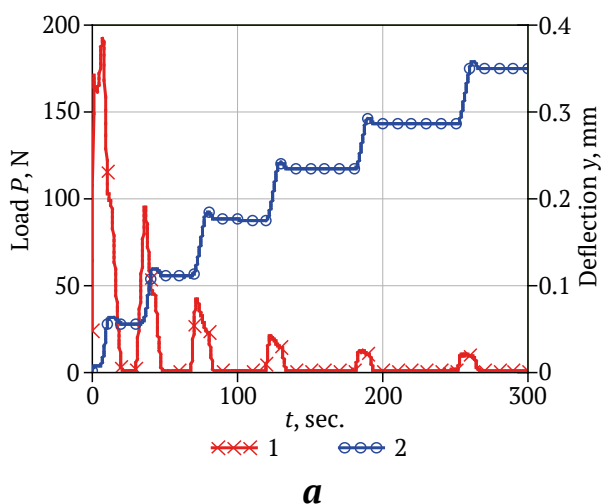


**Fig. 5.** Curves of time dependencies of load and deflection (*a*) and load dependence of deflection (*b*) under cyclic loading of specimen and GKC5-2

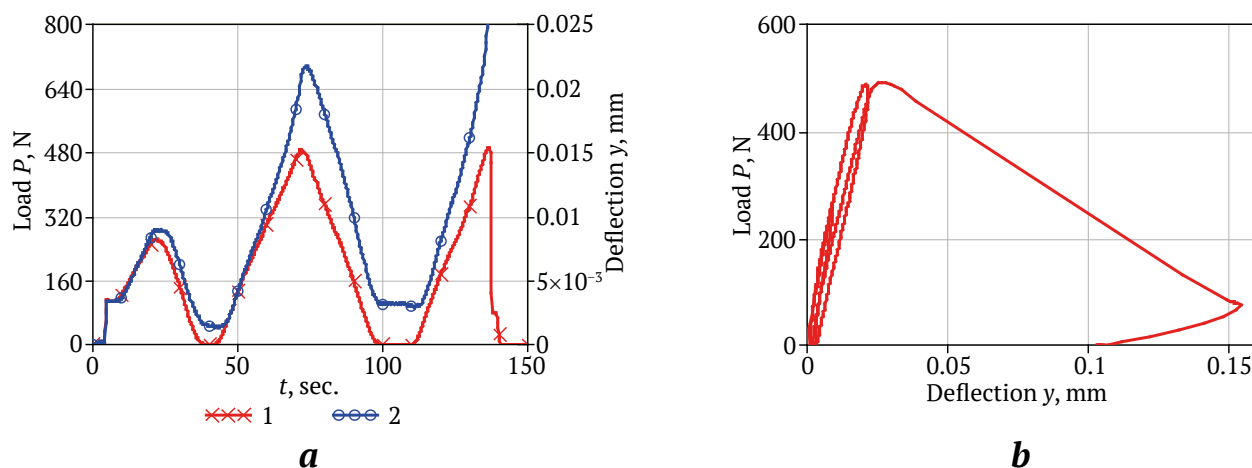


**Fig. 6.** Curves of time dependencies of load and deflection (a) and load dependence of deflection (b) under cyclic loading of specimen C1

Table 1

**Properties of specimens with rock-concrete interface**

Specimen	$P_{max}, N$	$K_{IC}, MPa \times \sqrt{m}$	Before test				After test			
			$V_p, m/s$	$V_s, m/s$	$f_0, Hz$	$Q^{-1} \times 10^{-3}$	$V_p, m/s$	$V_s, m/s$	$f_0, Hz$	$Q^{-1} \times 10^{-3}$
GGC2-1	216.30	0.395	4,019	2,538	22,848	5.26	3,942	2,515	8,992	15.63
GGC2-2	188.42	0.344	4,032	2,649	10,765	4.10	4,012	2,706	10,270	5.18
GGC3-1	154.66	0.282	3,831	2,418	10,205	3.43	–	–	–	–
GGC3-2	67.07	0.122	3,774	2,515	9,110	4.39	–	–	–	–
GKC1-1	229.03	0.418	4,125	2,953	10,402	6.06	4,044	2,917	10,102	4.27
GKC1-2	210.92	0.385	3,876	2,535	9,190	4.13	3,684	2,005	47,750	3.61
GKC2-2	292.63	0.534	4,136	2,665	11,374	4.67	4072	2,923	9,002	10.53
GKC3-1	262.79	0.480	3,831	2,502	9,925	2.72	3,684	1,857	48,910	4.29
GKC3-2	107.68	0.197	3,852	2,484	9,117	3.40	–	–	–	–
GKC5-1	100.35	0.183	3,780	2,500	9,360	5.65	3,549	1,919	50,900	2.77
GKC5-2	192.29	0.351	3,975	2,881	11,000	4.00	–	–	–	–
KKC2-1	238.32	0.435	3,937	3,337	9,620	6.67	–	–	–	–
KKC2-2	165.91	0.303	3,854	2,550	8,967	4.57	3,937	2,582	49,000	5.21
KKC3-1	139.00	0.254	3,872	2,841	10,402	6.33	3,633	2,477	–	–
KKC3-2	121.38	0.222	4,068	2,673	10,617	5.18	3,942	2,695	–	–
KKC5-1	167.38	0.306	4,010	2,574	11,240	4.18	3,989	2,929	10,342	7.75
KKC5-2	292.63	0.534	4,212	2,870	10,823	5.56	4,201	3,236	16,738	5.81
GUKC1-1	81.26	0.148	3,443	2,373	7,030	9.81	–	–	–	–
GUKC1-2	159.55	0.291	3,900	2,675	9,061	3.97	–	–	–	–
Average	178.29	0.323	3,922	2,660	10,581	4.95	3,890	2,563	26,200	6.51

Table 2

**Properties of concrete specimens**

Specimen	$P_{max}, N$	$K_{IC}, MPa \times \sqrt{m}$	Before test				After test			
			$V_p, m/s$	$V_s, m/s$	$f_0, Hz$	$Q^{-1} \times 10^{-3}$	$V_p, m/s$	$V_s, m/s$	$f_0, Hz$	$Q^{-1} \times 10^{-3}$
C1	492.3	0.899	3,571	2,540	22.6	7.29	3,120	2,100	–	–
C2	429.6	0.784	3,392	2,402	19.3	5.70	3242	1,920	–	–
C3	503.0	0.918	3,297	2,430	21.2	5.90	3,170	1616	–	–
C4	456.1	0.832	3,414	2,495	22.8	6.34	3,327	1,849	–	–
Average	470.2	0.858	3,418	2,466	21.5	6.31	3,215	1,808	–	–

Table 3  
 $K_{IC}$  fracture toughness coefficients of rocks and contacts between them without concrete [22, 23]

Specimen	$P_{max}, N$	$K_{IC}, MPa \times \sqrt{m}$
GG-1	639	0.832
GG-2	985	0.995
GG-3	988	1.089
GG-4	817	0.901
UG-1	833	0.919
GUK-1	825	0.950
GUK-2	1,100	1.161
GUK-3	1,194	1.317
GK-3	1,147	1.495
GK-5	1,225	1.351
KK-1	–	–
KK-2	2,039	2.447
KK-3	–	–
KK-4	2,232	2.461

After testing, no clear resonance could be obtained in the specimens due to the increased losses in the concrete that is indicated by dashes in Table 2.

For comparison, Table 3 presents the data from previous tests on specimens of rocks and their interfaces without concrete.

### 3. Findings Discussion

Let us analyze the shapes of the curves in Fig. 3–6, obtained when testing specimens in the conditions of specified cyclic bending strains with increasing maximum displacements in each subsequent cycle.

The peculiarities of plastic strain of the specimens deserve attention. They consisted in the increase of residual plastic strains after each strain cycle and manifested themselves in the form of a characteris-

tic loop-shaped pattern of curves  $P(y)$  with a shift to the right of each subsequent loop. The plots clearly show an area of extreme strain where the maximum load decreased with increasing number of cycles. Coefficient  $K_{IC}$  was calculated based on the highest maximum value  $P_{max}$ . For clarity, all the results of the  $K_{IC}$  testing are presented in the diagram in Fig. 7.

The analysis of  $K_{IC}$  values given in Tables 1 and 3, as well as in Fig. 7, allows drawing the following conclusions.

Without concrete, the interfaces have relatively high  $K_{IC}$  values, especially KKs, for which the  $K_{IC}$  is greater than 2. The presence of flintstone is generally characterized by high  $K_{IC}$  values even in the presence of thin carbonaceous interlayers. The absence of flintstone, such as in the case of GG, is characterized by reduced  $K_{IC}$  values. For pure concrete,  $K_{IC}$  has values close to those for the GG interfaces. For rock-concrete interfaces,  $K_{IC}$  values are extremely low. This can be explained by weak adhesion when forming the contact between them. The difference is especially evident when comparing the averages. The average  $K_{IC}$  value for the specimens without concrete is  $1.327 MPa \times \sqrt{m}$ , the average value for concrete is  $0.858 MPa \times \sqrt{m}$ , and for the specimens with concrete it was  $0.323 MPa \times \sqrt{m}$ , which is 4 times less than that for the specimens without concrete and 2.5 times less than that for the concrete specimens.

As follows from the data of summary Table 1, in most cases, the appearance of a fracture in a specimen middle part in bending tests leads to a decrease in both velocity  $V_p$  and velocity  $V_s$ . The changes were considered to be significant if they were beyond  $\pm 2\%$  of the original pre-test value. The proportion of specimens whose velocity  $V_p$  appeared unchanged, amounted to 42%, and that whose velocity  $V_s$  remained unchanged, 40%. At the same time, half of the specimens showed a decrease in  $V_p$ , while  $V_s$  showed both decrease and increase in equal proportions.  $F_0$  и  $Q^{-1}$  showed a change in all cases.

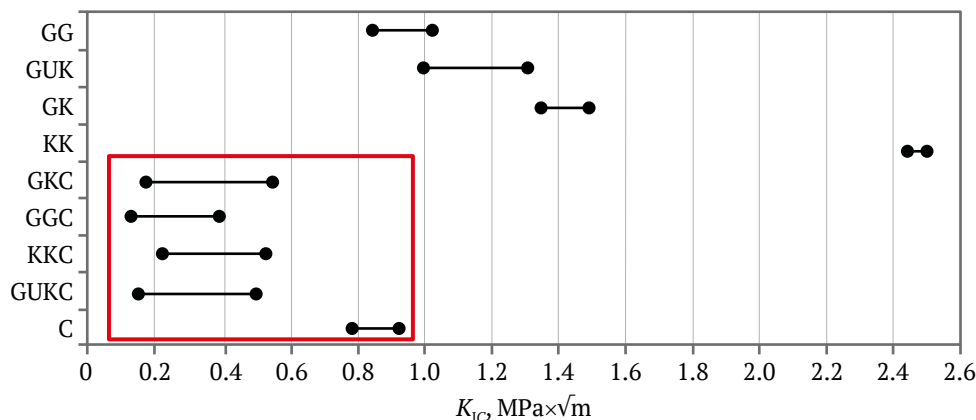


Fig. 7. Ranges of variation of  $K_{IC}$  coefficient for rocks, rock-concrete interfaces, and concrete (encircled)

Table 4

The relationship between the velocities of elastic waves  $V_p$ ,  $V_s$ , loss factor  $Q^{-1}$  in different combinations and  $K_{IC}$  in different combinations and

Indicator	$V_p$	$V_s$	$Q^{-1}$	$V_p, V_s$	$V_p, Q^{-1}$	$V_s, Q^{-1}$	$V_p, V_s, Q^{-1}$
$R$	0.674	0.447	0.190	0.685	0.675	0.533	0.685
$RMS$	0.093	0.306	0.124	0.099	0.096	0.110	0.098

Quantification of the changes in the mean values of  $V_p$  and  $V_s$  shows insignificant decreases, they amounted to 0.992 and 0.964 of the initial values. However, such small changes may not be a sufficiently reliable result. At the same time, the average value of  $Q^{-1}$  (loss factor) for a fracture formation due to a test showed an increase of 1.32 times that can be used to assess the condition of the interface between a rock and concrete when organizing nondestructive testing or monitoring of actual facilities.

Establishing the feasibility of predicting  $K_{IC}$  based on the acoustic properties of facilities is one of the important related objectives. In this case, such an assessment is made on the basis of the correlation coefficient  $R$  and root-mean-square deviation ( $RMS$ ). The correlation coefficients of different combinations of acoustic properties with  $K_{IC}$  of the specimens with rock-concrete interfaces were calculated using Statistica software. The results are presented in Table 4.

As follows from these data, the highest interdependence of  $K_{IC}$  and  $V_p$  is observed. When multivariate statistics is used, other properties allow the correlation coefficient to increase slightly. At the same time, even in this case at  $R = 0.685$ , although interdependence exists, it cannot be considered as very strong. Root-mean-square deviation  $RMS$  characterizes the accuracy of such a forecast. In this case, the root-mean-square deviation was 0.098  $MPa \times \sqrt{m}$ . The average value of  $K_{IC}$  was 0.323  $MPa \times \sqrt{m}$ . The relative accuracy was about 30%.

### Conclusion

The relevance of the experimental study of a rock-concrete interface fracture toughness coefficient  $K_{IC}$  was shown, which can be used in practice in mining industry in the design, construction, and operation of surface and underground structures, such as shafts and permanent mine workings, hydroelec-

tric dams, road and railroad tunnels, as well as other both underground and aboveground facilities having rock-concrete interface.

The current study investigated the fracture toughness of rock interfaces involving gypsum stone and concrete. For the rock-concrete interfaces, the values of the fracturing toughness coefficient of the first strain mode  $K_{IC}$  are extremely low. This can be explained by weak adhesion when forming the contact between them. The difference is especially evident when comparing the averages. The average  $K_{IC}$  value for the specimens without concrete is 1.327  $MPa \times \sqrt{m}$ , the average value for concrete is 0.858  $MPa \times \sqrt{m}$ , and that for specimens with concrete is 0.323  $MPa \times \sqrt{m}$ , which is 4 times less than that of the specimens without concrete and 2.5 times less than that of the concrete specimens.

Evaluation of the effect of an arising fracture on average values of longitudinal  $V_p$  and transverse  $V_s$  elastic wave velocities shows negligible reductions, which are 0.992 and 0.964 of the initial (pre-test) values, respectively. At the same time, the loss factor  $Q^{-1}$  at the formation of a tensile fracture due to testing shows an increase of 1.32 times, which can be accepted as statistically significant.

An evaluation of the feasibility to predict  $K_{IC}$  coefficient based on the acoustic properties showed that the highest correlation was observed with  $V_p$  velocity. When multivariate statistics is used, other properties allow the correlation coefficient  $R$  to increase slightly. At the same time, even in this case at  $R = 0.685$ , the correlation cannot be qualified as strong, although the relationship exists. The relative accuracy in this case is 30%.

The obtained results can be used in the design, operation, as well as organization of nondestructive testing and monitoring of industrial facilities of mining enterprises.

### References

1. Kochanov A.N., Odintsev V.N. Wave prefracturing of solid rocks under blasting. *Journal of Mining Science*. 2016;52(6):1080–1089. <https://doi.org/10.1134/S1062739116061613> (Orig. ver.: Kochanov A.N., Odintsev V.N. Wave prefracturing of solid rocks under blasting. *Fiziko-Tekhnicheskiye Problemy Razrabotki Poleznykh Iskopayemykh*. 2016;(6):38–48. (In Russ.))
2. Zvereva A.S., Sobissevich A.L., Gabsatarova I.P. Coda  $Q$  in the geophysical medium of the Northeast Caucasus. *Fizika Zemli*. 2024;(1):140–156. (In Russ.) <https://doi.org/10.31857/S0002333724010091>



3. Grabkin O.V., Zamaraev S.M., Lashchenov V.A. et al. *Geology and seismicity in the BAM region (from Baikal to Tynda). Structural-material complexes and tectonics*. Novosibirsk: Nauka Publ. House; 1983. 192 p. (In Russ.)
4. Griffith A.A. The phenomena of rupture and flow in solids. *Philosophical Transactions of the Royal Society of London. Series A, Containing Papers of a Mathematical or Physical Character*. 1921;221(582–593):163–198. <https://doi.org/10.1098/rsta.1921.0006>
5. Murakami Yu. (Ed.) *Handbook of stress intensity coefficients*. Vol. 2. Moscow; Mir Publ. House; 1990. 1016 p. (In Russ.)
6. Sezgin J.-G., Bosch C., Montouchet A. et al. Coupled hydrogen and phosphorous induced initiation of internal cracks in a large 18MnNiMo5 component. *Engineering Failure Analysis*. 2019;104:422–438. <https://doi.org/10.1016/j.engfailanal.2019.06.014>
7. Wang Y., MacDonald A., Xu L. et al. Engineering critical assessment and variable sensitivity analysis for as-welded S690 steels. *Engineering Failure Analysis*. 2020;109:104282. <https://doi.org/10.1016/j.engfailanal.2019.104282>
8. Beygi R., Carbas R. J. C., Barbosa A. Q. et al. A comprehensive analysis of a pseudo-brittle fracture at the interface of intermetallic of  $\eta$  and steel in aluminum/steel joints made by FSW: Microstructure and fracture behavior. *Materials Science and Engineering: A*. 2021;824:141812. <https://doi.org/10.1016/j.msea.2021.141812>
9. Eskandari S., Andrade Pires F. M., Camanho P. P. et al. Analyzing the failure and damage of FRP composite laminates under high strain rates considering visco-plasticity. *Engineering Failure Analysis*. 2019;101:257–273. <https://doi.org/10.1016/j.engfailanal.2019.03.008>
10. Mega M., Banks-Sills L. Comparison of methods for determination of fracture toughness in a multi-directional CFRP laminate. *Procedia Structural Integrity*. 2020;28:917–924. <https://doi.org/10.1016/j.prostr.2020.11.064>
11. Ryabchikov A., Kiviste M., Udras S. M. et al. The experimental investigation of the mechanical properties of steel fibre-reinforced concrete according to different testing standards. *Agronomy Research*. 2020;18:969–979. <https://doi.org/10.15159/ar.20.070>
12. Conforti A., Minelli F., Plizzari G. A., Tiberti G. Comparing test methods for the mechanical characterization of fiber reinforced concrete. *Structural Concrete*. 2018;19(3):656–669. <https://doi.org/10.1002/suco.201700057>
13. Valean C., Maravina L., Marghita M. et al. The effect of crack insertion for FDM printed PLA materials on Mode I and Mode II fracture toughness. *Procedia Structural Integrity*. 2020;28:1134–1139. <https://doi.org/10.1016/j.prostr.2020.11.128>
14. Wang Y., Hu X. Determination of tensile strength and fracture toughness of granite using notched three-point-bend samples. *Rock Mechanics and Rock Engineering*. 2017;50(1):17–28. <https://doi.org/10.1007/s00603-016-1098-6>
15. Rong H., Wang Y. J., Zhao X. Y., She J. Research on fracture characteristics of rock-concrete interface with different roughness. *Gongcheng Lixue/Engineering Mechanics* 2019;36(10):96–103. (In Chinese) <https://doi.org/10.6052/j.issn.1000-4750.2018.09.0485>
16. Kožar I., Torić Malić N., Simonetti D., Smolčić Ž. Bond-slip parameter estimation in fiber reinforced concrete at failure using inverse stochastic model. *Engineering Failure Analysis*. 2019;104:84–95. <https://doi.org/10.1016/j.engfailanal.2019.05.019>
17. Kožar I., Bede N., Mrakovčić S., Božić Ž. Layered model of crack growth in concrete beams in bending. *Procedia Structural Integrity*. 2021;31:134–139. <https://doi.org/10.1016/j.prostr.2021.03.022>
18. Lu D. X., Bui H. H., Saleh M. Effects of specimen size and loading conditions on the fracture behaviour of asphalt concretes in the SCB test. *Engineering Fracture Mechanics*. 2020;242:107452. <https://doi.org/10.1016/j.engfracmech.2020.107452>
19. Nazerigivi A., Nejati H. R., Ghazvinian A., Najigivi A. Effects of SiO<sub>2</sub> nanoparticles dispersion on concrete fracture toughness. *Construction and Building Materials*. 2018;171:672–679. <https://doi.org/10.1016/j.conbuildmat.2018.03.224>
20. Seidl S., Ríos J. D., Cifuentes H. Comparison of fracture toughness values of normal and high strength concrete determined by three point bend and modified disk-shaped compact tension specimens. *Frattura ed Integrità Strutturale*. 2017;11(42):56–65. <https://doi.org/10.3221/IGF-ESIS.42.07>
21. Ouchterlony F., Franklin J. A., Zongqi S. et al. Suggested methods for determining the fracture toughness of rock. *International Journal of Rock Mechanics and Mining Sciences & Geomechanics Abstracts*. 1988;25(2):71–96.



22. Voznesenskii A.S., Osipov Y.V., Ushakov E.I. et al. Effect of weak inclusions on the fracture toughness of interfaces between various rocks. *Engineering Failure Analysis*. 2023;146:107140. <https://doi.org/10.1016/j.engfailanal.2023.107140>
23. Voznesenskii A.S., Osipov Y.V., Ushakov E.I., Semyonov Y.G. Fracture toughness of interfaces between various minerals and rocks. *Procedia Structural Integrity*. 2023;46:155–161. <https://doi.org/10.1016/j.prostr.2023.06.027>
24. Mochugovskiy A.G., Mikhaylovskaya A.V., Zadorognyy M.Y., Golovin I.S. Effect of heat treatment on the grain size control, superplasticity, internal friction, and mechanical properties of zirconium-bearing aluminum-based alloy. *Journal of Alloys and Compounds*. 2021;856:157455. <https://doi.org/10.1016/j.jallcom.2020.157455>
25. Blanter M.S., Golovin I.S., Neuhäuser H., Sinning H.R. *Internal friction in metallic materials*. A handbook. Springer Series in Materials Science. Springer-Verlag Berlin, Heidelberg; 2007. 541 p.
26. Ushakov E.I., Voznesenskii A.S. The fracture toughness of interfaces between rocks and concrete. The results of experimental investigations. *Mendeley Data*. 2024;1. <https://doi.org/10.17632/792rfcf59m.1>

### Information about the authors

**Aleksandr S. Voznesenskii** – Dr. Sci. (Eng.), Professor of the Department of Physical Processes of Mining and of Geocontrol, University of Science and Technology MISIS, Moscow, Russian Federation; ORCID [0000-0003-0926-1808](https://orcid.org/0000-0003-0926-1808), Scopus ID [57210211383](https://orcid.org/57210211383); e-mail [asvoznensenskii@misis.ru](mailto:asvoznensenskii@misis.ru)

**Egor I. Ushakov** – PhD student of the Department of Physical Processes of Mining and of Geocontrol, University of Science and Technology MISIS, Moscow, Russian Federation; ORCID [0000-0003-3579-6515](https://orcid.org/0000-0003-3579-6515), Scopus ID [57467483000](https://orcid.org/57467483000); e-mail [m1800087@edu.misis.ru](mailto:m1800087@edu.misis.ru)

**Yaroslav O. Kutkin** – Cand. Sci. (Eng.), Associate professor of the Department of Physical Processes of Mining and of Geocontrol, University of Science and Technology MISIS, Moscow, Russian Federation; ORCID [0000-0003-2644-3371](https://orcid.org/0000-0003-2644-3371), Scopus ID [56554219800](https://orcid.org/56554219800); e-mail [kutkin.yo@misis.ru](mailto:kutkin.yo@misis.ru)

**Received** 08.10.2024

**Revised** 05.11.2024

**Accepted** 08.11.2024



## MINING ROCK PROPERTIES. ROCK MECHANICS AND GEOPHYSICS

Research paper

<https://doi.org/10.17073/2500-0632-2024-08-303>

УДК 624.131.4:66.094.35:678.6

**Experimental research of stress-strain properties of sandy soil when strengthened with polyurethane compounds**

T. V. Shilova , S. V. Serdyukov , A. N. Drobchik

N.A. Chinakal Institute of Mining, Siberian Branch, Russian Academy of Sciences, Novosibirsk, Russian Federation

shilovatanya@yandex.ru

**Abstract**

In a number of cases during construction and operation of engineering facilities, development of mineral deposits it is necessary to improve the properties of sandy soils by strengthening them with polymer compounds. Analysis of current research shows that the effect of flow rate and method of treatment with polyurethanes on the acquired properties of loose rocks is poorly understood. The paper presents the results of laboratory research of chemical strengthening of sandy soil with polyurethane compounds. Geomaterials typically produced by strengthening loose rock with highly elastic polymers have low strength properties and are stable under only minor loads. To improve the strength, a two-binder sandy soil treatment process is proposed, which includes sequential mixing of the soil with a two-component highly elastic slow-reacting compound and a small volume of a fast-curing one-component resin. The aim of the work is to experimentally investigate the dependence of strain and strength properties of sandy soil on the method of mixing with polyurethane compounds and the polymer volume flow rate. A standard one-component method of mixing samples with highly elastic resin at the resin-to-sand volume ratio from 0.05 to 0.4 and a two-component method including additional treatment with fast-curing one-component resin in the volume of 5% of the strengthened soil were experimentally tested. The effect of polyurethane resins on rock properties was evaluated by triaxial compression strength tests. Electron scanning microscopy was used to determine the content and distribution of cured polymers in the loose rock structure. It was found that the addition of a fast-curing polyurethane compound in the two-component mixing method leads to the formation of aggregates of cured polymer, binding mineral grains without continuous filling of intergranular voids. The presence of such aggregates improves the strength characteristics of sand up to 5 times that is 1.3–3 times more than at the standard one-component mixing with highly elastic resin at a resin-to-rock to be strengthened volume ratio up to 0.3. It was found that under triaxial compression conditions, the geomaterial obtained by the two-component mixing method withstands higher axial stresses. In case the volume ratio of resin to rock is more than 0.3, the strength of the produced geomaterial does not depend on the addition of the fast-curing compound. The study findings practical significance consists in increasing the strength of a sandy soil due to its low-volume strengthening with highly elastic polyurethanes.

**Keywords**

soil, sand, properties, strength, strengthening, technology, treatment, polyurethane, resin, geomaterial, testing, triaxial compression, failure, strain

**Acknowledgments**

This research was conducted as part of a state-funded research project (State Registration No. 121052500138-4, Research Topic Code FWNZ-2021-0001). The equipment of the RAS SB MAC GGGM was used in the work.

**For citation**

Shilova T.V., Serdyukov S.V., Drobchik A.N. Experimental research of stress-strain properties of sandy soil when strengthened with polyurethane compounds. *Mining Science and Technology (Russia)*. 2025;10(1):15–24. <https://doi.org/10.17073/2500-0632-2024-08-303>

## СВОЙСТВА ГОРНЫХ ПОРОД. ГЕОМЕХАНИКА И ГЕОФИЗИКА

Научная статья

**Экспериментальные исследования деформационно-прочностных свойств песчаного грунта при его укреплении полиуретановыми составами**

Т.В. Шилова , С.В. Сердюков , А.Н. Дробчик

Институт горного дела им. Н.А. Чинакала СО РАН, г. Новосибирск, Российская Федерация

shilovatanya@yandex.ru

**Аннотация**

При возведении и эксплуатации инженерных объектов, разработке месторождений твердых полезных ископаемых в ряде случаев необходимо улучшать свойства песчаных грунтов за счет их армирования полимерными составами. Анализ современных исследований показывает, что влияние расхода и



способа обработки полиуретанами на приобретенные свойства рыхлых пород слабо изучено. В работе представлены результаты лабораторных исследований химического закрепления песчаного грунта полиуретановыми составами. Геоматериалы, обычно получаемые при армировании рыхлых пород высокоэластичными полимерами, имеют низкие прочностные свойства и стабильны лишь при незначительных нагрузках. Для повышения прочности предложена технология двухрастворной обработки песчаного грунта, включающая последовательное смешение породы с двухкомпонентным высокоэластичным медленно реагирующим составом и малым объемом быстротвердеющей однокомпонентной смолы. Цель работы – экспериментальное исследование зависимости деформационно-прочностных свойств песчаного грунта от способа смешения с полиуретановыми составами и объемного расхода полимера. Экспериментально протестированы стандартный однорастворный способ смешения образцов с высокоэластичной смолой в соотношении объемов с песком от 0,05 до 0,4 и двухрастворный, включающий дополнительную обработку быстротвердеющей однокомпонентной смолой в объеме 5 % от укрепляемого грунта. Влияние полиуретановых смол на свойства породы оценивали по результатам прочностных испытаний методом трехосного сжатия. Для определения содержания и распределения отвержденных полимеров в структуре рыхлой породы использовался метод электронно-сканирующей микроскопии. Установлено, что добавление быстротвердеющего полиуретанового состава в двухрастворном способе смешения приводит к формированию агрегатов отвержденного полимера, связывающих минеральные зерна без сплошного заполнения межзерновых пустот. Наличие таких агрегатов повышает прочностные характеристики песка до 5 раз, что в 1,3–3 раза больше, чем при стандартном однорастворном смешении с высокоэластичной смолой в объемном соотношении с укрепляемой породой до 0,3. Установлено, что в условиях трехосного сжатия геоматериал, полученный при двухрастворном способе смешения, выдерживает более значительные осевые деформации. В случае объемного соотношения смолы и породы более 0,3 прочность получаемого геоматериала не зависит от добавки быстродействующего состава. Практическая значимость полученных результатов состоит в повышении прочности песчаного грунта при его малообъемном укреплении высокоэластичными полиуретанами.

#### Ключевые слова

грунт, песок, свойства, прочность, укрепление, технология, обработка, полиуретан, смола, геоматериал, испытание, трехосное сжатие, разрушение, деформация

#### Благодарности

Работа выполнена в рамках проекта НИР (номер государственной регистрации 121052500138-4, код (шифр) научной темы FWNZ-2021-0001). В работе использовано оборудование ЦКП ГТИ СО РАН.

#### Для цитирования

Shilova T.V., Serdyukov S.V., Drobchik A.N. Experimental research of stress-strain properties of sandy soil when strengthened with polyurethane compounds. *Mining Science and Technology (Russia)*. 2025;10(1):15–24. <https://doi.org/10.17073/2500-0632-2024-08-303>

### Introduction

The design, construction, and operation of engineering facilities, drifting and the sinking for mineral deposit development depend on the properties of soils and the surrounding loose rocks. The most problematic soils include sandy soils with loose structure, high hydraulic conductivity, and poor grading. These features contribute to the intensive manifestation of various negative physical processes, such as liquefaction, subsidence, and soil erosion. In complicated geotechnical conditions, strengthening with polymer compounds, chemical reagents interacting with each other and/or with groundwater is used to improve the properties of loose rocks [1–3]. Such methods are widely used in tunnel construction, underground space development, design of footings and foundations of structures<sup>1</sup> [4]. Various methods of injection

strengthening, mixing and tamping with cements, polymer resins are used [5–7]. Technical requirements and regulatory documents, GOST R 59706–2022, have been developed for a number of technologies, such as soil consolidation with cement and sodium silicate based mortars used in construction, reconstruction, and repair of engineering facilities

The advantage of polymer resins is their ability to diffuse into rocks and strengthen them during the polymerization process. This increases the stability of loose soils by binding the individual particles into a single matrix. One type of such compounds is polyurethane resins, which are used not only to strengthen loose rocks, but also to reduce their permeability and prevent fluid filtration [8–10]. Depending on a geotechnical problem to be solved, one-component or two-component polyurethane systems are used. In one-component systems, polymerization occurs by interaction with stratal water. As a rule, such a compound intensively foams, its volume increases several times. An additional advantage is relatively simple

<sup>1</sup> SP 22.13330.2016. Footings of Buildings and Structures. Updated version of SNiP 2.02.01–83. URL: [https://lentsiz.ru/wp-content/uploads/2019/01/11\\_SP-22.13330.2016-Osnovaniya-zdaniy-i-sooruzhenij.pdf](https://lentsiz.ru/wp-content/uploads/2019/01/11_SP-22.13330.2016-Osnovaniya-zdaniy-i-sooruzhenij.pdf)



pumping equipment for injection into rocks, while the disadvantages are limited storage time, difficulty in controlling the duration of polymerization, high sensitivity to water saturation of rocks and atmospheric moisture.

In two-component polyurethane systems, foamed polyurethane formation occurs as a result of interaction between isocyanate (component B) and polyester compound (component A), a mixture of polyfunctional hydroxyl-containing polyols with a foaming agent and a catalyst [11, 12]. Curing of such resins strongly depends on the uniformity of mixing and distribution of reagent molecules in the volume of the finished compound. The heterogeneity of the mixture impairs the interaction of substances, especially for fast-curing systems. Only resins with low viscosity and long curing time penetrate well into a rock pores. After diffusion and curing of a resin, the particles are “glued” together by the polymer with lesser residual porosity remained [13, 14]. In practice, the use of fast-curing compounds for rock and soil strengthening is complicated by the increase in viscosity due to the short reaction time. This limits the injection volume of a compound, depth and uniformity of its penetration into a rock [15–17]. The use of two-component slow-reacting, highly elastic polyurethane resins solves this problem. They are effective in the construction of cutoff curtains, waterproofing of soils, provide the level of permeability of sandy soil after strengthening corresponding to the values of practically impermeable rocks, about  $10^{-4}$ – $10^{-3}$   $\mu\text{m}^2$  [18, 19]. At the same time, geomaterials obtained by strengthening rocks with highly elastic polyurethanes have low mechanical strength and are stable only under minor loads [20, 21].

Laboratory testing on rock strengthening with subsequent determination of physical-mechanical, filtration properties of the produced geomaterials allow predicting the results of corresponding field works<sup>2</sup> [22, 23]. The analysis of known studies shows poor understanding of the effect of flow rate and method of polymer treatment on the acquired strength properties of loose and fractured rocks. The present work deals with a two-component method for increasing the mechanical strength of the produced geomaterials, involving sequential mixing of sandy soil specimens with a two-component highly elastic polyurethane compound and a small volume of a fast-acting one-component resin. The aim of the work is to determine the peculiarities of changes in the strength properties of sandy soil depending on the mixing method and polymer volume flow rate based on the

results of laboratory testing. The following tasks were set: to investigate the structure, strain and strength properties of geomaterials produced by the one-component and two-component methods of mixing sandy soil with polyurethane compounds and their different volume flow rates; to determine the relationship between the internal structure and strength characteristics of geomaterials, the effect of adding fast-acting polyurethane compound on the mechanical strength of the sand to be strengthened.

## Research Materials and Methods

### Materials

In the tests, a two-component slow-reacting highly elastic polyurethane resin (hereinafter SR compound) was used, which was designed for consolidation and waterproofing of soils, creation of cutoff curtains. The SR compound is produced by mixing components A and B in a volume ratio of 1:1 to a homogeneous consistency. Component A is a mixture of castor oil (40–41 vol. %), phenoxypropanol (20 vol. %), and low molecular weight polypropylene glycol (40–41 vol. %). Component B is a mixture of methylene diphenyl di-isocyanate (66–67 vol. %), polypropylene glycol (10 vol. %), propylene carbonate (21–23 vol. %). After mixing components A and B, the viscosity of the SR compound is about 95–120 MPa·s and remains low for a long time (tens of minutes). This promotes penetration of the ready-made compound into thin joints, fine-porous soils, increases the effect on a rock, reduces its filtration properties. Full curing time is about 3 h. Meanwhile, the mixture foams and increases in volume. When cured, the SR compound is an impermeable, elastic material, stable at small strains. Technical characteristics are given in Table 1.

To increase the rock strength, in the tests, a one-component fast-acting polyurethane resin (hereinafter, FR compound) was used to strengthen loose, unstable rocks in the course of the construction of underground structures, filling microcracks in concrete and stone structures. The polymerization reaction occurs when the polyurethane compound is mixed with water to a homogeneous consistency in a ratio of 1:1 to 9:1 (resin : water). A 5:1 ratio was used in the tests. Curing time is 90–180 s at a temperature of 25 °C. At the same time foaming occurs due to the release of carbon dioxide, which is a product of the interaction between isocyanate and water. In cured form, the FR compound is a fine-porous foam capable of withstanding significant dynamic and static loads. High viscosity of the compound, 800–1,000 MPa·s at 20 °C, reduces the zone of impregnation of rocks, especially in low-permeable soils, rocks containing thin cracks, etc. Technical characteristics of the FR resin are given in Table 1.

<sup>2</sup> Ortiz R.C. Mechanical behavior of grouted sands. [Master's dissertation]. Kentucky: University of Kentucky; 2015. 117 p.



Table 1

Properties of two-component polyurethane compounds

Indicator	SR compound	FR compound
Purpose	Waterproofing, creation of cutoff curtains, etc.	Strengthening of loose, unstable rocks, etc.
Volume ratio of components A to B	1:1	–
Resin : water volume ratio	–	1:1–9:1
Density (components A/B), g/cm <sup>3</sup>	1,01/1,21 at 23°C	1,614 at 20°C
Viscosity (components A/B/mixture), MPa·s	115/40/80 at 23°C	800–1,000 at 20°C
Curing time, s	about 10,800	90–180
Surface tension at 23°C, mN/m	35.7	–

Laboratory studies were carried out with sand samples taken from a quarry in the Novosibirsk district of the Novosibirsk region. For the tests we used fine sand, in which 90% by mass belonged to 0.2–0.25 mm particle size fraction. The rock was pre-dried to constant weight, the density of mineral particles and bulk density were determined, and the porosity factor was estimated from the obtained values. The particle and skeletal densities of the dry soil averaged 2.64 g/cm<sup>3</sup> and 1.66 g/cm<sup>3</sup>, respectively, and the estimated porosity coefficient was 0.65.

### Techniques

The effect of polymer resins on the properties of fine sand was investigated under laboratory conditions. The experiments included several stages: preparation of rock specimens mixed with polymers (geomaterial); strain-strength tests (triaxial compression strength tests); analysis of microstructure and porosity by scanning electron microscopy. Two methods of mixing sand with polyurethane resins were used in the experiments: one-component with ready mixture of components A and B (SR compound); two-component, sequentially with ready SR and FR compounds. In the case of the one-component method, the prepared mixture of components A and B (SR compound) was added to sand and mixed until a homogeneous mass was formed. In the case of the two-component method, sand was sequentially mixed with the prepared SR and FR compounds. Specimens (Fig. 1) were formed at the ratios of volumes of liquid resin and being strengthened loose rock of 0.05, 0.1, 0.2, 0.3 and 0.4 (Table 2). The produced mixture of sand with the reagents was placed into a steel cylindrical mold 50 mm in diameter and 120 mm high, compacted and aged for 24 h until complete curing of the polymers. The specimens were then extracted and machined at a stone-cutting machine, reducing the height to 100 mm.

Table 2

Polyurethane resin content in geomaterial specimens

Specimen No.	Mixing method	SR compound-to-rock volume ratio	FR compound-to-rock volume ratio
1.1	One-component	0.4	0
1.2	The same	0.3	0
1.3	The same	0.2	0
1.4	The same	0.1	0
1.5	The same	0.05	0
2.1	Two-component	0.4	0.05
2.2	The same	0.3	0.05
2.3	The same	0.2	0.05
2.4	The same	0.1	0.05
2.5	The same	0.05	0.05

The produced specimens of geomaterials were tested by triaxial compression testing method using GT 1.3.5 instrument<sup>5</sup>. Strength and strain characteristics were determined in accordance with GOST 12248.3–2020. The tests were performed at a lateral pressure of 100 kPa, axial strain rate of 0.5 mm/min with a vertical load limit of 5,000 kPa. Based on the tests results, the peculiarities of strain of the specimens and ultimate loads were identified, and the values of strain modulus were determined according to the technique recommended by GOST 12248.3–2020. Data recording and processing were carried out using the specialized software program Geotek Studio of SPE Geotek LLC.

<sup>5</sup> Automated triaxial compression instrument GT 1.3.5. URL: <https://npp-geotek.com/upload/iblock/3d5/3d5b19682b34abee1c6ee34f00e5d9d.pdf> [Дата доступа: май 2024].



Fig. 1. Geomaterial specimens for triaxial compression strength tests

The produced geomaterials were examined by scanning electron microscopy (SEM). Mineral grains, aggregates of cured polymer were identified from the obtained SEM images, and their content in the volume of strengthened rock was quantitatively estimated [24]. The spatial distribution of heterogeneities and voids, structural features of the geomaterials in accordance with the classification of [25] were determined. The samples for the study were taken along the axis, from the top, middle, bottom of the cylindrical specimens. Data analysis and processing were performed using a Mineral S7 automated analyzer of solids microstructure fragments of SIAMS Company.

### Findings and Discussion

The distribution features of cured polyurethane resins in fine sand samples were determined by SEM images. In the geomaterials produced by the one-component method of mixing rock with resin, the cured SR compound occupies a significant part of the void space. Residual porosity is due to voids located near the surface of mineral grains (Fig. 2). As the ratio of resin and rock volumes increases from 0.05 to 0.4, the void space filling with the cured SR compound increases from 43 to 75% or 1.7 times. The linear approximation of the relationship between the above parameters has a coefficient of determination  $R^2 = 0.83$  (Fig. 3).

In the specimens produced by the two-component method of mixing sand with polyurethane compounds, the aggregates of cured resins also occupy the majority of the pore space. The fast-curing FR compound occurs near the surface of mineral grains, binding them and forming aggregates with isolated pores in the polymer structure. In addition, residual voiding is due to pores located in the intergranular space (see Figure 2). Studies of samples from the middle and bottom parts of the specimens showed that

as the ratio of the volumes of SR resin and FR resin to the being strengthened sand increased from 0.1 to 0.45, the filling of the void space with cured polymers increased from 40 to 72 %, or 1.8 times (see Figs. 2, 3). The formation of aggregates of FR compound with closed pores near the surface of mineral grains can prevent the penetration of low-viscosity SR resin into unfilled voids. The structure of the produced geomaterial depends on the volume ratio of resins and sandy soil. If this ratio is greater than 0.3, the filling of void space with cured compounds is more than 60%, and the geomaterial has a basal structure characterized by a uniform distribution of mineral particles in the mass of the binding material. As the volume ratio of resin and rock decreases to 0.05–0.15, the void space filling with cured compounds decreases to 40–50%, and the produced geomaterial acquires a “contact” structure, in which the binding material occurs mainly at the contacts of grains (see Fig. 2)<sup>4</sup>.

The strain and strength properties of the produced geomaterials depend on the internal structure formed as a result of mixing with the polyurethane resins. The mechanical properties of sand strengthened with polyurethane compounds were determined using the diagrams “axial stress  $\sigma_v$  – relative axial strain  $\varepsilon_1$ ”, when the specimens were deformed at a rate of 0.5 mm/min to the value of relative strain  $\varepsilon_1 = 0.15$  (15%). It was found that in case of the one-component mixing method with resin-to-rock volume ratios of 0.05, 0.1, 0.2, and 0.3, the produced geomaterial fails with a pronounced strength limit (maximum stress), while at 0.4 it behaves as an elastomer. Moreover, its yield strength in the investigated range of relative strains was not achieved (GOST 4651–2014).

<sup>4</sup> Ortiz R.C. Mechanical behavior of grouted sands. [Master's dissertation]. Kentucky: University of Kentucky; 2015. 117 p.

The value of the axial stress maximum depends on the content of the highly elastic SR compound in the rock and increases by more than 2.5 times when the amount of the resin decreases 8 times. At  $\varepsilon_1 = 0.15$ , maximum strength was achieved at the resin-to-rock volume ratios of 0.2, 0.3, and minimum strength was achieved at 0.4. As the amount of the resin increases, the strain value corresponding to the ultimate strength limit of the geomaterial increases (Fig. 4). For the resin-to-rock volume ratios of 0.05, 0.1, 0.2,

the ultimate strength limit of the geomaterial is achieved at  $\varepsilon_1 \approx 0.025$ , 0.04, and 0.08, respectively (see Fig. 4).

In case of the two-component method of mixing sand with polyurethane resins with addition 5 vol. % of fast-acting resin FR, the pronounced strength limit of the geomaterials was observed when the SR+FR resins-to-loose rock volume ratios were 0.1, 0.15, 0.25. When the volume ratio reaches 0.35, 0.45, the geomaterial behaves similar to elastomers (Fig. 5).

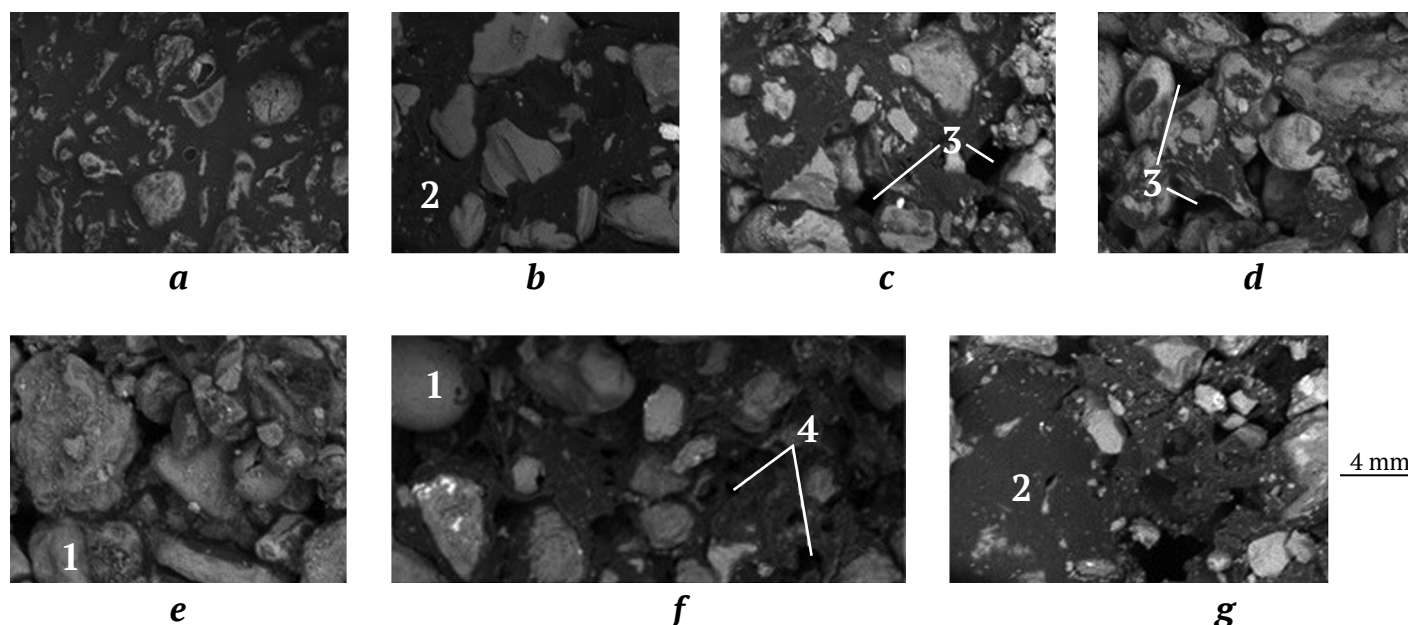


**Fig. 2.** Fragments of SEM images of geomaterials produced by mixing sand with polyurethane resins. One-component mixing method with a highly elastic SR compound at a volume ratio of resin to rock: *a* – 0.4; *b* – 0.3; *c* – 0.2; *d* – 0.1; *e* – 0.05. Two-component method of mixing with SR and FR compounds at the ratio of volumes of FR compound and strengthened rock of 0.05, SR compound and the rock: *f* – 0.2; *g* – 0.3. Legend: 1 – mineral grains; 2 – cured polymer; 3 – intergranular voids; 4 – closed pores in the structure of cured polymer

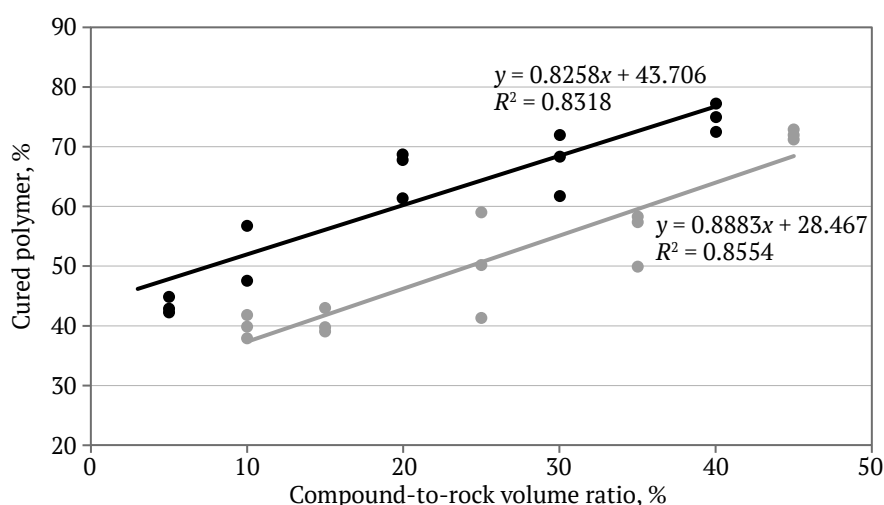


**Fig. 3.** Cured polymer content in the void volume as a function of the polyurethane resin-to-being strengthened rock (sand) volume ratio based on SEM image analysis. Black and gray circles are data of experimental studies of samples produced by one-component method of mixing sand with SR compound and by two-component method of mixing sand with SR and FR compounds, respectively. Black and gray lines are linear approximations of the experimental data

When the content of the resin compounds decreases 4.5 times, the strength limit increases by more than 9 times. For  $\varepsilon_1 = 0.15$ , the strength reaches peak at a SR resin-to-rock volume ratio of 0.05, and is minimum at that of 0.4. For the SR+FR compounds-to-rock volume ratios of 0.1, 0.15, and 0.25, the strength limit of the geomaterial is observed at  $\varepsilon_1 \approx 0.03, 0.05$  and 0.07, respectively (see Fig. 5, 6).

The specimens strain-strength tests data made it possible to determine the values of strain modulus of the geomaterials. The technique recommended by GOST 12248.3–2020 was used. It was found that

when using the one-component mixing method, an eightfold increase in the amount of SR resin reduces the strain modulus of the produced geomaterials by more than 10 times. The largest increase in the strain modulus was achieved when the resin-to-rock volume ratio decreased from 0.2 to 0.1.

The two-component mixing method with the addition of the fast-acting FR polyurethane compound leads to an increase in the geomaterial strain modulus when the SR resin-to-rock volume ratio is 0.05, 0.1, 0.2. If the value of this ratio is higher, the addition of the FR compound has little effect (Table 3).

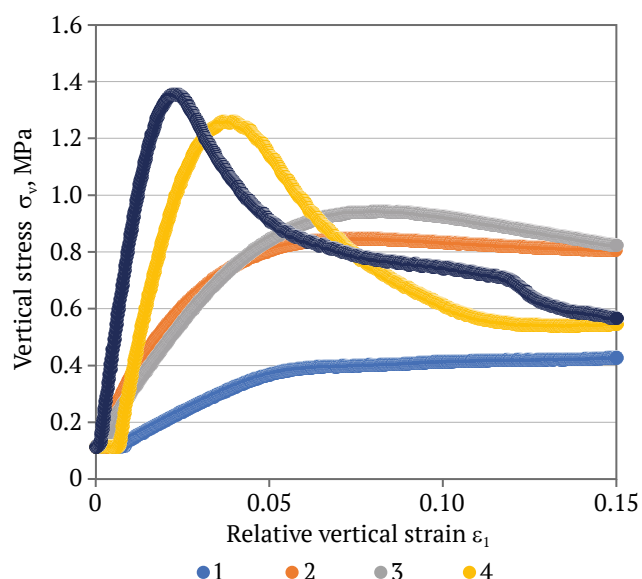


**Fig. 4.** Axial stress – relative axial strain" graphs of geomaterial specimens produced by the one-component method of mixing sand with highly elastic polyurethane resin SR. Resin-to-rock volume ratio (and cured polymer content determined by the graphs in Fig. 3): 1 – 0.4 (77%); 2 – 0.3 (68%); 3 – 0.2 (60%); 4 – 0.1 (52%); 5 – 0.05 (48%)

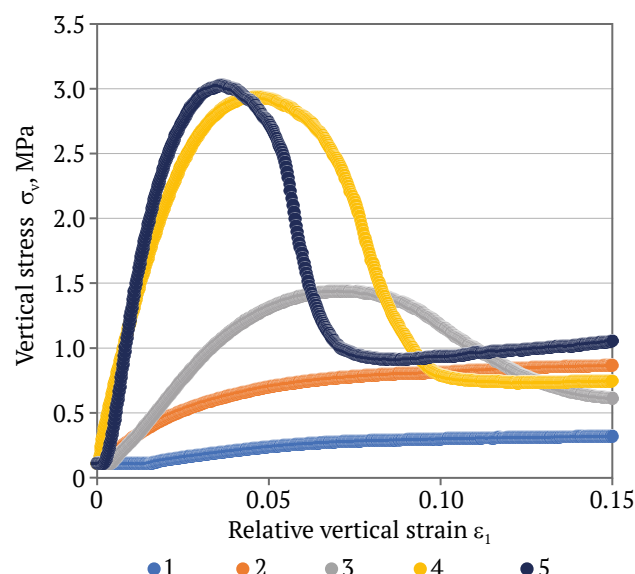


**Fig. 5.** Axial stress – relative axial strain" graphs of geomaterial specimens produced by the two-component method of mixing sand with highly elastic polyurethane resins SR and FR. Resin-to-rock volume ratio (and cured polymer content determined by the graphs in Fig. 3): 1 – 0.45 (68%); 2 – 0.35 (60%); 3 – 0.25 (51%); 4 – 0.15 (42%); 5 – 0.05 (37%)



**a**



**b**

**Fig. 6.** Examples of broken down and deformed geomaterials after triaxial compression tests at SR+FR resin-to-rock volume ratios of: a – 0.35, 0.45; b – 0.1, 0.15, 0.25



Table 3

Strain modulus of geomaterials as a function  
of SR compound-to-rock volume ratio

Sample number	SR compound-to-rock volume ratio	FR compound-to-rock volume ratio	Strain modulus, MPA
1.1	0.4	0	5.6
1.2	0.3	0	18.3
1.3	0.2	0	16.1
1.4	0.1	0	53.3
1.5	0.05	0	70.6
2.1	0.4	0.05	5.2
2.2	0.3	0.05	14.1
2.3	0.2	0.05	29.9
2.4	0.1	0.05	101.5
2.5	0.05	0.05	132.7

Comparing the results of the sand mechanical tests before and after strengthening with polyurethane resins, it can be noted that the application of the highly elastic resin at the resin-to-rock volume ratio no more than 0.3 increases the strength of the rock by 1.3–2.3 times. The addition of 5 vol. % of the fast-acting FR resin leads to an additional 1.6–2.2-fold increase in the strength. In the case of the highly elastic resin-to-rock volume ratios greater than 0.3, the nature of the geomaterial strain changes significantly. Compared to the loose rock not treated with the polymers, the strength decreases 1.3–1.7 times and is practically independent of the addition of the fast-acting resin. Such a geomaterial exhibits the properties of a composite elastomer. Its specimens deform without apparent failure and recover to nearly their original size after the load is removed (see Fig. 6).

The experimental studies have shown that under triaxial compression conditions the geomaterials produced by the two-component method of mixing sand with the SR and FR polyurethane compounds withstand higher mechanical loads than those produced by the one-component method of mixing with only one highly elastic resin. It is most pronounced at low resins-to-loose rock volume ratio (0.05, 0.1). At the volume ratios of 0.3, 0.4, the addition of the fast-acting resin has an insignificant effect on the value of the strain modulus of the produced geomaterial.

### Conclusion

The method of mixing sand with polyurethane compounds, the resin-to-loose rock to be strengthened volume ratio have a significant effect on the

distribution of mineral grains and binder in the produced geomaterial and its strain and strength properties. At the resins-to-rock volume ratio of 0.05–0.15 the filling of its void space with cured polymer is 40–50%. The produced geomaterial has a contact type of structure, in which a binding material is located in the places of contact between mineral grains. Specimens of such geomaterial withstand greater loads than the specimens with the highly elastic resin-to-rock volume ratio greater than 0.3, for which the filling of the void space with the binding polymer reaches 60% or more. As the geomaterial void space filling with cured highly elastic compound decreases from 75 to 43%, their mechanical strength increases more than 2.5 times. On the contrary, the strain value corresponding to the geomaterial strength limit increases with increasing the resin content.

Two-component method of sand mixing with addition of 5 vol. % of fast-curing polyurethane compound leads to intensive formation of aggregates of cured polymer in a loose rock, binding mineral grains without continuous filling of inter-grain voids that significantly increases the strength of the strengthened sand at relatively low consumption of the chemical reagents. The strength of the produced geomaterials increases 2–5 times in comparison with the loose rock before the chemical treatment and 1.3–2.3 times as compared to the one-component method of mixing with highly elastic resin at the resin-to-rock volume ratio less than 0.3. It was found that under triaxial compression conditions, the specimens produced by the two-component method of mixing with the resin compound withstand more significant loads than those produced by the one-component mixing with only one slowly reacting highly elastic resin. If the highly elastic resin-to-rock volume ratio was greater than 0.3, the geomaterials withstanding only low loads were formed, and the addition of the fast-acting compound is ineffective in this case.

The study findings practical significance consists in increasing the efficiency of using low-viscosity highly elastic polyurethane resins in solving problems of loose rock stabilization. The experimental studies have shown that the method of two-component mixing with the addition of fast-acting polyurethane resin significantly increases the rock strength. The pronounced nonlinear dependence of strain and strength properties of geomaterials on the method of mixing and polyurethane resins-to-rock volume ratio indicates the expediency of optimizing the modes of chemical treatment taking into account a geotechnical problem to be solved. This allows, on the one hand, reducing the consumption



of expensive polymers per unit volume of a rock, and, on the other hand, improving the mechanical properties of the produced geomaterials. In the future it is planned to investigate the regularities of changes in physical-mechanical and filtration pro-

perties of loose rocks when using other types of polymers, in particular, organomineral resins, to solve the problems of stabilization of loose rocks under conditions of rock pressure and filtration of underground fluids.

## References

1. Liu J., Qi X., Zhang D. et al. Study on the permeability characteristics of polyurethane soil stabilizer reinforced sand. *Advances in Materials Science and Engineering*. 2017;2017(1):5240186. <https://doi.org/10.1155/2017/5240186>
2. Shilova T., Serdyukov A., Serdyukov S., Ivanova O. Rock reinforcement by stepwise injection of two-component silicate resin. *Polymers*. 2022;14(23):5251. <https://doi.org/10.3390/polym14235251>
3. Penzev A.P., Samarin E.N., Shekhovtsova A.V. et al. Comparison of the efficiency of injection stabilization of sandy soils in field and laboratory conditions with solutions based on aliphatic epoxy resin. *Engineering Geology World*. 2023;XVIII(4):50–62. (In Russ.) <https://doi.org/10.25296/1993-5056-2023-18-4-50-62>
4. Israfilov K.A., Kharchenko I.Ya., Alekseev V.A. Stabilization of permeable soils with modified in-equation sus-pensions based on colloidal silica. *System Technologies*. 2021;(3):21–26. (In Russ.)
5. Ma S., Ma M., Huang Z. et al. Research on the improvement of rainfall infiltration behavior of expansive soil slope by the protection of polymer waterproof coating. *Soils and Foundations*. 2023;63(3):101299. <https://doi.org/10.1016/j.sandf.2023.101299>
6. Esmaeili M., Khajehei H. Mechanical behavior of embankments overlying on loose subgrade stabilized by deep mixed columns. *Journal of Rock Mechanics and Geotechnical Engineering*. 2016;8(5):651–659. <https://doi.org/10.1016/j.jrmge.2016.02.006>
7. Choobbasti A.J., Kutanaei S.S. Microstructure characteristics of cement-stabilized sandy soil using nanosilica. *Journal of Rock Mechanics and Geotechnical Engineering*. 2017;9(5):981–988. <https://doi.org/10.1016/j.jrmge.2017.03.015>
8. Vasiliev V.V. *Polymer compositions in mining*. Moscow: Nauka Publ. House; 1986. 294 p. (In Russ.)
9. Liu H., Wang F., Shi M., Tian W. Mechanical behavior of polyurethane polymer materials under triaxial cyclic loading: a particle flow code approach. *Journal of Wuhan University of Technology-Materials Science Edition*. 2018;33:980–986. <https://doi.org/10.1007/s11595-018-1922-9>
10. Safin A.G., Safin R.R. Geolift. The use of polyurethanestostabilize soils and strengthenbases. *Polymers in Construction*. 2024;1(12):26–29. (In Russ.)
11. Cornely W. Elastified silicate resins and polyurethane foam resins for the stabilization of strata-a comparison. In: *Proceedings of the 6th International Seminary Reinforcement and Sealing of Rock and Construction at the Beginning of 21st Century*. Ostrava, Czech Republic, February; 2001.
12. De Souza F.M., Kahol P.K., Gupta R.K. Chapter 1. Introduction to polyurethane chemistry. In: *Polyurethane Chemistry: Renewable Polyols and Isocyanates*. Pittsburg: ASC Publications; 2021. Pp. 1–24. <https://doi.org/10.1021/bk-2021-1380.ch001>
13. Sabri M.M.S., Vatin N.I., Alsaffar K.A.M. Soil injection technology using an expandable polyurethane resin: a review. *Polymers*. 2021;13(21):3666. <https://doi.org/10.3390/polym13213666>
14. Sabri M.M., Shashkin K.G. The mechanical properties of the expandable polyurethane resin based on its volumetric expansion nature. *Magazine of Civil Engineering*. 2020;(6):9811. <https://doi.org/10.18720/MCE.98.11>
15. Šňupárek R., Souček K. Laboratory testing of chemical grouts. *Tunnelling and Underground Space Technology*. 2000;15(2):175–185. [https://doi.org/10.1016/S0886-7798\(00\)00045-6](https://doi.org/10.1016/S0886-7798(00)00045-6)
16. Jinpeng Z., Limin L., Yang L. Mechanism and experiment of self-stress grouting reinforcement for fractured rock mass of underground engineering. *Tunnelling and Underground Space Technology*. 2023;131:104826. <https://doi.org/10.1016/j.tust.2022.104826>
17. Zadiraka A.A. The use of polyurethane formulations for composite devices bases and / or coatings of transport facilities. *Bulletin of Belgorod State Technological University named after. V.G. Shukhov*. 2017;2(4):72–75. (In Russ.) [https://doi.org/10.12737/article\\_58e61337c965d4.60850341](https://doi.org/10.12737/article_58e61337c965d4.60850341)
18. Shilova T.V., Serdyuk I.M., Serdyukov S.V. et al. Change in permeability of loose rocks in partial impregnation with high-elastic polymer. *Fiziko-Tekhnicheskiye Problemy Razrabotki Poleznykh Iskopae-mykh*. 2024;(1):26–32. (In Russ.) <https://doi.org/10.15372/FTPRPI20240103>



19. Velez D., Alumbrosos D., Carpintero D. et al. Chapter: Consolidation and waterproofing by injection of PU resins. Ilarion Dam-treatment on the spillway tunnel. In: Anagnostou G., Benardos A., Marinos V.P. (Eds.) *Expanding Underground-Knowledge and Passion to Make a Positive Impact on the World. Proceedings of the ITA-AITES World Tunnel Congress 2023 (WTC 2023)*. 12–18 May 2023, Athens, Greece. London: CRC Press; 2023. Pp. 1048–1056. <https://doi.org/10.1201/9781003348030-125>
20. Аскадский А.А. Деформация полимеров. М.: Химия; 1973. 448 с.  
Askadsky A.A. *Polymer deformation*. M.: Khimiya Publ. House; 1973. 448 p. (In Russ.)
21. Miranda L., Caldeira L., Serra J. B., Gomes R. C. Geotechnical characterization of a novel material obtained by injecting a closed cell expansive polyurethane resin into a sand mass. *Transportation Geotechnics*. 2023;42:101051. <https://doi.org/10.1016/j.trgeo.2023.101051>
22. Anagnostopoulos C.A., Papaliangas T., Manolopoulou S., Dimopoulos T. Physical and mechanical properties of chemically grouted sand. *Tunnelling and Underground Space Technology*. 2011;26(6):718–724. <https://doi.org/10.1016/j.tust.2011.05.006>
23. Liu J., Bu F., Bai Y. et al. Study on engineering properties of sand strengthened by mixed fibers and polyurethane organic polymer. *Bulletin of Engineering Geology and the Environment*. 2020;79:3049–3062. <https://doi.org/10.1007/s10064-020-01751-9>
24. Wang J., Li X., Wang C. et al. Quantitative analysis of the representative volume element of polymer grouting materials based on geometric homogenization. *Construction and Building Materials*. 2021;300:124223. <https://doi.org/10.1016/j.conbuildmat.2021.124223>
25. Bodi J., Bodi Z., Scucka J., Martinec P. Chapter 14. Polyurethane grouting technologies. In: Zafar F., Sharmin E. (eds.) *Polyurethane*. IntechOpen; 2012. Pp. 307–336. <https://doi.org/10.5772/35791>

#### Information about the authors

**Tatiana V. Shilova** – Cand. Sci. (Eng.), Senior Researcher of the Laboratory of physical methods of impact on the rock mass, N.A. Chinakal Institute of Mining, Siberian Branch, Russian Academy of Sciences, Novosibirsk, Russian Federation; ORCID [0000-0001-5056-9279](https://orcid.org/0000-0001-5056-9279), AuthorID [550745](https://orcid.org/550745); e-mail [shilovatanya@yandex.ru](mailto:shilovatanya@yandex.ru)

**Sergey V. Serdyukov** – Dr. Sci. (Eng.), the Head of the Laboratory of physical methods of impact on the rock mass, N.A. Chinakal Institute of Mining, Siberian Branch, Russian Academy of Sciences, Novosibirsk, Russian Federation; ORCID [0000-0002-1295-4122](https://orcid.org/0000-0002-1295-4122), Scopus ID [7003986765](https://orcid.org/7003986765), AuthorID [68479](https://orcid.org/68479); e-mail [ss3032@yandex.ru](mailto:ss3032@yandex.ru)

**Andrey N. Drobchik** – Research Engineer of the the Laboratory of physical methods of impact on the rock mass, N.A. Chinakal Institute of Mining, Siberian Branch, Russian Academy of Sciences, Novosibirsk, Russian Federation; ORCID [0009-0002-7567-6497](https://orcid.org/0009-0002-7567-6497), AuthorID [1118483](https://orcid.org/1118483); e-mail [valker.tiamant@mail.ru](mailto:valker.tiamant@mail.ru)

**Received** 30.08.2024

**Revised** 04.12.2024

**Accepted** 06.12.2024



## TECHNOLOGICAL SAFETY


Research paper

<https://doi.org/10.17073/2500-0632-2024-01-210>

UDC 622.41



## Influence of the sorption properties of potash salts on the gas environment in dead-end mine workings

A. N. Starikov<sup>1,2</sup> , S. V. Maltsev<sup>2</sup> , A. E. Sukhanov<sup>2</sup> <sup>1</sup> Perm Federal Research Center of the Ural Branch of the Russian Academy of Sciences, Perm, Russian Federation<sup>2</sup> Mining Institute of the Ural Branch of the Russian Academy of Sciences, Perm, Russian Federation [starikov4488@mail.ru](mailto:starikov4488@mail.ru)

### Abstract

The results of gas-air surveys conducted at the mines of the Verkhnekamsk potassium-magnesium salt deposit indicate that the volume of gaseous impurities recorded in the main ventilation drifts is often significantly lower than in the working areas of dead-end workings. Many studies attribute the reduction of gas impurities along the ventilation airflow path in potash mines not only to the dilution of harmful impurities due to fresh air leakage from intake drifts but also to the neutralization of gases through chemical reactions with the potash rock mass. Previous laboratory studies have shown that sylvinitite ( $\text{NaCl} + \text{KCl}$ ) is capable of absorbing impurities of toxic and combustible gases. Based on these laboratory findings, the present study was conducted under real mining conditions, taking into account the dynamics of gas impurities in the underground atmosphere and the dilution effect caused by air leakage. As part of this study, measurements of combustible and toxic gas concentrations were conducted in productive seams of varying mineral composition at one of the mines of the Verkhnekamsk potassium-magnesium salt deposit to assess the influence of potash salt properties on the gas balance in long dead-end workings. An analysis was conducted to assess the extent to which the properties of the potash rock mass influence changes in the concentration of combustible and toxic gases in the workings along the ventilation airflow path. The collected air samples were analyzed under laboratory conditions. The concentration of combustible gases, carbon monoxide, and carbon dioxide in the collected air samples was determined using gas chromatography with the CHROMOS GX-1000 instrument. The contribution of gas neutralization and dilution due to leakage from the ventilation ducting to the reduction of combustible and toxic gases in the outgoing airflow from the working area was evaluated. The results of the conducted tests established that in long dead-end chambers of seam AB (100 m or more), the volume of gaseous impurities decreases along the length of the working from the dead end to the entry. The study accounted for factors that could influence the reduction of gas concentration in the working area.

### Keywords

mine, gas regime, samples, gas concentration, sorption, leakage, gas survey, sylvinitite, potash rock mass, methane, carbon monoxide, carbon dioxide, hydrogen sulfide, ventilation, mine ventilation

### Acknowledges

This study was conducted as part of a major scientific project with financial support from the Ministry of Science and Higher Education of the Russian Federation (Agreement No. 075-15-2024-535 dated April 23, 2024).


### For citation

Starikov A. N., Maltsev S. V., Sukhanov A. E. Influence of the sorption properties of potash salts on the gas environment in dead-end mine workings. *Mining Science and Technology (Russia)*. 2024;10(1):25–33. <https://doi.org/10.17073/2500-0632-2024-01-210>

## ТЕХНОЛОГИЧЕСКАЯ БЕЗОПАСНОСТЬ

Научная статья

## Влияние сорбционных свойств калийных солей на газовую обстановку в тупиковых горных выработках

А. Н. Стариков<sup>1,2</sup> , С. В. Мальцев<sup>2</sup> , А. Е. Суханов<sup>2</sup> <sup>1</sup> Пермский федеральный исследовательский центр УрО РАН, г. Пермь, Российская Федерация<sup>2</sup> Горный институт УрО РАН, г. Пермь, Российская Федерация [starikov4488@mail.ru](mailto:starikov4488@mail.ru)

### Аннотация

Результаты газовоздушных съемок, выполняемых на рудниках Верхнекамского месторождения калийных и магниевых солей, показывают, что объем газообразных примесей, фиксируемый в главных вентиляционных штреках рудника, зачастую значительно меньше, чем в рабочих зонах тупиковых выработок.



Феномен снижения газовых примесей по пути движения вентиляционной струи воздуха на калийных рудниках во многих исследованиях связывают не только с разбавлением вредных примесей утечками свежего воздуха с воздухоподающих штреков, но и с нейтрализацией газов за счет их химических реакций с калийным массивом. Результаты исследований, проведенных ранее в лабораторных условиях, показали, что сильвинит ( $\text{NaCl} + \text{KCl}$ ) способен поглощать примеси токсичных и горючих газов. На основе результатов лабораторного изучения в рамках настоящей работы проведены исследования в условиях реального рудника, учитывающие динамику газовых примесей в атмосфере горных выработок и фактор разбавления газовых примесей утечками воздуха. В рамках работы выполнены замеры концентрации горючих и токсичных газов на продуктивных пластах разного минерального состава на одном из рудников ВМКМС для оценки влияния свойств калийных солей на газовый баланс в тупиковых выработках большой протяженности. Выполнен анализ степени влияния свойств калийного массива на изменение концентрации горючих и токсичных газов в выработках по пути движения вентиляционной струи воздуха. Анализ отобранных образцов воздуха проводился в лабораторных условиях. Концентрация горючих газов, оксида и диоксида углерода, содержащихся в отобранных образцах воздуха, производилась хроматографическим методом на приборе «ХРОМОС ГХ-1000». Оценена доля влияния нейтрализации газа и разбавления утечками вентиляционного трубопровода на снижение количества горючих и токсичных газов в исходящей из рабочей зоны струе воздуха. В результате проведенных экспериментов установлено, что в протяженных тупиковых камерах пласта АБ (100 м и более) количество газовых примесей снижается по протяженности выработки от тупика к устью. При проведении исследований учтены факторы, способные повлиять на снижение концентрации газа в рабочей зоне.

#### Ключевые слова

рудник, газовый режим, пробы, концентрация газа, сорбция, утечки, газовая съемка, сильвинит, калийный массив, метан, оксид углерода, диоксид углерода, сероводород, проветривание, рудничная вентиляция

#### Финансирование

Работа выполнена в рамках крупного научного проекта при финансовой поддержке Минобрнауки России (соглашение № 075-15-2024-535 от 23.04.2024).

#### Для цитирования

Starikov A. N., Maltsev S. V., Sukhanov A. E. Influence of the sorption properties of potash salts on the gas environment in dead-end mine workings. *Mining Science and Technology (Russia)*. 2024;10(1):25–33. <https://doi.org/10.17073/2500-0632-2024-01-210>

## Introduction

The Verkhnekamsk potassium-magnesium salt deposit (VPMSD) is mined using mechanized methods with continuous miner complexes for development and extraction. This method of ore extraction is almost always accompanied by the release of combustible and toxic gases from the rock mass during its fragmentation. Additionally, gas emissions originate from the broken ore stockpiled in the transfer hoppers and mine shuttle cars, as well as from the exposed potash rock mass adjacent to the mine workings. The accumulation of significant gas concentrations in the mine atmosphere is influenced by the release of free gases from the ore body. The primary composition of free gases at VPMSD includes combustible gases – methane ( $\text{CH}_4$ ) and hydrogen ( $\text{H}_2$ ) – and toxic gases such as hydrogen sulfide ( $\text{H}_2\text{S}$ ). Furthermore, internal combustion engines, welding operations, and other industrial activities, contribute to the accumulation of carbon monoxide ( $\text{CO}$ ) and other toxic gaseous impurities in the mine atmosphere<sup>1</sup> [1].

The dilution and removal of harmful impurities released in working areas, i.e., the creation of a safe

environment for normal physiological activity, are ensured through ventilation.

The fresh airflow, passing through the working area, carries away the released harmful impurities through the ventilation drifts to the ventilation shaft and then to the surface. Gas surveys at the mines of the Verkhnekamsk potassium-magnesium salt deposit are conducted to determine the relative gas content in working areas. The obtained values of relative gas content directly affect the calculation of the required volume of fresh air for mine working ventilation. Determining accurate concentrations of combustible and toxic gases in the mine atmosphere is critically important for designing an effective ventilation system for the working areas and ensuring safe conditions in the mine.

Statistical analysis of long-term gas-air survey results conducted at the mines of VPMSD shows that the volume of gaseous impurities recorded in the main ventilation drifts is often significantly lower than in dead-end faces [2].

The reduction in the volume of gaseous impurities along the ventilation airflow path cannot always be explained solely by the dilution of contaminated air due to leaks from intake workings. The phenomenon of decreasing gas impurity concentration

<sup>1</sup> Ushakov K. Z., Burchakov A. S., Medvedev I. I. *Mine Aerology*. Moscow: Nedra Publ. House; 1978.



along the ventilation airflow path in potash mines has previously attracted attention in several studies. For instance, Medvedev I. I. and Krasnoshtein A.E. [3] described the ability of potash salts.

To actively sorb gaseous impurities from the mine atmosphere. The authors attribute the nature of the gas neutralization process to the natural radioactivity of potash ores, which facilitates chemical reactions between gas molecules and mineral particles on the surface of the rock mass. Similarly, Selivanova S.A.<sup>2</sup> also described the sorption of harmful impurities from the air by potash salts through a series of chemisorption processes. These processes involve chemical reactions induced by the catalytic effect of ionizing radiation from the potassium-40 isotope and the high hygroscopicity of potash salts. The ability of potash salts to absorb inorganic and organic gaseous substances was also discussed in [4], where research findings contributed to the establishment of an underground allergology inpatient facility in an active potash mine. The processes of natural air purification in salt mines, influenced by the mineral composition of the rock mass, were previously examined in studies [5, 6]. Additionally, international literature associates the mechanism of air self-purification in salt mines with intermolecular attraction forces [7, 8].

The results of experimental studies presented in [9] have demonstrated in detail that sylvinit ( $\text{NaCl} + \text{KCl}$ ) is capable of absorbing impurities of toxic and combustible gases. The study analyzed the nature of gas sorption processes by potash salts and suggested that natural radioactivity does not play a primary role in gas absorption by the potash rock mass. A hypothesis was proposed that intermolecular interaction forces are the fundamental mechanism underlying the gas sorption process in the potash rock mass [10].

If the absorption of gaseous impurities from the mine atmosphere by potash salts can influence the gas balance within a dead-end working, it becomes necessary to account for these processes when conducting gas-air surveys, particularly during air sampling in dead-end workings [11]. Considering that the rock mass can actively absorb gaseous impurities, it can be assumed that the gas content in the air of a single working area may vary locally depending on the distance from the gas emission source. The risk of recording incorrect gas concentration values due

to variations in concentration along the length of the working may lead to inaccurate calculations of the required air volume, potentially affecting the safety of mining operations. Therefore, a more detailed examination of the gas conditions within the dead-end chamber is necessary.

Studies conducted by the authors of [9] under laboratory conditions confirm the ability of potash salts to sorb combustible and toxic gases. The objective of this study is to analyze the dynamics of gas impurity concentration reduction in underground mine workings of a potash mine. The main tasks of the study include conducting a series of experimental observations in an active potash mine, analyzing the extent to which the sorption properties of potash salts influence the gas conditions, and assessing the impact of air leakage from the ventilation ducting on the reduction of gas impurity concentrations within dead-end mine workings.

### Observation Methods

This study describes a series of experiments conducted in long dead-end stoping workings (over 100 m in length) at one of the VPMSD mines to analyze the relationship between changes in combustible and toxic gas concentrations along the ventilation airflow path from the gas emission source (from the face to the chamber entry). The research was carried out in productive seams AB and Kr-II to assess the influence of rock masses with different mineral compositions on gas concentration changes within the workings.

The general research approach involved air sampling and measuring airflow rates at multiple points along the entire length of the dead-end stopping working. All measurements during the experiment were performed while mining equipment was in operation and under stable ventilation conditions.

Air sampling was conducted to measure the concentration of combustible and toxic gases in the mine atmosphere, while airflow measurements were taken to determine gas volume and assess air leakage from the ventilation ducting. Sampling for combustible gases was performed using the “wet method”, a traditional technique for collecting poorly soluble gases ( $\text{CH}_4$ ,  $\text{H}_2$ ,  $\text{CO}$ ,  $\text{CO}_2$ ) [12], in which the sample was obtained through displacement using a 0.7 dm<sup>3</sup> glass container filled with water (Fig. 1). To determine the concentration of soluble gas impurities ( $\text{H}_2\text{S}$ ,  $\text{NO}$ , and  $\text{NO}_2$ ) in the mine atmosphere, samples were collected using 0.15 dm<sup>3</sup> medical syringes. Before sampling, 7 cm<sup>3</sup> of ammonium molybdate absorbent solution was added to the syringe with a pipette, and the sample container was sealed with a stopper (Fig. 2).

<sup>2</sup> Selivanova S.A. Hygienic aspects of formation and optimization of the physicochemical conditions of the internal environment in sylvinit structures. [Cand. Med. Sci. Dissertation] Perm: Perm State Medical University named after Academician E. A. Wagner; 2019.



Fig. 1. Sampling container for determining combustible gas concentration

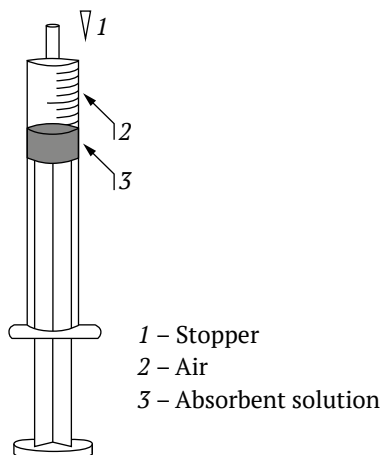


Fig. 2. Sampling syringe for determining hydrogen sulfide ( $H_2S$ ) concentration

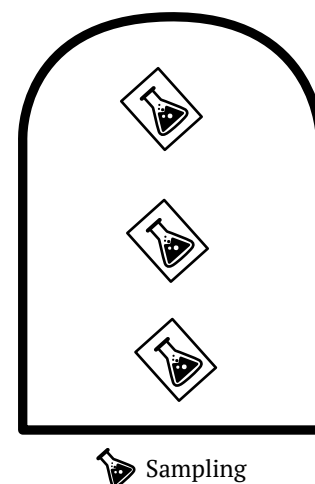


Fig. 3. Sampling method

At each sampling location, the sampling syringe was positioned vertically, and the stopper was removed. The plunger was then smoothly depressed to draw an air sample up to the  $0.15 \text{ dm}^3$  mark. Once the sample was collected, the syringe was sealed with the stopper and placed in a protective case for transport to the laboratory<sup>3</sup>.

At each sampling point, a minimum of three air samples were taken (Fig. 3) to determine the average gas volume passing through the working. The collected samples were transported to the laboratory within two hours and analyzed within 12 hours of collection.

The analysis of collected air samples was conducted under laboratory conditions. The separation of combustible gases ( $CH_4$  and  $H_2$ ), carbon monoxide ( $CO$ ), and carbon dioxide ( $CO_2$ ) in the collected air samples was performed using gas chromatography with the CHROMOS GX-1000 instrument. The chromatograph operates by separating the air sample into individual chemical components and determining their concentrations using a detector. The volumetric fraction of each component was then measured using the instrument's software<sup>4</sup>.

The mass concentration of hydrogen sulfide ( $H_2S$ ) was analyzed using the photometric method with ammonium molybdate reagent and a photoelectric colorimeter (KFK-3KM). This method is based on measuring the optical density of the compound formed when hydrogen sulfide is absorbed from the air by an ammonium molybdate solution [13]. The mass con-

centration of hydrogen sulfide was determined using a calibrated optical density–mass concentration relationship.

All measurements were performed in accordance with certified measurement methodologies<sup>5</sup> using approved measuring instruments that had undergone verification.

For the experiments, working areas in different productive seams at one of the VPMSD mines were selected. Field measurements were conducted in three stages: the first stage was carried out in seam Kr-II, while the second and third stages were conducted in seam AB. The primary criterion for selecting working areas was the presence of a long dead-end working – over 100 meters in length. The selected working areas were located within a single extraction site (panel), where preparatory mining operations were underway to develop a new extraction block, resulting in the significant length of the workings.

The experiment was designed to ensure uniform and simultaneous measurements at multiple points along the entire length of the chamber, as shown in Fig. 4.

**The first stage** of the study involved a series of measurements in the working area of seam Kr-II. The primary mineral composition of this seam consists of potassium chloride (KCl) – 29% and sodium chloride (NaCl) – 66% [14]. During this stage, the distance from

<sup>3</sup> Laptev V.N., Kazakov B.P., Levin L.Yu. et al. Device for gas sampling in mines to determine hydrogen sulfide content. Utility Model Patent. 2014; Laptev V.N., Isayevich A.G., Norina N.V. et al. Device for continuous sampling of a gas-air mixture over a specified time interval. Utility Model Patent. 2015.

<sup>4</sup> Chudin E.A. Computer program: software module for controlling the column thermostat of a gas chromatograph.

<sup>5</sup> FR.1.31.2022.42903 GSI. Measurement methodology for determining the volumetric fraction of oxygen, methane, and carbon dioxide, as well as the mass concentration of carbon monoxide, hydrogen sulfide, nitric oxide, and nitrogen dioxide in the atmosphere of mine workings, and for assessing gas emission levels based on combustible gases in mine workings and the mine as a whole; FR.1.31.2022.44212 Measurement methodology for determining the mass concentration of hydrogen sulfide (hydrosulfide, hydrogen sulfide) using ammonium molybdate reagent.

the chamber mouth to the face was 180 meters. The mining equipment operating in the working area included: Ural-20R continuous miner, BPS-25 transfer hopper, and VS-30 mine shuttle cars. entilation of the working area was provided by a VME-6 local ventilation fan. The fan was positioned in the extraction gallery, and air was supplied to the face using a forced ventilation system through a 500 mm diameter flexible ventilation duct (see Fig. 4). With this duct diameter and pipeline length, the fan's capacity ranged from 190 to 200 m<sup>3</sup>/min. The advance rate of the specified continuous mining complex averages 30 meters per shift. Air sampling in the working area was conducted during the third production shift, 30 minutes after the mining equipment began operating, and while it was in operation. Within the chamber, four measurement points were selected at 50-meter intervals from the face to the chamber mouth.

**The second stage** of the experiment was conducted in a dead-end chamber in seam AB. The mineral composition of this productive seam differs from that of seam Kr-II due to its higher potassium chloride (KCl) content – up to 39%. The experiment was carried out in a 130-meter-long dead-end working. At the time of the measurements, the mining complex in operation included: Ural-61 continuous miner, BP-14 transfer hopper, and VS-17V mine shuttle car. The technical productivity of this complex was 3 tons per minute. Ventilation of the working area was provided by a VME-6 local ventilation fan with a 500 mm diameter flexible ventilation duct. Under these operating conditions, the fan's capacity ranged from 200 to 210 m<sup>3</sup>/min. The average advance rate of the mining complex was 30 meters per shift. Within the chamber, five measurement points were selected at 30–35 meter intervals from the face to the chamber mouth. Measurements were conducted during the loading cycle of the mine shuttle car at the continuous miner.

The measurement stages for seams Kr-II and AB involved air sampling to determine the concentrations of methane (CH<sub>4</sub>), hydrogen (H<sub>2</sub>), carbon monoxide (CO), and oxygen (O<sub>2</sub>). Additionally, at each sampling location, the airflow volume was recorded. The total sampling time per stage, excluding preparation, did not exceed 10 minutes.

Seam AB at the VPMSD mines, unlike seam Kr-II, is characterized by a tendency to release hydrogen sulfide (H<sub>2</sub>S) during extraction [15]. Therefore, as a separate stage of the study, air samples were collected in the chamber of seam AB to determine hydrogen sulfide (H<sub>2</sub>S) concentration. These measurements were conducted one month later in another chamber within the same extraction block.

**The third stage** of the experiment was conducted in a 100-meter-long dead-end chamber in seam AB. The mining equipment operating in the working area included: Ural-61 continuous miner, BP-14 transfer hopper, VS-17V mine shuttle car. Ventilation of the working area was provided by a VME-6 local ventilation fan with a 500 mm diameter flexible ventilation duct, operating at 205–215 m<sup>3</sup>/min. Within the chamber, three measurement points were selected – at the face, midpoint, and chamber mouth. Measurements were taken during the loading cycle of the mine shuttle car at the continuous miner. The measurement series included air sampling to determine hydrogen sulfide (H<sub>2</sub>S) concentration, while airflow volume was recorded at each sampling point. Additionally, a mine gas analyzer was placed at the face near the continuous miner (see Fig. 4), which recorded and stored hydrogen sulfide (H<sub>2</sub>S) concentration values every 10 seconds. The sampling time for each measurement was 10 minutes. The following section presents the results of sample analysis from all stages of the experiment.

### Experiment results

The analysis of samples collected using chromatographic and photometric methods provides an assessment of changes in combustible and toxic gas concentrations along the outgoing airflow path in the chamber, from the face to the chamber mouth. Collecting three samples at each measurement point allows for an evaluation of data variability and determination of average concentration values. Sample processing was carried out under controlled laboratory conditions, ensuring compliance with all necessary environmental parameters. In accordance with the methodology, the concentration of combustible gases was analyzed by separately measuring methane (CH<sub>4</sub>) and hydrogen (H<sub>2</sub>) concentrations, followed by their summation, expressed as (%):

$$\Sigma = C_{\text{CH}_4} + C_{\text{H}_2}, \quad (1)$$

where C is concentration of the specified component, %.

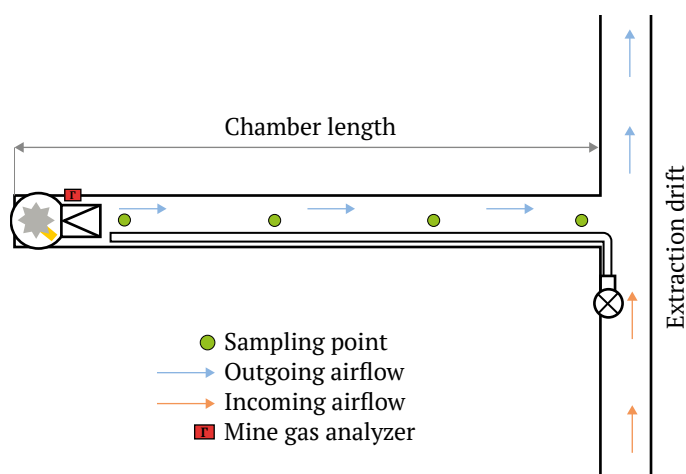


Fig. 4. Measurement scheme for seam Kr-II

The obtained concentration values for the studied components are presented as scatter plots, with trend lines plotted based on the average concentration values of each component.

Figs. 5 and 6 show the concentration values of combustible gases ( $\text{CH}_4 + \text{H}_2$ ) and carbon monoxide (CO) obtained from the analysis of samples collected along the entire length of the chamber in seam Kr-II during the first stage of the experiment.

According to the obtained results, a decrease in the volumetric fraction of the studied gas components was observed in the working area of seam Kr-II along the airflow path from the face to the chamber mouth. Over a 150-meter distance, the average concentration of combustible gases ( $\text{CH}_4 + \text{H}_2$ ) decreased by 10%, while the average concentration of carbon monoxide (CO) dropped by 17%.

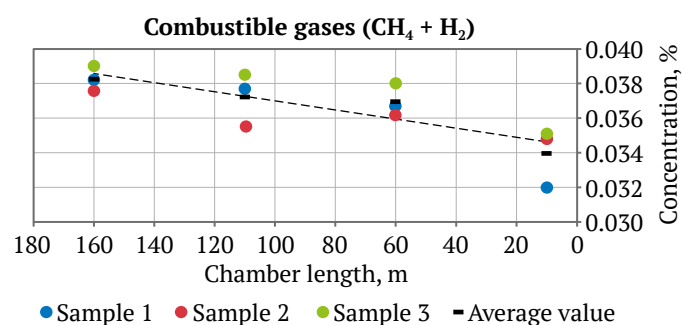


Fig. 5. Concentration of combustible gases in seam Kr-II

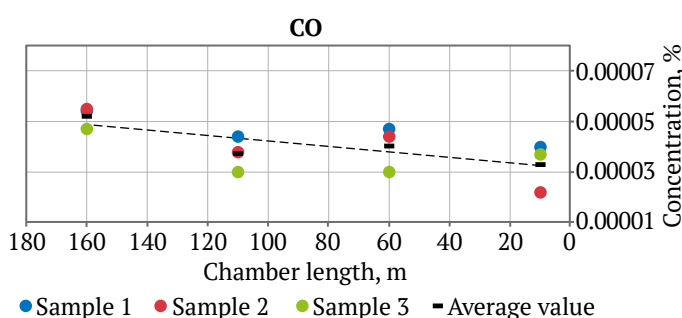


Fig. 6. Concentration of carbon monoxide in seam Kr-II

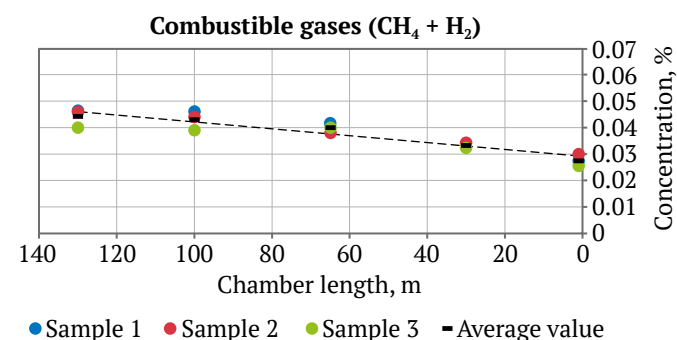


Fig. 7. Concentration of combustible gases in seam AB

The measured concentrations of combustible gases and carbon monoxide from air samples collected during the second stage of the experiment in seam AB are presented in Figs. 7 and 8.

The processing of air samples collected in the working area of seam AB indicates a decrease in gas impurity concentrations within the chamber atmosphere, along the airflow path from the face to the chamber mouth. Over a 130-meter distance, the average concentration of combustible gases ( $\text{CH}_4 + \text{H}_2$ ) decreased by 37%, while the carbon monoxide (CO) concentration dropped by 88%. Air sampling in seam AB, as part of the third stage of the experiment, was conducted alongside the continuous recording of hydrogen sulfide ( $\text{H}_2\text{S}$ ) concentrations at the face using a mine gas analyzer. The gas analyzer readings during the air sampling period are presented as a graph in Fig. 9.

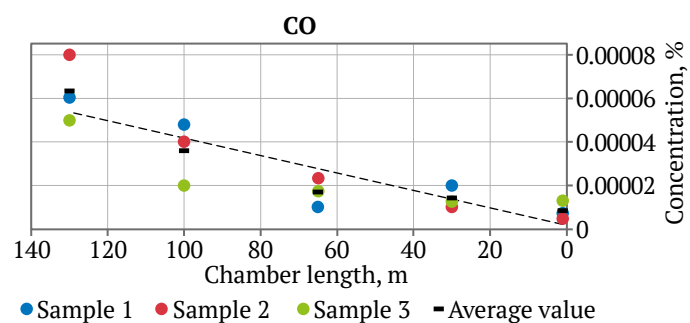


Fig. 8. Concentration of carbon monoxide in seam AB

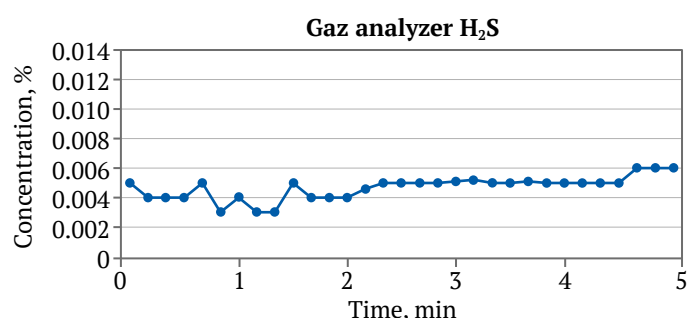


Fig. 9. Gas analyzer readings at the face

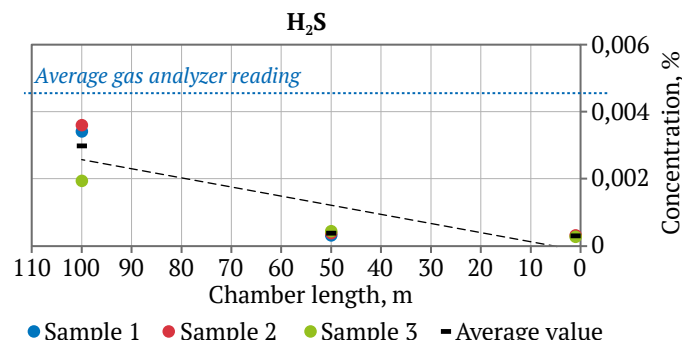


Fig. 10. Concentration of hydrogen sulfide in seam AB



Table 1  
Reduction in gas concentration in the stopping chamber

Seam	Reduction in concentration over 100 m, %		
	Combustible gases (CH <sub>4</sub> + H <sub>2</sub> )	Carbon monoxide CO	Carbon monoxide H <sub>2</sub> S
Seam Kr-II	9	12	–
Seam AB	35	76	90

The average concentration of hydrogen sulfide (H<sub>2</sub>S) recorded by the gas analyzer near the continuous miner, where gas is predominantly released from the rock mass, was 0.0047%. The hydrogen sulfide (H<sub>2</sub>S) concentration values obtained from the analysis of air samples collected during the third stage of the experiment in seam AB are presented in Fig. 10.

The analysis of air samples collected in the working area of seam AB shows a decrease in hydrogen sulfide (H<sub>2</sub>S) concentration along the outgoing airflow path from the face to the chamber mouth. Over a 100-meter distance, the average concentration of hydrogen sulfide in the air decreased by 90%.

### Analysis of Results

The measurement results obtained in this study clearly demonstrate a reduction in gas impurity concentrations in extended working areas as air moves from the face (gas emission source) to the mouth of the dead-end chamber. Air sampling in the working areas of seams Kr-II and AB provides insight into the impact of different mineral compositions on the absorption of gas impurities from the atmosphere in dead-end working [16].

The results indicate that the reduction in gas impurity concentrations in the working area of seam AB occurs more intensively compared to seam Kr-II, under identical dead-end chamber lengths. Table 1 presents the percentage reduction in gas impurity concentrations for different seams over a 100-meter section of the ventilation airflow path within the chamber. This 100-meter segment was chosen to ensure the standardization of conditions across all stages of the study.

The reduction in gas impurity concentration as air moves from the face to the chamber mouth can be attributed not only to the absorption of gaseous impurities by the rock mass<sup>6</sup> [17], but also to the dilution of the outgoing airflow due to fresh air leakage from the ventilation duct into the chamber atmosphere. The extent to which the sorption properties of

the rock mass influence the reduction of gas impurity concentrations in the outgoing airflow can only be accurately assessed by determining the volume of air leakage from the ventilation duct along the studied section [18].

At each stage of the study, measurements were taken to determine air leakage from the ventilation duct. Specifically, airflow was measured at the sampling points using a mine vane anemometer. The air velocity measurements recorded in this study showed no significant variation between the measurement points within the chamber. The air volume at each measurement point ranged from 200 to 215 m<sup>3</sup>/s, accounting for the acceptable calibration error of the anemometer at the recorded air velocities, calculated as  $+(0.03 + 0.02V)$ , where  $V$  is the measured velocity (m/s).

Since direct measurement of air leakage from the ventilation duct along the studied section of the chamber was not feasible, the leakage volume was estimated based on regulatory air leakage rates outlined in the official documentation used at VPMSD mines to calculate the required ventilation airflow in dead-end chambers<sup>7</sup>. The regulatory air leakage rate represents the maximum permissible leakage from the ventilation duct under normal conditions, assuming no structural damage and nominal performance of the local ventilation fan. Under standard operating conditions, for a 100-meter-long flexible ventilation duct, the air leakage coefficient is set at 1.07. Consequently, in the analyzed sections of the dead-end chambers in seams Kr-II and AB, the air volume at the face was considered 7% lower than the air volume passing through the chamber mouth.

With known airflow values, the measured gas concentrations (%) were converted into the gas volume passing through the studied points (m<sup>3</sup>/min). When assessing changes in gas volume (m<sup>3</sup>/min) along the working, the influence of air leakage from the ventilation duct on the concentration of harmful impurities in the ventilation airflow path (from the face to the chamber mouth) was excluded. Therefore, changes in gas volume along the working reflect the impact of the sorption properties of the rock mass surrounding the excavation on the gas balance within the dead-end chambers at VPMSD mines.

Table 2 presents the changes in the average volume of gas impurities passing through the working, as well as the sorption capacity of the rock mass for each seam, as determined in this experiment.

<sup>6</sup> Gorbatenko Yu.A. *Adsorption of toxic gas impurities from contaminated air*. 2014.

<sup>7</sup> Временная инструкция по расчету количества воздуха, необходимого для проветривания рудных шахт. 1983.



Table 2

## Reduction in gas volume in the studied working areas

Steam	Gas volume at measurement point, m³/min		Reduction, %
	Face	Chamber mouth	
Seam Kr-II (KCl 29%)			
Combustible gases (CH₄+H₂)	0.07099	0.06895	3*
Carbon monoxide CO	0.000072	0.000067	7
Seam AB (KCl 39%)			
Combustible gases (CH₄+H₂)	0.08170	0.05613	31
Carbon monoxide CO	0.000068	0.000017	75
Hydrogen sulfide H₂S	0.00566	0.00059	88

\* Within the combined measurement uncertainty of the applied methodologies

The data presented in Table 2 indicate that gas volume in dead-end chambers decreases from the face to the chamber mouth. The most intensive reduction in gas impurity concentrations occurs in the dead-end chambers of seam AB, which is consistent with laboratory experiments [7], where a higher KCl content in sylvinit was shown to have a stronger sorption effect on gas impurities.

The very minor reduction in combustible gases and carbon monoxide concentrations in seam Kr-II does not allow for definitive conclusions regarding the sorption properties of the rock mass in this seam. The slight variations observed may be attributed to the measurement uncertainty of the equipment and methodology. A more precise assessment of gas impurity reduction in seam Kr-II would require increasing the length of the studied working.

### Conclusion

This study involved a series of experimental observations conducted in underground dead-end workings of a potash mine, specifically in productive seams Kr-II and AB. Based on the results of the experiments, an analysis was performed to assess the impact of the sorption properties of potash salts on the gas environment within dead-end working areas. Additionally, the influence of air leakage from venti-

lation ducts on the reduction of gas impurity concentrations was evaluated.

The experimental investigations revealed that in extended dead-end chambers of seam AB (100 meters or longer), a gradual reduction in gas impurity concentrations was observed along the working, from the face to the chamber mouth. The obtained data align with previous laboratory experiments [9], which demonstrated that potash salts are capable of absorbing carbon monoxide (CO) and combustible gases, such as hydrogen (H<sub>2</sub>) and methane (CH<sub>4</sub>). Furthermore, this study included experiments in seam AB to examine the dynamics of hydrogen sulfide (H<sub>2</sub>S) concentration changes during ore extraction, as air moves from the face to the chamber mouth. The experimental results showed that the average sorption efficiency of sylvinit from seam AB (with KCl content of 39%) over a 100-meter ventilation path from the dead-end to the chamber mouth was: 31% for combustible gases (hydrogen (H<sub>2</sub>) and methane (CH<sub>4</sub>)), 75% for carbon monoxide (CO), and 88% for hydrogen sulfide (H<sub>2</sub>S). During the study, factors influencing gas concentration reduction in the working area were considered. Additionally, the ventilation duct leakage coefficient was accounted for when converting gas impurity concentrations to actual gas volume passing through the measurement control points.

This research continues the investigation of the sorption properties of potash salts concerning the absorption of combustible and toxic gas components from the mine atmosphere. The observations of the impact of potash salts' sorption characteristics on mine air composition in extended dead-end workings at the VPMSD mine serve as a continuation of a series of laboratory experiments [7]. The findings of this study will contribute to the further development of methodologies for evaluating factors affecting the mine atmosphere composition within dead-end workings. Additionally, the results will provide a basis for the development of a gas survey methodology for working areas in potash mines. In the future, the study is expected to be expanded to cover all VPMSD mines, enabling the accumulation of statistical data and the testing of an improved gas survey methodology for potash mining operations.

### References

1. Kuzminykh E. G., Levin L. Yu., Maltsev S. V. Distribution of exhaust gas products from machinery with internal combustion engines through the shaft ventilation system. *Gornoye Ekho*. 2023;(2):96–103. (In Russ.) <https://doi.org/10.7242/echo.2023.2.17>
2. Trushkova N. A. Investigation of the gas composition of mine air to assess the possibility of using recirculating ventilation. *Gornoye Ekho*. 2019;(3):84–87. (In Russ.) <https://doi.org/10.7242/echo.2019.3.23>
3. Medvedev I. I., Krasnoshtein A. E. *Aerology of potash mines*. Sverdlovsk: Academy of Sciences of the USSR; 1990. Pp. 119–126. (In Russ.)



4. Barannikov V.G., Krasnoshtein A.E., Papulov L.M. et al. *Speleotherapy in a potash mine*. Yekaterinburg: Publishing House of the Ural Branch of the Russian Academy of Sciences; 1996. Vol. 173. (In Russ.)
5. Puławska A., Manecki M., Flaszka M. et al. Origin, distribution, and perspective health benefits of particulate matter in the air of underground salt mine: a case study from Bochnia, Poland. *Environmental Geochemistry and Health*. 2021;43(9):3533–3556. <https://doi.org/10.1007/s10653-021-00832-2>
6. Calin M., Zoran M., Calin M. Radon levels assessment in some Northern Romanian salt mines. *Journal of Radioanalytical and Nuclear Chemistry*. 2012;293(2):565–572. <https://doi.org/10.1007/s10967-012-1686-1>
7. Yao N., Chen J., Feng R. et al. Mechanistic understanding of adsorption of low concentrations of N-nitrosodiethylamine in water by functional MIL-96: experiments and theoretical calculations. *Chemical Engineering Journal*. 2022;451(3):138761. <https://doi.org/10.1016/j.cej.2022.138761>
8. Yang D., Peng X., Peng Q. et al. Probing the interfacial forces and surface interaction mechanisms in petroleum production processes. *Engineering*. 2022;18:49–61. <https://doi.org/10.1016/j.eng.2022.06.012>
9. Sukhanov A.E., Bruev N.A., Gazizullin R.R., Starikov A.N. Research of sorption properties of salt on the example of gases contained in the atmosphere of potash mines. *Izvestija Tul'skogo Gosudarstvennogo Universiteta. Nauki o Zemle*. 2023;(1):495–507. (In Russ.) <https://doi.org/10.46689/2218-5194-2023-1-1-495-507>
10. Kuznetsova Y.L. Size evolution of a soluble aerosol particle in air. *Computational Continuum Mechanics*. 2022;15(1):31–44. <https://doi.org/10.7242/1999-6691/2022.15.1.3>
11. Barannikov V.G., Chereshev V.A. Hygienic assessment of air self-purification processes in a potassium mine. In: *Safety problems in the exploitation of mineral deposits in urban agglomerations: Abstracts of the International Symposium*. Moscow, Perm: 1995. Pp. 12–13. (In Russ.)
12. Isaevich A.G., Starikov A.N., Maltsev S.V. Improvement of air sampling method to determine relative concentration of combustion gases in mine air. *Mining Informational and Analytical Bulletin*. 2021;(4):143–153. (In Russ.) [https://doi.org/10.25018/0236\\_1493\\_2021\\_4\\_0\\_143](https://doi.org/10.25018/0236_1493_2021_4_0_143)
13. Norina N.V., Isaevich A.G. Methods and technical means of neutralization sulfur-containing gases in the atmosphere of potassium mines. *Izvestija Tul'skogo Gosudarstvennogo Universiteta. Nauki o Zemle*. 2021;(4):550–557. (In Russ.)
14. Smetannikov A.F., Filippov V.N. Some features of the mineral composition of salt rocks and their processed products using the example of Verkhnekamskoe salt deposit. *Problems of Mineralogy, Petrography and Metallogeny. Scientific Readings in Memory of P.N. Chirvinsky*. 2010;13:99–113. (In Russ.)
15. Zemskov A.N., Liskova M. Yu. Features formation of component composition of gases of potash fields. *Izvestija Tul'skogo Gosudarstvennogo Universiteta. Nauki o Zemle*. 2019;(2):88–97. (In Russ.)
16. Gazizullin R.R., Isaevich A.G., Levin L. Yu. Numerical modeling of the processes for removing harmful impurities from mine atmosphere during ventilation of dead-end workings using various methods. *Scientific Researches and Innovations*. 2011;5(2):127–129. (In Russ.)
17. Krasnoshtein A.E. *Physico-chemical mechanisms in the process of adsorption of toxic impurities from the mine atmosphere using potash salts*. Perm: Perm Polytechnic Institute; 1977. (In Russ.)
18. Zhu X., Wen H. Numerical simulation study on the influence of air leakage on oxygen concentration in goafs of fully mechanized caving mining with shallow buried and large mining height. *Frontiers in Earth Science*. 2023;11:1138925. <https://doi.org/10.3389/feart.2023.1138925>

### Information about the authors

**Alexey N. Starikov** – PhD-Student, Perm Federal Research Center of the Ural Branch of the Russian Academy of Sciences, Perm, Russian Federation; Engineer of the Department of Aerology and Thermophysics, Mining Institute of the Ural Branch of the Russian Academy of Sciences, Perm, Russian Federation; ORCID [0000-0001-9352-5612](https://orcid.org/0000-0001-9352-5612); e-mail [starikov4488@mail.ru](mailto:starikov4488@mail.ru)

**Stanislav V. Maltsev** – Cand. Sci. (Eng.), Head of the Mine Ventilation Sector of the Department of Aerology and Thermophysics, Mining Institute of the Ural Branch of the Russian Academy of Sciences, Perm, Russian Federation; ORCID [0009-0002-9887-1455](https://orcid.org/0009-0002-9887-1455)

**Andrey E. Sukhanov** – PhD-Student, Junior Researcher at the Department of Aerology and Thermophysics, Mining Institute of the Ural Branch of the Russian Academy of Sciences, Perm, Russian Federation; ORCID [0009-0002-7960-8344](https://orcid.org/0009-0002-7960-8344); e-mail [asukhanov@aerologist.ru](mailto:asukhanov@aerologist.ru)

**Received** 22.01.2024

**Revised** 16.09.2024

**Accepted** 17.09.2024



## TECHNOLOGICAL SAFETY

Research paper

<https://doi.org/10.17073/2500-0632-2024-07-283>

УДК 622.41:552.53

**Evaluation of variation of salt dust hygroscopic aerosol particle size as a function of relative air humidity**K. A. Chernyi  , G. Z. Faynburg  <sup>1</sup> Perm National Research Polytechnic University, Perm, Russian Federation [chernyy\\_k@mail.ru](mailto:chernyy_k@mail.ru)**Abstract**

The expansion of mining in potash mines has faced the problem of fresh air shortage, which cannot be solved within the current paradigm of self-contained ventilation. Prospects are related to sequential and recirculation ventilation, as well as the concept of “ventilation on demand”, requiring a detailed description of the processes of “self-cleaning” of a mine air from dust. Crushing a rock mass results in the formation of many aerosol hygroscopic salt particles, which in humid air conditions aggregate and settle on a drift floor. Accurate mathematical models are necessary for predicting the dispersion of these particles and associated gases. The paper considers the regularities and mechanisms of the effect of relative air humidity on the size of salt dust particles, aerosol hygroscopic salt particles of halite (NaCl) and sylvite (KCl). The interactions at the contact “salt surface – humid air” are described and the current understanding of the hysteresis processes and the stages of deliquescence and efflorescence (recrystallization) of hygroscopic aerosol particles are considered. Due to the fundamental difficulties of using modern experimental electronic equipment in the conditions of underground mines, data on oceanic aerosols of the same chemical composition were involved in the analysis. A number of models of hygroscopic growth of oceanic aerosol particles were reviewed and then adapted to the conditions of a potash mine atmosphere that made it possible to obtain average values of the factor of a salt aerosol particle hygroscopic growth. The good convergence of the known scientific data on the changes of the hygroscopic growth factor depending on relative air humidity for both oceanic aerosol and salt dust aerosol characteristic of a mine air was shown. The obtained theoretical-empirical data characterizing the changes in the size of salt particles depending on relative humidity were tested in model studies with salt aerosol. Young’s model was proposed to interpret and predict the changes in the size distribution of salt aerosol particles. The heuristic value of the proposed approach was confirmed by the example of the Young’s model record in log-log coordinates. The results of the study can be applied to calculate the processes of dust conditions formation in rock-salt and potash mines.

**Keywords**

potash mine, ventilation, safety, atmosphere, aerosol, halite, sylvite, sylvite, salt dust, deliquescence, efflorescence, hygroscopic growth factor, speleotherapy, model

**For citation**


Chernyi K.A., Faynburg G.Z. Evaluation of variation of salt dust hygroscopic aerosol particle size as a function of relative air humidity. *Mining Science and Technology (Russia)*. 2025;10(1):34–44. <https://doi.org/10.17073/2500-0632-2024-07-283>

## ТЕХНОЛОГИЧЕСКАЯ БЕЗОПАСНОСТЬ

Научная статья

**Оценка изменения размера гигроскопического аэрозоля соляной пыли в зависимости от относительной влажности воздуха**К. А. Черный  , Г. З. Файнбург  

Пермский национальный исследовательский политехнический университет, г. Пермь, Российская Федерация

 [chernyy\\_k@mail.ru](mailto:chernyy_k@mail.ru)**Аннотация**

Расширение масштабов добычи полезных ископаемых в калийных рудниках столкнулось с проблемой нехватки свежего воздуха, которую невозможно решить при текущей парадигме автономного проветривания. Перспективы связаны с последовательным и рециркуляционным проветриванием, а также концепцией «вентиляции по требованию», требующими детального описания процессов «самоочистки» рудничной атмосферы от пыли. Разрушение горных пород сопровождается выбросом солевых



аэрозолей, которые во влажной атмосфере укрупняются и осаждаются на поверхность. Для прогнозирования распространения этих частиц и сопутствующих газов необходимы точные математические модели. В статье рассматриваются закономерности и механизмы влияния относительной влажности воздуха на динамику размера соляной пыли – гигроскопических аэрозольных соляных частиц галита (NaCl) и сильвина (KCl). Описаны взаимодействия при контакте «соляная поверхность – влажный воздух» и рассмотрено современное представление о процессах гистерезиса, а также об этапах растворения и обратной кристаллизации гигроскопических аэрозольных частиц. В связи с принципиальными сложностями использования современного экспериментального электронного оборудования в условиях подземных рудников в анализ вовлечены данные по океаническим аэрозолям того же химического состава. На основе анализа ряда моделей гигроскопического роста океанических аэрозолей проведена их адаптация к условиям атмосферы калийного рудника, что позволило получить усредненные значения фактора гигроскопического роста соляной аэрозоли. Для океанического аэрозоля и соляной пыли рудничной атмосферы наблюдается хорошее соответствие известных данных динамики фактора гигроскопического роста от влажности воздуха. Полученные теоретико-эмпирические данные, характеризующие изменения размера соляных частиц в зависимости от относительной влажности, апробированы в модельных исследованиях с соляным аэрозолем. Для интерпретации и прогнозирования изменений размерного распределения соляных аэрозольных частиц предложено использовать модель Юнга. На примере записи модели Юнга в двойных логарифмических координатах подтверждена эвристическая ценность предложенного подхода. Результаты исследования могут быть применены для расчета процессов формирования пылевой обстановки в каменно-соляных и калийных рудниках.

#### Ключевые слова

калийный рудник, проветривание, безопасность, атмосфера, аэрозоль, галит, сильвин, сильвинит, соляная пыль, растворение, кристаллизация, фактор гигроскопического роста, спелеотерапия, модель

#### Для цитирования

Chernyi K.A., Faynburg G.Z. Evaluation of variation of salt dust hygroscopic aerosol particle size as a function of relative air humidity. *Mining Science and Technology (Russia)*. 2025;10(1):34–44. <https://doi.org/10.17073/2500-0632-2024-07-283>

### Introduction

The significant expansion of mineral extraction in current potash mines faced a problem of severe shortage of fresh air supply to a mine, which cannot be solved within the prevailing paradigm of autonomous independent ventilation of working areas. Under these conditions, almost all the prospects proved connected with sequential and (or) recirculation ventilation, as well as with the concept of “ventilation on demand”, which require an adequate description of the processes of ventilation of mine workings, including the processes of “self-cleaning” of a mine air from dust at the levels of atoms, molecules, and clusters [1].

Crushing of a rock mass during mining operations in potash mines is inevitably accompanied by the formation of many aerosol hygroscopic salt particles of various sizes, which get into the air and form an aerodisperse medium. Instrumental measurements [2–4] show that in the process of mutual collision in humid air conditions salt particles aggregate and intensively precipitate on a drift floor. All this requires a detailed calculation of gas and dust conditions in a multi-connected network of mine workings of different aerodynamic types and process purpose on the basis of mathematical models adequate to reality, one of the obligatory members of which is the “runoff” of an impurity due to various kinds of micro-level interactions. One such interaction is the effect of relative hu-

midity on the growth, consolidation, and coalescence of aerosols of the major potash mine rock minerals halite (NaCl) and sylvite (KCl). General regularities of such effect are known from phenomenological observations, but the details of these processes and their mathematical description required for digitalization of mine ventilation processes are missing [5, 6].

Moreover, the spectral size composition and dynamics of processes of interaction of salt aerosols with humid air have acquired independent significance in connection with the use of both underground spaces of rock-salt and potash mines for the purposes of so-called speleotherapy and ground sylvite speleoclimatic chambers for speleoclimatotherapy [7].

The present paper is devoted to the consideration of the issues of mathematical description of the relative humidity effect on the size of hygroscopic aerosol particles.

The purpose of the research presented below is to determine the regularities of changes in the distribution (in size) of salt dust particles depending on the relative humidity of air, required for digitalization of mine ventilation to calculate and control the dust conditions in mine workings.

Achieving this goal required implementing the following measures:

- to review current ideas about the nature of a salt crystalline particle behavior at changing relative air



humidity, its watering and efflorescence (recrystallization);

- to review the known physical models of hygroscopic particles growth, determine their applicability to the conditions of mine atmosphere;

- on the basis of known experimental and empirical data on hygroscopicity of salt-water aerosol particles to reveal and confirm the feasibility of their use in estimating the size change of hygroscopic salt dust aerosol particles in potash mines;

- on the basis of actual measurements in a field experiment in an air medium with salt aerosol to experimentally confirm the reliability of the results obtained on the basis of the proposed models of hygroscopic growth and the models of size distribution of salt aerosol particles in a mine atmosphere.

### Techniques

The mineralogical and chemical composition of a salt aerosol depends on the corresponding parameters of salt rocks surrounding the airspace of a mine [5, 6]. The composition of salt rocks in potash mines is diverse and has been studied in detail for geological and mining-metallurgical purposes [8, 9]. The main practically important rocks are those formed by sodium chloride (halite), potassium chloride (sylvin) and potassium-magnesium chloride (carnallite) minerals: halite, sylvinite (red, banded, and mottled), carnallite. The interaction of relatively “moisture-resistant” halite and sylvin with air is especially important for mine operation [10], since carnallite, being a double aqueous salt of potassium and magnesium chlorides  $KCl \cdot MgCl_2 \cdot 6H_2O$ , contains itself molecular moisture and quickly “spreads” in humid air.

It should be noted that the interaction of NaCl (halite), KCl (sylvin) aerosol particles and host rock (sylvinite) with humid air remains insufficiently studied due to the relative slowness of natural processes of moisture condensation/evaporation and due to the extreme technical complexity of ensuring the operation of modern electronic measuring equipment [11] in conditions of aggressive and explosive environment. All this significantly complicates the quantitative study of the physics of salt aerosols in the conditions of underground mines and implementing appropriate field experiments, supplemented by the problems of financing such works.

In contrast to this situation, research on the impact of salt-water aerosol on the formation of the Earth's climatic conditions, the trends and consequences of the dangerous change of which are visible to all, due to its importance for the fate of mankind, receives the necessary relatively generous funding,

despite the costliness of the experiments, which are increasingly being conducted with enviable persistence around the world.

Since salt-water aerosol is formed largely from NaCl and KCl particles, the results of salt-water aerosol studies (see, e.g., [12–14]) can and should certainly be taken into account as well-reliable instrumental studies for solving the problems discussed in this paper.

### Findings

#### *Current understanding of the mechanisms of deliquescence and efflorescence (recrystallization) of halite and sylvin aerosol particles*

The most important role in the interfacial interaction of water vapor and salt particles is played by the essential fact that halite (NaCl) and sylvin (KCl) minerals have cubic syngony. Therefore, positively charged metal atoms, sodium  $Na^+$  and potassium  $K^+$  and negatively charged chlorine atoms  $Cl^-$  are structurally equivalent and form ionic structures of high stability: one sodium/potassium ion ( $Na^+/K^+$ ) is surrounded by six chloride ions ( $Cl^-$ ) and, conversely, one chloride ion is surrounded by six sodium/potassium ions. Thus a NaCl/KCl salt crystal of even a few nanometers in size retains its crystal properties (in dry air).

Salt aerosol particles have a strong affinity for water and, being hygroscopic, are enveloped by atmospheric moisture molecules, watered, dissolved, and grow due to the condensation of water vapor on a crystal [15], and the growth rate of particles with increasing relative air humidity naturally increases [16].

Four characteristic stages of transition from dry salt crystals to spherical drops of fully deliquesced salt solution can be distinguished in the mechanism of salt particle deliquescence when changing relative humidity  $RH$ , which is the result of hydrosorption processes at a “salt surface – humid air” contact.

At the first stage, characteristic of low  $RH$  values, the force fields of atoms on the surface of a dry salt crystal are only partially compensated by the force fields of neighboring atoms in the crystal lattice, and therefore they are able to interact with the force fields of atoms of water vapor molecules, always contained in an air. This interaction leads to the attraction of water molecules from the air to the solid surface and the formation of brine condensate, but due to the rather small number of water molecules in the air, the surface is not destroyed. In addition, at low water vapor elasticity, simultaneously with the attraction, water molecules previously deposited on the surface of salt crystals are released into the surrounding air. Thus, at  $RH$  of about 10–20%, the shape of the salt

particles remains unchanged with preserving crystal surfaces corresponding to dry nonspherical crystal-line particles [17].

At the second stage, the characteristic  $RH$  values are up to 70–75%. Under these conditions, a film of loosely bound water appears on the surface of salt particles in a relatively short period of time, which is highly aggressive towards easily soluble salts, and a salt mineral begins to deliquesce. The amount of water increases due to condensation [15], a crystal becomes more and more deliquesced, and finally water molecules envelop all surfaces of the deliquescing particle. The cubic shape of the particle with its sharp edges and corners disappears due to the fact that surface-adsorbed water deliquesces the salt crystal surface predominantly at the corners and edges of the crystals, where the field strengths attracting water molecules are stronger. Cubic particles become first near-cubic and then near-spherical [18], i.e., rounded (Fig. 1, *a*).

With further interaction with water vapor and increasing  $RH$ , a particle becomes large enough in size and tends to become an inhomogeneous sphere with a water shell (Fig. 1, *b*) [19], and, as for “large” particles, with a solid, partially nonspherical salt crystal core.

The third stage of the interaction between salt crystals and water in air leads to complete deliquescence (dissolution) of the crystals. If the  $RH$  exceeds a critical value called the salt deliquescence point due to atmospheric humidity or the deliquescence relative humidity  $DRH$ , the solid inner core of a particle, a salt crystal, deliquesces completely in a liquid drop and disappears, forming a homogeneous spherical drop of saturated solution [13].

The fourth stage is characterized by the fact that as  $RH$  increases above the  $DRH$  value, up to about 85–90%, the salt particles continue to increase at a slower deliquescence rate and become spherical droplets of solution at high  $RH$  values (e.g., about 99%) [17].

This is the above 4-stage process of moisture condensation on the surface of a salt aerosol particle until its complete deliquescence.

The reverse process, the release of moisture from the drops into the surrounding atmosphere and the efflorescence (recrystallization) of a salt, is so different from the deliquescence process that we can speak of hysteresis.

First, as  $RH$  decreases, a drop of unsaturated water-salt aerosol with a fully deliquesced salt crystal loses water along the same equilibrium vapor pressure curve, but remains in a liquid state and looks like a supersaturated brine drop, gradually decreasing in size due to water evaporation.

However, instead of “drying out” and efflorescence (crystallizing) at  $RH$  equal to  $DRH$  as one might expect, the salt aerosols remain hydrated and the solution remains supersaturated up to much lower  $RH$  values. This behavior is due to the fact that at a certain degree of “drying”, to form a crystal, the hydrated  $Na^+$  and potassium  $K^+$  ions need to conjugate with  $Cl^-$  ions, and such atoms number should be enough for a crystal formation.

With a further decrease in relative humidity, having passed (after passing) the  $DRH$  value(s), a second critical relative humidity is reached, called an efflorescence point or Efflorescence Relative Humidity  $ERH$ , at which a salt particle begins to “solidify”, gradually drying out and efflorescing (recrystallizing), now already representing a “solid-liquid” system [15, 20].

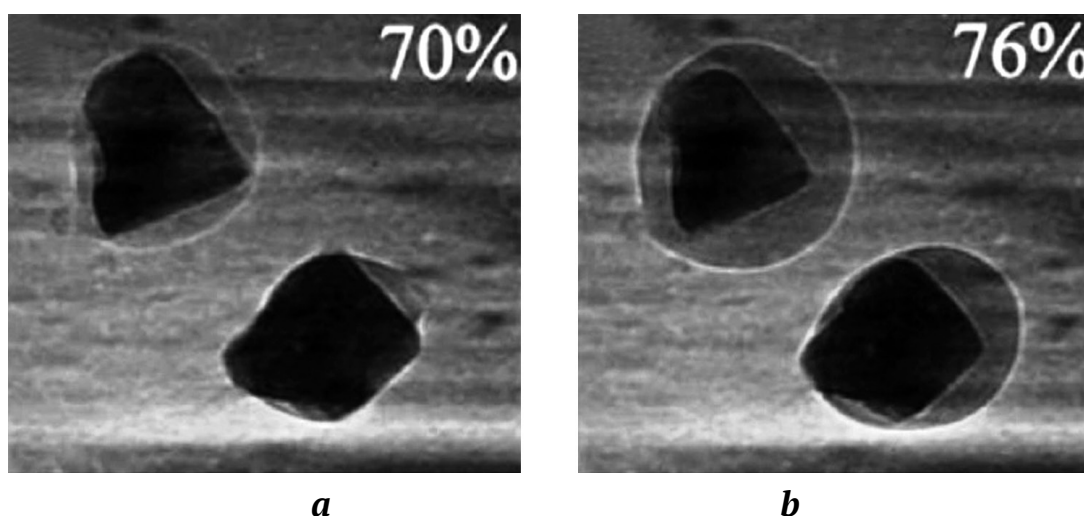


Fig. 1. Electron micrograph of sea salt crystal during deliquescence [15]:  
*a* –  $RH = 70\%$ ; *b* –  $RH = 76\%$



Since the *DRH* and *ERH* thresholds are different and relatively far apart in values, the presence of hysteresis leads to the fact that salt aerosol particles can exist in two forms, crystalline or aqueous, depending on the history (previous dynamics) of the *RH* change when the *RH* value is cycled. As a result, salt aerosol particles (both as solid, partially nonspherical salt crystals with a watery shell and as spherical droplets containing fully dissolved salt) can exist in the range of relative humidity values from about 45–50% to about 70–75%.

It should be noted that for sylvinites as a rock composed of different minerals with different *DRH* and *ERH* thresholds, the deliquescence and efflorescence processes may be even more complex than described above. Meanwhile, since the *ERH* of most salts and salt mixtures is about 40%, in most cases observed under ordinary aqueous atmospheric conditions with characteristic *RH* values typically greater than 40%, the hysteresis in the curve of changing particle size due to the difference in relative humidities of deliquescence (*DRH*) and efflorescence (*ERH*) can be neglected.

### Modeling the growth of hygroscopic salt particles

Many different physical models are now known that describe the growth of hygroscopic particles as a function of *RH* quite well.

To describe the changes of the dependence of the size (equivalent diameter) of a moistened aerosol particle  $D(RH)$  on *RH*, it is accepted to use a dimensionless value  $GF(RH)$ , particle growth factor:

$$GF(RH) = \frac{D(RH)}{D_0(RH)}, \quad (1)$$

where  $D_0(RH)$  is diameter of its dry base, a salt crystal at *RH* = 0%.

Note that, generally speaking, the growth factor at the same *RH* values depends on the absolute diameter of a dry particle that is especially evident for particles of a few tens of nm in size [11, 21, 22].

According to Koehler's *k*-theory [23], the hygroscopic properties of aerosol particles can be defined as a function of the *hygroscopicity parameter k* and *water activity*  $a_w$  in a drop of solution, defined as the ratio of the water vapor pressure over the flat surfaces of an aqueous salt solution to the vapor pressure over pure water at the same temperature. Under the condition of equilibrium of a salt aerosol droplet with water vapor and the nullity of the Kelvin effect describing the surface curvature that is true for particles of 100 nm and larger,  $a_w \approx RH/100$ , and Koehler's equation can be written as

$$GF(RH) = \left( 1 + k \frac{a_w}{1 - a_w} \right)^{1/3} \approx \left( 1 + k \frac{RH/100}{1 - RH/100} \right)^{1/3}, \quad (2)$$

from where it is well seen that the larger *k* is, the greater the slope of the graph of  $GF \approx GF(a_w) \approx GF(RH/100)$ . dependence is. The estimation for particles larger than 0.05 μm gives an error of substituting  $a_w$  for *RH* of no more than 5%, and, for particles larger than 0.1 μm, no more than 2%, which are quite acceptable for practical use.

Some of known literature data on hygroscopicity parameter *k* for salt aerosols are presented in Table 1.

For mixtures of soluble components, the hygroscopicity parameter can be approximated as the sum of its volume-weighted terms [23]:

$$k = \sum_i k_i \varepsilon_i, \quad (3)$$

where  $k_i$  is hygroscopicity parameter of an individual component of a mixture;  $\varepsilon_i$  is relative volume of a component in the mixture.

Our estimation of the range of the hygroscopicity parameter *k* variation for sylvinites gives the following: NaCl content in red sylvinites of the Kr-II formation of the Verkhnekamsk potassium-magnesium salt deposit varies within 71.51–73.20%, and that of KCl, 20.70–21.70%, while other components can be neglected. Then, taking into account the data of Table 1 for the salt aerosol (mixture of KCl and NaCl), characteristic of the air environment formed by potassium-magnesium salts, the hygroscopicity parameter varies in the range of 1.163 to 1.196, averaging 1.180.

A somewhat different (than (2)) model for describing the growth factor  $GF(RH)$  is presented in [16], according to which the model parameterization of  $GF(RH)$  is described by the following expression:

$$GF(RH) = A \cdot \left( \frac{2 - RH/100}{1 - RH/100} \right)^{1/3}, \quad (4)$$

where *A* is parameterization factor, for salt-water aerosol equal to

Table 1

Salt aerosols hygroscopicity parameter *k*

Nature of salt aerosol particles	<i>k</i>
Salt-water aerosol, $R^2 = 0.9980$ [24]	1.074
KCl particles of 100 nm in diameter, in the range $0.85 < a_w < 0.95$ [25]	$0.99 \pm 0.07$
NaCl particles of 100 nm in diameter, in the range $0.85 < a_w < 0.95$ [25]	1.12
NaCl [26]	1.34
NaCl [23]	0.91–1.33; 1.12 in average



$$A = \frac{4.0}{3.7} \approx 1.081.$$

The refinement of the dependence of the growth factor on water activity made in [27] to improve the approximation of experimental data suggests that the continuous hygroscopic growth of aerosol particles can be well described by the expression:

$$GF(RH) = \frac{D(RH)}{D_0(RH)} = \left( 1 + \left( a + b \frac{RH}{100} + c \left( \frac{RH}{100} \right)^2 \right) \frac{RH/100}{1 - RH/100} \right)^{\frac{1}{3}}, \quad (5)$$

where  $a$ ,  $b$ ,  $c$  are approximation parameters depending on a particle species, presented in Table 2 for NaCl particles according to [27].

Models describing the  $GF(RH)$  dependence in the form presented below [28–30] have become widely used:

$$GF(RH) = \left( 1 - \frac{RH}{100} \right)^g + C, \quad (6)$$

where  $g$  is so-called humidity factor;  $C$  is parameterization factor, the values of which for a number of salt aerosols are presented in Table 3.

A summary of the various experimental data obtained by different researchers and authors is presented in Fig. 2. The solid line indicates the average value of the salt aerosol particle growth factor, characteristic of potash mines air, as a function of  $RH$ .

Table 2

Values of  $a$ ,  $b$ ,  $c$  parameters of model (5)  
(according to [27])

Parameterization characteristics	$a$	$b$	$c$
No correction	3.89243	-4.49667	1.62110
With Kelvin correction	4.83257	-6.92329	3.27805
With Kelvin correction and sphericity correction	5.78874	-8.38172	3.92650

Table 3

Values of  $g$  and  $C$  parameters in parameterization (6)

Aerosol characterization	Humidity factor $g$	Parameterization factor $C$	Source
Salt-water aerosol accumulation mode (0.05 $\mu\text{m}$ in diameter)	-0.210	0.00	[28]
Salt-water aerosol, $R^2 = 0.9886$	-0.355	0.00	[24]
KCl according to experimental data of [31]	-0.325	0.05	Authors

The obtained results were used in the study of the size of aerosol particles in a model air medium as a function of  $RH$ , which simultaneously allowed to verify the adequacy of the above theoretical views with respect to the specific conditions of salt aerosol in an air medium.

### Experimental research

The authors selected a special model facility, a sylvinite chamber, which is an isolated room with the size of 2.0×3.5 m with controlled ventilation, all walls of which are lined with pressed salt sylvinite tiles 5–7 mm thick, manufactured by specialists of the Mining Institute of Perm Federal Research Center of the Ural RAS Branch, as a testing ground for experimental studies of the influence of relative air humidity on the counted size distribution of salt aerosol particles. The chamber ceiling 2.5 m high is ground halite, the floor is combined (passages are made of salt tiles cut from solid rock, and the rest of the area is coarsely crushed halite mixed with sylvinite).

The study of aerosol particle size distribution was carried out using an AZ-6 aerosol particle counter (PK. GTA-0.3-002), which allowed recording of aerosol particles of six size fractions: 0.3  $\mu\text{m}$  and above, 0.4  $\mu\text{m}$  and above, 0.5  $\mu\text{m}$  and above, 0.6  $\mu\text{m}$  and above, 0.8  $\mu\text{m}$  and above, 1  $\mu\text{m}$  and above. The measurement range of countable particle concentration was from  $10^2$  to  $3 \cdot 10^5 \text{ dm}^{-3}$ . The principle of the AZ-6 aerosol particle counter operation is optical and based on recording of scattered radiation. The tolerance limit of the basic relative error of aerosol counting concentration measurements in the range from  $3 \cdot 10^4$  to  $2.5 \cdot 10^5$  is  $\pm 40\%$ .

Relative humidity was recorded using an IVA-6A thermohygrometer, which allowed measuring temperature and relative humidity in the ranges from  $-20^\circ\text{C}$  to  $+60^\circ\text{C}$  and 0–98%, respectively. The tolerance limits of basic absolute error of relative humidity measurement at  $23^\circ\text{C}$  in the range of relative humidity of 0–90% is not more than 2%, and in the range of 90–98%, not more than 3%. The tolerance limit of absolute error of temperature measurement is not more than 0.1  $^\circ\text{C}$ .

Long-term studies of the slowly changing microclimate were conducted while the  $RH$  value decreased from 90% (such maximum humidity was recorded in the chamber after several days of rainy weather) to 62% (after several consecutive sunny days).

The results of studies of aerosol particle size distributions (distribution density  $dN(D)/dD$ , where the differential  $dN(D)$  determines the number of particles in a unit volume, usually in one liter,  $\text{dm}^{-3}$ , falling within a unit interval of diameter  $dD$ , usually in  $\mu\text{m}$ ; bringing to one dimensionality, the aerosol particle distribution density  $dN(D)/dD$  are expressed in  $\text{cm}^{-4}$ )

in a model air medium, presented in Fig. 3, clearly show a decrease in aerosol particle concentrations with decreasing  $RH$ , especially for particles of about  $0.3\text{--}0.5\text{ }\mu\text{m}$  in diameter. This is consistent with the mechanisms of salt particle watering and drying discussed above. While  $RH$  decreases, the particles gradually lose the water shell, decreasing in size, the mode of salt aerosol particle distribution shifts toward increasingly smaller particles, resulting in a decrease in the number of particles in the fixed particle size intervals of  $0.3\text{--}1\text{ }\mu\text{m}$ .

### Findings Discussion

The approximation of the spectral size distributions of salt aerosol particles presented in Fig. 3 was carried out according to the well-known Young's model [33–35]:

$$\frac{dN(D)}{d\lg D} = n^*(D_0) \left( \frac{D}{D_0} \right)^{-Y^*},$$

or

$$\frac{dN(D)}{dD} = B^* \cdot n^*(D_0) \left( \frac{D}{D_0} \right)^{-(Y^*+1)}, \text{ cm}^{-4}, \quad (7)$$

where  $dN(D)/d\lg D$  is distribution density of counted particle concentration,  $\text{cm}^{-3}$ ;  $N(D)$  is concentration of particles with diameter larger than  $D$ ,  $\text{cm}^{-3}$ ;  $D_0$  is arbitrarily chosen particle diameter in the range from about  $0.1\text{ }\mu\text{m}$  to  $10.0\text{ }\mu\text{m}$ , for which the validity of Young's model is reliably proved;  $n^*(D_0)$  is distribution density at  $D = D_0$ ,  $\text{cm}^{-3}$ ;  $Y^*$  is power exponent;  $B^* = 1 / (\ln 10) \approx 0.434$  is dimensional conversion factor,  $\text{cm}^{-1}$ .

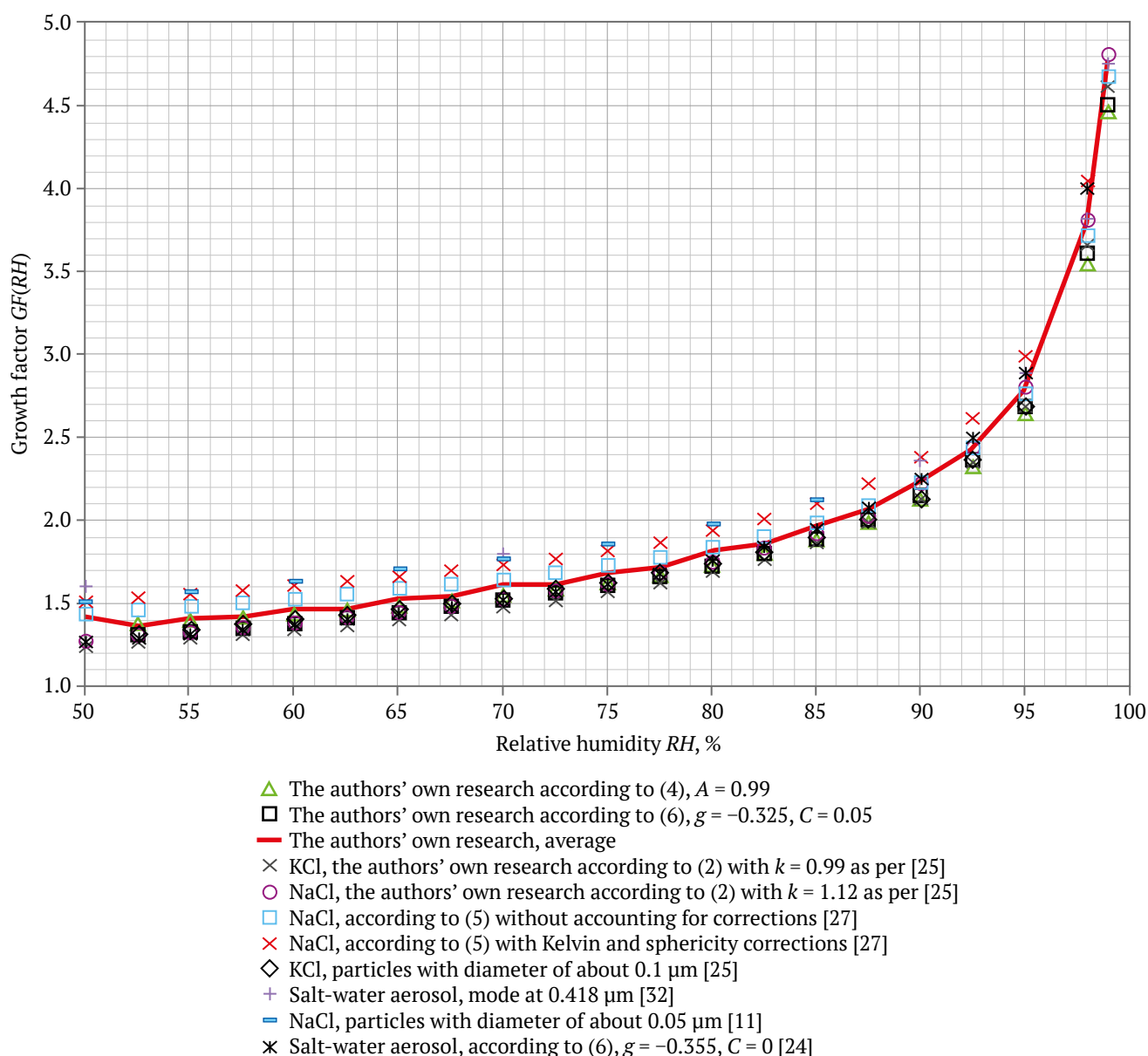


Fig. 2. Experimental and empirical data of growth factor of different salt aerosols depending on relative humidity

This write-up of Young's model to describe the continuous size distribution of the counted concentration was selected for the reason that equation (7), allowed for comparability with the relationships for the growth factor  $GF(RH)$ , also operating according to (1) with  $D/D_0$ . In addition, equation (7) in log-log coordinates depicts the distribution function as a straight line.

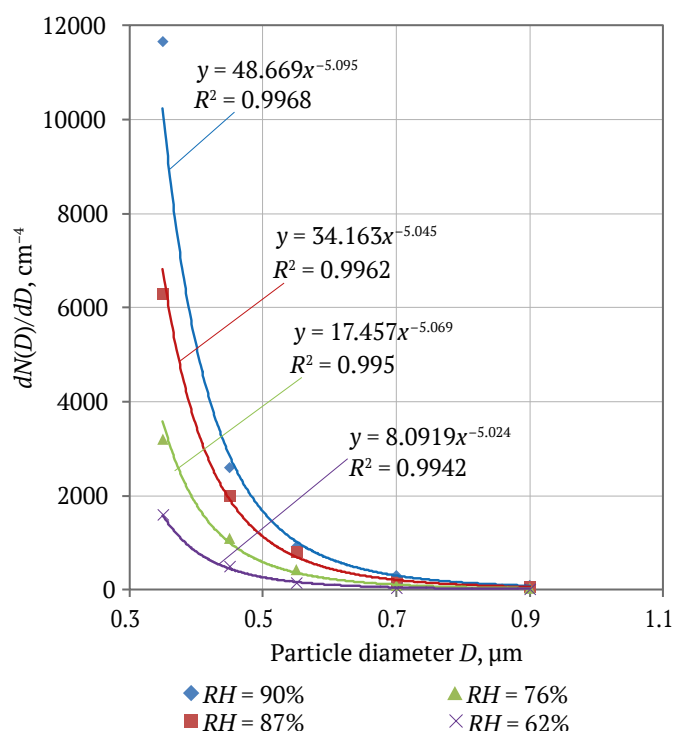


Fig. 3. Salt aerosol distributions by particle size at different relative humidity values

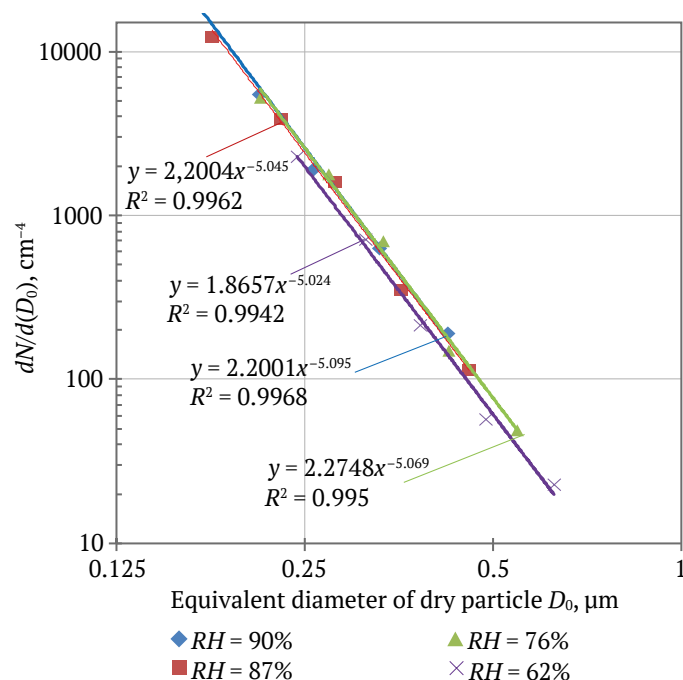


Fig. 4. Effective distribution of "dry" aerosol particles

The exponents of power in the functions approximating the power-series distributions of aerosol particles at different values of RH are not much different (see Fig. 3) and amount to  $Y^* = 4.06 \pm 0.03$ . This obtained value agrees well with historical results, according to which the values of the exponents of power in the Young's model for aerosols of different physical and chemical nature vary in the range  $Y^* = 2-5$  [36].

The values of the distribution density  $n^*(D_0)$  in the approximating expressions presented in Fig. 3 decrease as RH decreases that also agrees with the previously presented reasoning about the salt aerosol particles efflorescence processes and with the regularities of the considered Young's model.

The regularities of the changes in the distribution density  $n^*(D_0)$  depending on RH can be obtained by taking the particle diameter as the diameter of a "dry" particle at RH = 0 % and based on the averaged values of the hygroscopic growth factor obtained earlier and presented in Fig. 2. Fig. 4 shows the distributions of "dry" aerosol particles with diameter  $D_0$  calculated from (7) together with (1), based on the values of  $GF(90\%) = 2.13$ ;  $GF(87\%) = 1.97$ ;  $GF(76\%) = 1.65$ ;  $GF(62\%) = 1.44$ . According to Fig. 4 all distributions empirically recalculated to a "dry" residue for all considered cases of relative humidity were reduced in log-log coordinates to a single straight line and are described by the empirical expression

$$\frac{dN}{dD_0} = (2.14 \pm 0.18) \cdot (D_0)^{-(5.06 \pm 0.03)}. \quad (8)$$

The obtained results allowed not only to confirm the reliability of the regularities of hygroscopic growth of sea salt particles known in atmospheric and ocean physics, but also to generalize the Young's size distribution (8) for the conditions of a mine atmosphere that allows using it in modeling dust conditions in mine workings of potash mines.

## Conclusion

The study demonstrated uniform regularities of hygroscopic growth of salt aerosol particle sizes as a function of relative air humidity, characteristic of both sea air and the air of potash mines.

The shown high convergence of the hygroscopic growth factor values (with mean value of root-mean-square deviation of 0.11 in the interval of the factor change of 1.26–4.77) borrowed from known models and known scientific data on watering and reverse efflorescence of salt particles of salt-water aerosol with the results obtained by the authors in a model air environment, typical for the atmosphere of a salt mine,



confirms the feasibility of their use in modeling the processes of mine ventilation. The adapted for mine conditions expressions describing the size of hygroscopic aerosol particles consisting of halite (NaCl) and sylvin (KCl) crystals as a function of relative humidity allow building ventilation models adequate to actual conditions, required also in digitalization of potash mines ventilation.

The obtained averaged values of the growth factor for various conditions of particle watering and the confirmed reliability of application of Young's

model with a power coefficient in the expression  $dN(D)/dD$ , equal to  $-(5,06 \pm 0,03)$  can be used in the construction of mathematical models of salt dust behavior in mine workings and changing aerosol particle sizes at increasing and (or) decreasing relative air humidity that confirms their theoretical and practical significance for mine ventilation management.

Thus, the goals of the research presented in this paper have been achieved, and the set tasks have been solved in full.

## References

1. Faynburg G.Z. Problems in developing a new ventilation paradigm of mining system ore mines. *Proceedings of the Tula States University – Sciences of Earth*. 2024;1: 450–465. (In Russ.)
2. Isaevich A.G., Fainburg G.Z., Maltsev S.V. Experimental study of the changes dynamics in the fractional composition of salt aerosol in the cutting loading machine face of a potash mine. *Mining Informational and Analytical Bulletin*. 2022;(1):60–71. (In Russ.) [https://doi.org/10.25018/0236\\_1493\\_2022\\_1\\_0\\_60](https://doi.org/10.25018/0236_1493_2022_1_0_60)
3. Semin M.A., Isaevich A.G., Zhikharev S.Y. The analysis of potash salt dust deposition in roadways. *Journal of Mining Science*. 2021;57(2):341–353. <https://doi.org/10.1134/S1062739121020186>
4. Isaevich A., Semin M., Levin L. et al. A. Study on the dust content in dead-end drifts in the potash mines for various ventilation modes. *Sustainability*. 2022;14(5):3030. <https://doi.org/10.3390/su14053030>
5. Medvedev I.I., Krasnoshteyn A.E. *Dust control in potash mines*. Moscow: Nedra Publ. House; 1977. 192 p. (In Russ.)
6. Smetanin M.M. Safety system for dust factor in potash mines. *Journal of Mining Institute*. 2006;168:37–40. (In Russ.)
7. Faynburg G.Z., Chernyi K.A. *Natural scientific basis for the unconventional use of salt rocks from the Verkhnekamskoye deposit of potassium-magnesium salts*. Monograph. Perm: Publ. House of Perm National Research Polytechnic University; 2018. 212 p. (In Russ.)
8. Kudryashev A.I. *Verkhnekamskoe salt deposit*. Moscow: Geokniga; 2013. 185 p. (In Russ.)
9. Iblaminov R.G. Collision and lithogenic minerals of Permian Urals. In: *Problems of Mineralogy, Petrography and Metallogeny: Memory Scientific Readings of P.N. Chirvinsky*. 2024;27:50–58. (In Russ.) <https://doi.org/10.17072/chirvinsky.2024.50>
10. Fainburg G.Z., Chernyi K.A. Physical properties of salt rocks, which are forming specific parameters of air environment. *Proceedings of the Tula States University – Sciences of Earth*. 2023;(1): 67–80. (In Russ.)
11. Pinterich T., Spielman S.R., Wang Y. et al. A humidity-controlled fast integrated mobility spectrometer (HFIMS) for rapid measurements of particle hygroscopic growth. *Atmospheric Measurement Techniques*. 2017;10(12):4915–4925. <https://doi.org/10.5194/amt-10-4915-2017>
12. Kaloshin G.A. Modeling the Aerosol Extinction in Marine and Coastal Areas. *IEEE Geoscience and Remote Sensing Letters*. 2021;18(3):376–380. <https://doi.org/10.1109/LGRS.2020.2980866>
13. Kanngießner F., Kahnert M. Modeling optical properties of non-cubical sea-salt particles. *Journal of Geophysical Research: Atmospheres*. 2021;126(4):e2020JD033674. <https://doi.org/10.1029/2020JD033674>
14. Rosati B., Christiansen S., Dinesen A. et al. The impact of atmospheric oxidation on hygroscopicity and cloud droplet activation of inorganic sea spray aerosol. *Scientific Reports*. 2021;11:10008. <https://doi.org/10.1038/s41598-021-89346-6>
15. Zeng J., Zhang G., Long S. et al. Sea salt deliquescence and crystallization in atmosphere: An in situ investigation using X-ray phase contrast imaging. *Surface and Interface Analysis*. 2013;45(5):930–936. <https://doi.org/10.1002/sia.5184>



16. Lewis E.R., Schwartz S.E. Comment on “size distribution of sea-salt emissions as a function of relative humidity”. *Atmospheric Environment*. 2006;40(3):588–590. <https://doi.org/10.1016/j.atmosenv.2005.08.043>
17. Wise M.E., Biskos G., Martin S.T. et al. Phase transitions of single salt particles studied using a transmission electron microscope with an environmental cell. *Aerosol Science and Technology*. 2005;39(9):849–856. <https://doi.org/10.1080/02786820500295263>
18. Mikhailov E., Vlasenko S., Niessner R., Poschl U. Interaction of aerosol particles composed of protein and salts with water vapor: hygroscopic growth and microstructural rearrangement. *Atmospheric Chemistry and Physics*. 2004;4(2):323–350. <https://doi.org/10.5194/acp-4-323-2004>
19. Kanngießner F., Kahnert M. Optical properties of water-coated sea salt model particles. *Optics Express*. 2021;29(22):34926–34950. <https://doi.org/10.1364/OE.437680>
20. Zieger P., Vaisanen O., Corbin J.C. et al. Revising the hygroscopicity of inorganic sea salt particles. *Nature Communications*. 2017;8:15883. <https://doi.org/10.1038/ncomms15883>
21. Mikhaylov E.F., Vlasenko S.S., Ryshkevich T.I. Influence of chemical composition and microstructure on the hygroscopic growth of pyrogenic aerosol. *Izvestiya. Atmospheric and Oceanic Physics*, 2008;44(4):416–431. <https://doi.org/10.1134/S0001433808040038>
22. Wang X., Lei H., Berger R. et al. Hygroscopic properties of NaCl nanoparticles on the surface: a scanning force microscopy study. *Physical Chemistry Chemical Physics*. 2020;22(18):9967–9973. <https://doi.org/10.1039/d0cp00155d>
23. Petters M.D., Kreidenweis S.M. A single parameter representation of hygroscopic growth and cloud condensation nucleus activity. *Atmospheric Chemistry and Physics*. 2007;7(8):1961–1971. <https://doi.org/10.5194/acp-7-1961-2007>
24. Tijjani B.I., Sha’aibu F., Aliyu A. The Effect of Relative Humidity on Maritime Tropical Aerosols. *Open Journal of Applied Sciences*. 2014;4(6):299–322. <https://doi.org/10.4236/ojapps.2014.46029>
25. Carrico C.M., Petters M.D., Kreidenweis S.M. et al. Water uptake and chemical composition of fresh aerosols generated in open burning of biomass. *Atmospheric Chemistry and Physics*. 2010;10(11):5165–5178. <https://doi.org/10.5194/acp-10-5165-2010>
26. Drozd G., Woo J., Häkkinen S.A. K. et al. Inorganic salts interact with oxalic acid in submicron particles to form material with low hygroscopicity and volatility. *Atmospheric Chemistry and Physics*. 2014;14(10):5205–5215. <https://doi.org/10.5194/acp-14-5205-2014>
27. Kreidenweis S.M., Koehler K., DeMott P.J. et al. Water activity and activation diameters from hygroscopicity data – Part I: Theory and application to inorganic salts. *Atmospheric Chemistry and Physics*. 2005;5(5):1357–1370. <https://doi.org/10.5194/acp-5-1357-2005>
28. Swietlicki E., Zhou J.C., Covert D.S. et al. Hygroscopic properties of aerosol particles in the north-eastern Atlantic during ACE-2. *Tellus. Series B. Chemical and Physical Meteorology*. 2000;52(2):201–227. <https://doi.org/10.3402/tellusb.v52i2.16093>
29. Gysel M., McFiggans G. B., Coe H. Inversion of Tandem Differential Mobility Analyser (TDMA) Measurements. *Journal of Aerosol Science*. 2009;40(2):134–151. <https://doi.org/10.1016/j.jaerosci.2008.07.013>
30. Adam M., Putaud J.P., Martins dos Santos S. et al. Aerosol hygroscopicity at a regional background site (Ispra) in Northern Italy. *Atmospheric Chemistry and Physics*. 2012;12(13):5703–5717. <https://doi.org/10.5194/acp-12-5703-2012>
31. Jing B., Peng C., Wang Y. et al. Hygroscopic properties of potassium chloride and its internal mixtures with organic compounds relevant to biomass burning aerosol particles. *Scientific reports*. 2017;7:43572. <https://doi.org/10.1038/srep43572>
32. Köpke P., Hess M., Schult I., Shettle E. P. *Global Aerosol Data Set: Report No. 243*. Hamburg: Max-Planck-Institut für Meteorologie; 1997. 46 p.
33. Junge C.E. *Air Chemistry and Radioactivity*. New York: Academic Press; 1963. 382 p. (Trans. ver.: Junge C.E. *Air Chemistry and Radioactivity*. Moscow: Mir Publ. House; 1965. 424 p. (In Russ.))
34. Jaenicke R. Problems of the distribution of the global aerosol. *Russian Chemical Reviews*. 1990;59(10):959–972. <https://doi.org/10.1070/rc1990v059n10abeh003569>
35. Vasil’ev A.V. About using of analytical expressions in approximating experimentally measured size distribution functions of aerosol particles. In: *Natural and anthropogenic aerosols: Proceedings of the*



3<sup>rd</sup> International Conference. St. Petersburg, 24–27 September 2001. St. Petersburg: VVM Publ. House; 2001. Pp. 98–103. (In Russ.)

36. Ismailov F. I. *Atmospheric aerosol*. LAP LAMBERT Academic Publishing; 2019. 288 p. (In Russ.) <https://doi.org/10.36719/2019/288>

#### Information about the authors

**Konstantin A. Chernyi** – Dr. Sci. (Eng.), Associate Professor, Head of the Department of Life Safety, Perm National Research Polytechnic University, Perm, Russian Federation; ORCID [0000-0002-4700-0505](https://orcid.org/0000-0002-4700-0505), Scopus ID [57739104200](https://orcid.org/57739104200); e-mail [chernyy\\_k@mail.ru](mailto:chernyy_k@mail.ru)

**Grigorii Z. Faynburg** – Dr. Sci. (Eng.), Professor, Scientific Director of the Department of Mining, Perm National Research Polytechnic University, Perm, Russian Federation; ORCID [0000-0002-9599-7581](https://orcid.org/0000-0002-9599-7581), Scopus ID [57217891724](https://orcid.org/57217891724); e-mail [faynburg@mail.ru](mailto:faynburg@mail.ru)

**Received** 16.07.2024

**Revised** 24.11.2024

**Accepted** 24.12.2024



## ENVIRONMENTAL PROTECTION

Research paper

<https://doi.org/10.17073/2500-0632-2024-02-224>

UDC 669.054.8:628.315.2



## Preparation of adsorbents for the extraction of heavy metals from mining wastewater

E. I. Mirzaeva<sup>1</sup>  , N. F. Isaeva<sup>2</sup> , E. Ya. Yalgashev<sup>3</sup> , D. P. Turdiyeva<sup>4</sup> , R. M. Boymonov<sup>5</sup><sup>1</sup> National University of Science and Technology MISIS (Almalyk Branch), Almalyk, Republic of Uzbekistan<sup>2</sup> Tashkent Research Institute of Chemical Technology, Tashkent, Republic of Uzbekistan<sup>3</sup> Tashkent Institute of Chemical Technology, Tashkent, Republic of Uzbekistan<sup>4</sup> Mirzo Ulugbek National University of Uzbekistan, Tashkent, Republic of Uzbekistan<sup>5</sup> Islam Karimov Tashkent State Technical University, Tashkent, Republic of Uzbekistan [mirzaevaelena92@gmail.com](mailto:mirzaevaelena92@gmail.com)

### Abstract

Mining and metallurgical operations are inextricably connected with the consumption of large volumes of water and, consequently, the generation of liquid waste. The priority is to solve the problems of treatment and rational reclaiming of process waters with high content of valuable components. This will make it possible to obtain a significant environmental and economic effect, i.e. to bring profit directly to enterprises, save material resources and reduce the environmental impact in mining regions. Processing of copper-zinc ores is accompanied by the formation of metal-bearing wastewater with a wide range of associated metals and nonmetals with low concentrations of each individual component and pH fluctuations within wide ranges. These factors make it difficult to select a rational treatment technology, so enterprises have to pay for excessive metal-bearing discharges into the environment. Heavy metals are toxic, do not undergo decomposition, can be accumulated by aquatic plants and reach a human body through the food chain. Centralized accumulation of accidental discharges, surface and drainage water with subsequent treatment for use in recycled water supply can solve a number of environmental problems in the field of water resources protection. Adsorption of heavy metals by zeolites produced from inexpensive clay minerals due to the simplicity of the process, possibility of zeolite regeneration, high efficiency in  $\text{Cu}^{2+}$ ,  $\text{Zn}^{2+}$  and  $\text{Fe}^{2+}$  ion exchange with release of non-toxic  $\text{Na}^+$  cations into the environment is a good alternative to chemical precipitation. The purpose of this study is to optimize the conditions for producing zeolites from kaolin and bentonite with the assessment of the possibility of their use for the treatment of wastewater generated during mining and processing of ores from sulfide copper-polymetallic deposits. The technology of alkaline fusion of bentonite or kaolin with sodium hydroxide was used as a basis for zeolite synthesis from crude mining products. The novelty of the technological approach in obtaining zeolites from natural aluminosilicates in comparison with the published data is that the adjustment of the chemical composition of alkaline alloy for the synthesis of zeolites with a certain crystal structure was carried out using  $\text{Al}_2\text{O}_3$ – $\text{NaAlO}_2$  waste suspension. The alkaline alloy was dissolved in water, filtered, and subjected to hydrothermal crystallization. The phase composition of the zeolite adsorbents was studied. Through studying the recovery of heavy metals from model solutions, the mass composition and conditions of alkaline fusion processes as well as the hydrothermal crystallization mode were optimized. The achieved metal recovery of 95% from the model solutions with initial concentration (mg/L): 150  $\text{Cu}^{2+}$ , 180  $\text{Zn}^{2+}$  and 125  $\text{Fe}^{2+}$  allowed to draw the conclusion that zeolites based on bentonite and kaolin can be used in the treatment of metal-bearing wastewater.

### Keywords

ore, processing, ecology, wastewater, treatment, heavy metals, adsorption, aluminosilicates, kaolin, zeolites, bentonites, crystallization, diffractogram


### For citation

Mirzaeva E. I., Isaeva N. F., Yalgashev E. Ya., Turdiyeva D. P., Boymonov R. M. Preparation of adsorbents for the extraction of heavy metals from mining wastewater. *Mining Science and Technology (Russia)*. 2025;10(1):45–55. <https://doi.org/10.17073/2500-0632-2024-02-224>



## ОХРАНА ОКРУЖАЮЩЕЙ СРЕДЫ

Научная статья

**Получение адсорбентов для извлечения тяжелых металлов из сточных вод горнорудной промышленности**Е. И. Мирзаева<sup>1</sup> , Н. Ф. Исаева<sup>2</sup> , Э. Я. Ялгашев<sup>3</sup> , Д. П. Турдиева<sup>4</sup> , Р. М. Боймонов<sup>5</sup><sup>1</sup> Университет науки и технологий МИСИС (филиал в г. Алмалыке), г. Алмалык, Республика Узбекистан<sup>2</sup> Ташкентский научно-исследовательский химико-технологический институт, г. Ташкент, Республика Узбекистан<sup>3</sup> Ташкентский химико-технологический институт, г. Ташкент, Республика Узбекистан<sup>4</sup> Национальный Университет Узбекистана имени Мирзо Улугбека, г. Ташкент, Республика Узбекистан<sup>5</sup> Ташкентский государственный технический университет имени Ислама Каримова, г. Ташкент, Республика Узбекистан mirzaevaelena92@gmail.com**Аннотация**

Деятельность горно-металлургических предприятий неразрывно связана с потреблением больших количеств воды и соответственно образованием жидких отходов. Приоритетным является решение проблем переработки и рациональной утилизации технологических вод с высоким содержанием ценных компонентов. Это позволяет получать значимый эколого-экономический эффект, то есть приносить прибыль непосредственно предприятиям, экономить материальные ресурсы и снижать нагрузку на окружающую среду в горнопромышленных регионах. Переработка медно-цинковых руд сопровождается формированием металлоносных потоков с широким спектром сопутствующих металлов и неметаллов с низкой концентрацией каждого отдельного компонента и колебаниями pH в широких пределах. Указанные факторы затрудняют выбор рациональной технологии очистки, поэтому предприятиям приходится платить за сверхнормативные металлоносные сбросы в окружающую среду. Тяжелые металлы токсичны, не подвергаются разложению, могут аккумулироваться водными растениями и по пищевой цепи достигать организма человека. Централизованная аккумуляция случайных сбросов, поверхностных и дренажных вод с последующей очисткой для использования в оборотном водоснабжении может решить ряд экологических задач в области охраны водных ресурсов. Адсорбция тяжелых металлов цеолитами на основе недорогих глинистых минералов благодаря простоте процесса, возможности регенерации цеолитов, высокой эффективности ионообмена  $\text{Cu}^{2+}$ ,  $\text{Zn}^{2+}$  и  $\text{Fe}^{2+}$  с выделением в окружающую среду нетоксичных катионов  $\text{Na}^+$  является хорошей альтернативой химическому осаждению. Целью настоящей работы является оптимизация условий получения цеолитов на основе каолина и бентонита для очистки сточных вод, образующихся при добыче и переработке руды медно-колчеданно-полиметаллических месторождений. За основу синтеза цеолитов из необогащенной продукции горнодобывающей отрасли принята технология щелочного сплавления бентонита или каолина с гидроксидом натрия. Новизной технологического подхода при получении цеолитов из природных алюмосиликатов по сравнению с опубликованными данными является то, что корректировку химического состава щелочного сплава для синтеза цеолитов с определенной кристаллической структурой осуществляли с помощью отходов суспензии  $\text{Al}_2\text{O}_3$ – $\text{NaAlO}_2$ . Щелочной сплав растворяли в воде, фильтровали и подвергали гидротермальной кристаллизации. Изучен фазовый состав цеолитных адсорбентов. Путем сопоставления степени извлечения тяжелых металлов из модельных растворов были оптимизированы состав массы и условия процессов щелочного плавления, а также режим гидротермальной кристаллизации. Благодаря достигнутой степени извлечения металлов на уровне 95 % из модельных растворов с начальной концентрацией, мг/л: 150  $\text{Cu}^{2+}$ , 180  $\text{Zn}^{2+}$  и 125  $\text{Fe}^{2+}$ , цеолиты на основе бентонита и каолина могут быть использованы при очистке металлоносных вод.

**Ключевые слова**

руда, переработка, экология, сточные воды, очистка, тяжелые металлы, адсорбция, алюмосиликаты, каолин, цеолиты, бентониты, кристаллизация, дифрактограмма

**Для цитирования**

Mirzaeva E.I., Isaeva N.F., Yalgashev E.Ya., Turdiyeva D.P., Boymonov R.M. Preparation of adsorbents for the extraction of heavy metals from mining wastewater. *Mining Science and Technology (Russia)*. 2025;10(1):45–55. <https://doi.org/10.17073/2500-0632-2024-02-224>

**Introduction**

The development of mining industry is accompanied by the formation of specific technogenic systems, including mine, shaft, pit and under-dump waters, as well as mining-generated dust pollution [1].

Compounds of copper, zinc, lead, iron, and other heavy metals have a negative impact on the hydrosphere, as well as on the health of population, especially children [2]. Enterprises in ore processing apply various processes to maximize the recovery of nonfer-



rous metals from technogenic waters and their return to the production cycle [3]. However, monitoring of natural waters in the areas of mining and processing and nonferrous metallurgy activities impact indicates a clear exceeding of metal content sanitary norms in wastewater [4]. Discharge of ineffectively treated water by Almalyk mining and metallurgical combine (AMMC) caused exceeding the MPC of zinc, lead, copper, iron, manganese, and molybdenum in the water use section of the Akhangaran River [5]. In order to reduce the anthropogenic impact on the hydrosphere, it is advisable to remove harmful impurities in treatment devices at industrial enterprises using water resources.

In the practice of water treatment from moderately concentrated contaminants natural zeolites are increasingly used [6–8], the main advantage of which is cheapness. Despite the high selectivity of clinoptilolite towards heavy metals ( $\text{Pb}^{2+}$ ,  $\text{Cd}^{2+}$ ,  $\text{Cu}^{2+}$ ,  $\text{Co}^{2+}$ ,  $\text{Cr}^{3+}$ ,  $\text{Zn}^{2+}$ ,  $\text{Ni}^{2+}$ ,  $\text{Hg}^{+}$ ,  $\text{Fe}^{3+}$ ), the adsorption capacity of natural zeolites is several times less than that of synthetic zeolites [7, 9]. Therefore, researchers are increasingly interested in the synthesis of zeolites from clay minerals [10–12], waste coal rock [13–15], crushed stone [16] and other cheap wastes [17, 18]. V.V. Somerset et al. revealed the effect of reducing the concentration of Ni, Zn, Cd, and Hg after treatment of acid mine drainage water with zeolites (phojasite) [19]. The conversion of source components into zeolites with framework structure is carried out taking into account phase composition, chemical activity and thermal stability of the source mineral raw materials, as well as the intended field of application. Expensive single-phase zeolites such as NaA, NaX, or NaY are produced by two-stage crystallization from pure reagents at a strict ratio of  $\text{Na}_2\text{SiO}_3$ , NaOH and  $\text{NaAlO}_2$  [20, 21], since a one-stage hydrothermal crystallization does not allow obtaining zeolites of a certain structure without impurities of extraneous phases. Hydrothermal treatment of kaolin calcined at 550–650 °C (with insignificant content of quartz and other refractory minerals) with alkaline solution is preferable for synthesis of NaA zeolite due to favorable Si/Al ratio close to two. More thermally stable bentonite [10], kaolin as part of waste coal rock [13] are calcined at temperatures of about 800 °C, and additional sources of aluminum are resorted to at the hydrothermal stage. A promising way of processing low-grade mining products into adsorbents for wastewater treatment from heavy metals is fusion of silicon-aluminum-containing raw materials together with NaOH and subsequent hydrothermal crystallization of zeolites from soluble alkaline alloy products [14, 15, 22].

The purpose of this study is the synthesis of zeolite adsorbents from low-grade natural raw materials with high content of crystalline quartz. The goals of this study are as follows: 1) characterization of phase and elemental composition and thermal stability of Uzbek clay minerals; 2) determination of the influence of alkaline fusion conditions on the phase composition of the hydrothermal crystallization products; 3) evaluation of the efficiency of extraction of copper, zinc, iron, and lead (being common pollutants of mine and waste waters) from model aqueous solutions. The key task was to develop a low-cost adsorbent for use in mining and metallurgical industry.

### Research Materials and Methods

The natural clay minerals used in this work are Navbakhor bentonite (NB) and Angren variegated kaolin (VK); plus sodium aluminate suspension (SAS) was used. Sodium aluminate suspension is a residue produced when alumina wastes are processed into adsorbents of halide containing compounds. Its phase composition, %, is as follows:  $\text{NaAlO}_2$  – 30–33, NaOH – 1.5–2.5;  $\text{Na}_2\text{CO}_3$  – 0.3–0.5, water – the rest. The zeolites derived from bentonite and kaolin are hereinafter designated as NBS and VKS. The codes of prepared samples, conditions of their synthesis and phase compositions are given in Table 1. In addition, the following commercial ingredients were used: 99% sodium hydroxide, hydrochloric acid (36.5% HCl), and 99% polyethylene polyamine (PEPA). The bentonite had the following elemental composition, wt. %: O, 51.03; Si, 26.95; Al, 7.25; Mg, 1.42; K, 1.65; Fe, 7.21; Na, 1.24; Ca, 2.32; Ti, 0.32; S, 0.20 and P, 0.35. The kaolin contained, wt. %: O, 53.38; Si, 25.49; Al, 10.59; Mg, 0.1; K, 0.81; Ba, 0.22; Fe, 1.91; Pb, 0.05; Na, 0.12; Ca, 0.22. The sodium aluminate suspension with a density of 1.23 g/cm<sup>3</sup> after drying at 350 °C contained, wt. %: O, 41.57; Al, 30.37; Na, 25.82; C, 2.08; Cl, 0.14.

The conversion of clay raw materials into soluble sodium aluminates and aluminosilicates was carried out by alkaline fusion with NaOH [11], with adjusting the ratio of  $\text{SiO}_2/\text{Al}_2\text{O}_3$  and  $\text{Na}_2\text{O}/\text{SiO}_2$  in the mixture by addition of sodium aluminate suspension. The  $\text{SiO}_2/\text{Al}_2\text{O}_3$  molar ratio varied from 1.5 to 7.17, and  $\text{Na}_2\text{O}/\text{SiO}_2$  molar ratio varied 0.016 to 1.5. The bentonite and kaolin for the synthesis of 7-NBS and 6-VKS were preliminarily subjected to partial leaching of Ca, Mg, K and Fe impurities by heat treatment in 2M HCl solution followed by washing and drying at 120 °C. The ingredients mixture was wet milled in a ball mill for one hour, transferred to porcelain cups, dried at 80–120 °C, and then calcined with an exposure time of 3 h at 810 °C. The alkaline fusion products were pulverized, transferred to a retort with a stirrer,



and distilled water was added in the ratio of Liquid : Solid (L : S) from 2.9 : 1 to 6.6 : 1.

After stirring for 30 min, the liquid was filtered from the solid residue into a polypropylene retort [21], and inoculum crystals were added at the rate of 0.2 g of NaA or NaX fresh zeolite powder per 100 g of the reaction mass. In the synthesis of 8-NBS and 5-VKS, 60 g of PEPA were added to the clear filtrate, and the reaction mixtures for 9-11-NBS and 8-VKS samples were exposed to microwave radiation for 0.5 h before being placed into an autoclave (see Table 1). Each of the obtained clear solutions in a polypropylene retort was placed into an autoclave and kept at 35 °C for 15–25 h to reach equilibrium in the reaction mixture. The temperature was then raised to 80 °C and incubated for 4 h. The optimum temperature of the induction period and crystal growth stage was selected for each alkaline alloy solution depending on the results of phase analysis of samples taken every hour. The crystallized products were separated on a Nutch-filter, washed with water to neutral pH value of the liquid phase, dried, and calcined at 300 °C.

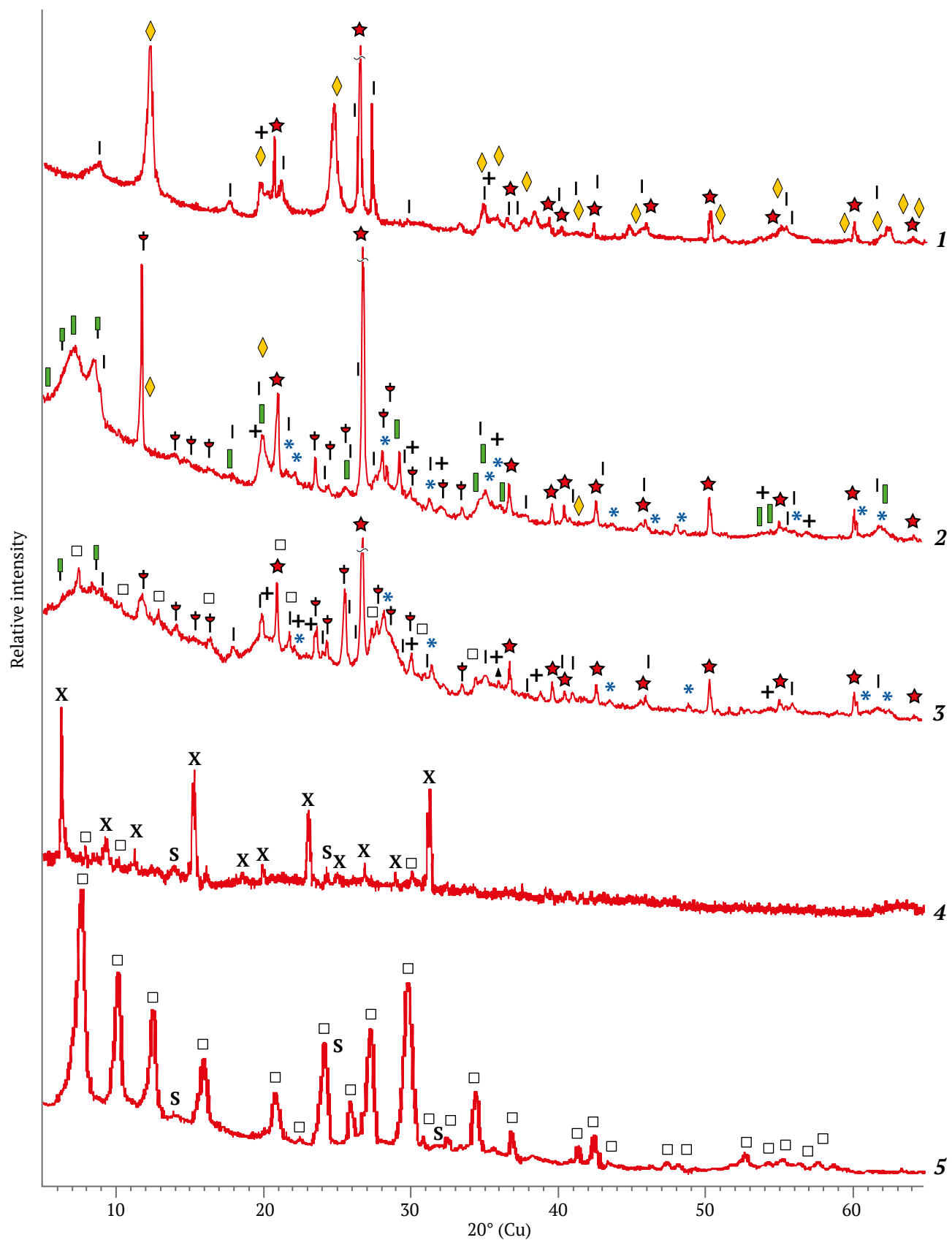
For the dynamic mode studies, 8-NBS and 6-VKS powders were molded by extrusion into pellets of 1.0 mm in diameter and 1.0–1.3 mm long. The molding mixture was prepared by mixing zeolite powder

with impurity-purified bentonite and carboxymethyl-cellulose solution. The pellets dried and calcined at 300 °C were treated with Na<sub>2</sub>CO<sub>3</sub> solution before adsorption. Under static conditions powdery adsorbents were used to evaluate the extent of heavy metal removal from a test solution. Conical retorts containing 100 ml each of the test solution and a precise weight suspension of the corresponding zeolite (0.05–1.0 g) were set into a shaker at 25 °C. The shaking time varied from 10 to 600 min. The dynamic tests were carried out in a column with a diameter of 1.25 cm at the height of the zeolite particles layer of 120 cm and liquid flow rate from 6 to 18 cm<sup>3</sup>/min. The degree of removal of harmful impurities from the water was evaluated by photocolometric method by the change in the concentration of the corresponding metals in contact with a zeolite sample. Zinc was determined as a complex compound with dithizone (analytical wavelength  $\lambda = 535$  nm), and copper, with lead diethyldithiocarbamate ( $\lambda = 430$  nm). We measured the optical density of the solutions of the complex compounds: zinc with dithizone (analytical wavelength  $\lambda = 535$  nm), copper with lead diethyldithiocarbamate ( $\lambda = 430$  nm), and iron with sulfosalicylic acid ( $\lambda = 430$  nm). Lead concentration was determined by chromate method at  $\lambda = 540$  nm using diphenylcarbazide.

Table 1

Effect of parameters of synthesis by alkaline fusion of 100 g of silicon-containing raw materials with NaOH and SAS on the crystallized products phase composition

Sample code	Ingredients of the mixture for alkaline fusion, g		Hydrothermal treatment			Molar ratio			Detected phases, %				
	NaOH	SAS	H <sub>2</sub> O, g	L/S ratio	Zeolite, 0.2 g	SiO <sub>2</sub> /Al <sub>2</sub> O <sub>3</sub>	Na <sub>2</sub> O/SiO <sub>2</sub>	H <sub>2</sub> O/Na <sub>2</sub> O	Zeolites			Impurities	
									NaA	NaX	NaP	Hydro-sodalite	SiO <sub>2</sub>
1-NBS	75.82	131.3	2175	14.7 : 1	NaA	1.5	1.5	130	13	–	–	43	11
2-NBS	49.8	89.9	1448	7.83 : 1	NaA	2.0	1.0	83.0	56	–	–	12	14
3-NBS	88.58	89.9	2199	10.2 : 1	–	2.0	1.5	84.0	8	–	–	75	8
4-NBS	98.85	64.97	2180	10.6 : 1	NaX	2.5	1.5	83.3	4	74	–	10	6
5-NBS	33.95	40.79	2513	17.7 : 1	NaX	3.3	0.6	240	4	63	6	–	9
6-NBS	1.24	–	240	2.66 : 1	NaA	7.17	0.016	860	4	–	–	7	88
7-NBS	55.05	100.8	1609	8.36 : 1	NaA	2.0	1.0	83.0	69	–	–	8	–
8-NBS	54.57	73.1	1609	8.87 : 1	NaX	2.5	1.0	83.0	2	79	–	3	–
9-NBS	49.8	89.9	1448	7.83 : 1	NaA	2.0	1.0	83.0	36	–	–	55	–
10-NBS	75.82	131.3	2175	9.40 : 1	–	1.5	1.5	130	–	–	–	82	–
11-NBS	98.85	64.97	2180	10.6 : 1	–	2.5	1.5	83.3	–	–	–	76	10
1-VKS	52.65	67.13	1370	8.64 : 1	NaA	2.0	1.0	83.0	64	–	–	8	–
2-VKS	89.3	67.13	2057	11.0 : 1	NaA	2.0	1.5	83.1	8	–	–	75	–
3-VKS	59.92	43.53	1370	9.2 : 1	NaX	2.5	1.0	83.0	6	78	–	4	–
4-VKS	37.62	20.67	824	7.0 : 1	–	3.3	0.6	83.2	10	24	38	–	–
5-VKS	59.92	43.53	1370	9.17 : 1	NaX	2.5	1.0	83.0	–	75	–	25	–
6-VKS	60.05	12.62	1194	8.64 : 1	NaA	2.0	1.0	83.0	83	–	–	3	–
7-VKS	49.48	46.91	1194	7.87 : 1	–	1.5	1.0	83.0	25	–	–	64	–
8-VKS	89.3	67.13	1370	8.64 : 1	–	2.0	1.0	83.0	6	–	–	90	–



◆ kaolinite; ★ quartz; | illite; + tridomite; □ zeolite NaA;  
■ montmorillonite; \* cristobalite; ● carbon; ▽ mixed-layer smectite-quartz; ▲ NaOH  
▤ mixed-layer illite-smectite; X zeolite NaX; S hydroxysodalite;

Fig. 1. Diffractograms: 1 – VK; 2 – NB; 3 – 4-NBS (alkaline fusion at 800 °C – 5 h); 4 – 8-NBS; 5 – 6-VKS

Adsorption capacity was determined according to the following formula:

$$A = (C_{ini} - C_{fin})V \cdot \frac{100}{m},$$

where  $A$  – adsorption capacity;  $C_{ini}$  – Initial concentration of a substance, g/l;  $C_{fin}$  – concentration of the substance under study in the solution in equilibrium conditions, g/l;  $m$  – mass of adsorbent, g;  $V$  – volume of model solution, l [11]. The elemental composition of the studied samples was determined using a scanning electron microscope (SEM) EVOMA 10 (Zeiss). X-ray phase analysis (XRD) diffractograms of the source substances and the synthesized zeolites were obtained on an Emmyrean diffractometer using  $\text{CuK}\alpha$  radiation, and the thermograms, on a HESON HS-TGA-103 derivatograph with a heating rate of  $10^\circ\text{C}/\text{min}$ .

### Experimental results

It followed from the diffractograms, Fig. 1, that the source materials taken were a mixture of different minerals and differed significantly in molar ratio:  $\text{SiO}_2/\text{Al}_2\text{O}_3 = 4.64$  (kaolin) and 7.17 (bentonite), one of the most important characteristics for the synthesis of zeolites.

In the diffractogram of kaolin, slightly broadened reflections with  $d = 0.714$ ;  $0.446$ ;  $0.357$ ;  $0.2568$ ;  $0.2504$ ;  $0.2387$ ;  $0.2343$ ;  $0.221$ ;  $0.1989$ ;  $0.1790$ ;  $0.1666$ ;  $0.1490$ ;  $0.1375$ ;  $0.701$ ;  $0.129$ ;  $0.1236$  nm were attributed to the manifestation of the rock-forming mineral kaolinite. Kaolinite is a layered aluminosilicate with the following chemical formula:  $\text{Al}_2\text{Si}_2\text{O}_5(\text{OH})_4$  [6], where the  $\text{SiO}_2/\text{Al}_2\text{O}_3$  molar ratio is equal to 2, same to NaA zeolite. The relative intensity of the basal reflections of kaolinite was less than that of quartz; in addition, reflections attributed to illite, a hydromicaeous potassium-bearing mineral ( $\text{K}_{<1}\text{Al}_2[\text{Al,Si}]_4\text{O}_{10}$ ·

$(\text{OH})_2 \cdot n \text{H}_2\text{O}$  ( $d = 0.998$ ;  $0.498$ ;  $0.421$ ;  $0.333$ ;  $0.320$ ;  $0.298$ ;  $0.256$ ;  $0.243$ ;  $0.239$ ;  $0.224$ ;  $0.218$ ;  $0.212$ ;  $0.198$ ;  $0.166$ ,  $0.164$ ;  $0.150$  nm) were observed. The process of dehydroxylation of kaolinite into amorphous metakaolin occurred in the range of  $490$ – $610^\circ\text{C}$ , while illite and quartz did not undergo phase transformation up to  $800^\circ\text{C}$  (Fig. 2, thermogram 1).

The rock-forming mineral of bentonite was montmorillonite from the smectite group, identified by the main reflections with  $d = 0.568$ ;  $0.704$ ;  $0.809$ ;  $0.4472$ ;  $0.3422$ ;  $0.3053$ ;  $0.2598$ ;  $0.1711$ ;  $0.1672$ , and  $0.1504$  nm along with the reflections of quartz and mixed-layer phases: smectite-quartz and smectite-illite (see Fig. 1, diffractogram 2). The indicated reflections partially coincided with those from illite, kaolinite, and  $\alpha$ -cristobalite that is characteristic of fine clay deposits [10]. After calcination of bentonite at  $600$ – $650^\circ\text{C}$  kaolinite and montmorillonite were not identified radiographically, but the background in the region of angles  $2\theta = 18$ – $32^\circ$  from the amorphous products of their dehydroxylation increased, the reflections from illite were preserved, but the reflection from crystalline polymorphs of  $\text{SiO}_2$  prevailed. The phases of tridymite,  $\alpha$ -cristobalite, and micaceous minerals identified in the bentonite and kaolin were preserved after heat treatment at  $850^\circ\text{C}$  and therefore required thermochemical activation with alkaline reagents [11]. In the alloys of bentonite or kaolin with NaOH at  $800^\circ\text{C}$ , the intensity of quartz lines was 50% of the initial one, but sharply decreased with increasing the fusion temperature to  $810^\circ\text{C}$ . The thermogram of natural bentonite in combination with the data of X-ray phase analysis after its calcination at  $550^\circ\text{C}$  confirmed that the change in the shape and some shift of the reflections of montmorillonite were due to the transformation of most of the swelling phase of montmorillonite into illite, which is not prone to swelling.

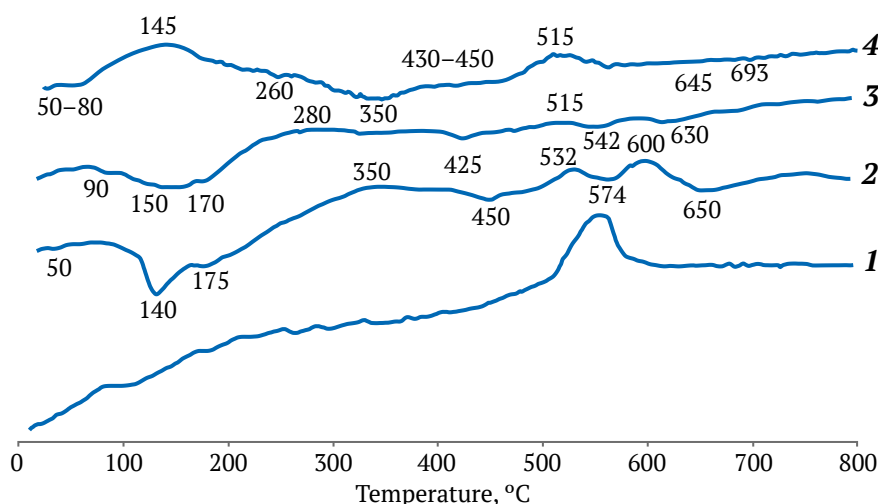


**Fig. 2.** Thermograms of components used in the synthesis of zeolite adsorbents: 1 – variegated colored kaolin (VK); 2 – Navbakhor bentonite (NB); 3 – alkaline fusion for sample 4-NBS; 4 – alkaline fusion for sample 2-VKS



Molecular water was removed at 50, 140 and 175 °C with a mass loss of 9.2%, and dehydroxylation of structural OH-groups with a mass loss of 1.8% occurred at 450, 574 and 650 °C (see Fig. 2, thermogram 2).

The sodium aluminate suspension after water removal was a mixture of X-ray amorphous sodium aluminates in terms of  $\text{NaAlO}_2$  and crystalline phases, %: gibbsite, 28.7;  $\text{NaOH}$ , 10.9;  $\text{Na}_2\text{CO}_3$ , 1.98, and  $\text{NaCl}$ , 0.024. After the calcination at 810 °C, broad reflections from  $\gamma\text{-NaAlO}_2$  ( $d = 0.425$ ; 0.294; 0.259; 0.215; 0.1994; 0.1970; 0.1881; 0.1747 nm) and  $\text{NaAl}_{11}\text{O}_{17}$  ( $d = 1.128$ ; 0.569; 0.280; 0.2518; 0.2424; 0.2380 nm) appeared on the diffractogram instead of the halo from amorphous phases. The transformation of gibbsite into  $\gamma\text{-Al}_2\text{O}_3$  was indicated by reflections with  $d = 0.198$  and 0.139 nm. Crystalline  $\text{Na}_2\text{CO}_3$  was identified by low-intensity narrow reflections with  $d = 0.2963$ ; 0.26; 0.254; 0.236; 0.218 nm. The codes of zeolites obtained under optimal conditions, the amount of ingredients in the mixtures for alkaline fusion and hydrothermal treatment of their leaching products, as well as the results of X-ray phase analysis of the synthesized zeolites are presented in Table 1.

### Findings Discussion

The optimal conditions of thermochemical decomposition of initial silicon sources were selected by comparing the diffractograms of the alkaline alloys obtained at temperatures of 800, 810, and 830 °C and intended for synthesis of samples 1-NBS, 4-NBS, 2-VKS, and 6-VKS with the results of the analysis of the solid residues from aqueous leaching. It was shown that almost complete conversion of montmorillonite, kaolinite, and  $\text{SiO}_2$  polymorphs into sodium aluminosilicates can be achieved by the calcination of the alkaline mixtures at a temperature of at least 810 °C for 3 h. Narrow reflections from nepheline  $\text{NaAlSiO}_4$  with  $d = 0.4192$ ; 0.3834; 0.3262; 0.3011; 0.2884 nm and very broad reflections with  $d = 0.53$ ; 0.432; 0.282; 2.55; 2.30 nm from  $2\text{NaAlO}_2 \cdot 3\text{H}_2\text{O}$  were observed at the alkaline alloy diffractograms for 1-NBS, 10-NBS, and 7-VKS samples with silicon deficiency ( $\text{SiO}_2/\text{Al}_2\text{O}_3 = 1.5$ ).  $\text{SiO}_2/\text{Al}_2\text{O}_3 \geq 2$  and  $\text{Na}_2\text{O}/\text{SiO}_2 = 1$ , background enhancement in the region of angles  $2\theta = 5\text{--}35^\circ$  from amorphous aluminosilicates and  $\text{SiO}_2$  was observed in the diffractograms, and the crystals of high-temperature aluminosilicate  $\text{Na}_4\text{Al}_2\text{Si}_2\text{O}_9$  ( $d = 0.4213$ ; 0.2584; 0.1822, and 0.1487 nm) were formed instead of nepheline. The traces of the high-temperature form of  $\text{NaAlSiO}_4$  ( $d = 0.423$  and 0.2592 nm), weak reflections of  $\alpha$ -cristobalite ( $d = 0.4013$ ; 0.3132; 0.2852; 0.2481; 0.193; 0.187 nm), which did not react with  $\text{NaOH}$  or  $\text{Na}_2\text{CO}_3$ , and a hydromica that did not contain constitutional water

( $d = 0.436$ ; 0.302; 0.260; 0.225; 0.202 nm) manifested themselves. In the diffractogram of the 4-NBS alloy with some surplus of sodium compounds, in addition to the  $\text{Na}_4\text{Al}_2\text{Si}_2\text{O}_9$  crystalline phase, reflections with  $d = 0.5302$ ; 0.3563; 0.3041; 0.2574; 0.2403; 0.1885, and 0.1754 nm from  $\text{Na}_2\text{SiO}_3$  were also detectable. In the alkaline alloys, as a rule, the  $\text{Na}_4\text{Al}_2\text{Si}_2\text{O}_9$  phase predominated, whose reflections intensity changed in the series: 8-VKS  $\approx$  6-VKS  $<$  1-VKS  $<$  7-NBS  $<$  2-NBS. Both forms of soluble sodium aluminosilicates were also present in the diffractograms of the other alkaline alloys.

Decreasing grinding time or duration of heat treatment of the alkaline alloys was accompanied by the appearance of reflections of quartz at  $2\theta = 20.8^\circ$ ;  $26.14^\circ$ ;  $36.6^\circ$ ;  $50.21^\circ$ ;  $59.82^\circ$  and those of  $\gamma\text{-Al}_2\text{O}_3$  around  $2\theta = 55.2^\circ$  in the diffractograms. It was shown in separate experiments that fusion of bentonite or kaolin with sodium hydroxide alone at 810 °C was less effective than combining  $\text{NaOH}$  with a suspension of sodium aluminate at the ratio of alkaline components  $\text{NaOH} : \text{Na}_2\text{CO}_3 = 5 : 1$  and equivalent amount of  $\text{Na}_2\text{O}$ . The products of alkaline fusion at temperatures above 800 °C, namely, amorphous silicates, weakly crystallized sodium aluminates, and crystalline  $\text{NaAlSiO}_4$ ,  $\text{Na}_4\text{Al}_2\text{Si}_2\text{O}_9$  and  $\text{Na}_2\text{SiO}_3$ , were well soluble in water and were thermodynamically unstable due to a large number of breaks and free ends of bonds in the places of their breakage [23]. At an optimum temperature of 80 °C, pH = 12–13, and 4 h autoclave exposure, the dissolved products of alkaline fusion crystallized predominantly into zeolites of NaX ( $\text{SiO}_2/\text{Al}_2\text{O}_3 \approx 2.5$ ), NaA ( $\text{SiO}_2/\text{Al}_2\text{O}_3 \approx 2.0$ ) or NaP ( $\text{SiO}_2/\text{Al}_2\text{O}_3 \approx 3/33$ ) type depending on the elemental composition (see Table 1). The characteristic diffraction peaks with  $d = 1.230$ ; 0.870; 0.710; 0.550; 0.37; 0.328; 0.298, and 0.262 nm were assigned to NaA zeolite, and the peaks with  $d = 1.447$ ; 0.885; 0.754; 0.573; 0.380, and 0.288 nm [24], to NaX zeolite. If the alkaline fusion process was carried out at a temperature of 800 °C, amorphous  $\text{SiO}_2$ , its crystalline polymorphs, and unreacted micaceous minerals strongly polluted the end product (see Fig. 1, diffractogram 3). When the mass same to that at the 4-NBS diffractogram was fused at 810 °C, the  $\text{SiO}_2$  peak area ( $2\theta = 26.6^\circ$ ) was 18 times less than that of the NaX zeolite phase ( $2\theta = 6.02^\circ$ ) [25].

It was found by varying the time of hydrothermal treatment of the dissolved alkaline alloys filtrate for samples 2-NBS, 4-NBS, 1-VKS, 4-VKS, and 5-VKS that the introduction of inoculum crystals NaA or NaX reduced the crystallization time from 7 to 3–4 h with a total yield of zeolite phases of 56–78%. Reducing the time of the hydrothermal treatment to 1–2 h sharply reduced the yield of the target products, and

in diffractograms, the intensity of basic reflections of zeolite phases at  $2\theta = 6.1\text{--}7.18^\circ$  amounted to 8–15% of the quartz peak at  $2\theta = 26.6^\circ$ . The crystallization of the alkaline alloy solution at  $810^\circ\text{C}$  for more than 4 h increased the yield of NaA and/or NaX zeolites by 7–8%, but led to an increase in the content of extraneous phases such as hydroxysodalite (peaks with  $d = 0.633$ ;  $0.365$ ;  $0.258$ ;  $0.239$ , and  $0.211$  nm [24]. The increase of crystallization time during the synthesis of sample 6-VKS from 3.5 h (see Table 1, Fig. 3) to 5 h was accompanied by an increase in the yield of NaA zeolite from 83 to 84%, and that of hydroxysodalite from 3 to 11% that complied with the findings of studies [14, 26]. The increased silicon content ( $\text{SiO}_2/\text{Al}_2\text{O}_3 = 2.5\text{--}3.3$ ) and applying NaX crystal inoculum at the hydrothermal treatment of alkaline bentonite alloy solutions with sodium aluminate suspension led to prevailing formation of the NaX zeolite phase with  $d = 0.1447$ ;  $0.885$ ;  $0.754$ ;  $0.573$ ;  $0.481$ ;  $0.442$ ;  $0.394$ ;  $0.381$  nm (see Table 1).

$\text{Na}^+$  cations played an important role in zeolitization by stabilizing the basic bonds of zeolite frameworks under hydrothermal conditions [27]. Not only the degree of destruction of the initial crystalline substances during fusion to form water-soluble substances, but also the alkalinity of the resulting solution for crystallization depended on the amount of sodium compounds during fusion. The slightly alkaline medium ( $\text{pH} = 8\text{--}8.5$ ) during the synthesis of 6-NBS sample at  $\text{Na}_2\text{O}/\text{SiO}_2$  ratio of 0.016 without addition of sodium aluminate suspension led to the formation of amorphous silica with a minimum of crystalline phases.  $\text{pH} \geq 14$  during the hydrothermal stage of synthesis of 1-NBS, 3-NBS, 10-NBS, 11-NBS, 2-VKS, and 7-VKS caused a clear predominance of hydroxysodalite phase. Table 1 shows that from 64 to 90% of hydroxysodalite were formed without NaA or NaX inoculum crystals during hydrothermal treatment of alkaline alloy solutions with  $\text{SiO}_2/\text{Al}_2\text{O}_3$  ratio in the range of 1.5–2.5. The reflections with  $d = 0.6293$ ;  $0.3649$ ;  $0.2814$ ;  $0.2573$ ;  $0.209$ ;  $0.1812$ ;  $0.17398$ ;  $0.1572$ ;  $0.15263$ ;  $0.1483$ , and  $0.14425$  nm in the diffractograms were assigned to the hydroxysodalite phase. According to literature sources hydroxysodalite is a hydrophilic zeolite with variable composition like  $\text{Na}_6\text{Al}_6\text{Si}_6\text{O}_{24} \cdot 8\text{H}_2\text{O}$  [22],  $\text{Na}_8[\text{AlSi}_4\text{O}_{16}(\text{OH})_2] \cdot 2\text{H}_2\text{O}$  and others [16, 28]. As was noted in the reviews [23, 26], the skeleton of NaA zeolite –  $\text{Na}_{12}\text{Si}_{12}\text{Al}_{12}\text{O}_{48} \cdot 27\text{H}_2\text{O}$ , formed as a result of hydrothermal crystallization from nepheline solutions with the calculated ratio of  $\text{SiO}_2/\text{Al}_2\text{O}_3 = 2$ , is subject to cracking at high alkalinity, which caused the formation of hydrosodalite. Hydroxysodalite crystals are known to have a cubic shape with an ordered aluminosilicate framework, in

which sodalite cells enclose small-sized pores [29], which can be useful in the extraction of metal ions from aqueous solutions [28]. In our experiments, 10-NBS and 8-VKS adsorbents consisting predominantly of hydroxysodalite were obtained without introduction of inoculum crystals but with microwave treatment. The introduction of NaA zeolite inoculum crystals into the microwave-treated reaction mixture clearly reduced not only the amount of useless quartz, but also prevented the formation of NaA zeolite crystals that was somewhat different from the conclusions drawn in [27], devoted to the conversion of fly ash into A-type zeolites with the use of microwave treatment.

### Study of adsorption properties

Multiphase nature of the synthesized adsorbents, including two types of metastable zeolite structures A and X, along with the stable phases of hydroxysodalite and NaP zeolite caused the specificity of their adsorption properties. The samples with the predominance of hydrosodalite or NaP zeolite were characterized by higher density and low specific surface area, about  $33\text{--}76$   $\text{m}^2/\text{g}$ , in comparison with metastable NaA and NaX zeolites with similar ratio of  $\text{SiO}_2/\text{Al}_2\text{O}_3$  with a specific surface area of up to  $300$   $\text{m}^2/\text{g}$ . The large volume of cavities characteristic of hydroxysodalite allowed adsorbents such as 10-NBS, 11-NBS, and 8-VKS adsorb some amount of metal ions from water, but extremely slowly. The tests under static conditions (see Fig. 3) were conducted with solutions of concentrations typical for polymetallic mine

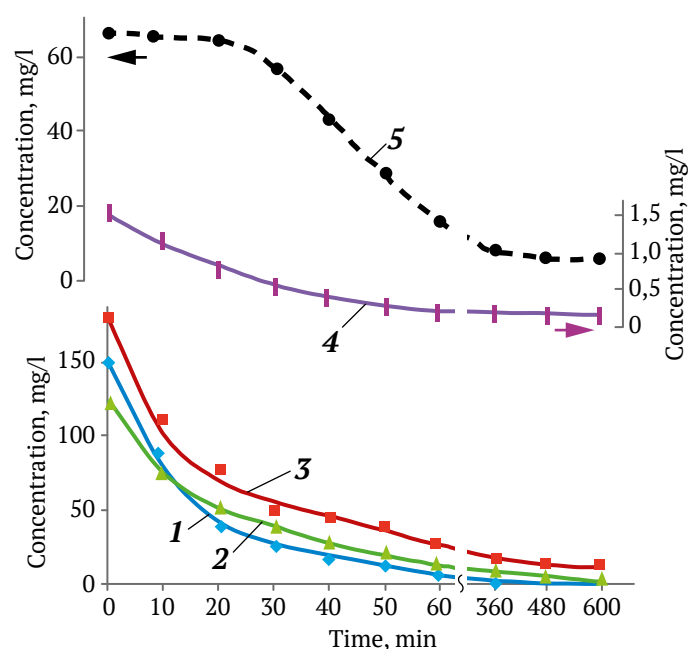


**Fig. 3.** Effect of contact time of zeolites with water containing heavy metal ions on the change of solution concentration in the systems: 1 –  $\text{Cu}^{2+}/6\text{-VKS}$ , 2 –  $\text{Fe}^{2+}/8\text{-NBS}$ , 3 –  $\text{Zn}^{2+}/4\text{-VKS}$ , 4 –  $\text{Pb}^{2+}/10\text{-NBS}$ , 5 –  $\text{Cu}^{2+}/4\text{-VKS}$



waters [2], including the Almalyk ore field, which includes copper-porphyry and copper sulfide-polymetallic deposits with sulfides prevailing [30]. However, monitoring of natural waters in the zone of influence of mining-and-processing and nonferrous metallurgy enterprises indicates an obvious exceeding of sanitary norms in wastewater. At a concentration of less than 0.003M and pH about 5 (Fig. 3, curves 1–4) metals were present in solutions practically in the form of divalent cations. The adsorption capacity for 10 h of the experiment did not exceed (g/100 g) 0.38Cu<sup>2+</sup> for 8-VKS and 0.27 Pb<sup>2+</sup> in the case of 10-NBS, whereas for the same period the capacity of 100 g of 6-VKS zeolite with A-type structure containing about 3% hydroxysodalite reached, g: 29.2 Cu<sup>2+</sup>; 28.4 Zn<sup>2+</sup>; 18.3 Fe<sup>2+</sup> and 3.1 Pb<sup>2+</sup>. Due to the increase of pH up to 5.1 in contact with 0.05 g of zeolite as a result of ion exchange Cu<sup>2+</sup> → 2Na<sup>+</sup>, the competition between metal cations and excess of protons decreased, and immobilization of hardly soluble hydroxocomplexes on the adsorbent surface occurred, so the copper compounds adsorption efficiency reached 97%. When the zeolite weight was increased to 0.06 g, the degree of removal of these metals from dilute solutions was not less than 98.5% that agrees with literature data [18, 19] for fly ash-based zeolites. The maximum iron and zinc compounds adsorption capacity was recorded for 8-NBS zeolite, where the predominant phase was NaX zeolite, g/100 g: 20.8 Fe<sup>2+</sup> and 28.7 Zn<sup>2+</sup>. Hybrid sample 4-VKS, which included predominantly NaP zeolite structure and some NaX and NaA, absorbed lead better than 10-NBS – 1.2 Pb<sup>2+</sup> (g/100 g), but was significantly inferior to samples 6-VKS and 8-NBS. Increased content of hydroxysodalite and SiO<sub>2</sub> phases (crystalline or amorphous) deteriorated the ability of adsorbents to extract metal cations. At adsorption from 1M solutions (potential liquid ore), where molecular forms of heavy metals prevailed, removal of toxic elements occurred mainly by precipitation mechanism with formation of Cu(OH)<sub>2</sub> precipitate, and only at increasing pH up to 6.5 due to high dose of zeolite the degree of the removal reached 80%.

The tests of optimal samples in dynamic mode showed that when passing model solutions through

a layer of zeolites 8-NBS and 6-VKS with a height of 1.2 m, the efficiency of purification from Cu<sup>2+</sup>, Zn<sup>2+</sup> and Fe<sup>2+</sup> cations was not less than 95%, and that for Pb<sup>2+</sup>, about 82%.

The concentration of copper cations as a result of adsorption on zeolites 8-NBS and 6-VKS decreased, mg/L: from 150 to 1.2–0.5 Cu<sup>2+</sup>, for zinc, from 180 to 8.9–7.5 Zn<sup>2+</sup>, for iron, from 125 to 0.8–0.4 Fe<sup>2+</sup>, for lead, from 1.5 to 0.3–0.27 Pb<sup>2+</sup>. The results of adsorption on the zeolites synthesized from local mineral raw materials by alkaline fusion with waste Al<sub>2</sub>O<sub>3</sub>–NaAlO<sub>2</sub> suspension were confirmed in the process of treatment of actual under-dump water of Kulchulak deposit. The degree of purification of the water with concentrations, mg/l: Cu – 138, Zn – 169, Fe – 83, Pb – 1.8 in the presence of sulfur and silver compounds and pH 4.9 was at least 80%. After the concentrations of Cu<sup>2+</sup>, Zn<sup>2+</sup> and Fe<sup>2+</sup> at the outlet of the adsorption column exceeded about 10 mg/L, the possibility of regeneration of zeolites, saturated with heavy metal cations, by passing Na<sub>2</sub>CO<sub>3</sub> solution was proved in principle. Zeolites 8-NBS and 6-VKS can be used for the treatment of the process water of Almalyk mining and metallurgical combine.

### Conclusion

Preliminary alkaline fusion of crude clay minerals with waste sodium aluminate suspension provided effective generation of active silicon and aluminum particles, allowed to increase the yield of zeolite structure products and sharply (up to the complete absence) reduce the amount of useless impurities of quartz and mullite. The tendency to form hydroxysodalite was enhanced at excessive increase of alkalinity and duration of the hydrothermal stage.

Under water treatment process parameters comparable to commercial adsorption technologies, it is possible to reduce the concentration of copper, zinc, and iron to practically the level of MPCs in drinking water. The zeolites synthesized from crude mineral raw materials with high quartz content can be used in process water treatment to reduce water consumption by mining and metallurgical enterprises from external sources.

### References

1. Rastanina N.K., Kolobanov K.A. Impact of technogenic dust pollution from the closed mining enterprise in the Amur Region on the ecosphere and human health. *Mining Science and Technology (Russia)*. 2021;6(1):16–22. <https://doi.org/10.17073/2500-0632-2021-1-16-22>
2. Zvereva V.P., Frolov K.R., Lysenko A.I. Formation of mine drainage in the Far Eastern region and its impact on the ecosphere and public health. *Mining Science and Technology (Russia)*. 2022;7(3):203–215. <https://doi.org/10.17073/2500-0632-2022-3-203-215>
3. Shadrinova I.V., Orekhova N.N. Technological and environmental and economic aspects processes for advanced recycling of water originating from mining operations, with recovery of heavy metals. *Mining Informational and Analytical Bulletin*. 2015;(S1):177–191. (In Russ.)



4. Kataeva S.E., Shulyak E.V., Bryl V.I., Chaban N.G. On the issue of heavy metal content in the aquatic environment of Slavutych city. Moscow; 2000. Pp. 751–752. (In Russ.)
5. Fayzieva M.F. On the issue of sanitary protection of reservoirs in Uzbekistan. *Vestnik Nauki i Obrazovaniya*. 2016;(4):70–72. (In Russ.)
6. Collins F., Rozhkovskaya A., Outramb J. G., Millarb G. J. A critical review of waste resources, synthesis, and applications for Zeolite LTA. *Microporous and Mesoporous Materials*. 2020;291:109667. <https://doi.org/10.1016/j.micromeso.2019.109667>
7. Tasić Ž.Z., Bogdanović G.D., Antonijević M.M. Application of natural zeolite in wastewater treatment – A review. *Journal of Mining and Metallurgy*. 2019;55A(1):67–79 <https://doi.org/10.5937/JMMA1901067T>
8. Belova T.P., Ratchina T.I., Gavrilenko Yu.S. Sorption of copper, nickel and cobalt by natural zeolite from aqueous solutions. *Mining Informational and Analytical Bulletin*. 2014;12:76–80. (In Russ.)
9. Milicevic S., Povrenovic D., Milosevic V., Martinovic S. Predicting the copper adsorption capacity on different zeolites. *Journal of Mining and Metallurgy*. 2017;53A(1):57–63.
10. Srilai S., Tanwongwal W., Onpetch K. et al. Synthesis of Zeolite X from bentonite via hydrothermal method. *Materials Science Forum*. 2020;990:144–148. <https://doi.org/10.4028/www.scientific.net/msf.990.144>
11. Ma H., Yao Q., Fu Y. et al. Synthesis of zeolite of type A from bentonite by alkali fusion activation using  $\text{Na}_2\text{CO}_3$ . *Industrial & Engineering Chemistry Research*. 2009;49(2):454–458. <https://doi.org/10.1021/ie901205y>
12. Buronov F., Fayzullayev N. Synthesis and application of high silicon zeolites from natural sources. In: *AIP Conference Proceedings. The 1st International Conference on Problems and Perspectives of Modern Science: ICPPMS-2021*. 10–11 June 2021, Tashkent, Uzbekistan. 2022;2432:050004. <https://doi.org/10.1063/5.0089557>
13. Jin Y., Li L., Liu Z. et al. Synthesis and characterization of low cost zeolite NaA from coalgangue by hydrothermal method. *Advanced Powder Technology*. 2021;32:791–801 <https://doi.org/10.1016/j.appt.2021.01.024>
14. Kong D., Jiang R. Preparation of NaA Zeolite from High Iron and Quartz Contents Coal Gangue by Acid Leaching-Alkali Melting Activation and Hydrothermal Synthesis. *Crystals*. 2021;11(10):1198. <https://doi.org/10.3390/cryst11101198>
15. Ma H., Zhu H., Wu C. et al. Study on compressive strength and durability of alkali-activated coal gangue-slag concrete and its mechanism. *Powder Technology*. 2020;368:112–124. <https://doi.org/10.1016/j.powtec.2020.04.054>
16. Kuroki S., Hashishin T., Morikawa T. et al. Selective synthesis of zeolites A and X from two industrial wastes: Crushed stone powder and aluminum ash. *Journal of Environmental Management*. 2019;231:749–756. <https://doi.org/10.1016/j.jenvman.2018.10.082>
17. Koukoulas N., Vasilatos C., Itskosa G. et al. Removal of heavy metals from wastewater using CFB-coal fly ash zeolitic materials. *Journal of Hazardous Materials*. 2010;173(1–3):581–588. <https://doi.org/10.1016/j.jhazmat.2009.08.126>
18. Hamadi A., Nabih K. Synthesis of zeolites materials using fly ash and oil shale ash and their applications in removing heavy metals from aqueous solutions. *Hindawi Journal of Chemistry*. 2018;2018(1):6207910. <https://doi.org/10.1155/2018/6207910>
19. Somerset V., Petrik L., Iwuoha E. Alkaline hydrothermal conversion of fly ash filtrates into zeolites 2: Utilization in wastewater treatment. *Journal of Environmental Science and Health, Part A*. 2005;40(8):1627–1636. <https://doi.org/10.1081/ESE-200060675>
20. Bessa R., Costa L., Oliveira C. et al. Kaolin-based magnetic zeolites A and P as water softeners. *Microporous and Mesoporous Materials*. 2017;245:64–72. <https://doi.org/10.1016/j.micromeso.2017.03.004>
21. Tayraukham P., Jantarit N., Osakoo N., Wittayakun J. Synthesis of pure phase NaP2 zeolite from the gel of NaY by conventional and microwave-assisted hydrothermal methods. *Crystals*. 2020;10(10):951. <https://doi.org/10.3390/cryst10100951>
22. Wajima T., Munakata K., Ikegami Y. Conversion of waste sandstone cake into crystalline zeolite X using alkali fusion. *Materials Transactions*. 2010;51(5):849–854. <https://doi.org/10.2320/matertrans.MH200905>
23. Lee Y.-R., Soe J.T., Zhang S. et al. Synthesis of nanoporous materials via recycling coal fly ash and other solid wastes: A mini review. *Chemical Engineering Journal*. 2017;317:821–843. <https://doi.org/10.1016/j.cej.2017.02.124>
24. Kunecki P., Panek R., Wdowin M. et al. Influence of the fly ash fraction after grinding process on the hydrothermal synthesis efficiency of Na-A, Na-P1, Na-X and sodalite zeolite types. *International Journal of Coal Science & Technology*. 2021;8(2):291–311 <https://doi.org/10.1007/s40789-020-00332-1>



25. Hu T., Gao W., Liu X. et al. Synthesis of zeolites Na-A and Na-X from tablet compressed and calcinated coal fly ash. *Royal Society Open Science*. 2017;4:170921. <https://doi.org/10.1098/rsos.170921>
26. Yang L., Qian X., Yuan P. et al. Green synthesis of zeolite 4A using fly ash fused with synergism of NaOH and Na<sub>2</sub>CO<sub>3</sub>. *Journal of Cleaner Production*. 2019;212:250–260. <https://doi.org/10.1016/j.jclepro.2018.11.259>
27. Mallapur V.P., Oubagaranadin J.U.K. A brief review on the synthesis of zeolites from hazardous wastes. *Transactions of the Indian Ceramic Society*. 2017;76(1):1–13. <https://doi.org/10.1080/0371750X.2016.1231086>
28. Golbad S., Khoshnoud P., Abu-Zahra N. Hydrothermal synthesis of hydroxy sodalite from fly ash for the removal of lead ions from water. *International Journal of Environmental Science and Technology*. 2017;14(1):135–142. <https://doi.org/10.1007/s13762-016-1133-x>
29. Shabani J.M., Omotola B., Oyekola O., Petrik L. Synthesis of hydroxy sodalite from coal fly ash for bio-diesel production from waste-derived maggot oil. *Catalysts*. 2019;9(12):1052. <https://doi.org/10.3390/catal9121052>
30. Vasilevsky B.B., Yezhkov Yu.B., Rakhimov R.R. et al. *Problems of large-volume gold and copper deposits in Uzbekistan*. Tashkent; 2012. 116 p. (In Russ.)

### Information about the authors

**Elena I. Mirzaeva** – PhD (Eng.), Associate Professor of the Department of Metallurgy, University of Science and Technology MISIS (Almalyk branch), Almalyk, Republic of Uzbekistan; ORCID [0009-0003-4198-2274](https://orcid.org/0009-0003-4198-2274); e-mail [mirzaevaelena92@gmail.com](mailto:mirzaevaelena92@gmail.com)

**Nurkhon F. Isaeva** – PhD (Eng.), Doctoral Student, Tashkent Scientific Research Institute of Chemical Technology, Tashkent, Republic of Uzbekistan; ORCID [0000-0001-8513-6975](https://orcid.org/0000-0001-8513-6975); e-mail [nurhonisaeva@gmail.com](mailto:nurhonisaeva@gmail.com)

**Elmurod Ya. Yalgashev** – Doctoral Student, Senior Researcher, Tashkent Institute of Chemical Technology, Tashkent, Republic of Uzbekistan; ORCID [0000-0001-7921-2206](https://orcid.org/0000-0001-7921-2206); e-mail [chemyalgashev@mail.ru](mailto:chemyalgashev@mail.ru)

**Dilnoza P. Turdiyeva** – Doctoral Student, Junior Researcher, National University of Uzbekistan named after Mirzo Ulugbek, Tashkent, Republic of Uzbekistan; ORCID [0009-0000-3216-5801](https://orcid.org/0009-0000-3216-5801); e-mail [turdievadilnoza34@gmail.com](mailto:turdievadilnoza34@gmail.com)

**Rufatjon M. Boymonov** – Senior Lecturer of the Department of Machinery and Equipment of Oil and Gas Industry and Pipeline Transport Systems, Tashkent State Technical University named after Islam Karimov, Tashkent, Republic of Uzbekistan; e-mail [rufatjonboymonov1992@gmail.com](mailto:rufatjonboymonov1992@gmail.com)

**Received** 26.02.2024

**Revised** 07.06.2024

**Accepted** 10.09.2024



## BENEFICIATION AND PROCESSING OF NATURAL AND TECHNOGENIC RAW MATERIALS

Research paper

<https://doi.org/10.17073/2500-0632-2023-08-142>

UDC 550.8

**Material composition of magnetic fractions of copper-smelting slag flotation tailings**

A.L. Kotelnikova , E.S. Zolotova

*Zavaritsky Institute of Geology and Geochemistry of the Ural Branch of the Russian Academy of Sciences (IGG UB RAS), Yekaterinburg, Russian Federation* [zolotova@igg.uran.ru](mailto:zolotova@igg.uran.ru)**Abstract**

Finely ground tailings from flotation processing of waste copper reverberatory smelting slags of the Sredneuralsky Copper Smelter (“SUMZ technical sands”) was accumulated in significant amounts and may pose a threat to the environment as a potential source of heavy metals. At the same time, the waste can be considered as a promising source of useful components due to relatively high contents of zinc (3.3–3.9%) and copper (0.4–0.5%). Development of technologies for recycling the “technical sands” is a promising task of nonferrous metallurgy and requires their comprehensive study. The purpose of this research was to study the material composition of magnetic fractions of the “SUMZ technical sands” and assess the prospects of extraction of useful components (zinc and copper) from their flotation tailings using wet magnetic separation. Chemical analyses of the obtained fractions were carried out at the Center for Collective Use “Geoanalitik” of the Institute of Geology and Geochemistry, UB RAS by inductively coupled plasma mass spectrometry method using an Elan-9000 quadrupole mass spectrometer. Phase analyses were carried out at the Ural-M Collective Use Center of the Institute of Metallurgy, UB RAS by X-ray phase analysis using a Bruker D8 Advance diffractometer. The magnetic properties of the magnetic separation fractions were studied by thermomagnetic analysis. After treating the tailings by wet magnetic separation, the yield of the magnetic fraction (48 kA/m) was approximately 83%, that of the weakly magnetic fraction (200 kA/m) was 11%, and that of the non-magnetic fraction, 6%. The data on the phase and chemical composition of the tailings magnetic separation fractions were obtained. It was found that zinc and copper were distributed relatively uniformly among the fractions with a slightly higher content of copper in the non-magnetic fraction and that of zinc in the weakly magnetic fraction. The dependence of magnetic susceptibility of the “technical sands” minerals on the presence of isomorphic impurities in them was confirmed. The joint evaluation of the data of X-ray phase and thermomagnetic analyses showed that at practically identical X-ray diffraction patterns the thermomagnetic curves in the range of 20–700°C demonstrate significant differences between the magnetic separation fractions. All the obtained thermomagnetic curves are irreversible. At the used parameters of wet magnetic separation, this method proved inefficient for the “technical sands” separation, and additional research is required to find optimal methods of the tailings pretreatment and magnetic intensity modes. The research findings contribute to the study of magnetic properties of copper-smelting slag processing tailings and are of interest for the development of new flow schemes for their utilization and recycling.

**Keywords**

copper smelting production, mineral waste, copper smelting slag, flotation processing tailings, recycling, magnetic separation, thermomagnetic analysis, magnetic fractions, magnetic properties, fayalite ( $\text{Fe}_2\text{SiO}_4$ ), forsterite ( $(\text{MgMn})\text{SiO}_4$ ), diopside ( $\text{CaZn}(\text{Si}_2\text{O}_6)$ ), magnetite ( $\text{Fe}_3\text{O}_4$ ), sphalerite ( $\text{ZnS}$ ), zincite ( $\text{ZnO}$ )

**Acknowledgments**

The research was carried out within the framework of the State Assignment of IGG UB RAS, project No. 123011800011-2.

This work was made possible by the active participation of Sergey Grigorievich Komlev, a specialist in the field of mineral processing, and Victor Sergeevich Ivanchenko, a well-known scientist in the field of magnetometry. This paper is for their cherished memory.

The authors express profound gratitude to V. F. Ryabinin, the initiator of geoecological research at the Institute of Geology and Geochemistry, UB RAS, for help in conducting the research, and to D. V. Kiseleva and D. S. Reutov for assistance in assaying.

**For citation**

Kotelnikova A.L., Zolotova E.S. Material composition of magnetic fractions of copper-smelting slag flotation tailings. *Mining Science and Technology (Russia)*. 2025;10(1):56–66. <https://doi.org/10.17073/2500-0632-2023-08-142>




## ОБОГАЩЕНИЕ, ПЕРЕРАБОТКА МИНЕРАЛЬНОГО И ТЕХНОГЕННОГО СЫРЬЯ

Научная статья

**Вещественный состав магнитных фракций хвостов флотации медеплавильных шлаков**А.Л. Котельникова , Е.С. Золотова  

Институт геологии и геохимии им. академика А. Н. Заварицкого УрО РАН, г. Екатеринбург, Российская Федерация

 [zolotova@igg.uran.ru](mailto:zolotova@igg.uran.ru)**Аннотация**

Тонкоизмельченные отходы флотационной переработки отвальных медеплавильных шлаков отражательной плавки Среднеуральского медеплавильного завода («технические пески СУМЗ») накоплены в значительных объемах и могут представлять опасность для окружающей среды как потенциальный источник тяжелых металлов. В то же время они могут рассматриваться как перспективный источник полезных компонентов вследствие относительно высокого содержания цинка (3,3–3,9 %) и меди (0,4–0,5 %). Разработка технологий по утилизации «технических песков» является перспективной задачей цветной металлургии и невозможна без их всестороннего исследования. Целью наших исследований являлись изучение вещественного состава магнитных фракций «технических песков СУМЗ» и оценка перспектив извлечения полезных компонентов (цинка и меди) из хвостов флотации с использованием мокрой магнитной сепарации. Химический анализ полученных фракций выполнен в Центре коллективного пользования «Геоаналитик» Института геологии и геохимии УрО РАН методом масс-спектрометрии с индуктивно связанной плазмой на квадрупольном масс-спектрометре Elan-9000. Фазовый анализ выполнен в центре коллективного пользования «Урал-М» Института металлургии УрО РАН методом рентгенофазового анализа на дифрактометре Bruker D8 Advance. Магнитные свойства фракций магнитной сепарации изучены методом термоманитного анализа. После обработки отхода методом мокрой магнитной сепарации выход магнитной фракции (48 кА/м) составил приблизительно 83 %, слабомагнитной (200 кА/м) – 11 %, немагнитной – 6 %. Получены данные о фазовом и химическом составе фракций магнитной сепарации отхода. Отмечено, что цинк и медь распределяются по фракциям относительно равномерно с несколько повышенным содержанием меди в немагнитной, а цинка – в слабомагнитной фракции. Подтверждена зависимость магнитной восприимчивости минералов «технических песков» от наличия в них изоморфных примесей. Совместная оценка данных рентгенофазового и термоманитного анализов показала, что при практически идентичных рентгенограммах термоманитные кривые в интервале 20–700 °С демонстрируют существенные различия фракций магнитной сепарации. Все полученные термоманитные кривые необратимые. При использованных параметрах мокрой магнитной сепарации для разделения «технических песков» данный метод малоэффективен, необходимы дополнительные исследования по поиску оптимальных способов предподготовки отходов и режимов напряженности магнитного поля. Результаты исследований вносят вклад в изучение магнитных свойств отходов переработки медеплавильных шлаков, представляют интерес для разработки новых схем их утилизации и повторной переработки.

**Ключевые слова**

медеплавильное производство, минеральные отходы, медеплавильные шлаки, хвосты флотационной переработки, утилизация, магнитная сепарация, термоманитный анализ, магнитные фракции, магнитные свойства, фаялит ( $\text{Fe}_2\text{SiO}_4$ ), форстерит ( $(\text{MgMn})\text{SiO}_4$ ), диопсид ( $\text{CaZn}(\text{Si}_2\text{O}_6)$ ), магнетит ( $\text{Fe}_3\text{O}_4$ ), сфалерит ( $\text{ZnS}$ ), цинкит ( $\text{ZnO}$ )

**Благодарности**

Исследования выполнены в рамках Государственного задания ИГГ УрО РАН, тема № 123011800011-2. Эта работа стала возможной благодаря деятельному участию в ней Сергея Григорьевича Комлева, специалиста в области обогащения полезных ископаемых, и Виктора Сергеевича Иванченко, известного ученого в области магнитометрии. Светлой их памяти авторы посвящают эту статью. Авторы выражают глубокую признательность В. Ф. Рябину, инициатору геоэкологических исследований в Институте геологии и геохимии УрО РАН, за помощь в проведении исследований, Д. В. Киселевой и Д. С. Реутову за помощь в проведении аналитических работ.

**Для цитирования**

Kotelnikova A. L., Zolotova E. S. Material composition of magnetic fractions of copper-smelting slag flotation tailings. *Mining Science and Technology (Russia)*. 2025;10(1):56–66. <https://doi.org/10.17073/2500-0632-2023-08-142>



## Introduction

Mining and metallurgical wastes occupy vast areas around the world and cause significant environmental damage [1–3]. Nonferrous metallurgy wastes are particularly dangerous for the environment due to high content of heavy metals [4–6].

At present time, flotation method is most often used for slag processing at copper smelters [7–9]. As a result, a concentrate of copper-containing components is obtained and the processing tailings, “technical sands”, which are a finely dispersed and mechanically activated materials, are produced. These tailings find limited application in construction [10] and for reclamation of disturbed territories [11, 12]; there are ongoing developments in the application of copper-smelting slag flotation tailings for industrial wastewater treatment [13]. However, for the most part the tailings are buried and, to date, have been accumulated in significant volumes in the areas where smelters operate. The “technical sands” can cause contamination of groundwater, surface water, soil, and plants [14, 15].

Copper-smelting slag flotation tailings can be considered as a potential source of useful components [16, 17]. The development and implementation of technologies involving processing and recycling of technogenic waste is an extremely urgent task for current industries, sustainable nature management, and environmental conservation [18–20]. The solution of the problem of multipurpose utilization of copper-smelting slag flotation tailings requires their comprehensive study.

The Ural and Siberian regions are among the main production centers of nonferrous metallurgy in Russia. In 1994–1995, Sredneuralsky Copper Smelter (OJSC SUMZ) and Kirovograd Copper Smelter began processing of waste cast slag as a source of copper-zinc concentrate. The material composition of the OJSC SUMZ flotation tailings [21–23] accumulated in the amount of more than 10 mln t, has been studied in detail. According to preliminary estimates, this amount may contain about 340 kt of zinc, 43 kt of copper, 43 kt of lead, as well as 3.5 mln t of iron. The “technical sands” of SUMZ contain up to 4% zinc and up to 0.5% copper. Acid leaching method is applicable for their extraction. Maximum recovery of zinc (up to 77 %) and copper (up to 64 %) was achieved using sulfuric acid (in concentration of 300 g/dm<sup>3</sup>) [24]. For increasing zinc and copper recovery it is necessary to take into account the “technical sands” phase composition, their distribution among mineral phases, as well as grinding fineness [25] and magnetic properties of the waste.

The studies on the extraction of valuable components from copper-smelting slags by magnetic separation are known in literature [25, 26]. It was established

by the example of JSC Svyatogor converter copper-smelting slag flotation tailings that the change in magnetic field strength (1,200, 800, 400 E) in wet magnetic separation, grinding size, and the method of slag cooling practically does not affect the iron content in the resulting iron concentrate [25]. Chinese scientists proposed a combined process of direct reduction and magnetic separation of copper-smelting slag flotation tailings using limestone [26]. However, not enough attention has been paid to the mineral composition of the resulting magnetic fractions.

The purpose of our research was to study the material composition of Sredneuralsky copper smelter waste cast slag processing tailing magnetic fractions and to assess the prospects for the extraction of useful components (zinc and copper) from the flotation tailings using wet magnetic separation. In this connection the following problems were solved: fractionation of SUMZ copper-smelting slag processing tailings by wet magnetic separation; determination of chemical and phase composition of the obtained magnetic fractions; characterization of their magnetic properties using thermomagnetic analysis; evaluation of the efficiency of the flotation tailings separation by wet magnetic separation methods.

## Research Subjects and Methods

Waste cast slag from reverberatory smelting at the Sredneuralsky copper smelter is subjected to grinding first at cone crushers to a fraction of 10 mm, then at ball mills to 0.05 mm. The subsequent extraction of copper concentrate is carried out by flotation. The liquid concentrate and tailings (“technical sands”) are separately thickened in radial thickeners and filtered. Vacuum filters were used to dewater the tailings.

«SUMZ technical sands” is a finely dispersed material of the following grain size: (–0.21 + 0.10) mm, 1.1–4.1%; (–0.1 + 0.05) mm, 21–30%; < 0.05 mm, 69–75%. Their chemical composition is as follows, wt. %: FeO – 32.3; SiO<sub>2</sub> – 31; Fe<sub>2</sub>O<sub>3</sub> – 14.29; Al<sub>2</sub>O<sub>3</sub> – 7.05; CaO – 4.53; Zn – 3.28; MgO – 1.64; S – 1.32; K<sub>2</sub>O – 0.74; Na<sub>2</sub>O – 0.64; As – 0.53; Cu – 0.44; Ba – 0.43; TiO<sub>2</sub> – 0.26; Pb – 0.2; P<sub>2</sub>O<sub>5</sub> – 0.1; MnO – 0.09 [23].

The separation of the SUMZ copper-smelting slag flotation tailings into magnetic fractions was performed at the Department of Mineral Processing, Faculty of Mining and Mechanical Engineering, Ural State Mining University. For the separation of magnetic fractions the method of wet magnetic separation was used<sup>1</sup>, characterized by the continuity of

<sup>1</sup> Svertkov A.A., Chekmenev A.N., Bratus S.V., Sharkhov V.V. Patent No. RU 2013109184 A, Russian Federation, IPC B03C1/00. Method of wet magnetic separation of magnetite ores and devices for its implementation: appl. 2013109184/03, 28.02.2013; publ. 10.09.2014.



the separation process, which was provided by creation (in the working chamber) of the magnetic field with the intensity decreasing in the direction of pulp movement.

The chemical and phase compositions of the obtained fractions were determined at the Center for Collective Use “Geoanalitik” of the Institute of Geology and Geochemistry, UB RAS by inductively coupled plasma mass spectrometry (ICP-MS) using an Elan-9000 quadrupole mass spectrometer (Perkin-Elmer, Canada). The phase analyses were carried out at the Ural-M Collective Use Center of the Institute of Metallurgy, UB RAS by X-ray phase analysis using a Bruker D8 Advance diffractometer (Bruker AXS GmbH, Germany).

The study of magnetic properties of the “technical sands” was carried out at the Institute of Geophysics, UB RAS. The thermomagnetic analysis method was used to determine the total magnetization of the magnetic separation fractions. The scheme of the installation is presented in the monograph [27]. The samples magnetic susceptibility was measured using a commercially available KT-3 kappometer.

### Research Findings and Discussion

The “SUMZ technical sands” are finely dispersed materials (particle size <0.05 mm) consisting of a mixture of fayalite, pyroxene, iron-containing glassy phase of acidic and basic compositions, magnetite, hematite, wustite, spinelides, sulfides, and intermetallics. Magnetite and sulfides are confined to the glass phase. A characteristic feature of the “sands” is the increased content of zinc (about 3.3–3.9%) and copper (0.4–0.5%) at Zn/Cu ratio of 7.5. Zinc is present in all the phases. Silicate zinc is contained in the fayalite and the glass phase. Other heavy metals including copper are predominantly concentrated in the sulfides and intermetallics. According to the literature data [25] primary copper minerals are represented by chalcopyrite, cubanite, and cuprite, which are usually accompanied by secondary copper minerals, covellite and bornite. The total mass fraction of the copper-bearing minerals is 1.5%. About 50% of iron is contained in the fayalite. The bulk of alkali and alkaline-earth elements, as well as aluminum and silicon, are encapsulated in the glass phase [23].

Magnetic properties of the SUMZ copper-smelting slag processing tailings are governed by the magnetic properties of its constituent minerals. Almost all mineral phases of the “technical sands” are magnetics, capable of magnetizing in a magnetic field. This is due to the fact that they usually include atoms with their own magnetic moment due to the presence of unpaired electrons, such as  $\text{Fe}^{2+}$ ,  $\text{Fe}^{3+}$ .

Therefore, the application of magnetic field could not provide desirable separation of the “SUMZ technical sands”. The yield of magnetic fraction was 83.27%, that of weakly magnetic fraction, 10.85%, and that of non-magnetic fraction, 5.88% (Table 1).

In addition, the presence of glass (up to 30 wt.% in the SUMZ slags) has a significant effect on the separation of the copper-smelting slag flotation tailings using wet magnetic separation. It was found for copper-smelting slags of Karabashmed that crushing in centrifugal-impact apparatuses (disintegration) occurs with a low degree of selectivity due to their glassy structure [28].

The cooling conditions of the copper-smelting cast slag, which serves as a source material for the investigated “technical sands”, are markedly different from natural ones. As a consequence, homogenized mineral individuals represent a smaller part of the volume. The predominant part of the waste is represented by to varying extent crystallized glass [23, 29]. In the clastic material of the “SUMZ technical sands”, fine clastic glass representing fragments of forming minerals at different stages of homogenization of their composition quantitatively dominates. The glass fills interstitials between olivine, magnetite, and sulfide mineral individuals. The glass composition (according to microanalyzer data) is as follows: 30–50% silica, 7 to 20% alumina, up to 10% alkaline metals, 1.5–10% zinc, up to 1% copper, and up to 30% iron oxides [30]. The presence of complex cryptocrystalline structures, solid solution decomposition structures, the structures of elements substitution in the crystalline lattice of minerals in the form of hems on the periphery of grains reduces the degree of the slag disintegration selectivity when crushed.

The chemical analysis of the obtained magnetic fractions of the “SUMZ technical sands” (Table 2) showed that zinc and copper are distributed relatively evenly among the fractions. Some increase of copper content in the non-magnetic fraction and that of zinc content in the weakly magnetic fraction was found.

Table 1  
Results of separation of copper-smelting slag flotation tailings by wet magnetic separation

Fraction	Magnetic field strength, kA/m	Weight, g	Yield, %
Magnetic	48	119.52	83.27
Weakly magnetic	200	15.57	10.85
Non-magnetic	–	8.44	5.88
Total	–	143.53	100.00



According to the historical studies, zinc-bearing magnetite phase is observed in copper-smelting slag processing tailings [21, 23]. This fact can be regarded as one of the manifestations of incomplete homogenization of the mineral. It can be assumed that the increase of zinc content in the weakly magnetic fraction is connected with this fact. The presence of zinc was also determined in wustite, which is inferior in quantity to magnetite in the “technical sands”, but also contains a certain amount of zinc.

Copper remains predominant in the non-magnetic fraction, most likely due to the presence of emulsion impregnation of matte [23] and copper-bearing minerals in the glass [25].

The mineral basis of the “technical sands” are silicates (about 84%) represented by olivines, pyroxenes, and glass phase. The secondary phases are oxides of iron and nonferrous metals (about 14%), sulfides (about 2%) (Table 3). Intermetallics are present in small amounts.

The indicated mineral phases (see Table 3) have the corresponding crystal lattices. However, it should be noted that most of the minerals of the “technical sands” have not yet reached full homogenization. The peculiarity of the majority of the mineral fragments in the clastic material of the tailings is noticeable deviations from stoichiometric compositions.

According to the data of X-ray phase analysis the olivines in the “SUMZ technical sands” have predom-

inantly fayalite composition ( $\text{Fe}_{1.64}, \text{Ca}_{0.04}, \text{Zn}_{0.15})(\text{Si}_{0.85}, \text{Al}_{0.27})\text{O}_4$ . The studies of the magnetic properties of olivines [31, 32] have shown that at low temperatures antiferromagnetic ordering occurs in them, with the magnetic cell coinciding with the crystallographic one.

Pyroxenes in the “SUMZ technical sands” are ferrosilicates of the following composition:  $(\text{Fe}, \text{Mg}, \text{Ca}, \text{Zn})_{2.0}\text{Si}_{1.9}\text{O}_{6.0}$  with Al impurities. It was noted earlier that augite  $(\text{Ca}, \text{Fe}, \text{Mg})[\text{SiO}_3]_2$  individuals are sometimes found in waste slags [33]. Trivalent iron and copper cations are often found in the crystal lattice of pyroxenes.

The main segregations of magnetite, sulfides, nonferrous metal oxides and intermetallics are concentrated in the glassy phase of the “technical sands”. The grains of these minerals are well bounded, of various sizes, including nanocrystalline ones. Magnetite also forms complex intergrowths with fayalite. Pure magnetite in flotation tailings is rare; its composition can be represented by the following structural formula:  $(\text{Fe}_{2.8}, \text{Al}_{0.5}, \text{Si}_{0.1}, \text{Zn}_{0.1})\text{O}_4$ . It often includes copper, while Cr, Ti, Cd, Sn cations are occasionally found. Magnetite is a typical ferromagnet [34]. Magnetite crystals and grains are themselves natural permanent magnets, having the strength and polarity of a true magnet. But the presence of isomorphic impurities in magnetite composition will reduce the magnetic susceptibility.

Table 2

Data of chemical analysis of magnetic fractions of copper-smelting slag flotation tailings, wt. %

Fraction	SiO <sub>2</sub>	Al <sub>2</sub> O <sub>3</sub>	MnO	CaO	MgO	P <sub>2</sub> O <sub>5</sub>	Cu	Zn	Pb	As	Fe <sub>tot</sub>
Initial “sands”	32.4	2.9	0.04	4.39	0.98	0.05	0.18	1.17	0.06	0.07	35.5
Magnetic	32.4	3.1	0.04	4.54	1.01	0.05	0.19	1.20	0.07	0.07	37.8
Weakly magnetic	35.2	3.3	0.04	5.15	1.28	0.06	0.15	1.36	0.07	0.06	34.8
Non-magnetic	37.2	3.9	0.05	5.01	1.71	0.07	0.24	1.20	0.07	0.05	33.1

Table 3

Mineral composition of magnetic fractions of copper-smelting slag flotation tailings according to X-ray phase analysis, wt. %

Mineral	Initial “SUMZ technical sands”	Magnetic fraction	Weakly magnetic fraction	Non-magnetic fraction
Fayalite $\text{Fe}_2\text{SiO}_4$	48.2	51.3	64.6	64.5
Forsterite $(\text{MgMn})\text{SiO}_4$	15.4	10.0	9.0	10.0
Diopside $\text{CaZn}(\text{Si}_2\text{O}_6)$	20.4	19.9	19.3	19.6
Magnetite $\text{Fe}_3\text{O}_4$	13.7	15.7	4.1	1.4
Sphalerite $\text{ZnS}$	1.8	1.8	1.9	1.3
Zincite $\text{ZnO}$	0.5	1.3	1.1	3.2



Wustite ( $\text{Fe}_{0.9}, \text{Al}_{0.02}, \text{Si}_{0.01}, \text{Zn}_{0.04}$ )O and hematite ( $\text{Fe}, \text{Al}, \text{Si}_{0.4}$ ) $_2\text{O}_3$ , sometimes with admixtures of Zn and Sn, were found in the “SUMZ technical sands”. They are antiferromagnetic minerals whose magnetic susceptibility is small but positive [35]. When a magnetic field is applied, isomorphous impurities will have a significant effect on the magnetic susceptibility of these minerals.

Pyrrhotite-like sulfides in the “technical sands” have the following compositions ( $\text{Pb}, \text{Fe}, \text{Cu}, \text{Zn}, \text{Si}_{0.08}, \text{Sn}_{0.07}$ )S,  $\text{FeS} \cdot \text{Cu}_2\text{S}$ , ( $\text{Pb}, \text{Fe}, \text{Cu}$ ) $_{1.06}\text{S}$ , ( $\text{Pb}, \text{Fe}, \text{Si}_{0.44}, \text{Ca}_{0.18}$ ) $_{1.1}\text{S}$ . Pure pyrrhotite is a ferromagnetic [36]. Just like magnetite, it has its own magnetic moment and is capable of creating a magnetic field around it.

Diamagnetics in the “SUMZ technical sands” are represented by copper metal, antimony-bearing intermetallics, sulfides (chalcosine and sphalerite), cuprite and zincite, anhydrite of ( $\text{Ca}_{0.74}\text{Ca}, \text{Na}, \text{Al}, \text{Mg}$ ) $\text{SO}_4$ , composition, aluminum and silicon hydroxides.

96% of magnetite, more than 80% of silicate and sulfide phases belong to the magnetic fraction (Table 4). Such distribution of the substances can be connected with thin impregnation of magnetic minerals in the glass phase and the formation of intergrowths with silicates, as well as with the change in the magnetic structure of mineral phases, arising in the presence of isomorphous impurities in the crystal structure of minerals when magnetic field is applied.

Isomorphous impurities (in the crystal lattice of the “technical sands” silicates) of cations possessing their own magnetic moment due to the presence of unpaired electrons, for example,  $\text{Fe}^{2+}$ ,  $\text{Mn}^{2+}$ ,  $\text{Fe}^{3+}$ ,  $\text{Mn}^{3+}$ ,  $\text{Mn}^{4+}$ ,  $\text{Ni}^{2+}$ ,  $\text{Cu}^{2+}$ , as well as magnetite and pyrrhotite inclusions lead to the appearance of areas of increased magnetization inside silicate grains and thin aggregates of silicate minerals and glass, preserved after crushing of the copper-smelting slag. Therefore, more than 80% of the silicates are concentrated in the magnetic fraction.

The concentration of diamagnetics in the magnetic fraction (see Table 4) can be explained both by electrostatic capture of small grains of diamagnetic minerals and the presence of dusty particles of magnetite and/or pyrrhotite dispersed in them.

The distribution of magnetite in the magnetic fractions depends on its chemical composition, as well as on the degree of disintegration (disclosing) intergrowths with fayalite and glass phase. The more impurities in the crystal lattice of magnetite, the lower the magnetic susceptibility. Magnetite was detected even in the non-magnetic fraction.

According to the XRD data, copper is predominantly concentrated in the pyrrhotite-like sulfides. The distribution of zinc by mineral phases is as follows: 15–20% of the total zinc content belong to magnetite, 30–35% to silicates (olivine), 20–25% to zincite, and up to 20% to sphalerite.

The joint evaluation of the data of X-ray phase and thermomagnetic analyses of the copper-smelting cast slag flotation tailings showed that at practically identical X-ray diffraction patterns thermomagnetic curves in the range of 20–700°C demonstrate significant differences of the magnetic separation fractions (Fig. 1).

All the obtained thermomagnetic curves are irreversible. The magnetic properties of the “sands” magnetic separation fractions are determined by the presence of magnetite and pyrrhotite-like sulfides.

The magnetic fraction reaches Curie temperatures between 470 and 520°C upon heating, indicating the presence of an isomorphous series of ferromagnetic minerals.

When the weakly magnetic fraction is heated, an increase in magnetic susceptibility after cooling by about 20% is observed (Curie temperature ranges 420 to 570°C). Two inflections are noticeable on the cooling curve; one probably corresponds to the magnetite formed during cooling, the other corresponds to the admixture of initial ferromagnetic

**Distribution of minerals in magnetic fractions of copper-smelting slag flotation tailings taking into account weight yield of fractions, wt. %**

Table 4

Mineral	Magnetic fraction	Weakly magnetic fraction	Non-magnetic fraction
Fayalite $\text{Fe}_2\text{SiO}_4$	79.81	13.09	7.09
Forsterite $(\text{MgMn})\text{SiO}_4$	84.17	9.87	5.94
Diopside $\text{CaZn}(\text{Si}_2\text{O}_6)$	83.63	10.57	5.82
Magnetite $\text{Fe}_3\text{O}_4$	96.13	3.27	0.61
Sphalerite $\text{ZnS}$	84.04	11.56	4.29
Zincite $\text{ZnO}$	77.69	8.56	13.50

minerals with the same Curie temperature as that of the strongly magnetic fraction.

When heating the non-magnetic fraction, the Curie temperature was 550°C, which indicates some presence of ferromagnetic minerals, while cooling resulted in the formation of magnetite, due to which the magnetic susceptibility increased about 3 times.

The precursors of magnetite formed during cooling of weakly magnetic and non-magnetic fractions are probably iron hydroxides and isomorphously substituted ferromagnetic minerals: magnetite and pyrrhotite.

The thermograms analysis showed that the magnetic separation fractions contain quite a large amount of impurities that significantly reduce their magnetic susceptibility and, correspondingly, magnetic strength. Therefore, a more complete separation of the “technical sands” requires an increase in magnetic field strength, possibly rather considerable, using superconducting magnetic systems [37].

Thus, the copper-smelting slag flotation tailing phase composition, mineral magnetic properties and structural features determine the low efficiency of the “technical sands” separation by generally accepted methods of wet magnetic separation. For their successful separation, the material preparation is necessary prior to magnetic separation.

As is known, the existing flowsheets of iron ore beneficiation based on magnetic separation and developed on the principle of staged separation of waste tailings with obtaining finished concentrate, only in the last operation are applicable and efficient for rich ores. In the beneficiation of finely impregnated lean ores, there are problems associated with reducing the coarseness of the material fed to magnetic separation. The maximum complete disclosing (releasing) of minerals is achieved only when grinding to the size of the extracted mineral grains that entails an increase in both energy costs and overgrinding of the ore components, including already disclosed minerals [38].

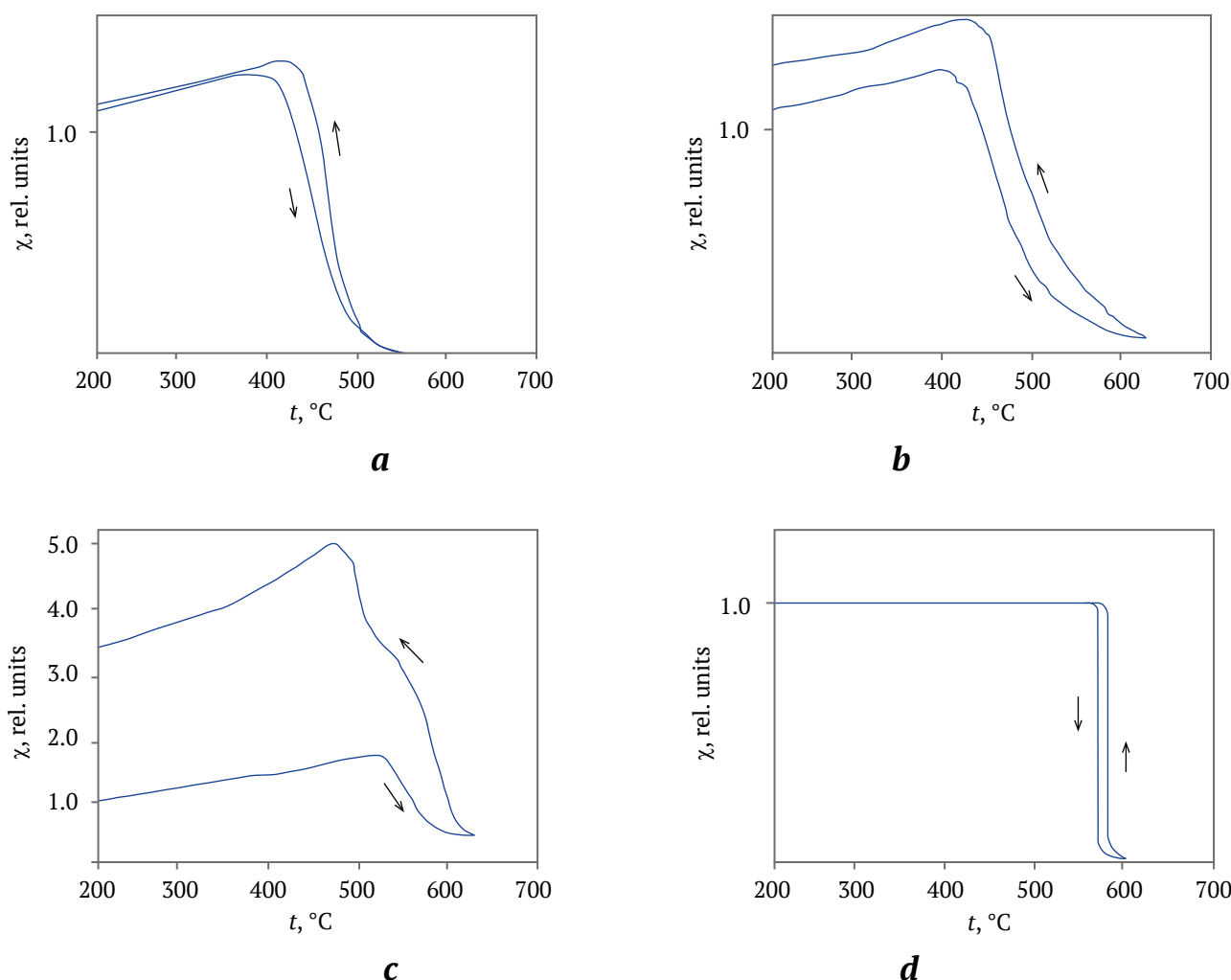


**Fig. 1.** Thermomagnetograms: *a* – magnetic fraction of “SUMZ technical sands” (measurement limit of 10 mV); *b* – weakly magnetic fraction (measurement limit of 3 mV); *c* – non-magnetic fraction (measurement limit of 0.3 mV); *d* – natural magnetite from Abakan deposit (measurement limit of 10 mV)



Ultrafine grinding of minerals [25] using ball and bead mills leads to the destruction of crystal integrity and defect formation with the appearance of X-ray- amorphous layers, as well as increasing their hydration and solubility. It was found that sulfide minerals undergo such structural and chemical changes as sulfatization and amorphization under mechanical impacts [39].

In the process of magnetite grinding to 0.04–0.02 mm its primary domain structure is broken that first of all causes the growth of coercive force of the particles. This contributes to increased flocculation and entrapment of significant amounts of non-metallic particles into the floccules that reduces the efficiency of separation of magnetite and non-metallic minerals. At the same time, the specific magnetic susceptibility of magnetic particles finer than 0.02 mm sharply decreases that contributes to the loss of overground magnetite with tailings. It was also revealed that during mechanical processing (crushing, grinding) the defectivity of magnetite structure increases, which leads to magnetite transformation towards magnetite-martite-hematite [40].

The processes of slurry and defect formation reduce the separation selectivity. To reduce the negative effects of these processes, the introduction of surfactants into the grinding process was proposed [39].

The disadvantages of mechanical disclosure can be avoided by applying a high-voltage pulse method of disclosure of solids, including glass [41], which demonstrates high selectivity and efficiency, as well as allows the process regulating and automating.

The separation selectivity can be also improved by using a spiral separator, which makes it possible to remove grains of iron-bearing minerals of different densities from inter-cycle operations as they are disclosed to avoid overgrinding [42].

### Conclusion

For the first time for the Sredneuralsky copper smelter copper-smelting slag flotation tailings (“SUMZ technical sands”) the material composition of magnetic fractions was studied and thermomagnetic curves were obtained. The “technical sands” have pronounced magnetic properties, as they contain ferromagnetic minerals and isomorphic impurities – cations with their own magnetic

moment in the crystal lattices of minerals. Magnetite is concentrated in the magnetic fraction (about 97 %). The increase of copper and zinc contents in the non-magnetic fraction is probably due to non-stoichiometry of olivine, as well as the presence of microinclusions.

The joint evaluation of the data of X-ray phase and thermomagnetic analyses showed that at practically identical X-ray diffraction patterns the thermomagnetic curves in the range of 20–700 °C demonstrate significant differences of the fractions of the copper-smelting slag flotation tailings magnetic separation. All the obtained thermomagnetic curves are irreversible. Therefore, a more complete separation of the “technical sands” requires an increase in the magnetic field strength. We believe that the use of thermomagnetic analysis to assess the magnetic susceptibility of the fractions will be useful for quality control of the produced concentrates at all stages of the separation.

Phase composition, magnetic properties of minerals of the “technical sands” and their structural features: the presence of cryptocrystalline structures, complex mineral intergrowths, solid solution decomposition structures, the structures of elements substitution in the mineral crystals in the form of hems on the periphery of grains – all of this reduces the efficiency of the “technical sands” separation by conventional methods of wet magnetic separation. For their successful separation an additional research to find optimal methods of the tailings pretreatment and modes of magnetic field strength is required.

The “technical sands” pretreatment should include up-to-date methods of disintegration and separation of hard-dressable finely impregnated lean ores, such as ultrafine grinding using high-voltage pulses, spiral separation with withdrawal of iron-bearing minerals of different densities (as they are disclosed) from inter-cycle operations to avoid overgrinding, use of surfactants to reduce slurry and defect formation. For magnetic separation, the application of high-gradient wet magnetic separation with superconducting magnetic system would be promising.

The research findings contribute to the study of magnetic properties of copper-smelting slag processing tailings and are of interest for the development of new flow schemes for their utilization and recycling.



## References

1. Bexeitova R., Veselova L., Kassymkanova K.K. et al. The problem of environmental safety of the fields of mining industrial production of arid zone of Kazakhstan. *Geodesy and Cartography*. 2018;44(4):146–155. <https://doi.org/10.3846/gac.2018.4314>
2. Worlanyo A.S., Jiangfeng L. Evaluating the environmental and economic impact of mining for post-mined land restoration and land-use: A review. *Journal of Environmental Management*. 2021;279:111623. <https://doi.org/10.1016/j.jenvman.2020.111623>
3. Covre W.P., Ramos S.J., da Silveira Pereira W.V. et al. Impact of copper mining wastes in the Amazon: Properties and risks to environment and human health. *Journal of Hazardous Materials*. 2022;421:126688. <https://doi.org/10.1016/j.jhazmat.2021.126688>
4. Izydorczyk G., Mikula K., Skrzypczak D. et al. Potential environmental pollution from copper metallurgy and methods of management. *Environmental Research*. 2021;197:111050. <https://doi.org/10.1016/j.envres.2021.111050>
5. Jia L., Liang H., Fan M. et al. Spatial distribution characteristics and source appointment of heavy metals in soil in the areas affected by non-ferrous metal slag field in the dry-hot valley. *Applied Sciences*. 2022;12(19):9475. <https://doi.org/10.3390/app12199475>
6. Men D., Yao J., Li H. et al. The potential environmental risk implications of two typical non-ferrous metal smelting slags: contrasting toxic metal(loid)s leaching behavior and geochemical characteristics. *Journal of Soils and Sediments*. 2023;23:1944–1959. <https://doi.org/10.1007/s11368-023-03468-0>
7. Mamonov S.V., Gazaleeva G.I., Dresvyankina T.P. et al. Improvement of technological indices of copper smelters slags processing on the basis of their slow cooling and ultra-fine grinding. *News of the Higher Institutions. Mining Journal*. 2018;(2):83–90. (In Russ.) <https://doi.org/10.21440/0536-1028-2018-2-83-90>
8. Sibanda V., Sipunga E., Danha G., Mamvura T.A. Enhancing the flotation recovery of copper minerals in smelter slags from Namibia prior to disposal. *Heliyon*. 2020;6(1):e03135. <https://doi.org/10.1016/j.heliyon.2019.e03135>
9. Zhou H., Liu G., Zhang L., Zhou C. Mineralogical and morphological factors affecting the separation of copper and arsenic in flash copper smelting slag flotation beneficiation process. *Journal of Hazardous Materials*. 2021;401:123293. <https://doi.org/10.1016/j.jhazmat.2020.123293>
10. Alp İ., Deveci H., Süngün H. Utilization of flotation wastes of copper slag as raw material in cement production. *Journal of hazardous materials*. 2008;159(2–3):390–395. <https://doi.org/10.1016/j.jhazmat.2008.02.056>
11. Guman O.M., Dolinina I.A., Makarov A.B., Rudoi A. G. The use of waste processing waste slag for land reclamation of the mining complex. *News of the Higher Institutions. Mining Journal*. 2010;(4):43–49 (In Russ.)
12. Guman O.M., Makarov A.B., Wegner-Kozlova E.O. Technogenic formations as a recultivation material. *Upravlenie Tekhnosferoi*. 2020;3(4):447–461 (In Russ.) <https://doi.org/10.34828/Udsu.2020.35.32.004>
13. Zhai Q., Liu R., Wang C. et al. A potential industrial waste–waste synchronous treatment scheme of utilizing copper slag flotation tailings to remediate Cr (VI)-containing wastewater. *Journal of Environmental Chemical Engineering*. 2022;10(3):107685. <https://doi.org/10.1016/j.jece.2022.107685>
14. Zolotova E.S., Ryabinin V.F., Kotelnikova A.L., Ivanova N.S. Assessment of element mobility from copper smelting waste slag into forest soils. *Lithosphere (Russia)*. 2020;20(5):717–726. (In Russ.) <https://doi.org/10.24930/1681-9004-2020-20-5-717-726>
15. Zolotova E., Kotelnikova A., Ryabinin V. The content of toxic elements in soil-plant system based on ombrotrophic peat with the copper smelting slag recycling waste. *Pollution*. 2023;9(1):286–298. <https://doi.org/10.22059/poll.2022.346474.1551>
16. Kart E. U. Evaluation of sulphation baking and autogenous leaching behaviour of Turkish metallurgical slag flotation tailings. *Physicochemical Problems of Mineral Processing*. 2021;57(4):107–116. <https://doi.org/10.37190/ppmp/138839>
17. Gümüşsoy A., Başyigit M., Kart E. U. Economic potential and environmental impact of metal recovery from copper slag flotation tailings. *Resources Policy*. 2023;80:103232. <https://doi.org/10.1016/j.resourpol.2022.103232>
18. Svetlov A. V. Development of enrichment methods for low-grade non-ferrous metallurgy objects in the Murmansk region. *Mineralogy of Technogenesis*. 2018;(19):205–216. (In Russ.)
19. Tian H., Guo Z., Pan J. et al. Comprehensive review on metallurgical recycling and cleaning of copper slag. *Resources, Conservation and Recycling*. 2021;168:105366. <https://doi.org/10.1016/j.resconrec.2020.105366>



20. Araujo F.S., Taborda-Llano I., Nunes E.B., Santos R.M. Recycling and reuse of mine tailings: A review of advancements and their implications. *Geosciences*. 2022;12(9):319. <https://doi.org/10.3390/geosciences12090319>
21. Makarov A.B., Guman O.M., Dolinina I.A. Mineral composition of waste slag processing from the Sredneuralsk copper smelter and assessment of their potential environmental hazard. *Bulletin of the Ural Branch of the Russian Mineralogical Society*. 2010;(7):80–86. (In Russ.)
22. Grudinsky P.I., Dyubnov V.G. Research of the process of sulphating roasting of zinc-containing tailings in copper production using iron sulfates. *International Research Journal*. 2018;(12–1):83–87. (In Russ.) <https://doi.org/10.23670/IRJ.2018.78.12.014>
23. Kotelnikova A.L., Ryabinin V.F. The composition features and perspective of use for the copper slag recycling waste. *Lithosphere (Russia)*. 2018;18(1):133–139. (In Russ.). <https://doi.org/10.24930/1681-9004-2018-18-1-133-139>
24. Reutov D.S., Khalezov B.D. The search for optimal conditions for sulfuric acid leaching to recover copper and zinc from flotation tailings copper slag. *Butlerov Communications*. 2015;44(12):199–203. (In Russ.)
25. Bulatova K.V., Gazaleeva G.I. (sci. ed.) *Modern technologies for processing technogenic raw materials*. Monograph. Yekaterinburg: JSC “IPP “Ural Worker”; 2019. 200 p. (In Russ.)
26. Li S., Guo Z., Pan J. et al. Stepwise utilization process to recover valuable components from copper slag. *Minerals*. 2021;11(2):211. <https://doi.org/10.3390/min11020211>
27. Filatov V.V., Ivanchenko V.S., Glukhikh I.I. *Petromagnetism in ore geophysics*. Ekaterinburg: UGGU; 2011. 414 p. (In Russ.)
28. Gorlova O.E., Orekhova N.N., Kolodezhnaya E.V. et al. Providing a rationale for an integrative criterion to predict the potential selective disintegration of technology-related, complex structured raw materials. *Vestnik of Nosov Magnitogorsk State Technical University*. 2023;21(3):15–26. <https://doi.org/10.18503/1995-2732-2023-21-3-15-26>
29. Sanakulov K.S., Khasanov A.S. *Processing of slag in copper production*. Tashkent: Fan Publ. House; 2007. 206 p. (In Russ.)
30. Erokhin Yu.V., Kozlov P.S. Fayalite from slags of the Sredneuralsk copper smelter (Revda city). *Mineralogy of Technogenesis*. 2010;(11):32–40. (In Russ.)
31. Belley F., Ferré E.C., Martín-Hernández F. et al. The magnetic properties of natural and synthetic  $(\text{Fe}_x, \text{Mg}_{1-x})_2\text{SiO}_4$  olivines. *Earth and Planetary Science Letters*. 2009;284(3–4):516–526. <https://doi.org/10.1016/j.epsl.2009.05.016>
32. Geiger C.A., Vielreicher N.M., Dachs E. Are the thermodynamic properties of natural and synthetic  $\text{Mg}_2\text{SiO}_4\text{--Fe}_2\text{SiO}_4$  olivines the same? *American Mineralogist: Journal of Earth and Planetary Materials*. 2021;106(2):317–321. <https://doi.org/10.2138/am-2021-7764CCBY>
33. Erokhin Yu.V., Kozlov P.S. Magnetite slags from the Sredneuralsk cooper smelter. *Mineralogy of Technogenesis*. 2013;(14):29–37. (In Russ.)
34. Ziese M., Esquinazi P.D., Pantel D. et al. Magnetite ( $\text{Fe}_3\text{O}_4$ ): a new variant of relaxor multiferroic. *Journal of Physics: Condensed Matter*. 2012;24(8):086007–086015. <https://doi.org/10.1088/0953-8984/24/8/086007>
35. Pelevin A.E. Magnetic susceptibility of weakly magnetic rock minerals. In: *Scientific foundations and practice of processing ores and technogenic raw materials: materials of the XXIV International Scientific and Technical Conference held as part of the XVII Ural Mining Decade*. Yekaterinburg, April 09–12, 2019. Ekaterinburg: Publ. House “Fort Dialog-Iset”; 2019. Pp. 314–316. (In Russ.)
36. Pisakin B.N. Identification features of pyrrhotite as a cation-deficient magnetic mineral. *Vestnik of Saint Petersburg University. Earth Sciences*. 2004;1(7):3–12. (In Russ.)
37. Karmazin V.I., Karmazin V.V. *Magnetic methods of enrichment*. Moscow: Nedra Publ. House; 1984. 416 p. (In Russ.)
38. Gzogyan T.N., Golovin Yu.I., Tyurin A.I., Gzogyan S.R. Effect of intergrowth boundaries between mineral species of ferruginous quartzite on ore pretreatment. *Journal of Mining Sciences*. 2017;(3):154–162. (In Russ.)
39. Yusupov T.S., Urakaev F.Kh., Isupov V.P. Prediction of structural-chemical change in minerals under mechanical impact during grinding. *Journal of Mining Sciences*. 2015;(5):161–168. (In Russ.)
40. Gzogyan T.N. On the issue of genetic defectiveness of magnetite from the Mikhailovskoye KMA deposit. *Obogashchenie Rud*. 2002;(3):29–33. (In Russ.)
41. Kharlov A.V. Generators for electric-discharge technologies and their technical applications (review). *Instruments and Experimental Techniques*. 2022;65(1):1–28. <https://doi.org/10.1134/S0020441221060154>



42. Prokopyev S.A., Prokopyev E.S., Emelyanova K.K., Napolskikh S.A. High-quality magnetite–hematite concentrate production by spiral separation. *Gornyi Zhurnal*. 2021;(6):86–90. (In Russ.) <https://doi.org/10.17580/gzh.2021.06.07>

### Information about the authors

**Alla L. Kotelnikova** – Cand. Sci. (Geol.-Mineral.), Senior Researcher, Laboratory of Geochemistry and Ore Forming Processes, Zavaritsky Institute of Geology and Geochemistry of the Ural Branch of the Russian Academy of Sciences, Yekaterinburg, Russian Federation; ORCID [0000-0003-4968-1938](https://orcid.org/0000-0003-4968-1938); e-mail [kotelnikova@prm.uran.ru](mailto:kotelnikova@prm.uran.ru)

**Ekaterina S. Zolotova** – Cand. Sci. (Biol.), Senior Researcher, Laboratory of Geochemistry and Ore Forming Processes, Zavaritsky Institute of Geology and Geochemistry of the Ural Branch of the Russian Academy of Sciences, Yekaterinburg, Russian Federation; ORCID [0000-0002-5892-9205](https://orcid.org/0000-0002-5892-9205); e-mail [zolotova@igg.uran.ru](mailto:zolotova@igg.uran.ru)

**Received** 12.08.2023

**Revised** 13.06.2024

**Accepted** 13.08.2024




## MINING MACHINERY, TRANSPORT, AND MECHANICAL ENGINEERING

Research paper

<https://doi.org/10.17073/2500-0632-2024-01-179>

UDC 62-13:62-52:62-51:62-59:62-64:62-66

**Impact of the technical condition of main pumps  
on fuel consumption in a hydraulic excavator**M. G. Rakhutin<sup>1</sup>  , V. H. Tran<sup>2</sup> , A. E. Krivenko<sup>1</sup>   , Q. Kh. Giang<sup>3</sup> <sup>1</sup> University of Science and Technology MISIS, Moscow, Russian Federation<sup>2</sup> Le Quy Don Technical University, Hanoi, Vietnam<sup>3</sup> Thanh Dong University, Hai Duong City, Vietnam [Krivenko.ae@misis.ru](mailto:Krivenko.ae@misis.ru)**Abstract**

During the operation of hydraulic excavators, the technical condition of pumps deteriorates due to wear, leading to increased internal clearances, fluid leakage, a reduction in volumetric efficiency, and higher energy losses, ultimately resulting in excessive fuel consumption. The objective of this study was to determine the optimal service life of pumps, taking into account the growing fuel overconsumption during operation. The following tasks were addressed: developing a mathematical model for pump ownership costs, incorporating progressive fuel overconsumption; designing an algorithm and conducting computer simulations using Simulink-Matlab; and assessing the increase in fuel consumption. The study examines the impact of the technical condition of the main hydraulic pumps on fuel overconsumption using the Komatsu PC2000-8 hydraulic excavator as a case study. Based on the proposed pump operation cost model, which accounts for the increase in fuel consumption over time, dependencies between fuel overconsumption and pump wear were established. Computer modeling was performed in Simulink-Matlab and Excel based on the developed calculation methodology and software algorithm. Relationships between the excavator's fuel overconsumption and the technical condition of the pumps were identified. A mathematical model for pump ownership costs is presented, taking into account the progressive fuel overconsumption during operation, along with the resulting equation for determining the optimal service life of pumps to minimize total costs, including pump acquisition and fuel expenses. This expression considers the technical condition of the main pumps, their rate of deterioration, fuel costs, and pump replacement costs. A fuel overconsumption indicator was introduced, defined as the ratio of the difference between actual fuel consumption per 1 m<sup>3</sup> of excavated material and fuel consumption at nominal efficiency of the main pumps (nominal fuel consumption) to the nominal fuel consumption. The application of this criterion, in conjunction with the proposed equation for determining the optimal pump service life, allows for a data-driven selection of the critical wear threshold for the main pumps, reducing total ownership and fuel costs by up to 17%, depending on economic and mining-engineering conditions.

**Keywords**

mining machinery, hydraulic mining excavator, pump technical condition, hydraulics, pump, condition, operation, modeling, leakage, efficiency, wear, costs, algorithm, consumption, overconsumption, optimal service life


**For citation**

Rakhutin M. G., Tran V. H., Krivenko A. V., Giang Q. Kh. Impact of the technical condition of main pumps on fuel consumption in a hydraulic excavator. *Mining Science and Technology (Russia)*. 2025;10(1):67–74. <https://doi.org/10.17073/2500-0632-2024-01-179>



## ГОРНЫЕ МАШИНЫ, ТРАНСПОРТ И МАШИНОСТРОЕНИЕ

Научная статья

**Влияние технического состояния главных насосов гидравлического экскаватора на расход топлива**М. Г. Рахутин<sup>1</sup> , В. Х. Чан<sup>2</sup> , А. Е. Кривенко<sup>1</sup>  , К. К. Занг<sup>3</sup> <sup>1</sup> Университет науки и технологий МИСИС, г. Москва, Российская Федерация<sup>2</sup> Государственный технический университет им. Ле Куй Дона, г. Ханой, Вьетнам<sup>3</sup> Университет Тхань Донг, г. Хайзыонг, Вьетнам [Krivenko.ae@misis.ru](mailto:Krivenko.ae@misis.ru)**Аннотация**

В процессе эксплуатации гидравлических экскаваторов вследствие износа изменяется техническое состояние насосов. Увеличиваются зазоры, переток жидкости, снижается объемный КПД, возрастают потери энергии, что приводит к перерасходу топлива. Целью работы являлось определение рационального срока эксплуатации насосов с учетом перерасхода топлива, который возрастает в процессе эксплуатации. Решены задачи: создание математической модели затрат на владение насосом с учетом перерасхода топлива, возрастающего в процессе эксплуатации, разработка алгоритма и компьютерного моделирования в программе Simulink-Matlab, оценка увеличения расхода топлива. В статье на примере гидравлического экскаватора Komatsu PC2000-8 показано влияние технического состояния главных насосов гидравлического экскаватора на перерасход топлива. На основе предлагаемой модели затрат на эксплуатацию насоса с учетом повышения расхода топлива в процессе эксплуатации получены зависимости перерасхода топлива от технического состояния насосов. По разработанной методике расчета и программному алгоритму выполнено компьютерное моделирование в программах Simulink-Matlab и Excel. Получены зависимости перерасхода топлива гидравлического экскаватора от технического состояния насосов. Представлены математическая модель затрат на владение насосом с учетом перерасхода топлива, возрастающего в процессе эксплуатации, и полученное на ее основе выражение для определения рационального срока эксплуатации насосов для минимизации затрат на приобретение насосов и топлива, учитывающее техническое состояние главных насосов, скорость его изменения, стоимость топлива и замены насоса. Предложен показатель, характеризующий перерасход топлива, определяемый отношением разницы между фактическим расходом топлива на 1 м<sup>3</sup> экскавируемой горной массы и расходом топлива при номинальных значениях КПД основных насосов (номинальным расходом) к номинальному расходу. Использование предлагаемого критерия совместно с выражением для определения рационального срока эксплуатации насосов позволит обоснованно выбирать значение предельного состояния основных насосов и уменьшить суммарные затраты на владение насосом и на расход топлива до 17 % в зависимости от экономических и горнотехнических факторов эксплуатации с учетом экономических и горнотехнических факторов эксплуатации.

**Ключевые слова**

горные машины, карьерный гидравлический экскаватор, техническое состояние насосов, гидравлика, насос, состояние, эксплуатация, моделирование, утечки, КПД, износ, затраты, алгоритм, расход, перерасход, рациональный срок

**Для цитирования**

Rakhutin M. G., Tran V. H., Krivenko A. V., Giang Q. Kh. Impact of the technical condition of main pumps on fuel consumption in a hydraulic excavator. *Mining Science and Technology (Russia)*. 2025;10(1):67–74. <https://doi.org/10.17073/2500-0632-2024-01-179>

**Introduction**

Leakage of the working fluid in the discharge mechanism of positive displacement pumps in the hydraulic drive of mining excavators is inherent in the design phase and, on average, accounts for 5% of the operating flow rate at working pressure. A lower leakage volume results in deteriorated lubrication and cooling conditions for the components of the discharge mechanism, leading to overheating and eventual pump failure. The leakage volume is directly de-

pendent on the clearance size in the pump discharge mechanism [1–3]. As the components wear, the clearances in the discharge mechanism increase, leading to higher leakage of the working fluid, a decrease in pump efficiency, and an increase in fuel consumption. The aim of the study was to determine the optimal service life of pumps, taking into account the excess fuel consumption that increases during operation. The impact of increasing leakage on the productivity of a mining excavator can be assessed



through the volumetric efficiency of the hydraulic machine. As established in previous studies, the effect of pump wear on energy consumption occurs in two stages: 1. The power reserve of the drive fully compensates for the energy losses caused by increasing internal leakage in the pump. At this stage, the machine's productivity remains unchanged, but the specific energy consumption per cubic meter of mined material increases; 2. The power reserve of the drive is insufficient to compensate for the energy losses due to volumetric leakage in the pump, resulting in a decrease in machine productivity, while the specific energy consumption per cubic meter of mined material continues to rise. During operation, including in axial piston pumps of hydraulic excavators, component wear increases internal clearances, allowing fluid to leak through them. This leads to energy losses and increased (excess) fuel consumption. Replacing pumps based on the increase in excess fuel consumption can help reduce total fuel costs and ownership costs over the pump's operational lifetime. Establishing an optimal service interval for the pump will enable timely replacement planning and better forecasting of future expenses [4–6]. Determining the relationship between “excess” fuel consumption and the technical condition of the pump (leakage volume) will allow for defining the most optimal volumetric efficiency range, considering minimal productivity losses, excess fuel consumption, and ownership costs.

### Methods

In a hydraulic excavator, all primary and auxiliary operations are performed using a hydraulic drive. The primary operations, which include digging, swinging to dump, bucket unloading, and swinging back to the face<sup>1</sup>, are carried out using variable-displacement axial piston pumps, commonly referred to in technical literature<sup>2</sup> [7–9] as main or primary pumps. Wear of the converting and displacing mechanisms in high-pressure hydraulic pumps leads to increased clearances and distortion of the geometry of components operating in sliding or rolling contacts. As clearances increase, hydraulic fluid leakage rises, causing a decrease in the pump's volumetric efficiency and an increase in energy consumption for performing useful work, as confirmed by previous studies [10–12]. Ulti-

mately, this process results in excess fuel consumption of the internal combustion engine. Replacing the pump resolves the issue of fuel overconsumption but entails additional costs. To achieve the objective of determining the optimal service life of pumps, the following tasks were formulated: developing a mathematical model for pump ownership costs, accounting for fuel overconsumption that increases over time, designing an algorithm and conducting computer modeling in Simulink-Matlab, evaluating the increase in fuel consumption over the pump's service life.

The study examined the impact of the technical condition of HPV375 axial piston pumps on the fuel consumption of the Komatsu PC2000-8 mining hydraulic excavator. Within the scope of the research, it was assumed that energy losses in the friction pairs of the excavator's mechanisms remain constant and were therefore not considered in the calculations.

The main pumps of the excavator's hydraulic system supply hydraulic fluid to the hydraulic motors of the working equipment and the swing mechanism. Depending on the phase of the excavator's work cycle, some hydraulic motors may remain idle or, conversely, operate under maximum load. The load on the excavator's mechanisms determines the working pressure in the hydraulic system, and, in turn, the magnitude of internal leakage and friction forces in the pump's discharge mechanism changes proportionally to pressure variations. Thus, to accurately assess energy losses in the main hydraulic pumps, it is necessary to consider the properties of the excavated rock mass, the temperature of the hydraulic fluid, the level of fluid leakage, as well as the velocities and accelerations of moving components [13, 14].

Leakage through the clearances of the axial piston pump mechanisms depends on several factors, the most significant being the pressure difference between the inlet and outlet of the clearance and the flow resistance of the clearance, which is determined by its shape and cross-sectional area. Under otherwise identical conditions, leakage increases with rising pressure differential. This occurs during the displacement of hydraulic fluid from the pump's working chamber. During the filling phase of the working chamber, leakage is nearly absent.

Leakage in the working chambers of the HPV375+375 pump's discharge mechanism can be represented as four main components: fluid bypass in the annular clearance between the plunger and the working chamber wall  $Q_{pc}$ , leakage in the spherical joint connecting the plunger base to the slipper pad, leakage through the flat clearance between the slipper pad and the swashplate, leakage at the contact surface between the cylinder block and the valve plate  $Q_{bp}$ .

<sup>1</sup> GOST R 55165–2012. Mining equipment. Open-pit single-bucket excavators with a bucket capacity exceeding 4 m<sup>3</sup>. General technical requirements and test methods.

<sup>2</sup> Zang K.K. Substantiation and selection of hydraulic system cooler parameters for a mining hydraulic excavator operating in the Socialist Republic of Vietnam. [Author's abstract of the dissertation for the degree of Cand. Sci. (Eng.)]. Moscow: MISIS; 2021. 21 p.

These leakages are not only unavoidable by design but also essential, as the hydraulic fluid lubricates component surfaces subjected to forces generated by working pressure, thereby reducing wear.

When calculating fluid bypass through the clearance between the plunger and the working chamber wall, it is essential to consider that due to lateral forces arising during the transmission of torque from the drive shaft to the plunger group, the plunger assumes an eccentric position in the working chamber, despite tight tolerances and high manufacturing precision. The fluid flow rate in the eccentric annular clearance is determined by the following equation [15, 16]:

$$Q_{pc} = \frac{\pi d_p h_{pc}^3 (p_c - p_0)}{12 \mu l} (1 + 1.5 \lambda^2) - \frac{\pi d_p h_{pc} v}{2}, \quad (1)$$

where  $d_p$  – pump plunger diameter, m;  $h_{pc}$  – average clearance between the plunger and the working chamber wall, m;  $p_c, p_0$  – working pressure of the pump and casing pressure, respectively, Pa;  $\mu$  – dynamic viscosity of the working fluid, Pa·s;  $\lambda = e/h_{pc}$  – relative eccentricity of the plunger in the working chamber;  $e$  – plunger eccentricity relative to the cylinder walls, m;  $v$  – plunger velocity, m/s;  $l$  – length of the plunger section inside the cylinder at a given moment, m:

$$l = l_0 + R(1 - \cos \omega t) \operatorname{tg} \gamma, \quad (2)$$

where  $l_0$  – average length of the plunger section inside the cylinder, m;  $R$  – radius of the working chamber axes, m;  $\omega$  – angular velocity of the cylinder block, rad/s;  $\gamma$  – tilt angle of the swashplate, degrees.

The axial velocity of an individual piston relative to the cylinder is determined by:

$$v = \omega R \operatorname{tg} \gamma \sin \omega t. \quad (3)$$

Leakage of the working fluid through the clearance between the piston and the slipper is calculated using the following expression [17]:

$$Q_{bp} = \frac{\pi h_{bp}^3 (p_1 - p_0)}{3 \mu \left( \operatorname{tg}^2 \beta_2 - \operatorname{tg}^2 \beta_1 + 2 \ln \left| \frac{\operatorname{tg} \beta_2}{\operatorname{tg} \beta_1} \right| \right)}, \quad (4)$$

where  $h_{bp}$  – clearance between the piston and the slipper, m;  $p_1, p_0$  – pressure in the slipper chamber and in the pump casing chamber, respectively, Pa;  $\beta_1, \beta_2$  – design angles of the piston and slipper, rad.

Leakage calculations for other components of the axial piston pump follow a similar approach.

The current GOST 13823–78 standard specifies failure criteria only for fixed-displacement axial piston pumps and does not establish limits for variable-displacement pumps with a control system powered by the main flow. However, according to existing engineering practices, there comes a point

when further operation of a variable-displacement axial piston pump becomes impractical, including due to excessive fuel consumption. For mining hydraulic excavators, the failure threshold of variable main pumps should be determined considering both mining-technical and economic operating conditions [18].

## Results and discussion

A comprehensive mathematical model, incorporating the listed leakage formulas for the critical components of the fluid discharge mechanism in axial piston pumps of the hydraulic system in a mining excavator, was developed in Simulink-Matlab. In recent years, Simulink-Matlab, along with other popular CAD and CAE systems, has been widely and successfully used for digital prototyping of equipment operating processes in the mining industry [19]. Additionally, the model included constraints and conditions that directly and indirectly affect the leakage volume of the working fluid in the clearances. These include: pump working chamber cycle parameters, design parameters of the discharge mechanism, time and load parameters of the mining hydraulic excavator's duty cycle, temperature of the hydraulic fluid.

As part of the numerical experiment, the volumes of hydraulic fluid leakage were determined for high-pressure pumps in the hydraulic system of a mining hydraulic excavator, considering different levels of discharge mechanism wear: from a new pump (clearances  $h_{pc} = h_{cv} = h_{ps} = h_{ss} = 5 \mu\text{m}$ ) to a pump in operation for several years (clearances  $h_{pc} = h_{cv} = h_{ps} = h_{ss} = 20 \mu\text{m}$ ).

The fuel overconsumption values corresponding to pump leakage losses are presented in Table 1. The graphs showing the dependence of fuel overconsumption on hydraulic fluid temperature for four levels of discharge mechanism wear (Fig. 1) indicate that as clearances increase, fuel overconsumption rises exponentially. For example, at a hydraulic fluid temperature of 70 °C increasing the clearance size in the discharge mechanism of an axial piston pump by a factor of 2, 3, and 4 results in fuel overconsumption due to hydraulic fluid leakage increasing by factors of 8, 27, and 64, respectively. This relationship can be expressed by the function  $x = y^3$ .

The fuel overconsumption during working operations, depending on the clearance between the piston and the cylinder block at different hydraulic fluid temperatures, is shown in Fig. 2.

The impact of hydraulic fluid temperature on power losses in a hydraulic excavator was analyzed in [20]. However, that study did not consider the effect of pump technical condition on power losses.

It should be noted that a power loss of 1 kWh results in an excess fuel consumption of 207–218 g.

Table 1

Fuel overconsumption during primary duty cycle operations depending on the clearance between the piston and cylinder block

HF temperature, °C	Fuel overconsumption, L/h × 10 <sup>-3</sup>															
	Digging				Swing to dump				Bucket unloading				Swing to face			
	Clearance size, μm															
	5	10	15	20	5	10	15	20	5	10	15	20	5	10	15	20
20	46	98	226	448	24	28	36	52	28	34	50	78	18	18	22	30
40	82	208	510	1.036	36	44	66	102	42	58	94	156	26	30	38	54
60	138	406	1.040	2.146	48	66	110	186	60	90	164	294	34	42	60	92
80	224	720	1.896	3.946	64	98	178	316	80	138	274	510	44	58	92	152
100	342	1.178	3.156	6.604	82	138	272	506	104	200	428	826	56	80	136	234

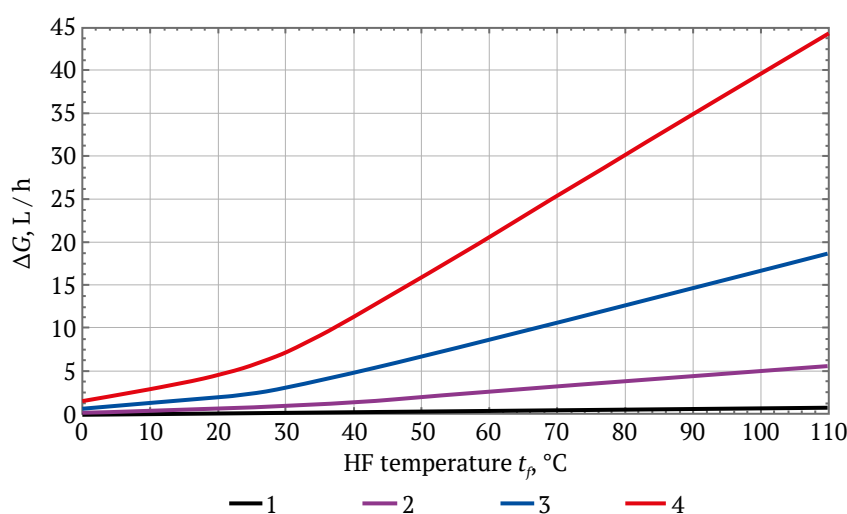


Fig. 1. Power losses at different clearance widths: 1 – 5 μm; 2 – 10 μm; 3 – 15 μm; 4 – 20 μm

In Chan V. H.'s study<sup>3</sup>, a mathematical model was developed to calculate the ownership cost of the main hydraulic excavator pump and the expenses associated with excess fuel consumption:

$$V = Z_e + Z_g \left[ \frac{v_{\eta} T}{\eta_n} + \frac{v_{\eta}^2 T^2}{\eta_n^2} \right] + \frac{C}{T}, \quad (5)$$

where  $Z_e$  – pump operating costs, RUB/h;  $Z_g$  – fuel costs at the initial moment of operation, RUB/h;  $C$  – pump replacement cost, RUB;  $\eta_n$  – volumetric efficiency of the pump at the initial moment of operation;  $v_{\eta}$  – rate of volumetric efficiency degradation, %/h;  $T$  – service life, h.

Based on the proposed model, an expression was derived to determine the replacement interval:

$$T_{opt} = \sqrt{\frac{2\eta_n C}{v_{\eta} Z_g}}. \quad (6)$$

<sup>3</sup> Chan V. H. Optimization of pump replacement intervals for mining hydraulic excavators operating in Vietnam. [Author's abstract of the dissertation for the degree of Cand. Sci. (Eng.)]. Tver; 2024. 21 p.

Using the calculated replacement interval will help minimize pump acquisition costs and fuel consumption throughout the pump's operational life until replacement.

From the equation, it is evident that the replacement interval increases proportionally to the square root of the pump replacement cost and decreases with lower fuel costs and higher volumetric efficiency degradation rates during operation.

Furthermore, the equation indicates that the fixed operating costs of the pump do not affect the optimal replacement interval (Fig. 3).

To evaluate fuel overconsumption, the study proposes the  $K_{ef}$  indicator, which characterizes excess fuel consumption and is determined by the ratio of the difference between the actual fuel consumption per cubic meter of excavated material  $G_f$  and the fuel consumption at the initial volumetric efficiency  $G_n$  to the fuel consumption at the initial volumetric efficiency:

$$K_{ef} = \frac{G_f - G_n}{G_n}.$$

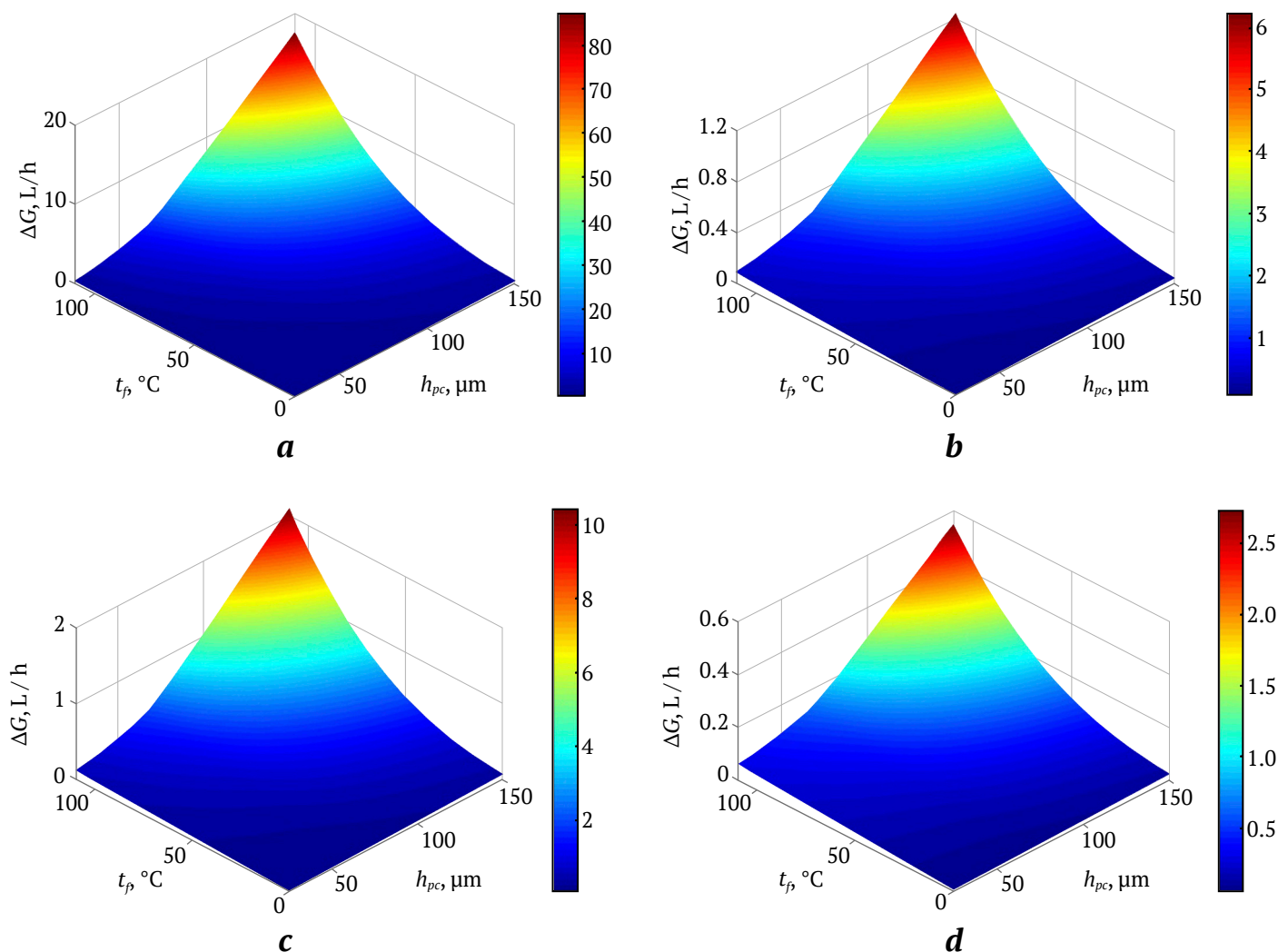


**Fig. 2.** Fuel overconsumption during working operations:  
a – digging; b – swing to dump; c – bucket unloading; d – swing to face

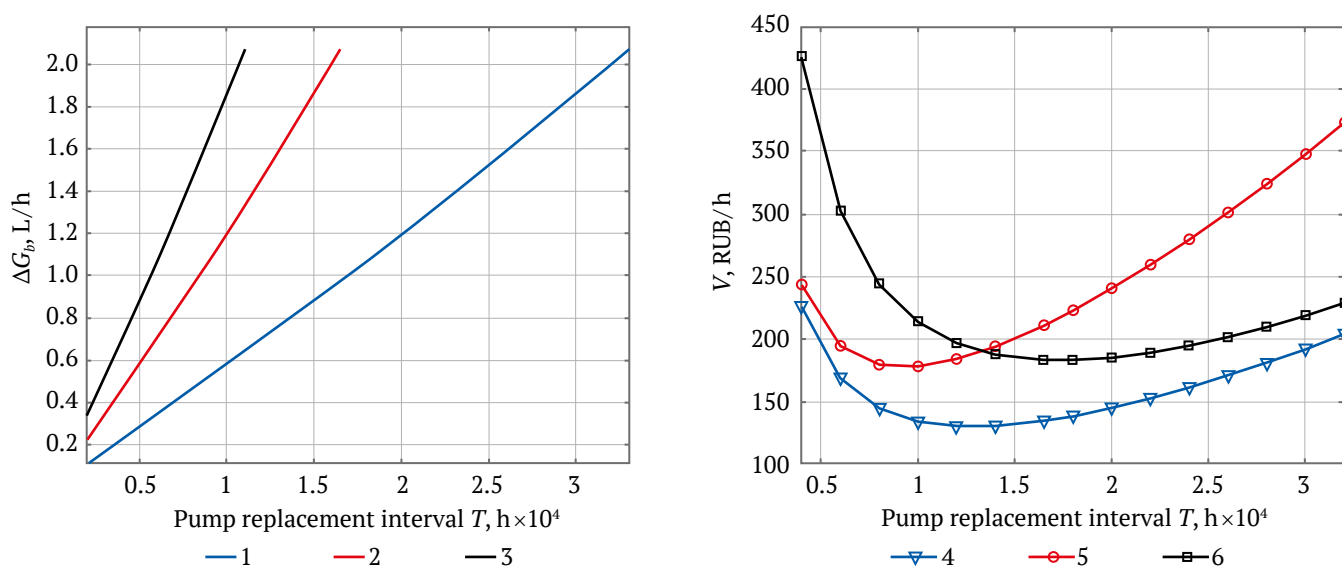


**Fig. 3.** Impact of the replacement interval for main pumps:

a – on fuel overconsumption; b – on fuel costs and pump replacement costs:

1 –  $v_n = 0.5 \cdot 10^{-3} \text{ \%}/h$ ; 2 –  $v_n = 1 \cdot 10^{-3} \text{ \%}/h$ ; 3 –  $v_n = 1.5 \cdot 10^{-3} \text{ \%}/h$ ; 4 –  $v_n = 1 \cdot 10^{-3} \text{ \%}/h$ ,  $C_{zn} = 800 \text{ 000 RUB}$ ,  $D = 35 \text{ RUB/L}$ ; 5 –  $v_n = 1 \cdot 10^{-3} \text{ \%}/h$ ,  $C_{zn} = 800 \text{ 000 RUB}$ ,  $D = 70 \text{ RUB/L}$ ; 6 –  $v_n = 1 \cdot 10^{-3} \text{ \%}/h$ ,  $C_{zn} = 1 \text{ 600 000 RUB}$ ,  $D = 35 \text{ RUB/L}$



The  $K_{ef}$  value is zero when the nominal and actual fuel consumption are equal, i.e., at the initial moment of operation. If the actual fuel consumption becomes twice the nominal value (which is not permissible in operation), the coefficient reaches one.

Using the proposed fuel efficiency coefficient and the derived equation for pump replacement intervals will enable data-driven decisions regarding the definition of critical pump conditions and optimal replacement timing. This approach can reduce total pump ownership and fuel costs by up to 17%, depending on the economic and mining-technical operating conditions.

### Conclusion

1. Using the developed algorithm and computer modeling in Simulink-Matlab, a relationship was established between fuel overconsumption, hydraulic fluid viscosity, and clearance size in the HPV375 axial piston pump of the Komatsu PC2000-8 excavator.

2. A mathematical model was developed for pump ownership costs, accounting for increasing fuel overconsumption over the pump's service life. Based on this model, an expression was derived to determine the optimal pump service life, aimed at minimizing pump acquisition and fuel costs, while considering the technical condition of the main pumps, its degradation rate, fuel price, and pump replacement costs.

3. A new indicator was proposed to characterize fuel overconsumption, defined as the ratio of the difference between actual fuel consumption per 1 m<sup>3</sup> of excavated material and the fuel consumption at the initial pump efficiency to the fuel consumption at initial efficiency.

4. Implementing the proposed fuel overconsumption indicator and the equation for pump replacement intervals will allow for more accurate planning of replacement timing and future expenditures. Additionally, this approach can reduce total pump ownership and fuel costs by up to 17%, depending on economic and mining-technical operating factors.

### References

1. Chen Y., Zhang J., Xu B. et al. Multi-objective optimization of micron-scale surface textures for the cylinder/valve plate interface in axial piston pumps. *Tribology International*. 2019;138:316–329. <https://doi.org/10.1016/j.triboint.2019.06.002>
2. Mnatsakanyan V.U., Surina N.V., Belyankina O.V., Sizova E.I. Assembly accuracy of power cylinders for powered roof supports in longwalls. *Eurasian Mining*. 2023;(1):50–54. <https://doi.org/10.17580/em.2023.01.11>
3. Bergada J.M., Kumar S., Davies D.L., Watton J. A complete analysis of axial piston pump leakage and output flow ripples. *Applied Mathematical Modelling*. 2012;36(4):1731–1751. <https://doi.org/10.1016/j.apm.2011.09.016>
4. Xia L., Quan L., Cao D. et al. Research on energy saving characteristics of large hydraulic excavator boom driven by dual hydraulic-gas energy storage cylinder. *Journal of Mechanical Engineering*. 2019;55(20):240–248. (In Chinese) <https://doi.org/10.3901/JME.2019.20.240>
5. Yu Y., Do T.C., Yin B. et al. Improvement of energy saving for hybrid hydraulic excavator with novel powertrain. *International Journal of Precision Engineering and Manufacturing-Green Technology*. 2023;10:521–534. <https://doi.org/10.1007/s40684-022-00437-9>
6. Lukashuk O.A., Komissarov A.P., Letnev K.Y. Increasing power efficiency of open-pit excavators. In: *IOP Conference Series: Materials Science and Engineering*. 2020;709(2):022083. <https://doi.org/10.1088/1757-899X/709/2/022083>
7. Zhuraev A. Study of the effect of hydraulic systems operation on the general performance of a hydraulic excavator. *The American Journal of Engineering and Technology*. 2021;3(10):36–42. <https://doi.org/10.37547/tajet/Volume03Issue10-07>
8. Litvin O.I., Khoreshok A.A., Dubinkin D.M. et al. Analysis of methods for calculating the productivity of open-pit hydraulic shovels and backhoes. *Russian Mining Industry*. 2022;(5):112–120. (In Russ.) <https://doi.org/10.30686/1609-9192-2022-5-112-120>
9. Vukovic M., Leifeld R., Murrenhoff H. Reducing fuel consumption in hydraulic excavators – a comprehensive analysis. *Energies*. 2017;10(5):687. <https://doi.org/10.3390/en10050687>
10. Buryi G.G., Poteryaev I.K. Determination of the optimal strength and speed of soil digging of a single-bucket hydraulic excavator with a spherical shape bucket. *Sustainable Development of Mountain Territories*. 2022;14(2):321–329. (In Russ.). <https://doi.org/10.21177/1998-4502-2022-14-2-321-329>
11. Hidayat H., Aviva D., Muis A., Halik A. Failure analysis of excavator hydraulic pump. In: *IOP Conference Series Materials Science and Engineering*. 2022;1212(1):012052. <https://doi.org/10.1088/1757-899X/1212/1/012052>



12. Ovchinnikov N.P. Assessment of mine water solid phase impact on section pumps performance in the development of kimberlite ores. *Mining Science and Technology (Russia)*. 2022;7(2):150–160. <https://doi.org/10.17073/2500-0632-2022-2-150-160>
13. D'Andrea D., Epasto G., Bonanno A. et al. Failure analysis of anti-friction coating for cylinder blocks in axial piston pumps. *Engineering Failure Analysis*. 2019;104:126–138. <https://doi.org/10.1016/j.engfailanal.2019.05.041>
14. Xu B., Hu M., Zhang J., Su Q. Characteristics of volumetric losses and efficiency of axial piston pump with respect to displacement conditions. *Journal of Zhejiang University – Science A*. 2016;17:186–201. <https://doi.org/10.1631/jzus.A1500197>
15. Li R., Liu J., Ding X., Liu Q. Study on the influence of flow distribution structure of piston pump on the output of pulsation pump. *Processes*. 2022;10(6):1077. <https://doi.org/10.3390/pr10061077>
16. Hong H., Zhao Ch., Zhang B. et al. Flow ripple reduction of axial-piston pump by structure optimizing of outlet triangular damping groove. *Processes*. 2020;8(12):1664. <https://doi.org/10.3390/pr8121664>
17. Khorin V.N. *Volumetric hydraulic drive of downhole equipment*. 3<sup>rd</sup> ed., revised and add. Moscow: Nedra Publ. House; 1980. 415 p. (In Russ.)
18. Surina N.V., Mnatsakanyan V.U. Automated process design system for mining equipment repair. *Gornyi Zhurnal*. 2019;(7):90–95. (In Russ.) <https://doi.org/10.17580/gzh.2019.07.08>
19. Rakhutin M.G. Methodology of substantiation of limit states of hydraulic drive elements of mining machines. *Mining Informational and Analytical Bulletin*. 2011;(S1):508–519. (In Russ.)
20. Rakhutin M.G., Giang Kh.Q., Krivenko A.E., Tran H.V. Evaluation of the influence of the hydraulic fluid temperature on power loss of the mining hydraulic excavator. *Journal of Mining Institute*. 2023;261:374–383. (In Russ.)

#### Information about the authors

**Maxim G. Rakhutin** – Dr. Sci. (Eng.), Professor of the Department of Mining Equipment, Transport and Mechanical Engineering, University of Science and Technology MISIS, Moscow, Russian Federation; ORCID [0000-0001-5873-5550](https://orcid.org/0000-0001-5873-5550), Scopus ID [57200152323](https://orcid.org/57200152323); e-mail [rahutin.mg@misis.ru](mailto:rahutin.mg@misis.ru)

**Van Hiep Tran** – Cand. Sci. (Eng.), Lecturer of the Mechanical Engineering Faculty, Le Quy Don Technical University, Hanoi, Vietnam; ORCID [0000-0003-0962-5835](https://orcid.org/0000-0003-0962-5835); e-mail [hieptv@lqdtu.edu.vn](mailto:hieptv@lqdtu.edu.vn)

**Alexander E. Krivenko** – Cand. Sci. (Eng.), Associate Professor of the Department of Mining Equipment, Transport and Mechanical Engineering, University of Science and Technology MISIS, Moscow, Russian Federation; ORCID [0000-0001-7198-4447](https://orcid.org/0000-0001-7198-4447), Scopus ID [57210220257](https://orcid.org/57210220257); e-mail [Krivenko.ae@misis.ru](mailto:Krivenko.ae@misis.ru)

**Quoc Khanh Giang** – Cand. Sci. (Eng.), Dean of the Faculty of Mechanical Engineering, Thanh Dong University, Hai Duong City, Vietnam; ORCID [0009-0006-8589-5609](https://orcid.org/0009-0006-8589-5609); e-mail [khanhgq@thanhdong.edu.vn](mailto:khanhgq@thanhdong.edu.vn)

**Received** 20.01.2024

**Revised** 01.06.2024

**Accepted** 17.09.2024











## POWER ENGINEERING, AUTOMATION, AND ENERGY PERFORMANCE

Research paper

<https://doi.org/10.17073/2500-0632-2024-05-262>

UDC 621.833:622.232.8

**Mechatronic system for running-in and testing of mechanical transmissions in mining shovels****S.I. Malafeev<sup>1,2</sup> , A.A. Malafeeva<sup>3</sup>  , V.I. Konyashin<sup>1</sup>  , A.A. Novgorodov<sup>1</sup>  **<sup>1</sup> Joint Power Co., Ltd., Moscow, Russian Federation<sup>2</sup> Vladimir State University named after A. G. and N. G. Stoletov, Vladimir, Russian Federation<sup>3</sup> Russian Presidential Academy of National Economy and Public Administration (Vladimir Branch), Vladimir, Russian Federation [simalafeev@gmail.com](mailto:simalafeev@gmail.com)**Abstract**

The mechanical transmissions of the hoist and drag winches, as well as the crowd mechanisms of mining shovels, operate under highly variable and shock cyclic loads. These severe operating conditions impose stringent quality requirements on both the manufacturing and assembly of such transmissions. The lifecycle management process for these gearboxes includes running-in and acceptance testing at the manufacturing plant, followed by diagnostics and condition monitoring during field operation. Test benches designed for these purposes must closely replicate the operating conditions experienced by the transmission in actual service. The developed test bench is designed to perform running-in (initial wear-in of mating surfaces) and quality control testing of hoist and crowd winch gearboxes installed in electric mining shovels of the following models: EKG-8US, EKG-10, EKG-12K, EKG-15M, EKG-18, EKG-20KM, and EKG-32R. These operations are carried out as part of the standard acceptance testing procedure. The test bench is equipped with DC excavator motors rated at 350 kW (drive motors) and 560 kW (loading motor). The hoist winch gearbox from the EKG-15M shovel serves as the torque multiplier. Two intermediate shafts are connected via an intermediate coupling, with the loading motor driving one of these shafts. Motor control is implemented using standard DC transistor converters with PWM control, identical to those used in mining shovels equipped with DC main drives. The running-in and testing processes are carried out using the mutual loading method, which enhances energy efficiency by allowing regenerative energy to be reused within the system. The test bench software is based on the Pulsar-7 information and diagnostics system, which supports the following operational modes: 1. Interactive manual control, enabling the operator to verify the functionality and calibration of test bench components. 2. Automatic control of the running-in and testing processes, where pre-programmed sequences from a built-in library generate the required control commands for each specific test type. Available test modes include: unloaded running-in, running-in under constant load, running-in under variable load and rotational speed, excavation cycle simulation. 3. Automated test report generation, including the ability to view and print previously generated reports. 4. Software configuration and auxiliary functions, including an embedded help system. A mathematical model of the mechatronic system was developed and used to simulate the running-in process of the EKG-15M crowd gearbox in Simulink. The developed test bench system has been successfully implemented at Joint Power Co., Ltd. (Moscow) and IZ-KARTEX named after P.G. Korobkov.

**Keywords**

mining machinery, mechatronics, shovel, gearbox, running-in, testing, simulation, control, system, test bench


**For citation**

Malafeev S.I., Malafeeva A.A., Konyashin V.I., Novgorodov A.A. Mechatronic system for running-in and testing of mechanical transmissions in mining shovels. *Mining Science and Technology (Russia)*. 2025;10(1):75–83. <https://doi.org/10.17073/2500-0632-2024-05-262>



## ЭНЕРГЕТИКА, АВТОМАТИЗАЦИЯ И ЭНЕРГОЭФФЕКТИВНОСТЬ

Научная статья

**Мехатронная система для обкатки и испытаний механических передач карьерных экскаваторов**С. И. Малафеев<sup>1,2</sup>  , А. А. Малафеева<sup>3</sup>  , В. И. Коняшин<sup>1</sup>  , А. А. Новгородов<sup>1</sup>  <sup>1</sup> ООО «Компания «Объединенная Энергия», г. Москва, Российская Федерация<sup>2</sup> Владимирский государственный университет имени А.Г. и Н.Г. Столетовых, г. Владимир, Российская Федерация<sup>3</sup> Российская академия народного хозяйства и государственной службы при Президенте Российской Федерации (Владимирский филиал), г. Владимир, Российская Федерация [simalafeev@gmail.com](mailto:simalafeev@gmail.com)**Аннотация**

Механические передачи подъемных и тяговых лебедок, а также механизмы напора карьерных экскаваторов находятся под действием наибольших знакопеременных ударных нагрузок. Поэтому к качеству изготовления механических передач предъявляются повышенные требования. Процесс управления жизненным циклом редукторов включает обкатку и испытания нового изделия на предприятии, диагностику и контроль в процессе эксплуатации. Стенды для этих целей должны обеспечивать максимальное соответствие режима испытаний условиям эксплуатации механической передачи. Разработанный стенд предназначен для обкатки (приработки сопряженных соединений) и контроля качества изготовления и сборки редукторов лебедок подъема и напора электрических карьерных экскаваторов ЭКГ-8ус, ЭКГ-10, ЭКГ-12К, ЭКГ-15М, ЭКГ-18, ЭКГ-20КМ, ЭКГ-32Р в условиях приемо-сдаточных испытаний. В стенде применены двигатели экскаваторные постоянного тока мощностью 350 кВт (приводные машины) и мощностью 560 кВт (нагружающая машина). В качестве мультипликатора использован редуктор лебедки подъема экскаватора ЭКГ-15М. Два промежуточных вала объединены промежуточной вставкой. Нагружающий двигатель соединен с одним валом. Для управления двигателями использованы типовые транзисторные преобразователи постоянного тока с широтно-импульсным регулированием, применяемые на экскаваторах с главными приводами постоянного тока. Обкатка и испытания редукторов проводятся методом взаимной нагрузки. Программное обеспечение испытательного стенда реализовано на основе информационно-диагностической системы Пульсар-7. При этом обеспечиваются следующие режимы работы: 1. Интерактивное управление компонентами стенда в ручном режиме. В этом режиме оператор может проверять функционирование компонентов стенда, выполнять их настройку. 2. Автоматическое управление процессом обкатки испытаний. Подпрограммы из имеющейся библиотеки обеспечивают формирование требуемых в соответствии с видом испытания последовательностей управляющих команд. Предусмотрены режимы обкатки без нагрузки, с постоянной нагрузкой, переменными нагрузкой и угловой скоростью, воспроизведения цикла экскавации. В процессе испытания производится автоматическое создание протокола по испытываемому изделию. 3. Формирование протоколов испытания. Оператор может просматривать и выводить на печать любые ранее сформированные протоколы. 4. Настройка программы и вспомогательные функции, в том числе справочная подсистема. На основе составленного математического описания мехатронных систем выполнено исследование процессов при обкатке редуктора напора ЭКГ-15Мс помощью Simulink. Разработанный стенд реализован в ООО Компания «Объединенная Энергия» и внедрен в ООО «ИЗ-КАРТЭКС имени П.Г. Коробкова».

**Ключевые слова**

горные машины, мехатроника, экскаватор, редуктор, обкатка, испытание, моделирование, регулирование, система, стенд

**Для цитирования**

Malafeev S. I., Malafeeva A. A., Konyashin V. I., Novgorodov A. A. Mechatronic system for running-in and testing of mechanical transmissions in mining shovels. *Mining Science and Technology (Russia)*. 2025;10(1):75–83. <https://doi.org/10.17073/2500-0632-2024-05-262>

**Introduction**

The mechanical transmissions of mining shovels and other mining machinery are critical components that significantly affect the reliability and operational efficiency of these machines [1, 2]. The hoist and drag winch gearboxes, as well as the crowd mechanisms, are subjected to highly variable cyclic shock loads during operation. These loads accelerate wear and reduce the service life of gearboxes. Consequently, stringent man-

ufacturing quality requirements are applied to their transmission components [3]. The lifecycle management of such gearboxes includes running-in and acceptance testing at the manufacturer's site, followed by diagnostics and condition monitoring during field operation [4, 5]. The integration of digital twin technology offers promising prospects, enabling the creation of digital gearbox models and their verification during running-in and acceptance testing [6].



The running-in process serves several purposes, including initial wear-in of mating surfaces, detection of assembly defects, and adjustment of components and assemblies, all of which contribute to extending the service life of the gearboxes [7, 8]. Running-in plays a key role in ensuring stable performance of mechanical systems, acting as a transitional process that involves complex interactions between friction, lubrication, surface roughness, plastic deformation, and wear [9, 10]. During this process, key tribological parameters (such as surface roughness, surface texture, friction coefficient, and wear rate) evolve until they stabilize under steady-state conditions [11, 12]. The final tribological state achieved during running-in largely determines the long-term performance characteristics of the gearbox [13]. The running-in process is developed individually for each gearbox type, involving a stepwise sequence of modes, from no-load operation to operation under nominal load, covering various speeds and rotational directions [14, 15]. The duration of running-in and testing depends on the specific design and operating conditions of the gearbox.

Test benches designed for running-in and testing must be capable of simulating all required test modes, automating test execution and data processing, and minimizing energy consumption [14, 15]. Test benches must closely replicate the actual operating conditions of the mechanical transmission during testing. Currently, the mutual loading method using electric machines is the most widely used approach for gearbox testing, where the shafts are connected via a gearbox and a torque multiplier multiplier [16]. This method uses identical drive motors and mechanical transmissions (gearbox and multiplier). For manufacturers producing a variety of gearbox designs, the ability to test units with different gear ratios is particularly important <sup>1</sup>.

This paper examines the design and implementation of an automated system for the running-in and testing of hoist and crowd winch gearboxes for mining shovels, developed by Joint Power Co., Ltd. (Moscow).

### Objective and tasks

*The objective of this study* is to analyze, design, and model test bench equipment for the running-in and testing of mechanical transmissions used in the main drives of electric mining shovels.

#### Key tasks:

1) to develop of functional diagrams for test benches for the running-in of hoist and crowd winch gearboxes in mining shovels, ensuring that the

benches are effective for testing mechanical transmissions of different excavator models with various gear ratios;

2) to develop and analyze the mathematical models describing the mechatronic systems of test benches for the running-in of gearboxes in both single-motor and dual-motor drives, using the mutual loading method;

3) to study the mechatronic system models of the test benches using MATLAB-Simulink;

4) to implement the mechatronic system for the test bench at IZ-KARTEX named after P.G. Korobkov.

### 1. Functional diagram of the system

The functional diagram of the mechatronic system for the running-in of dual-motor hoist drive gearboxes is shown in Fig. 1. The mechatronic system is powered by the 0.4 kV plant power supply network through the circuit breaker QF, power transformer T, and diode rectifier R. A capacitor C is installed in the DC link. The tested gearbox is driven by two DC motors — M1 and M2. The low-speed shaft of the gearbox G is connected to the shaft of the loading motor M3 via a torque multiplier MP. The motors M1, M2, and M3 are controlled by regulating the voltage applied to their armature windings using transistor bridge converters – TC1, TC2, and TC3, respectively. The field windings of the motors are connected in series and powered by the output of the transistor converter TCO. A transistor switch TS and ballast resistor R are used to dissipate excess energy in the DC link in case of emergency. The torque on the motor shafts is measured using torque couplings MM1 and MM2. The testing process is controlled by a dedicated operator PC, with all test programs and results stored on a server.

The test bench uses power equipment and an information and control system originally developed for mining shovels equipped with DC main drives and transistor power converters [17].

The running-in and testing of the gearboxes is carried out using the mutual loading method. The power inputs of the transistor converters TC1, TC2, and TC3 are connected in parallel to the DC link. The field windings of the electric machines are supplied by the output of TCO, which operates in current stabilization mode. Motors M1 and M2 operate in motor mode, controlled by a dual-loop control system, consisting of an inner current loop and an outer voltage loop [17, 18]. To stabilize the angular speed, positive feedback from the armature current is used. In this configuration, one motor acts as the master, while the other follows as the slave. Motor M3 operates in generator mode, maintaining constant armature current.

<sup>1</sup> Malafeev S.I. Russian Patent No. 2779712. IPC G01R31/34. Test Bench for DC Electric Machines and Mechanical Transmissions. Published on September 12, 2022. Bulletin No. 26.

The power take-off points from the DC link for all drives are unified, meaning that the power drawn from the network equals the losses in the electric machines and the transistor converters. For the running-in and testing of crowd winch gearboxes, only a single drive motor is used – for example, M1.

The test bench configuration shown in Fig. 1 allows for the running-in and testing of gearboxes with different gear ratios using a single stationary torque multiplier.

## 2. Analysis of the test bench mechatronic system

The structural diagram of the mechatronic system for the test bench is shown in Fig. 2. The designations used in the diagram are as follows: TC1, TC2, TC3 – transistor converters for motor control; ACS1, ACS2, ACS3 – armature current sensors of the DC motors; CR1, CR2, CR3 – current regulators; VR – voltage regulator; CL – current limiter unit; IS1, IS2 – intensity setpoints;  $H_{c1}(s)$ ,  $H_{c2}(s)$ ,  $H_{c3}(s)$  – transfer functions of the transistor converters controlling DC motors M1, M2, M3, respectively;  $H_{cur1}(s)$ ,  $H_{cur2}(s)$ ,  $H_{cur3}(s)$  – transfer functions of the current regulators;  $H_v(s)$  – transfer function of the voltage regulator in the speed control system;  $k_{cur}$  – gain of the corrective positive current feedback;  $H_f(s)$  – transfer function of the filter in the voltage control loop;  $r_1$ ,  $r_2$ ,  $r_3$  – armature winding resistances of the DC motors;  $L_1$ ,  $L_2$ ,  $L_3$  – armature winding inductances of the DC motors;  $c_1$ ,  $c_2$ ,  $c_3$  – motor constants of the DC motors;  $k_{i1}$ ,  $k_{i2}$ ,  $k_{i3}$  – gains of the current sensors DT1, DT2, DT3, respectively;  $k_u$  – gain of the voltage sensor;  $J_1$  – equivalent moment of iner-

tia of the rotating masses referred to the drive motor shaft;  $J_2$  – equivalent moment of inertia referred to the loading motor shaft;  $k_{m1}$  and  $k_{m2}$  – transmission ratios of the gearbox and the torque multiplier, respectively;  $c_{12}$  – stiffness of the mechanical connection;  $k_{v1}$ ,  $k_{v2}$  – viscous friction coefficients simulating losses in the mechanical transmissions;  $U_1$ ,  $U_2$ ,  $U_3$  – armature voltages of the electric machines;  $i_1$ ,  $i_2$ ,  $i_3$  – armature currents of the electric machines;  $\Omega_1$  and  $\Omega_2$  – angular speeds of the drive motors and the loading machine, respectively;  $\varphi_1$  and  $\varphi_2$  – rotation angles of the gearbox output shaft and the torque multiplier input shaft;  $T_1$  and  $T_2$  – electromagnetic torques of the first and second drive motors;  $T$  – torque at the gearbox output shaft;  $u_{ss}$  – speed setpoint voltage for the drive motors;  $u_{cs}$  – load torque setpoint voltage (armature current setpoint for the loading motor). For the transistor converters, the following applies:  $H_{c1}(s) = k_{c1}$ ,  $H_{c2}(s) = k_{c2}$ ,  $H_{c3}(s) = k_{c3}$ , where  $k_{c1}$ ,  $k_{c2}$ ,  $k_{c3}$  are the gains of the corresponding converters. The control system uses a proportional voltage regulator with a gain of  $k_v$ , i.e.,  $H_v(s) = k_v$ , and a first-order low-pass filter

$$H_f(s) = \frac{k_f}{k_f s + 1},$$

where  $k_f$  и  $T_f$  are the filter gain and time constant, respectively. Proportional-integral controllers are used as current regulators.

In the dual-motor drive, identical electric machines are used, so  $H_{p1}(s) \approx H_{p2}(s)$ ;  $H_{i1}(s) \approx H_{i2}(s)$ ;  $r_1 \approx r_2$ ;  $L_1 \approx L_2$ ;  $c_1 \approx c_2$ ;  $k_{i1} \approx k_{i2}$ . For crowd gearbox testing, only one drive motor is used (see Fig. 3).

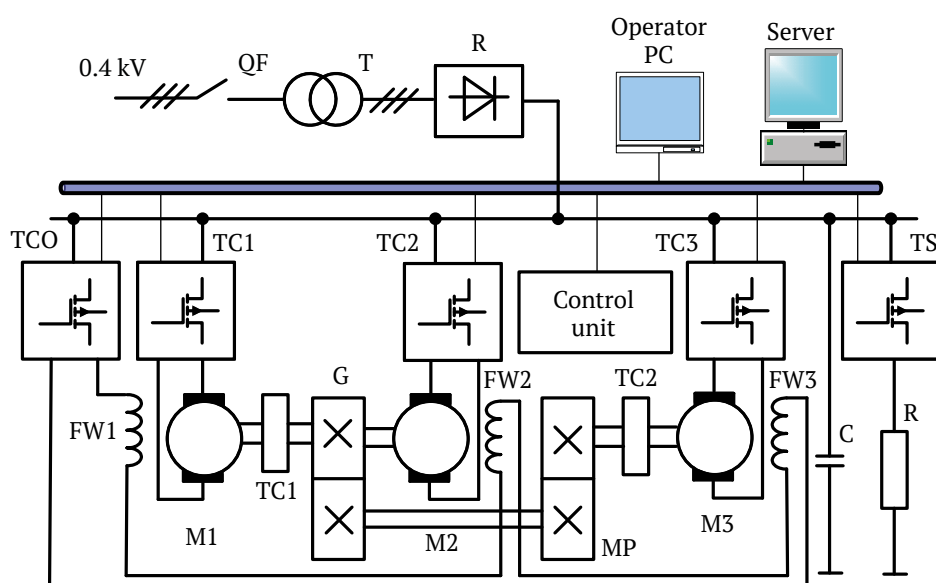


**Fig. 1.** Functional diagram of the mechatronic system for running-in hoist gearboxes: QF – circuit breaker; T1 – power transformer; R – rectifier; TC0, TC1, ..., TC3 – transistor bridge converters; TS – transistor switch; C – DC link capacitor; BR – ballast resistor; M1 – loading DC motor; M2, M3 – drive DC motors; FW1, ..., FW3 – field windings of motors M1, M2, M3, respectively; MP – torque multiplier; G – tested gearbox; TC1, TC2 – torque measuring couplings

The power drawn from the supply network under steady-state running-in conditions equals the total power losses in the powertrain components. For the system shown in Fig. 2, the total power drawn from the supply can be expressed as:

$$P_c = \Delta P_t + \Delta P_r + P_c + \sum_{i=1}^3 \Delta P_{mi} + \sum_{i=1}^4 \Delta P_{tci} + \Delta P_g + \Delta P_{mp} + \sum_{i=1}^3 P_{fwi},$$

where  $\Delta P_t$  – transformer losses;  $\Delta P_r$  – rectifier losses;  $P_c$  – losses in the DC link capacitor;

$$\sum_{i=1}^3 \Delta P_{mi} -$$

total losses in the electric machines;

$$\sum_{i=1}^4 \Delta P_{tci} -$$

total losses in the transistor converters;  $\Delta P_g$  – gearbox losses;  $\Delta P_{mp}$  – torque multiplier losses;

$$\sum_{i=1}^3 \Delta P_{fwi} -$$

active power consumed by the field windings of the electric machines.

The losses in each component can be approximately determined using their efficiency values under the corresponding operating modes.

### 3. Mechatronic system modeling

The system model was studied using Simulink during the running-in process of the EKG-15M crowd winch gearbox. The simulation was performed for a system equipped with DC motors M1 (DPE350D-2) and M3 (DPE560D-2). The gear ratio of the crowd gearbox is 92.59, and the transmission ratio of the torque multiplier is 31.359.

Figs. 4 and 5 show the results of the simulation for the running-in process of the EKG-15M crowd gearbox (with a gear ratio of 92.59). Fig. 4 presents oscillograms of system processes at different angular speeds

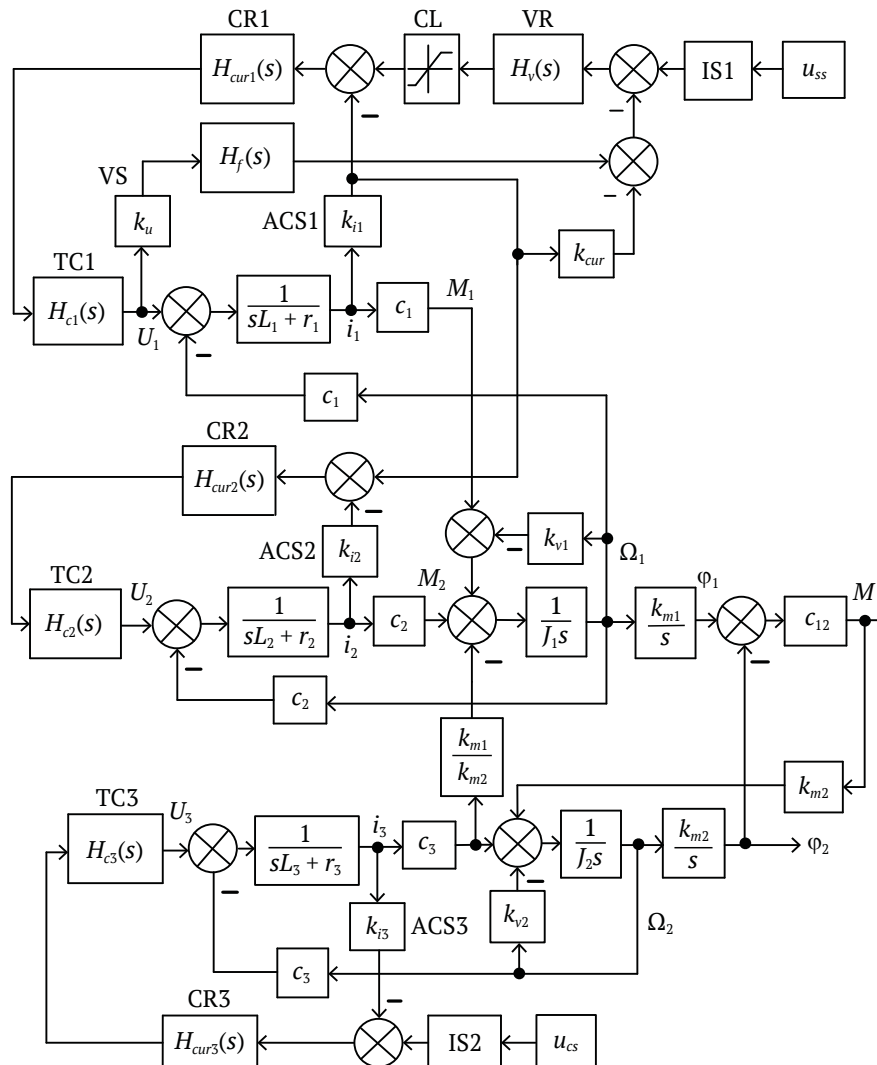


Fig. 2. Structural diagram of the mechatronic system for running-in the hoist winch gearbox

and load torques. During the time interval from 0 to 40 seconds, the drive accelerates to an angular speed of 20 rad/s, with a load torque of 1.6 kN·m applied to the low-speed shaft. At 40 seconds, the angular speed increases to 30 rad/s, while the load torque at the output shaft remains 1.6 kN·m. At 80 seconds, the angular speed of the drive motor increases to 50 rad/s. At 120 seconds, the load torque increases to 9 kN·m, and at 160 seconds, the load torque further rises to 16.5 kN·m.

Fig. 5 shows oscillograms of the mechatronic system's processes during harmonic variation of the drive motor's angular speed, with a period of 62.8 seconds. Throughout the process, the loading machine maintains a constant torque, with its armature current set at 100 A. During the first half of the cycle, the load torque acts as a braking force. In the second half, it aligns with the torque produced by the drive motor.

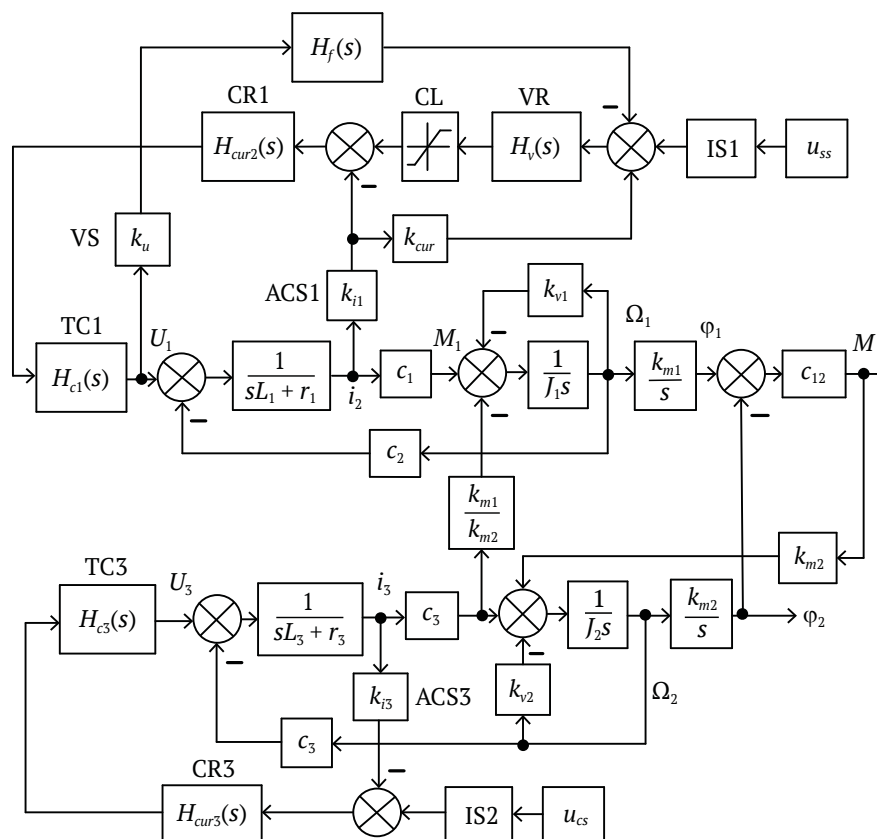


Fig. 3. Structural diagram of the mechatronic system for running-in the crowd winch gearbox

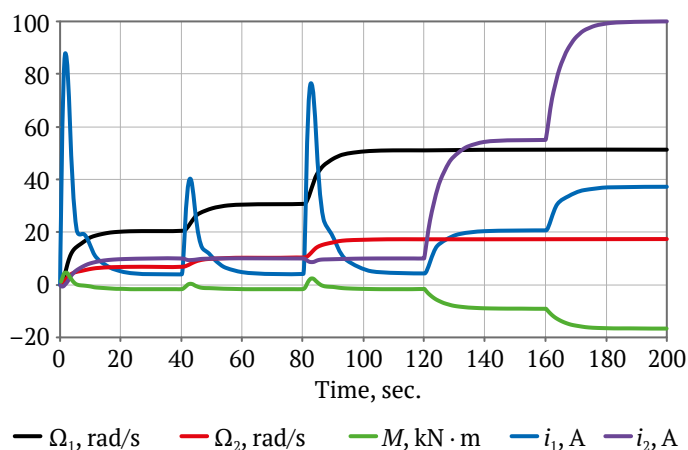


Fig 4. Oscillograms recorded during the running-in of the crowd winch gearbox at different angular speeds and load torques

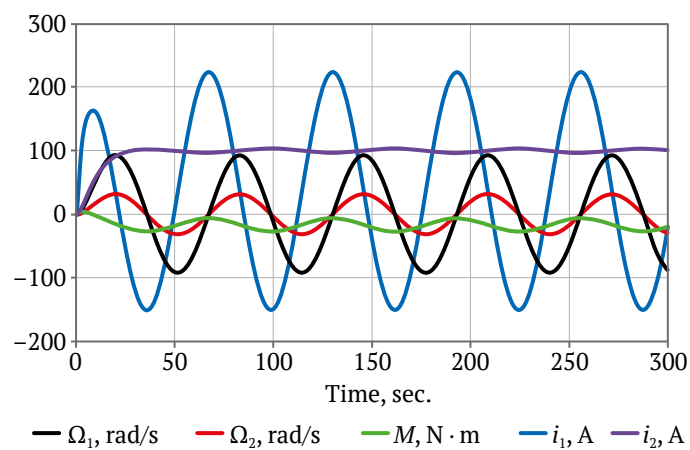


Fig. 5. Oscillograms recorded during the running-in of the crowd winch gearbox under harmonic variation of the drive motor's angular speed and constant load torque

#### 4. Practical implementation of the test bench

The developed test bench is designed for the running-in process (initial wear-in of mating surfaces) and quality control testing of hoist and crowd winch gearboxes used in electric mining shovels of the following models: EKG-8US, EKG-10, EKG-12K, EKG-15M, EKG-18, EKG-20KM, and EKG-32R. These operations are performed as part of the acceptance testing procedure. An external view of the test bench is shown in Fig. 6.

The test bench is equipped with DC excavator motors, including two 350 kW drive motors and one 560 kW loading motor. The hoist winch gearbox from the EKG-15M excavator serves as the torque multiplier, with a gear ratio of 31.359. The system includes two intermediate shafts, which are linked by an intermediate coupling, and the loading motor is connected to one of these shafts. Motor control is handled by standard DC transistor converters with pulse-width modulation (PWM) — the same type of converters used in mining shovels with DC main drives [17]. Drive motor speed range: 0 to 1000 rpm. Load torque range at the loading motor output shaft: 0 to 7.5 kN·m.

The test bench software is based on the Pulsar-7 information and diagnostics system [17], supporting the following operating modes:

**Interactive manual control of test bench components.** In manual mode, the operator can check the functionality of the bench components and perform calibration. The software automatically detects the

status of the circuit breakers (indicating whether they have tripped) and verifies the readiness of the power converters and monitoring instruments.

**Automatic control of the running-in and testing process.** Pre-programmed sequences from the built-in test library generate the required control commands for each specific test type. The software supports various modes, including no-load running-in, running-in under constant load, running-in with variable load and angular speed, and excavation cycle simulation [18]. The operator selects the desired mode via the computer interface. The current values of key monitored parameters — including the rotational speeds of the motors and gearbox shafts, torque, and motor currents — are displayed on the monitor in real time. During testing, the system automatically generates a test report for the tested unit, with data recorded to the hard disk in real time. The software also supports synchronized operation with external instruments used to monitor vibration levels, bearing temperatures, and kinematic deviations in gear meshing, among other parameters.

**Test report generation.** The operator can view and print any previously generated test reports. Each report includes: a text section listing the measurement results required by the test methodology for each specified mode; a graphical section, where the operator can select parameters to display their time-dependent trends recorded during the test.

Software configuration and auxiliary functions, including an integrated help system.



Fig. 6. Test bench installed in the workshop



### Conclusions and recommendations

1. The voltage stabilization algorithms under consideration rely on an analytical solution to the problem of power flow determination in the electrical system. Running-in and testing of mining shovel transmissions improve manufacturing quality and ensure that product characteristics meet the required specifications. Gearbox running-in enables the initial wear-in of mating surfaces, identifies assembly and installation defects, and allows for the adjustment of assembly units and components. The running-in mode is developed individually for each gearbox type. The process is carried out in several stages, ranging from no-load operation to operation under nominal load, at various speeds and directions of rotation.

2. The developed equipment package ensures the implementation of all required test modes, automation of both testing processes and data processing, while also minimizing energy consumption. The test bench equipment allows for the running-in and testing of gearboxes with various gear ratios using a single setup: for hoist winch gearboxes, gear ratios range from 25.43 (EKG-10) to 82.56 (EKG-32); for crowd

winch gearboxes, gear ratios range from 60 (EKG-10) to 90.6 (EKG-20K). Drive motor speed control range: 0 to 1000 rpm. Load torque control range at the output shaft of the loading motor: 0 to 7.5 kN·m. Test bench power supply voltage: 380 V; frequency: 50 Hz. Three-phase supply with grounded neutral. Power consumption: 400 kW.

3. The mutual loading method used for the running-in and testing process ensures efficient use of electrical energy by utilizing regenerated energy.

4. The test bench incorporates power equipment and the Pulsar-7 information and control system, both originally developed for mining shovels equipped with DC main drives and transistor power converters. The system supports both manual control of individual components and fully automated management of the running-in and testing processes.

5. The successful deployment and operation of the test bench at IZ-KARTEX named after P.G. Korobkov confirms its high technical performance. The electrical equipment and software are recommended for use in organizing transmission testing for heavy mining machinery of various types.

### References

1. Quan Z., Ge L., Wei Z., Li Y.W., Quan L. A survey of powertrain for energy-efficient heavy-duty machinery technologies. In: *Proceedings of the IEEE*. 2021;109(3):279–308. <https://doi.org/10.1109/jproc.2021.3051555>
2. Khoreshok A.A., Kudrevatykh A.V., Ashcheulov A.S. et al. Increasing life of pit dump truck motor-wheel gearboxes by introducing the monitoring of the actual technical condition. *Mining Science and Technology (Russia)*. 2021;6(4):267–276. (In Russ.) <https://doi.org/10.17073/2500-0632-2021-4-267-276>
3. Drygin M.Yu., Kuryshkin N.P. Increasing the quality of excavators' planetary reduction gearboxes on the basis of dimensional analysis and geometrical characteristics of tooth wheels. In: *Journal of Physics: Conference Series, Volume 944, XI International scientific and technical conference "Applied Mechanics and Dynamics Systems"*. 14–16 November 2017, Omsk, Russian Federation. <https://doi.org/10.1088/1742-6596/944/1/012030>
4. Mao Y., Tong J., Chin Z.Y. et al. Transmission error and vibration-based condition monitoring of gear wear with contaminated lubricant. *Wear*. 2023;523:2047–2060. <https://doi.org/10.1016/j.wear.2023.204760>
5. Gericke B.L., Sushko A.E., Gericke P.B., Efremenkova A.B. Digital technologies used in technical diagnostics, assessment of technical condition, maintenance and repair of mining machines and equipment. In: *Journal of Physics: Conference Series, Volume 2052, 3<sup>rd</sup> International Scientific and Practical Conference on Mathematical Modeling, Programming and Applied Mathematics (MMPAM 2021)*. 6–7 September 2021, Veliky Novgorod, Russia. <https://doi.org/10.1088/1742-6596/2052/1/012016>
6. Algin V.B., Ishin N.N. Reliability of technically complicated items in terms of "Industry 4.0". *Topical Issues of Mechanical Engineering*. 2017;6(6):43–54. (In Russ.)
7. Blau P.J. On the nature of running-in. *Tribology International*. 2005;38(11–12):1007–1012. <https://doi.org/10.1016/j.triboint.2005.07.020>
8. Jamaría J., Ammarullaha M.I., Afifa I.Y. et al. Running-in Analysis of Transmission Gear. *Tribology in Industry*. 2021;43(3):434–441. <https://doi.org/10.24874/ti.1092.04.21.08>
9. Voynov K.N. *Generalizations in tribology*. St. Petersburg: Publishing and Polygraphic Association of Higher Educational Institutions; 2024. 250 p. (In Russ.)
10. Kragelsky I.V., Kombarov V.S. Calculation of value of stable roughness after running-in (elastic contact). *Wear*. 1969;14(2):137–140.



11. Sjöberg S., Sosa M., Andersson M., Olofsson U. Analysis of efficiency of spur ground gears and the influence of running-in, *Tribology International*. 2016;93A:172–181. <https://doi.org/10.1016/j.triboint.2015.08.045>
12. Wang Q., Ma B., Liang Y. et al. Effects of operating conditions on the tribological behavior of a wet multi-disc clutch during the running-in process. *Tribology International*. 2023;179:108096. <https://doi.org/10.1016/j.triboint.2022.108096>
13. Khonsari M.M., Ghatrehsamani S., Akbarzadeh S. On the running-in nature of metallic tribo-components: A review. *Wear*. 2021;474–475:203871. <https://doi.org/10.1016/j.wear.2021.203871>
14. Ivanov V.P. Running-in of gears of mining machines. *Mining Mechanical Engineering and Machine-Building*. 2016;(2):55–59.
15. Streltsov V.V., Popov V.N., Karpenkov V.F. *Resource-saving accelerated running-in of repaired engines*. Moscow: Kolos; 1995. 175 p. (In Russ.)
16. Gervais G.K. *Industrial tests of electric machines*. Leningrad: Energoatomizdat; 1984. 408 p.
17. Malafeev S.I., Serebrennikov N.A. Increasing energy efficiency of mining excavators through upgrade of electrical equipment and control systems. *Ugol'*. 2018;(10):30–34. (In Russ.) <https://doi.org/10.18796/0041-5790-2018-10-30-34>
18. Malafeev S.I., Novgorodov A.A., Konyashin V.I. Bench tests of the quarry excavators main electric drives. In: *XI International Conference on Electrical Power Drive Systems (ICEPDS)*. Saint Petersburg, Russia, October 04–07, 2020. <https://doi.org/10.1109/icepds47235.2020.9249257>

#### Information about the authors

**Sergey I. Malafeev** – Dr. Sci. (Eng.), Professor of the Department of Computer Engineering and Control Systems, Vladimir State University named after Alexander and Nikolay Stoletovs, Vladimir, Russian Federation; Chief Scientific Officer, Joint Power Co., Ltd., Moscow, Russian Federation; ORCID [0000-0002-7691-3442](https://orcid.org/0000-0002-7691-3442); e-mail [simalafeev@gmail.com](mailto:simalafeev@gmail.com)

**Alevtina A. Malafeeva** – Dr. Sci. (Eng.), Professor of the Department of Information Technology, Russian Presidential Academy of National Economy and Public Administration (Vladimir Branch), Vladimir, Russian Federation; ORCID [0009-0000-3141-874X](https://orcid.org/0009-0000-3141-874X), Scopus ID [26422368500](https://scopus.org/0000-0000-3141-874X); e-mail [amalafeeva@rambler.ru](mailto:amalafeeva@rambler.ru)

**Vladimir I. Konyashin** – Cand. Sci. (Eng.), Senior Researcher at the Innovation Department, Joint Power Co., Ltd., Moscow, Russian Federation; ORCID [0009-0007-7183-0780](https://orcid.org/0009-0007-7183-0780), Scopus ID [56582464300](https://scopus.org/0009-0007-7183-0780); e-mail [solytonik@yandex.ru](mailto:solytonik@yandex.ru)

**Andrey A. Novgorodov** – Head of the Mechatronic Systems Design Department, Joint Power Co., Ltd., Moscow, Russian Federation; ORCID [0009-0000-7557-0145](https://orcid.org/0009-0000-7557-0145), Scopus ID [57192383884](https://scopus.org/0009-0000-7557-0145); e-mail [novgorodov@jpc.ru](mailto:novgorodov@jpc.ru)

**Received** 13.05.2024

**Revised** 30.08.2024

**Accepted** 05.09.2024



## POWER ENGINEERING, AUTOMATION, AND ENERGY PERFORMANCE


Research paper

<https://doi.org/10.17073/2500-0632-2024-10-362>

УДК 622.44:62-83

**Assessment of energy efficiency improvement strategies for ventilation and hoisting systems during the reconstruction of the Molibden mine**R. V. Klyuev   

Moscow Polytechnic University, Moscow, Russian Federation

 [kluev-roman@rambler.ru](mailto:kluev-roman@rambler.ru)**Abstract**

The economic efficiency of high-performance mining enterprises largely depends on the parameters and operating modes of energy-intensive equipment. Ventilation fans and hoisting machines are traditionally considered among the most energy-intensive equipment. This study focuses on analyzing the operation of the main ventilation fans and hoisting equipment at the Molibden mine and on developing measures to ensure optimal operating conditions aimed at improving energy efficiency and reducing operating costs. The paper presents methods for evaluating the efficiency of mine ventilation systems, including analytical approaches applied in system design and performance assessment. The study draws on operational data from the Molibden mine. The analysis revealed that the ventilation fans were operating inefficiently, with excessive specific energy consumption. Consequently, the replacement of electric motors is proposed to reduce energy use and operational expenditures. Calculations indicate that the expected economic benefit from replacing the ventilation fan motors at the Molibden mine amounts to 4.9 million rubles per year. Based on an analysis of the hoisting equipment characteristics, a required motor power assessment was performed. The study demonstrates that the use of modern multi-rope hoisting systems with balanced designs is essential for improving operational efficiency. Measures to optimize equipment utilization are proposed, which would reduce the specific energy consumption associated with ore extraction. An analysis of eight years of data revealed an inverse correlation between ore output and specific energy use: a 10–15% increase in productivity results in a 2–5% reduction in specific energy consumption. Avoiding periods of low equipment utilization and implementing automated control systems can significantly enhance overall system efficiency. The findings of this study may be applicable to mining enterprises operating under similar conditions, particularly those engaged in deep-level mining.

**Keywords**

mine, energy efficiency, ventilation fans, mine ventilation systems, hoisting machines, electric motor, ore extraction, specific energy consumption, economic benefit

**For citation**

Klyuev R.V. Assessment of energy efficiency improvement strategies for ventilation and hoisting systems during the reconstruction of the Molibden mine. *Mining Science and Technology (Russia)*. 2025;10(1):84–94. <https://doi.org/10.17073/2500-0632-2024-10-362>

**ЭНЕРГЕТИКА, АВТОМАТИЗАЦИЯ И ЭНЕРГОЭФФЕКТИВНОСТЬ**

Научная статья

**Обоснование решений по повышению энергоэффективности  
вентиляторных установок и подъемных машин  
в условиях реконструкции рудника «Молибден»**Р. В. Ключев   

Московский политехнический университет, г. Москва, Российская Федерация

 [kluev-roman@rambler.ru](mailto:kluev-roman@rambler.ru)**Аннотация**

Экономическая эффективность высокопроизводительных горных предприятий во многом определяется параметрами и режимами работы энергоёмких машин. Традиционно вентиляторные установки и подъёмные машины считаются одними из самых энергоёмких. Исследования направлены на анализ работы вентиляторных установок главного проветривания и подъёмных установок рудника, а также на разработку мероприятий по обеспечению рациональных режимов их работы с целью повышения



энергоэффективности и снижения эксплуатационных затрат. В работе описаны методы расчета систем проветривания, включая аналитические, которые используются для проектирования и анализа режимов работы систем проветривания. В исследовании использованы данные о режимах работы систем рудника «Молибден». Выявлено, что вентиляторные установки работают неэффективно, с завышенным удельным расходом электроэнергии. В связи с этим предложены мероприятия по замене электродвигателей, что позволит снизить энергопотребление и эксплуатационные затраты. Расчеты показывают, что экономический эффект от замены двигателей вентиляторной установки на руднике «Молибден» составит 4,9 млн руб. в год. На основе анализа характеристик подъемных установок рудника проведен проверочный расчет мощности электродвигателей подъемных машин. Отмечено, что для повышения эффективности подъемных систем необходимо использовать современные многоканатные установки с уравновешенной конструкцией. Предложены меры по загрузке технологического оборудования, что позволит снизить удельный расход электроэнергии на добычу руды. Анализ данных за 8 лет показал обратную корреляцию между объемом добычи руды и удельным расходом электроэнергии. Увеличение производительности на 10–15 % снижает удельный расход энергии на 2–5 %. Исключение периодов низкой загрузки оборудования и внедрение автоматизированных систем управления позволяют повысить эффективность установок в целом. Результаты исследования могут быть использованы для горнодобывающих предприятий с аналогичными условиями эксплуатации, особенно при глубокой разработке месторождений.

#### Ключевые слова

рудник, энергоэффективность, вентиляторные установки, системы проветривания, подъемные машины, электродвигатель, добыча руды, удельный расход электроэнергии, экономический эффект

#### Для цитирования

Klyuev R.V. Assessment of energy efficiency improvement strategies for ventilation and hoisting systems during the reconstruction of the Molibden mine. *Mining Science and Technology (Russia)*. 2025;10(1):84–94. <https://doi.org/10.17073/2500-0632-2024-10-362>

## Introduction

Mine ventilation systems are essential engineering infrastructures that ensure safe and efficient working conditions in underground environments [1]. Unlike open-pit operations, where natural airflow plays a key role, underground mines are confined spaces with limited air exchange and an increased risk of emergencies [2, 3]. Ventilation systems are especially critical at gassy coal mines, where methane emissions into mine workings are difficult to predict [4, 5]. These emissions pose serious challenges for maintaining stable airflow, as well as for removing hazardous gases, dust, and excess heat generated by mining operations [6–8], particularly in relation to production output and the geometry of mine workings [9].

As the mining industry advances, it becomes increasingly important to assess the risk of accidents, develop scientifically sound methods for evaluating mine aerological hazards [1, 3], and implement modern tools and algorithms for setting appropriate ventilation modes in underground operations [10–12]. The complexity and diversity of system components call for integrated solutions that ensure the core functions of mine ventilation systems [13]. At the same time, engineering decisions must also reflect energy and cost efficiency, both of which play a decisive role in the overall performance of mining operations [14–16].

Ventilation fans – often with installed capacities of 5–7 MW at large-scale mines – and hoisting ma-

chines are among the most energy-intensive equipment in the industry. Their performance directly affects overall productivity, as they are critical components of the mine's material handling and safety infrastructure [17]. Modern hoisting systems are typically equipped with variable-speed electric drives to ensure reliable and efficient operation. Improving energy efficiency and optimizing the operation of both ventilation and hoisting systems therefore remains a pressing priority.

**Research object.** This study focuses on the Tyrnyauz Tungsten-Molybdenum Plant (TTMP), which is scheduled to resume operations in 2025.

**The aim of the study** is to analyze the performance of the main mine ventilation fans and hoisting machines and to develop strategies for optimizing their operation.

**Methods.** Evaluating the operating modes of mine ventilation systems and fans, as well as the performance of hoisting machines and their electric drives, is a complex engineering task. It requires a combination of theoretical and empirical approaches, the analysis of experimental data, and the use of modern computational techniques. The proposed optimization strategies for ventilation and hoisting systems are based on a techno-economic assessment. The central idea of the study is to determine the appropriate power ratings for the electric drives used in the main ventilation and hoisting systems at the reconstructed mine, with the goal of improving energy efficiency.



### Existing ventilation system at the Molibden mine

The Molibden mine is divided into two sections, each with an independent ventilation layout and equipment: the North-Western section and Central Shafts No. 1 and No. 2. Ventilation at the mine is provided by three types of axial-flow fans: VOKD-3.0, VOKD-2.4, and VOD-21. The VOKD-3.0 and VOKD-2.4 models are designed for main ventilation in large underground mines and shafts. Both are based on the TsAGN-K-06 aerodynamic design and have a standardized construction. Airflow is periodically adjusted by turning the impeller blades, while fine-tuning is achieved through intermediate guide vanes. The synchronous motors are excited using thyristor-based excitation systems equipped with reversing devices. The VOD series consists of reversible axial fans in-

tended to replace the older VOK and VOKD models. These fans are built on the K-84 aerodynamic design. Airflow reversal is achieved by changing the direction of the impeller's rotation, while the intermediate guide vanes are fixed at an angle of 104° relative to the plane of the impeller's rotation.

### Inspection and analysis of the main ventilation fans at the Molibden mine of the Tyrnyauz Tungsten-Molybdenum Plant

The consolidated results of the inspection and performance analysis of the main ventilation fans (MVF) provide a comprehensive overview of their operation. Table 1 presents key parameters describing the performance of the ventilation fans used in the mine's ventilation system.

Table 1

Key performance parameters of main ventilation fans at the Molibden mine

No.	Parameter	Level 4 MVF-4	Level 4 MVF-1	Level 4 MVF-4a	Level 9 MVF-3	Level 6 MVF-6
1	Fan type	ВОКД-3,0	ВОКД-2,4	ВОД-21	ВОД-21	ВОКД-3,0
2	Impeller diameter, m	3	2.4	2.1	2.1	3.0
3	Impeller speed, rpm	600	735	750	750	600
4	Impeller peripheral speed, m/s	94.2	92.2	82.4	82.4	94.2
5	Airflow through the fan, m <sup>3</sup> /s	90.4	64.7	56.0	76.0	96.7
6	Air delivered to the mine, m <sup>3</sup> /s	73.7	47.9	42.7	61.3	91.4
7	Air losses in fan units, m <sup>3</sup> /s	16.7	16.8	13.3	14.9	5.3
	Air losses, % of fan airflow	18.5	25.9	23.8	19.6	5.5
8	Total pressure generated by fan, mm H <sub>2</sub> O	111.3	29.2	16.4	9.6	191.4
9	Total mine pressure drop, mm H <sub>2</sub> O	90.7	21.0	16.4	10.0	0.9
10	Natural draught pressure, mm H <sub>2</sub> O	1.2	1.5	–	1.4	2.3
11	Total mine depression, mm H <sub>2</sub> O	91.9	22.5	16.4	11.4	3.2
12	Acoustic fluidity of the fan network, kg·s/m <sup>5</sup>	1.0	0.37	0.29	0.14	6.75
13	Resistance of sealing structures near the fan unit, кПа	0.32	0.074	0.093	0.032	1.6
	normal value, кПа	1.39	0.9	0.73	0.24	–
14	Mine resistance, кПа	0.0169	0.0114	0.009	0.0029	0.0218
15	Total resistance on fan, кПа	0.0138	0.0085	0.0052	–	0.02
16	Mine equivalent opening, m <sup>2</sup>	2.9	3.6	4.0	7.0	2.7
17	Total equivalent opening for fan, m <sup>2</sup>	3.3	4.2	5.3	–	2.6
18	Fan motor type	СДВ-15-64-10У3	А-13-42-8	СД-2-85-47-8У4	СД-13-42-8	СДВВ-15-39-10
19	Rated power, kW	1250	400	500	500	800
20	Power consumed from grid, kW	426.7	210	130	150	360
21	Shaft power of the fan, kW	393.4	187	116.3	135.5	326.5
22	Static efficiency of the fan: Based on electrical data weighted average	0.25 0.7	0.09 0.7	0.08 0.72	0.05 0.72	0.55 0.7
23	Specific power consumption from the grid, kW/m <sup>3</sup> : actual standard	5.79 1.86	4.74 0.48	3.04 0.25	2.45 0.15	3.94 3.13



End of Table 1

No.	Parameter	Level 4 MVF-4	Level 4 MVF-1	Level 4 MVF-4a	Level 9 MVF-3	Level 6 MVF-6
24	Specific power consumption at the shaft, kW/m <sup>3</sup> : actual standard	5.33 1.73	4.29 0.45	2.72 0.24	2.21 0.14	3.57 2.95
25	Excess power use above standard, kW	289.6	188.7	119.0	141.0	74.0
26	Fan annual operating time, h	8570	8570	8570	8570	8570
27	Annual excess energy consumption of the fan unit, thousand kWh	2481.9	1617.2	1208.4	634.2	634.2
28	Electricity cost, RUB/kWh	6.0	6.0	6.0	6.0	6.0
29	Annual cost of excess fan energy consumption, thousand RUB	14891.4	9702	6118.8	7250.4	3805.2

Table 2

Fan specifications in the mine ventilation system

No.	Parameter	Fan specification				
		VOKD-2.4		VOKD -3.0		VOD-21
1	Impeller diameter, m	2400		3000		2100
2	Impeller speed (range), rpm	600	750	500	600	750
3	Airflow rate (range) $Q$ , m <sup>3</sup> /s	17–133	22–167	42–220	52–265	25–123
4	Static pressure $H$ , kgf/m <sup>2</sup>	300–110	475–170	340–94	450–135	350–100
5	Power consumption range, kW	50–400	100–780	125–825	200–1420	100–430
6	Static efficiency $\eta_{fan}$	0.6–0.77		0.6–0.77		0.6–0.81
7	Rotor moment of inertia, kg·m <sup>2</sup>	4600		14200		2800
8	Fan weight (without motor), kg	18885		32000		11000
9	Installation dimensions, mm					
	length	18340		18535		13120
	height	3500		4480		3190
	width	3500		4480		3585

According to Table 1 (item 23), the main ventilation fans operate inefficiently in terms of energy use. Further investigation is required, along with the development of measures aimed at reducing the specific electricity consumption. As shown in Table 1 (items 19, 20, and 21), the installed motor capacities for MVF-4, MVF-1a, MVF-3, and MVF-6 significantly exceed the actual power drawn from the grid. A required motor power assessment should be carried out for the main ventilation fans.

#### Required motor power assessment for main ventilation fans

The motor power for ventilation fans is calculated using the following formula:

$$P = \frac{QH}{102\eta_{fan}}, \quad (1)$$

where  $Q$  is the airflow rate, m<sup>3</sup>/s;  $H$  is the static pressure, kg/m<sup>2</sup>;  $\eta_{fan}$  is the fan efficiency.

The motor is sized 10–15% above the calculated value to account for possible voltage drops:

$$P_{motor} = k_r P, \quad (2)$$

where  $k_r$  is the power reserve factor,  $k_r = 1.1–1.15$ .

The values of  $Q$ ,  $H$ , and  $\eta_{fan}$  are presented in Table 2.

Table 3 provides information on the motors installed in the main ventilation fans.

For MVF-1 (VOKD-2.4 fan), the required motor power assessment yielded the following results:

$$P = 170.7–463.9 \text{ kW}; P_{motor} = 510.3 \text{ kW}.$$

The installed motor is model A-13-42-8 with a rated power of 400 kW.

Similar calculations were performed for the other main ventilation fans, and the results are summarized in Table 4

The calculations showed that the installed motor power significantly exceeds the required power determined by the assessment (see Table 4). It would be reasonable to replace them with lower-power motors. The final decision should be based on a techno-economic analysis, elements of which are presented below.



Table 3

Main ventilation fan motor specifications

MVF ID	Fan model	Motor model	Quantity	Rated power, kW	Rated voltage, V	Rated current, A	Rated speed, rpm	Efficiency, %	Power factor cos φ
MVF-1	VOKD -2.4	A-13-42-8	1	400	6000	48	735	92.8	0.85
MVF -1a	VOD-21	SD-2-85-47-8U4	1	500	6000	57	750	95	0.9
MVF -3	VOD-21	SD-13-42-8	2	500	6000	57.1	750	94	0.9
MVF -4	VOKD -3.0	SDV-15-64-10U3	1	1250	6000	141	600	95.3	0.9
MVF -6	VOKD -3.0	SDVV-15-39-10	2	800	6000	90.5	600	94.3	0.8

Table 4

Required motor power assessment results

MVF ID	Motor power range, kW	Calculated motor power, kW	Rated motor power, kW	Suggested replacement motor
MVF-1	170.7–463.9	510.3	400	–
MVF -1a	142.9–201.0	221.1	500	SDV-15-34-12 motor, rated power: 400 kW
MVF -3	142.9–201.0	221.1	500	
MVF -4	382.3–584.5	642.9	1250	SDVV-15-39-10 motor, rated power: 800 kW
MVF -6	382.3–584.5	642.9	800	–

### Brief description and technical characteristics of hoisting systems at the Molibden mine

Two hoisting systems are currently in operation at the Molibden mine, located at the Kapitalnaya and North-West shafts. The Kapitalnaya shaft uses a simple single-rope hoisting system equipped with a drum-type hoist (model ShPM 4×36). However, such systems are characterized by low productivity, poor static balance, and other limitations. To improve the efficiency and reliability of hoisting operations at modern mining enterprises, multi-rope hoisting systems with balanced configurations are widely used. These provide higher productivity and reduce vibration during operation.

The primary function of the hoisting machine is to transport personnel and materials between levels 12 and 4 in a double-deck cage (type 2UKN-3.6-1). The technical specifications of the hoisting system at the Kapitalnaya shaft are presented in Table 5.

At the North-West shaft, a multi-rope hoisting machine of the MK-2.25×4 type is installed. The hoist features a single-motor drive operating on a generator–motor system. Its purpose is to transport personnel and materials between levels 4 and 1. The system is statically balanced by two flat-strand tail ropes. The hoist operates with a counterweight. The MK-2.25×4 hoisting machine is equipped with a gearbox. The gearbox is connected to the motor shaft via specially designed extended gear couplings. The technical specifications of the hoisting system are presented in Table 6.

Table 5

Technical specifications of the hoisting system at the Kapitalnaya shaft

No.	Parameter	Specification
1	Shaft depth to the lowest level, m	597
2	Shaft inclination angle, degrees	90
3	Hoisting machine type	ShPM 4×36
4	Hoisting height, m	600
5	Headframe height, m	18
6	Head sheave diameter, mm	3000
7	Number of service levels	8
8	Average hoisting speed, m/s	11
9	Hoisting cycles per day	14
10	Over-travel height, m	18
11	Cage type	2UKN-3.6-1
12	Rope type	PK-RO (6×36)+(7×71)
13	Gearbox type	Single-stage gearbox
14	Gear ratio	9,5
15	Number of drums	1 (welded from two segments)
16	Drum diameter, mm	4000
17	Drum width, mm	3500
18	Number of rope layers	1
19	Speed limiter type	RSO-5912
20	Static rope tension, N	175000
21	Static tension difference, N	117600
22	Conveyance mass, kg	4412
23	Maximum design load, kg	3700
24	Counterweight mass, kg	6250
25	Number of underground personnel per shift	276



Table 6

**Technical specifications of the hoisting system  
MK-2.25×4 at the North-West shaft**

No.	Parameter	Specification
1	Shaft depth to the lowest level, m	597
2	Shaft inclination angle, degrees	90
3	Hoisting machine type	MK 2.25×4
4	Hoisting height, m	300
5	Number of service levels	4
6	Average hoisting speed, m/s	9.5
7	Sheave diameter, mm	2250
8	Over-travel height, m	7
9	Hoisting cycles per hour	18.2
10	Cage type	TKP-4.5
11	Sheave lining	PP-45
12	Number of ropes	4
13	Rope diameter, mm	21.5
14	End load, t: material hoisting personnel hoisting	14.6 10
15	Counterweight mass, t	10
16	Number of tail ropes	2
17	Gearbox type	TsDN-130
18	Gear ratio	7.35
19	Conveyance mass, t	7.6
20	Payload capacity, t	7.0
21	Number of underground personnel per shift	276

**Required motor power assessment  
for the hoisting machine**

At the Kapitalnaya shaft, the following hoisting machines are in operation: a hoist equipped with a DA-170/29-12 electric motor rated at  $P = 670$  kW; a hoist equipped with a PE-172-5K electric motor rated at  $P = 630$  kW, operating on a generator–motor system. The estimated required power of the hoist drive motor at the Kapitalnaya shaft is determined by the following formula:

$$P_{cal} = \rho \frac{k}{\eta_g} P_{useful}, \quad (3)$$

where  $\rho$  is a coefficient determined from the dynamic operation characteristics, which depends on the moment of inertia of the hoist, its imbalance, and the velocity multiplier;  $k$  is a coefficient accounting for additional resistance-related load;  $\eta_g$  is the gearbox efficiency;  $P_{useful}$  is the useful power required for lifting a payload of mass  $m_{pl}$ , excluding system losses.

For a hoisting system with a single conveyance and a counterweight:

$$P_{useful} = \frac{(1 - \psi) g m_{pl} v_{avg}}{1000}, \quad (4)$$

where  $\psi$  is a coefficient accounting for the degree of mass balancing between the payload  $m_{pl}$  and the counterweight;  $v_{avg}$  is the average conveyance speed, m/s.

The coefficient  $\psi$  can be calculated using the following expression:

$$\psi = \frac{m_{cw} - m_{pl}}{m_c}, \quad (5)$$

where  $m_{cw}$  is the counterweight mass, kg;  $m_c$  is the conveyance mass, kg;  $m_{pl}$  is the payload mass, kg.

To account for potential voltage drops in the electrical network, the motor power is selected 10–15% higher than the calculated value:

$$P_{motor} = (1.1 - 1.15) P_{cal}. \quad (6)$$

For the hoisting system at the Kapitalnaya shaft (see Table 5):  $m_{cw} = 6250$  kg;  $m_c = 4412$  kg;  $m_{pl} = 3700$  kg.

The calculated results of the hoisting motor power assessment are presented in Table 7.

Table 7

**Results of required motor power assessment  
for the hoisting machine**

Parameter	Value
Coefficient $\psi$	0.497
Useful power $P_{useful}$ , kW	200.6
Estimated required power of the hoist drive motor $P_{cal}$ , kW	453.12
Coefficient $\rho$	1.6
Coefficient $k$	1.2
Gearbox efficiency $\eta_g$	0.88
Motor power $P_{motor}$ , kW	521.1

The calculated motor power satisfies the requirements of the motor currently installed on the hoisting machine at the Kapitalnaya shaft.

**Methodology for estimating  
the economic benefit of optimal utilization  
of processing equipment**

A study of the relationship between energy consumption and ore production volumes at the Molibden mine has shown that the specific energy consumption is strongly dependent on the mine's daily productivity. An analysis of data over an eight-year period revealed that the correlation between monthly ore production volumes and energy consumption ranged from 0.309 to 0.730. This indicates that an increase in ore output tends to result in a reduction in specific energy consumption.



An analysis of the ore production dataset showed a high degree of variability, as evidenced by a large standard deviation. Skewness and kurtosis were also observed, indicating an uneven distribution of values. Approximately 50% of the recorded values were significantly below the average, which suggests a predominance of periods with relatively low productivity. Therefore, reducing specific energy consumption at the Molibden mine requires limiting the duration of low-productivity operation and ensuring maximum equipment utilization.

To better understand how equipment utilization affects energy consumption, it is also necessary to analyze the structure of energy use at the mine. This involves disaggregating the total energy consumption into individual processes (such as drilling, blasting, transportation, crushing, and beneficiation) and examining the energy consumption of each technological stage. This analysis would allow for identifying the most energy-intensive operations and determining optimal operating modes for their implementation [18–20]. In addition, the potential for implementing automated production control systems should be considered. These systems can help maintain stable and high equipment utilization and minimize energy losses resulting from inefficient operating conditions.

Table 8 presents the results of the statistical analysis of the ore production dataset. Both the complete dataset (including all recorded values) and a truncated version (excluding values below the mean) were analyzed. This approach was used to evaluate the impact of excluding low-productivity periods on the overall statistical characteristics of the ore mass distribution.

The statistical parameters of the truncated data set were calculated using a theoretical method based

on the Gram–Charlier distribution. The initial moment  $S$  of the random variable  $Q \geq m_Q$  is defined as:

$$d_s = \frac{1}{P(Q \geq m_Q)} \int_{m_Q}^{\infty} Q^s f(Q) dQ, \quad (7)$$

where  $P(Q \geq m_Q)$  is the probability that the values of  $Q$  in the truncated data set exceed the mean value  $m_Q$  of the original data set:

$$P(Q \geq m_Q) = \int_{m_Q}^{\infty} f(Q) dQ; \quad (8)$$

and  $f(Q)$  is the theoretical differential probability density function of the random variable  $Q$ .

When the mean value of the extracted ore increases by

$$\Delta m_Q = m'_Q - m_Q \quad (9)$$

the specific energy consumption decreases by the amount  $\Delta\omega$ :

$$\Delta\omega = (a_2 m_Q + b_2) - (a_2 m'_Q + b_2) = a_2 \Delta m_Q, \quad (10)$$

where  $a_2$  and  $b_2$  are the coefficients of the regression equation:  $\omega = a_2 Q + b_2$  (see Table 1);

$$\Delta\omega\% = \frac{\Delta\omega}{m_\omega} \cdot 100\%, \quad (11)$$

and  $m_\omega$  is the mean specific energy consumption.

The annual energy savings due to improved equipment utilization is calculated as:

$$\Delta W = \Delta\omega m_Q \cdot 12. \quad (12)$$

Table 9 presents the results of the eight-year calculation.

The relationships between the mean extracted ore mass and energy savings, along with the corresponding approximating functions, are presented in Fig. 1.

Table 8

Results of ore production parameter calculations for the original data set ( $Q$ ) and the truncated data set ( $Q'$ )

Year	Parameters of the original data set ( $Q$ )				Parameters of the truncated data set ( $Q'$ )				$P(Q \geq m_Q)$
	Mean $m_Q$	Std. deviation $\sigma_Q$	Skewness $A_Q$	Kurtosis $E_Q$	Mean $m_Q$	Std. deviation $\sigma_Q$	Skewness $A_Q$	Kurtosis $E_Q$	
1	316654	17684.7	0.0242	-0.884	331276	10110.2	0.515	1.81	0.498
2	321507	19443	0.628	-0.149	338543	13826.6	1.09	3.93	0.458
3	307690	26296	-0.11	-1.333	329750	14257	0.252	1.15	0.509
4	293556	29153	0.453	-0.708	319041	19075.5	0.853	3.25	0.47
5	313330	17720	1.25	1.57	329176	15817.6	1.303	3.84	0.417
6	324532	16496	1.05	0.129	339753	13151.6	1.106	3.69	0.43
7	327409	13743	0.146	0.084	338556	8708.1	1.111	4.25	0.49
8	324966	12102	0.512	-0.959	335743	7900	0.761	2.93	0.466

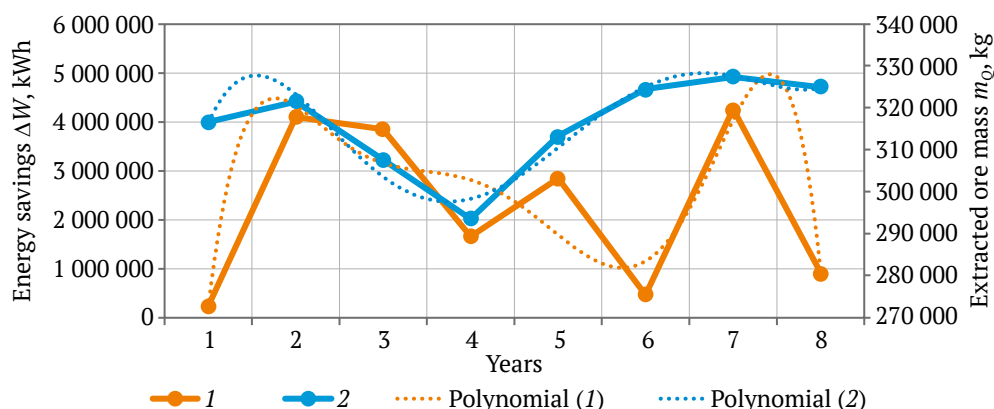


**Fig. 1.** Energy savings and extracted ore volume, along with their corresponding approximating functions:  
1 – annual variation in energy savings; 2 – annual variation in extracted ore mass;  
trend lines represent polynomial models used for approximation of dependencies (1) and (2)

Table 9

Results of calculations for changes in specific power consumption  $\Delta\omega$  and electricity losses  $\Delta W$

Year	$\Delta\omega$ , kWh/t	$\Delta\omega$ , %	$\Delta W$ , kWh
1	0.061	0.315	231135
2	1.063	5.75	4101347
3	1.043	5.11	3852665
4	0.471	2.41	1660842
5	0.757	3.88	2847939
6	0.119	0.636	465320
7	1.09	5.63	4265685
8	0.238	1.32	928772

The expected energy savings are defined as the expected value of  $\Delta W$ :

$$m_{\Delta W} = \frac{\sum_{i=1}^n \Delta W}{n}, \quad (13)$$

where  $m_{\Delta W} = 2,294,213$  kWh.

The cost of electricity under a two-rate tariff scheme is calculated as:

$$C = P_{\max} a + Wb. \quad (14)$$

The monetary savings are then determined as:

$$\Delta C = C_1 - C_2, \quad (15)$$

where  $C_1$  is the electricity cost at the current consumption level:  $C_1 = P_{\max} a + W_1 b$ .

The electricity cost at full equipment utilization is as follows:

$$C_2 = P_{\max} a + W_2 b.$$

where  $a = 4300$  rubles/kW and  $b = 6.0$  rubles/kWh.

Thus,

$$\Delta C = (W_1 - W_2)b = \Delta Wb. \quad (16)$$

### Economic benefit from replacing fan motor drives

According to the calculations (see Table 4), the electric motors installed in MVF-4, MVF-1a, and MVF-3 are significantly oversized relative to the actual load. For example: MVF-4:  $P_{cal} = 642.9$  kW;  $P_{rated} = 1250$  kW; MVF-1a and MVF-3:  $P_{cal} = 221.1$  kW;  $P_{rated} = 500$  kW. It is proposed to replace the motor of MVF-4 with an SDVV-15-39-10 motor rated at 800 kW, and the motors of MVF-1a and MVF-3 with SDV-15-34-12 motors rated at 400 kW.

The economic benefit of motor replacement is calculated as:

$$\Delta R = 0.12\Delta K + \Delta C_w, \quad (17)$$

where

$$\Delta K = K_1 - K_2,$$

here,  $K_1$  is the total cost of the currently installed motors: 8.47 million rubles;  $K_2$  is the total cost of the proposed replacement motors: 8.20 million rubles;  $\Delta K = 0.27$  million rubles. The motor cost values are presented in Table 10.

The cost of saved electricity is calculated using the two-rate tariff  $C$ .

Motor power losses, kW:

$$\Delta P = \Delta P_1 - \Delta P_2, \quad (18)$$

where  $\Delta P_1$  and  $\Delta P_2$  are the power losses of the existing and replacement motors, respectively.

Table 10

Motor costs

Motor type	Motor cost, million rubles
SDV-15-64-10U3	5.51
SD-2-85-47-8U4 SD-13-42-8	0.99
SDVV-15-39-10	4.0
SDV-15-34-12	1.4



Electricity losses, kWh:

$$\Delta W = \Delta P T, \quad (19)$$

where  $T$  is the annual operating time of the fans,  $T = 8570$  h.

Main electrical losses in the stator winding, kW:

$$P_{e1} = m I_{rated}^2 r_1 10^{-3}, \quad (20)$$

where  $r_1$  is the active resistance of the stator winding,  $\Omega$ , calculated as,

$$r_1 = \frac{\rho_v \omega_1 l_{avg}}{n_e q_e a}, \quad (21)$$

where  $\rho_v$  is the conductor resistivity adjusted for temperature (75 or 130°):  $\rho_{v(75)} = (1/47) \cdot 10^{-6}$ ,  $\Omega \cdot m$ ;  $\rho_{v(130)} = (1/39) \cdot 10^{-6}$ ,  $\Omega \cdot m$ ;  $\omega_1$  is the number of winding turns;  $l_{avg} = 2(l_1 + l_2)$  is the average turn length;  $n_e q_e$  is the effective conductor cross-section,  $mm^2$ ;  $a$  is the number of parallel branches in the winding.

Excitation losses, kW:

$$P_v = \frac{(I_{v rated}^2 r_v + 2 \Delta U_{bc} I_{v rated}) \cdot 10^3}{\eta_v}, \quad (22)$$

where  $\Delta U_{bc} = 1$  V – voltage drop at the brush contact;  $\eta_v = 0.80$ – $0.85$  – excitation system efficiency; and  $r_v$  is the field winding resistance,  $\Omega$ ,

$$r_v = \rho_v \frac{2 p \omega_1 l_{avg}}{q_l}. \quad (23)$$

Mechanical losses, comprising bearing friction and ventilation losses, kW:

$$P_{mech} = 3.68 p \left( \frac{v_r}{40} \right)^3 \sqrt{l_1}, \quad (24)$$

where  $v_r$  is the rotor peripheral speed, m/s; and  $l_1$  is stator length, m.

Additional load losses, kW:

$$P_{add} = 0.005 P_{rated}. \quad (25)$$

Total motor losses, kW:

$$\Delta P_1 = P_e + P_v + P_{mech} + P_{add}. \quad (26)$$

The results of the motor loss calculations are provided in Table 11.

Total electricity losses and the corresponding are presented in Table 12.

Table 12

Total energy losses and economic benefit

Parameter	Value
Total losses in the first motor $\Delta P_1$ , kW	216.91
Total losses in the first motor $\Delta P_2$ , kW	129.5
Loss difference $\Delta P$ , kW	87.4
Energy losses $\Delta W$ , kWh	749,018
Cost savings $\Delta C$ , million rubles	4.87
Economic benefit $\Delta R$ , million rubles	4.9

## Conclusion

1. The main mine ventilation fans at the Molibden mine operate with excessive specific energy consumption. An inspection of the fan units revealed that actual energy consumption significantly exceeds the standard values (for example, for MVF-4 the actual consumption was  $5.79 \text{ kW/m}^3$  compared to the standard  $1.86 \text{ kW/m}^3$ ). Required motor power assessments showed that the installed motors are oversized (e.g., 1250 kW for MVF-4 versus the calculated requirement of 642.9 kW). It is proposed to replace the motors with more appropriately rated units (e.g., 800 kW instead of 1250 kW for MVF-4), which will reduce energy consumption and operating costs. The expected annual economic benefit from motor replacement is 4.9 million rubles due to reduced energy losses.

2. An eight-year data analysis revealed an inverse correlation between ore output and specific energy consumption. A 10–15% increase in productivity leads to a 2–5% decrease in specific energy consumption. Reducing periods of low equipment utilization and implementing automated control systems can help minimise energy losses. The estimated annual energy savings amount to 4.87 million rubles.

3. The Kapitalnaya shaft currently operates with an outdated single-rope hoisting system (ShPM 4×36), which has limited productivity and lacks static balance. It is recommended to upgrade to modern multi-rope

Table 11

Power loss calculation results for all motors

Motor type	Electrical losses in the stator winding $P_e$ , kW	Excitation losses $P_v$ , kW	Mechanical losses $P_{mech}$ , kW	Additional load losses $P_{add}$ , kW	Total motor losses $\Sigma P$ , kW
SDV-15-64-10U3	90.66	16.1	16.4	6.25	129.4
SD-2-85-47-8U4 SD-13-42-8	10.1	14.5	2.07	2.5	29.17
SDVV-15-39-10	32.98	20.8	7.83	4	65.6
SDV-15-34-12	6.28	10.82	2.21	2	21.3



systems (e.g., MK-2.25×4), which provide higher performance, reduced vibration, and a statically balanced design. Required motor power assessments confirmed that the installed motor capacity (670 kW) meets the calculated requirements. In addition, modernizing the control systems could further improve the overall efficiency of the hoisting operation.

4. A theoretical method based on the Gram–Charlier distribution was used to calculate the statistical parameters of the truncated dataset. Equations were derived to calculate and forecast ore production volumes and the corresponding energy savings.

5. The implementation of the proposed measure will not only improve energy efficiency but also enhance environmental performance by reducing emissions. The findings of this study may be applicable to other mining operations with similar working conditions.

6. Future research may explore the use of artificial intelligence for forecasting equipment operating modes and optimizing energy consumption in real time. A detailed breakdown of energy use across key processes (e.g., crushing, transportation) is needed to enable targeted efficiency improvements.

## References

1. Balovtsev S.V. Higher rank aerological risks in coal mines. *Mining Science and Technology (Russia)*. 2022;7(4):310–319. <https://doi.org/10.17073/2500-0632-2022-08-18>
2. Pelipenko M.V., Balovtsev S.V., Aynbinder I.I. Integrated accident risk assessment in mines. *Mining Informational and Analytical Bulletin*. 2019;(11):180–192. (In Russ.) <https://doi.org/25018/0236-1493-2019-11-0-180-192>
3. Liu J., Ma Q., Wang W. et al. Risk level assessment and co prediction of underground mines for poisoning and asphyxiation accidents. *Sustainability (Switzerland)*. 2022;14(24):16640. <https://doi.org/10.3390/su142416640>
4. Brigida V.S., Zinchenko N.N. Methane release in drainage holes ahead of coal face. *Journal of Mining Science*. 2014;50:60–64. <https://doi.org/10.1134/S1062739114010098>
5. Dzhioeva A.K., Brigida V.S. Spatial non-linearity of methane release dynamics in underground boreholes for sustainable mining. *Journal of Mining Institute*. 2020;245:522–530. <https://doi.org/10.31897/PMI.2020.5.3>
6. Semin M., Kormshchikov D. Application of artificial intelligence in mine ventilation: a brief review. *Frontiers in Artificial Intelligence*. 2024;7:1402555. <https://doi.org/10.3389/frai.2024.1402555>
7. Du D., Lei W., Li X., Li Z. Research on simulation and optimization of complex ventilation system in multiple level of Shaxi copper mine. *Journal of Applied Science and Engineering*. 2024;27(10):3283–3293. [https://doi.org/10.6180/jase.202410\\_27\(10\).0002](https://doi.org/10.6180/jase.202410_27(10).0002)
8. Wang J., Xiao J., Xue Y. et al. Optimization of airflow distribution in mine ventilation networks using the modified sooty tern optimization algorithm. *Mining, Metallurgy and Exploration*. 2024;41(1):239–257. <https://doi.org/10.1007/s42461-023-00895-y>
9. Semin M.A., Popov M.D. Theoretical analysis of the influence of distributed heat sources on the stability of air flow in inclined mine workings. *Sustainable Development of Mountain Territories*. 2024;16;3(61):1374–1383. (In Russ.) <https://doi.org/10.21177/1998-4502-2024-16-3-1374-1383>
10. Bosikov I.I., Klyuev R.V., Silaev I.V., Stas G.V. Comprehensive assessment of formalized ventilation difficulty and technological processes in coal mines. *Sustainable Development of Mountain Territories*. 2023;15(3):516–527. <https://doi.org/10.21177/1998-4502-2023-15-3-516-527>
11. Li S., Huang Y., Qiu G. et al. Research and application of dust removal performance optimization of exhaust ventilation system in fully-mechanized excavation rock tunnel. *Tunnelling and Underground Space Technology*. 2025;155:106160. <https://doi.org/10.1016/j.tust.2024.106160>
12. Chen J., Zhi Y. Experimental study on the dust control performance of rotating fog curtain under the perturbation of long-pressure and short-pumping ventilation. *Scientific Reports*. 2024;14(1):29844. <https://doi.org/10.1038/s41598-024-81560-2>
13. Bosikov I.I., Klyuev R.V., Mayer A.V., Stas G.V. Development of a method for analyzing and evaluating the optimal state of aerogasodynamic processes in coal mines. *Sustainable Development of Mountain Territories*. 2022;14(1):97–106. (In Russ.) <https://doi.org/10.21177/1998-4502-2022-14-1-97-106>
14. Valiev N.G., Golik V.I., Gabaraev O.Z., Lebzin M.S. Algorithm for determining the efficiency of combining metamining technologies. *Mining Informational and Analytical Bulletin*. 2022;(11–2):52–62. (In Russ.) [https://doi.org/10.25018/0\\_236\\_1493\\_2022\\_112\\_0\\_52](https://doi.org/10.25018/0_236_1493_2022_112_0_52)
15. Nevskaya M.A., Raikhlin S.M., Chanysheva A.F. Assessment of energy efficiency projects at Russian mining enterprises within the framework of sustainable development. *Sustainability (Switzerland)*. 2024;16(17):7478. <https://doi.org/10.3390/su16177478>



16. Petrov V.L., Kuznetsov N.M., Morozov I.N. Electric energy demand management in mining industry using smart power grids. *Mining Informational and Analytical Bulletin*. 2022;(2):169–180. (In Russ.) [https://doi.org/10.25018/0236\\_1493\\_2022\\_2\\_0\\_169](https://doi.org/10.25018/0236_1493_2022_2_0_169)
17. Giraud L., Galy B. Fault tree analysis and risk mitigation strategies for mine hoists. *Safety Science*. 2018;110(Part A):222–234. <https://doi.org/10.1016/j.ssci.2018.08.010>
18. Klyuev R., Bosikov I., Gavrina O. et al. Improving the energy efficiency of technological equipment at mining enterprises. *Advances in Intelligent Systems and Computing*. 2021;1258:262–271. [https://doi.org/10.1007/978-3-030-57450-5\\_24](https://doi.org/10.1007/978-3-030-57450-5_24)
19. Shchemeleva Y.B., Sokolov A.A., Labazanova S.H. Development of hardware and a system for analyzing energy parameters based on simulation in SimInTech. *Journal of Physics: Conference Series*. 2022;012082. <https://doi.org/10.1088/1742-6596/2176/1/012082>
20. Pervuhin D.A., Trushnikov V.E., Abramkin S.E. et al. Development of methods to improve stability of underground structures operation. *International Journal of Engineering, Transactions B: Applications*. 2025;38(2):472–487. <https://doi.org/10.5829/ije.2025.38.02b.20>

### Information about the author

**Roman V. Klyuev** – Dr. Sci. (Eng.), Professor of the Department of the Automation and Control, Moscow Polytechnic University, Moscow, Russian Federation; ORCID [0000-0003-3777-7203](https://orcid.org/0000-0003-3777-7203), Scopus ID [57194206632](https://orcid.org/57194206632); e-mail [kluev-roman@rambler.ru](mailto:kluev-roman@rambler.ru)

**Received** 04.10.2024

**Revised** 07.02.2025

**Accepted** 14.02.2025